

GEOTECHNICAL, GEOLOGICAL AND EARTHQUAKE ENGINEERING

# PRACTICAL SOIL DYNAMICS

**Case Studies in Earthquake and  
Geotechnical Engineering**

MILUTIN SRBULOV



Springer

# PRACTICAL SOIL DYNAMICS

# GEOTECHNICAL, GEOLOGICAL AND EARTHQUAKE ENGINEERING

---

Volume 20

---

## *Series Editor*

Atilla Ansal, *Kandilli Observatory and Earthquake Research Institute,  
Boğaziçi University, Istanbul, Turkey*

## *Editorial Advisory Board*

Julian Bommer, *Imperial College London, U.K.*

Jonathan D. Bray, *University of California, Berkeley, U.S.A.*

Kyriazis Pitilakis, *Aristotle University of Thessaloniki, Greece*

Susumu Yasuda, *Tokyo Denki University, Japan*

For further volumes:  
<http://www.springer.com/series/6011>

# Practical Soil Dynamics

Case Studies in Earthquake  
and Geotechnical Engineering

*by*

MILUTIN SRBULOV

*United Kingdom*



Springer

Dr. Milutin Srbulov  
United Kingdom  
[srbulov@aol.com](mailto:srbulov@aol.com)

ISSN 1573-6059  
ISBN 978-94-007-1311-6 e-ISBN 978-94-007-1312-3  
DOI 10.1007/978-94-007-1312-3  
Springer Dordrecht Heidelberg London New York

Library of Congress Control Number: 2011928823

© Springer Science+Business Media B.V. 2011

No part of this work may be reproduced, stored in a retrieval system, or transmitted in any form or by any means, electronic, mechanical, photocopying, microfilming, recording or otherwise, without written permission from the Publisher, with the exception of any material supplied specifically for the purpose of being entered and executed on a computer system, for exclusive use by the purchaser of the work.

Every effort has been made to contact the copyright holders of the figures and maps which have been reproduced from other sources. Anyone who has not been properly credited is requested to contact the publishers, so that due acknowledgement may be made in subsequent editions.

Printed on acid-free paper

Springer is part of Springer Science+Business Media ([www.springer.com](http://www.springer.com))

# Preface

Karl Terzaghi formally defined soil mechanics as a separate discipline by publishing his first book in 1925. Although soil mechanics involves soil statics and dynamics, only soil statics has become well established while soil dynamics remained in a rudimentary stage until recent developments in the field of earthquake engineering. Geotechnical earthquake engineering is formally defined as a new discipline by the first international conference on geotechnical earthquake engineering held in Tokyo in 1995. An essential part of geotechnical earthquake engineering is soil dynamics.

Engineering codes and standards have followed to some extent developments in research in ground vibrations and earthquake engineering. Recent EN 1998-5 (2004) provides norms and information on a limited range of subjects only such as topographic amplification factors, liquefaction of levelled ground but not slopes, loading on retaining walls but not reinforced soil and seismic bearing capacity of shallow foundations but not piled foundations and not on soil-structure interaction. Such limitations are understandable as codes and standards are based on best practice and when a consensus on best practice is absent then codes remain brief. However, engineering practice require acceptable solutions for many subjects not covered by the existing codes. ISO 23469 (2005) use similar approach to EN 1998-5 (2004).

This volume provides information on the basic mechanisms and factors affecting the behaviour of ground and buried structures in cyclic conditions in order to help engineering judgement. The analyses are based on well known engineering principles and methods that are familiar to many readers. The accuracy and precision of the simple analyses are demonstrated for actual case histories instead of using numerical analyses and laboratory testing, which have their disadvantages such as complexity, high cost and long duration. The equations provided in this volume are suitable for hand calculations.

United Kingdom

M. Srbulov

## References

- EN 1998-5 (2004) Eurocode 8 – design of structures for earthquake resistance, part 5: foundations, retaining structures and geotechnical aspects. European Committee for Standardization, Brussels
- ISO 23469 (2005) Bases for design of structures – seismic actions for designing geotechnical works. International Organization for Standardization
- Terzaghi K (1925) Erdbaumechanik auf bodenphysikalisher grundlage. Deuticke, Vienna, Austria

# Acknowledgements

I was honoured and privileged to work with Professor Nicholas Ambraseys as his assistant (i.e. associate after the completion of my PhD in 1994) on a number of research projects supported by the Engineering and Physical Science Research Council of the United Kingdom and by the EPOCH program of the Community of European Countries at Imperial College in London (UK) during the period 1991–1997. The simplified approach used in our research is directly applicable to routine engineering practice. My initial involvement with earthquake engineering was a starting point for further work concerning soil dynamics and ground vibration related issues while working on a number of projects worldwide for Mott MacDonald Ltd.

Dr E.T.R. Dean of Caribbean Geotechnical Design Limited (Trinidad) and Soil Models Limited (UK) reviewed several of my papers and was of great help with his detailed and precise comments for the improvement of initial versions of the papers. He kindly reviewed the initial version of this volume and made a significant contribution towards the improvement of the clarity and readability of the text.

Several of my former colleagues influenced my professional carrier and hence this volume. Professor Milan Maksimovic persuaded me to switch profession from concrete structures to geotechnics right after my graduation. He pioneered studies of soil mechanics paid by Energoprojekt Co. at Imperial College in the U.K. The MSc soil mechanics study in 1984/85 enabled me to obtain the position of a research assistant later. Professor Petar Anagnosti (former principal geotechnical engineer of Energoprojekt Co. and former vice president of the International Society for Soil Mechanics and Foundation Engineering) and Mr Aleksandar Bozovic (former technical director of Energoprojekt Co. and former chairman of the committee on seismic aspects of dam design of the International Commission of Large Dams) encouraged me to apply for the position of a research assistant at Imperial College.

The editor of European Earthquake Engineering and Ingegneria Sismica journals Professor Duilio Benedetti accepted kindly for publication 20 of my papers related to geotechnical earthquake engineering in the period 1995 to end of 2010. Numerous publications of my papers encourage me to work more in the field of geotechnical earthquake engineering and related topics such as ground vibration. Dr. Massimo Tognetti from Patron Editore provided publisher's consent to use material from my

papers published in the journals European Earthquake Engineering and Ingegneria Sismica.

Ms Petra D. van Steenbergen – a senior publishing editor for geosciences with the publisher Springer showed interest in my proposals for writing books and arranged for the awards of the contracts with the help from Ms Cynthia deJonge.

The idea for writing books came from my wife Radmila, who had no time to do it herself but, instead, provided encouragement and stimulation.

# Contents

<b>1</b>	<b>Introduction</b>	<b>1</b>
1.1	Scope . . . . .	1
1.2	Codes and Standards . . . . .	1
1.2.1	National . . . . .	1
1.2.2	International . . . . .	2
1.3	Existing Methods . . . . .	2
1.3.1	Using Graphs . . . . .	2
1.3.2	Using Formulas . . . . .	13
1.3.3	Using Computer Software . . . . .	18
1.3.4	Using Small Scale Physical Models . . . . .	18
1.3.5	Using Large Scale Prototypes . . . . .	19
1.4	General Comments on Simple Analyses . . . . .	21
1.4.1	Application and Users . . . . .	21
1.4.2	Input Data and Time Involved . . . . .	21
1.4.3	Cost and Risks . . . . .	21
1.5	Summary . . . . .	21
	References . . . . .	22
<b>2</b>	<b>Main Ground Motion Sources and Properties</b> . . . . .	<b>27</b>
2.1	Introduction . . . . .	27
2.2	Earthquakes . . . . .	27
2.2.1	Earthquake Magnitude . . . . .	28
2.2.2	Principal Earthquake Hazards . . . . .	29
2.3	Industry . . . . .	35
2.3.1	Transport . . . . .	35
2.3.2	Construction and Demolition . . . . .	35
2.3.3	Blasting in Construction and Mining . . . . .	36
2.4	Summary . . . . .	36
	References . . . . .	36
<b>3</b>	<b>Typical Ground Motions, Recording, Ground Investigations and Testing</b> . . . . .	<b>39</b>
3.1	Introduction . . . . .	39

3.2	Main Ground Wave Types and Effects . . . . .	39
3.2.1	Main Types . . . . .	39
3.2.2	Main Effects . . . . .	41
3.3	Instruments and Recording . . . . .	41
3.3.1	Geophones . . . . .	43
3.3.2	Accelerometers . . . . .	44
3.4	Processing of Records . . . . .	47
3.4.1	Filtering . . . . .	47
3.4.2	Baseline Correction . . . . .	50
3.5	Site Investigation . . . . .	51
3.5.1	Surface (Non-intrusive) . . . . .	51
3.5.2	Deep (Intrusive) . . . . .	55
3.6	Laboratory Testing of Soil Samples . . . . .	58
3.6.1	Shear Strength . . . . .	58
3.6.2	Stiffness . . . . .	60
3.6.3	Shear Strength and Stiffness . . . . .	61
3.6.4	Soil Permeability . . . . .	63
3.7	Summary . . . . .	64
	References . . . . .	65
<b>4</b>	<b>Soil Properties Used in Simple Analyses . . . . .</b>	<b>67</b>
4.1	Introduction . . . . .	67
4.2	Shear Strength and Stiffness . . . . .	67
4.2.1	Non-cohesive Soil . . . . .	67
4.2.2	Cohesive Soil . . . . .	70
4.3	Permeability . . . . .	71
4.4	Summary . . . . .	71
	References . . . . .	72
<b>5</b>	<b>Fast Sliding of Non-liquefied Soil . . . . .</b>	<b>73</b>
5.1	Introduction . . . . .	73
5.2	Mechanism and Factors . . . . .	73
5.3	Existing Methods . . . . .	74
5.3.1	Co-seismic Stage . . . . .	74
5.3.2	Post-seismic Stage . . . . .	74
5.4	Simple Model for Post-seismic Stage . . . . .	75
5.5	Case Histories . . . . .	78
5.5.1	Maidipo Slide in China . . . . .	79
5.5.2	Catak Slide in Turkey . . . . .	80
5.5.3	Usoy Slide in Tajikistan . . . . .	80
5.5.4	Vajont Slide in Italy . . . . .	81
5.5.5	Higashi Takezawa Slide in Japan . . . . .	82
5.6	Discussion and Conclusions . . . . .	83
	References . . . . .	84

<b>6 Flow of Liquefied Sandy Soil . . . . .</b>	85
6.1 Introduction . . . . .	85
6.2 Mechanism and Factors . . . . .	86
6.3 Existing Methods . . . . .	86
6.4 Simple Models . . . . .	87
6.4.1 Potential of Liquefaction of Soil Slopes . . . . .	87
6.4.2 Flow of Liquefied Slope . . . . .	89
6.5 Case Histories . . . . .	91
6.5.1 Lower San Fernando Dam in California . . . . .	91
6.5.2 Sheffield Dam in California . . . . .	92
6.5.3 Calaveras Dam in California . . . . .	93
6.5.4 Fort Peck Dam in Montana – USA . . . . .	94
6.5.5 North Dike of Wachusett Dam in Massachusetts – USA . . . . .	94
6.5.6 La Marquesa Dam in Chile . . . . .	94
6.5.7 La Palma Dam in Chile . . . . .	96
6.5.8 Route 272 Embankment in Higashiarekinai – Japan . .	97
6.5.9 Vlietepolder Deposit, Zeeland Province in Netherlands . . . . .	98
6.5.10 Helsinki Harbour Fill in Finland . . . . .	99
6.5.11 Lake Merced Bank in California . . . . .	99
6.5.12 Hachiro-Gata Road Embankment in Akita – Japan .	101
6.5.13 Lake Ackerman Road Embankment in Michigan – USA . . . . .	101
6.5.14 Aberfan Coal Mine Waste in Wales – UK . . . . .	102
6.6 Discussion and Conclusions . . . . .	102
References . . . . .	107
<b>7 Massive Retaining Walls . . . . .</b>	111
7.1 Introduction . . . . .	111
7.2 Mechanism and Factors . . . . .	111
7.2.1 Bearing Capacity of Soil Under Wall Base . . . . .	112
7.2.2 Stability Against Sliding at Wall Base . . . . .	116
7.2.3 Stability Against Overturning Around the External Edge . . . . .	116
7.2.4 Stability Against Deep Seated Soil Slip . . . . .	117
7.3 Existing Methods . . . . .	118
7.3.1 Empirical by Formulas . . . . .	118
7.3.2 Numerical by Computer Software . . . . .	121
7.3.3 Experimental on Small Scale Models . . . . .	122
7.4 Simple Models and Assumptions . . . . .	122
7.4.1 Dynamic Increment of Active Soil Lateral Force . .	122
7.4.2 Co-seismic Slip . . . . .	124
7.4.3 Post-seismic Slip . . . . .	124

7.5	Case Histories . . . . .	125
7.5.1	Quay Walls at Kobe Port in Japan . . . . .	125
7.5.2	Quay Wall at Kalamata Harbour in Greece . . . . .	128
7.5.3	Quay Wall at San Antonio Port in Chile . . . . .	131
7.6	Discussion and Conclusions . . . . .	133
	References . . . . .	134
<b>8</b>	<b>Slender Retaining Walls . . . . .</b>	<b>137</b>
8.1	Introduction . . . . .	137
8.2	Mechanism and Factors . . . . .	137
8.2.1	Stability Against Forward Rotation . . . . .	139
8.2.2	Stability Against Backward Rotation . . . . .	139
8.2.3	Flexural Capacity . . . . .	139
8.2.4	Capacity of Strut or Tie Against Break . . . . .	139
8.2.5	Pull Out Capacity of Tie or Anchor . . . . .	139
8.3	Existing Methods . . . . .	140
8.3.1	Empirical by Formulas . . . . .	140
8.3.2	Numerical by Computer Software . . . . .	143
8.3.3	Experimental on Prototypes and Small Scale Models . . . . .	144
8.4	Simple Model and Assumptions . . . . .	144
8.4.1	Dynamic Increment of Active Soil Lateral Force . . . . .	144
8.5	Case Histories . . . . .	145
8.5.1	Embedded Wall of Cut and Cover Sepolia Station in Greece . . . . .	145
8.5.2	Anchored Wall at Kerameikos Station in Greece . . . . .	146
8.5.3	Sheet Pile Quay Walls in Akita Port in Japan . . . . .	147
8.6	Discussion and Conclusions . . . . .	148
	References . . . . .	149
<b>9</b>	<b>Shallow Foundations . . . . .</b>	<b>151</b>
9.1	Introduction . . . . .	151
9.2	Mechanism and Factors . . . . .	152
9.2.1	Bearing Capacity of Soil Under Foundation . . . . .	152
9.2.2	Stability Against Sliding . . . . .	152
9.2.3	Stability Against Overturning . . . . .	152
9.2.4	Settlement During and After Earthquake . . . . .	152
9.3	Existing Methods . . . . .	152
9.3.1	Empirical Using Formulas and Charts . . . . .	152
9.3.2	Numerical Using Computers . . . . .	153
9.3.3	Experimental on Small Scale Models and Prototypes . . . . .	153
9.4	Simple Models and Assumptions . . . . .	155
9.4.1	Earthquake Affected . . . . .	155
9.4.2	Machinery Affected . . . . .	158
9.4.3	Settlement Caused by Soil Vibration . . . . .	160
9.5	Case Histories . . . . .	164

9.5.1	Kawagishi-cho Apartment Building Foundation Failure in Japan . . . . .	164
9.5.2	Terveler Building Foundation Failure in Adapazari – Turkey . . . . .	165
9.5.3	Gas Turbine Foundation Vibration in Gabon . . . . .	167
9.5.4	Settlement of Foley Square Building Foundation Caused by Pile Driving at Manhattan in New York City – USA . . . . .	170
9.5.5	Settlement of a Quay Wall in Kobe Caused by the 1995 Hyogoken-Nanbu Earthquake in Japan . . . . .	171
9.6	Discussion and Conclusion . . . . .	175
	References . . . . .	176
<b>10</b>	<b>Piled Foundations</b> . . . . .	179
10.1	Introduction . . . . .	179
10.2	Mechanism and Factors . . . . .	180
10.2.1	Kinematic Interaction . . . . .	180
10.2.2	Inertial Interaction . . . . .	180
10.3	Existing Methods . . . . .	181
10.3.1	Simplified Analyses . . . . .	181
10.3.2	Rigorous Numerical Analyses . . . . .	182
10.3.3	Small Scale Models . . . . .	182
10.3.4	Full Scale Test Prototypes . . . . .	182
10.4	Simple Model . . . . .	183
10.4.1	Kinematic Effects . . . . .	183
10.4.2	Inertial Effects . . . . .	184
10.5	Case Histories . . . . .	187
10.5.1	Ten Storey Building in Mexico City . . . . .	187
10.5.2	Twelve Storey Building in Yokohama – Japan . . . . .	188
10.5.3	Imperial Valley County Services Building in California . . . . .	189
10.5.4	Dumbarton Bridge in California . . . . .	190
10.5.5	Northwest Connector in California . . . . .	191
10.5.6	Painter Street Bridge in California . . . . .	193
10.5.7	Meloland Road Overpass in California . . . . .	194
10.5.8	Ohba-Ohashi Road Bridge in Japan . . . . .	195
10.5.9	Landing Road Bridge in New Zealand . . . . .	196
10.5.10	Yachiyo Bridge in Japan . . . . .	198
10.5.11	Hanshin Expressway in Kobe – Japan . . . . .	199
10.6	Discussion and Conclusions . . . . .	200
	References . . . . .	204
<b>11</b>	<b>Tunnels, Vertical Shafts and Pipelines</b> . . . . .	207
11.1	Introduction . . . . .	207
11.2	Mechanism and Factors . . . . .	208
11.3	Existing Methods . . . . .	209

11.3.1	Empirical Based on Formulas and Graphs . . . . .	209
11.3.2	Numerical Analyses Using Computer Programs . . . .	216
11.3.3	Experimental on Small Scale Models and Prototypes .	217
11.4	Simple Methods and Assumptions . . . . .	217
11.5	Case Histories . . . . .	217
11.5.1	Cut and Cover Daikai Station in Japan . . . . .	217
11.5.2	Bolu Highway Twin Shotcrete Supported Bench Pilot Tunnels in Turkey . . . . .	222
11.5.3	Duzce Pipelines in Turkey . . . . .	227
11.6	Discussion and Conclusions . . . . .	229
	References . . . . .	229
<b>12</b>	<b>Ground Vibration Caused by Industry . . . . .</b>	<b>233</b>
12.1	Introduction . . . . .	233
12.2	Transportation and Ground Compaction . . . . .	237
12.2.1	Introduction . . . . .	237
12.2.2	Mechanism and Factors . . . . .	237
12.2.3	Existing Methods . . . . .	238
12.2.4	Simple Model and Assumptions . . . . .	240
12.2.5	Case History . . . . .	242
12.2.6	Summary . . . . .	245
12.3	Pile Driving . . . . .	246
12.3.1	Introduction . . . . .	246
12.3.2	Mechanism and Factors . . . . .	246
12.3.3	Existing Methods . . . . .	247
12.3.4	Simple Model and Assumptions . . . . .	249
12.3.5	Case History . . . . .	251
12.3.6	Summary . . . . .	252
12.4	Blasting . . . . .	252
12.4.1	Introduction . . . . .	252
12.4.2	Mechanism and Factors . . . . .	253
12.4.3	Existing Methods . . . . .	253
12.4.4	Simple Model and Assumptions . . . . .	254
12.4.5	Case History from a Limestone Quarry in Istanbul .	255
12.4.6	Summary . . . . .	257
12.5	Discussion and Conclusions . . . . .	258
	References . . . . .	258
<b>Index</b>	<b>261</b>	

# List of Symbols

Symbol	Description
$\varphi$	equivalent friction angle at the base of a sliding block
$\bar{\alpha}$	inclination to the horizontal of an equivalent block, angle along tunnel circumference
$(N_1)_{60}$	normalized blow count from the standard penetration tests
$\ddot{\theta}, \dot{\theta}$	rotational acceleration, velocity
$\ddot{u}, \dot{u}$	ground horizontal acceleration, velocity
$A_{(o)}$	cross section area, (o) coefficient
$a_{(p)h(top),g}$	horizontal acceleration, (p) peak, (top) at the ground surface, (g) ground
$A_f$	foundation area
$A_{fault}$	fault rupture area
$a_{peak,surface,depth}$	peak horizontal ground acceleration at ground surface/depth in the free field
$A_{pilecap}$	area of pile cap for a pile group or twice the cross section area of a single pile
$A_r$	nominal amplitude of a vibrating roller
$a_{structure}$	structural acceleration
$b$	translational slide toe length, coefficient
$B(')$	structural height above its foundation, foundation width (') effective
$B_f$	diameter of an equivalent circular foundation
$b_{q,\gamma,c}$	foundation base inclination factors
$b_s$	width of a vertical slice into which a potential sliding mass is divided
$c(')$	a correction coefficient, coefficient of viscous damping, (') soil cohesion in terms of effective stresses (total-pore water pressure)
$c_o$	coefficient of an embedded foundation
$c_t$	coefficient
$c_u$	shear strength of fine grained soil (clayey) including rate effect in undrained condition

$C_\theta$	dynamic stiffness coefficient in rotation
$D$	diameter of the middle of a tunnel lining, average diameter of a circular cylinder
$d_{(h)}$	horizontal distance between forces or places, minimal distance from location of interest to the surface projection of a fault (or epicentral distance where the location of a causative fault has not been reported), pile diameter, wall embedment depth
$D_{50}$	an average diameter of soil particles
$D_b$	distance to blast location
$d_f$	earthquake source to observation site distance
$D_f$	foundation depth
$d_g$	design ground displacement
$D_p$	external pile diameter
$d_p$	pile wall thickness for hollow piles
$d_{p,h}$	peak horizontal ground displacement
$d_{q,\gamma,c}$	foundation depth factors
$D_r$	soil relative density
$D_s$	maximum surface displacement of a tectonic fault, depth of a vibration source
$e$	soil void ratio, eccentricity of mass centre of gravity with respect to a pile cap underside level, embedment depth of a cylinder, eccentricity of the resultant force on footing area
$E_{(p)}$	Young's modulus, (p) pile
$E_{(s)a,(s)p}$	lateral (s) static active (a) and passive (p) force on a wall
$E_{ff}$	theoretical free-fall energy of a hammer
$E_J$	flexural stiffness
$E_m$	actual energy delivered by hammer
$f$	frequency of ground motion
$F_{(o,f)}$	factor of safety against sliding of translational landslide, (o) initial, (f) final
$F_I$	resultant horizontal acting force over pile cap area due to kinematic interaction
$F_{N,R(T),O}$	(N) normal and strike-slip, (R) reverse (T thrust), (O) unspecified faulting type indicator
$F_{p(np),d,r,s,b}$	various factor of safety for a wall
$F_s$	factor of safety against soil failure
$g$	gravitational acceleration
$G_{max}$	average equivalent (or maximum) ground shear modulus
$g_{q,\gamma,c}$	ground surface inclination factors
$G_s$	specific gravity of soil solids, equivalent linear soil shear modulus
$H$	height drop of centre of displaced soil mass, soil layer thickness, rectangular tunnel wall height

$h$	thickness of a translational slide, retained depth of soil behind a wall, depth of water in front of a wall, height of the centre of a mass, soil depth
$H_d$	drop height of a mass
$h_f$	hypocentral depth
$H_l$	distance from a foundation level to the level of soft layer below
$h_w$	wall height
$I_o$	polar moment of mass inertia around the centroid, (o) with respect to its base
$i_{q,\gamma,c}$	factors for foundation load inclination
$I_\theta$	mass moment of inertia of structure with respect to the top of a foundation
$J$	second moment of cross sectional area
$j$	depth of water level below the ground surface behind a wall
$k$	coefficient of material damping, ratio between horizontal and vertical overburden stress
$K$	static stiffness coefficient, constant
$K_{(s)a,(s)p,o}$	coefficient of static (s), active (a), passive (p), at rest (o) lateral soil pressure
$k_c$	ratio between the critical horizontal acceleration at which the factor of safety against soil failure is 1 and the gravitational acceleration
$k_p$	ratio between the peak horizontal ground acceleration and the gravitational acceleration
$k_s$	structural stiffness in horizontal direction
$K_s$	coefficient of punching shear, of lateral effective stress acting on pile shaft
$k_{y,x}$	ratios between the vertical and horizontal inertial and the gravitational acceleration,
$k_\theta$	stiffness coefficient in rocking
$K_\theta$	static stiffness coefficient in rotation
$L$	flow path length of the centre of displaced soil mass, pile depth/length, length of a translational slide
$L_f$	length of a tectonic fault area
$l_k$	critical length for buckling
$L_p$	pile shaft length
$L_{p(n,1,2),a(1,2,3)}$	lever arm of a lateral force (p) passive, (n) net, (a) active side mass
$m$	
$M_1$	bending moment at pile top due to horizontal displacement $\Delta$
$M_2$	bending moments at pile tops due to inertial effects
$m_b$	body wave magnitude of an earthquake
$M_d$	tamper mass
$M_L$	local (Richter) earthquake magnitude
$M_o$	seismic moment

$m_s$	mass (s) of a structure
$M_s$	surface wave magnitude of an earthquake
$M_w$	moment magnitude of an earthquake
$M_{\Delta,\theta}$	bending moment at the top of wall/column of a rectangular tunnel due to differential horizontal ground drift $\Delta$ and wall/column rotation $\theta$
$M_\alpha$	bending moment in a tunnel lining in perpendicular direction to the tunnel axis
$M_\omega$	resultant overturning moment, base reaction moment
$n$	soil porosity
$N(\cdot)$	axial force on a sliding surface, ( $\cdot$ ) submerged
$n_d$	number of standard deviations
$N_{eqv}$	equivalent number of uniform stress cycles
$N_k$	cone penetration test factor
$n_m$	vibration mode number
$N_{piles}$	number of piles
$N_q$	pile end bearing coefficient
$N_{q,\gamma,c}$	bearing capacity factor of a shallow foundation
$N_{SPT}$	standard penetration test blow count
$OCR$	over consolidation ratio
$P_{(o)}$	number of standard deviations, (o)
$p/\gamma$	so called pressure height of fluid
$\dot{p}_{(o)}$	effective overburden stress
$P_I$	horizontal interaction force between soil and foundation, axial force on the interface between two sliding blocks
$p_a$	atmospheric pressure
$P_{critical}$	critical force to cause buckling of a strut
$P_f$	maximum force amplitude
$PI$	soil plasticity index
$p_s$	line vertical load acting on a vertical slice
$P_{w,n,p,a}$	axial force in pile from static and inertial load, axial force acting on the interface, imbalanced water lateral force, lateral force on a wall (n) net, (p) passive, (a) active
$P_\alpha$	axial force in a tunnel lining in perpendicular direction to the tunnel axis
$q_{(f)}$	surcharge at foundation level, (f) ultimate bearing stress
$R$	resistance force caused by turbulence (collision of particles) and viscosity (rate effects), vertical component of the resultant force at wall base, radius of a circular slip surface, average radius of a circular cylinder/tunnel
$r_{(o)}$	radius of embedded (equivalent) cylinder, vertical shaft radius
$R_I$	resistance force of a pile group with at least two piles in direction of $\Delta$
$r_d$	stress reduction factor with depth

$r_f$	minimum horizontal distance at which Reyleigh waves appear at the surface from body waves
$R_{x,y}$	resultants of horizontal and vertical forces respectively acting on a vertical slice
$S$	axial pile stiffness, ground type coefficient
$S_a$	horizontal structural acceleration
$S_f$	average slip of a tectonic fault during an earthquake
$s_{q,\gamma,c}$	foundation shape factors
$s_{r,t}$	radial and tangential displacements of a circular cylinder
$S_{S,A}$	soft and stiff soil sites indicators
$S_{\omega,\theta}$	dynamic stiffness coefficient, in horizontal direction – $\omega$ , in rotation - $\theta$
$t$	time
$T_{(C,D)}$	shear force on a sliding surface, duration of sliding of a translational landslide, period of horizontal ground vibration, (C,D) periods of structural vibration
$T_1$	transversal force at pile top due to horizontal displacement $\Delta$
$T_2$	transversal forces at pile tops due to inertial effects
$T_e$	equivalent fundamental period of structural and ground vibration
$T_h$	fundamental period of horizontal ground vibration
$T_n$	Period of vibration of a soil layer
$T_r$	fundamental period of rocking structural and ground vibration
$T_s$	fundamental period of horizontal structural vibration
$T_{\Delta,\theta}$	transversal force at the top of wall/column of a rectangular tunnel due to differential horizontal ground drift $\Delta$ and wall/column rotation $\theta$
$T_\alpha$	shear force in a tunnel lining in perpendicular direction to the tunnel axis
$u_{1,2}$	slope and toe displacements of a translational slide
$u_{b,1,2}$	amplitude of horizontal displacements, (b) maximum amplitude of base horizontal displacements, (1) in one direction – down slope, (2) in two directions – of a level ground
$u_i$	radial horizontal displacement of a vertical shaft before soil yield
$u_{w(s)}$	pore water pressure at the base of a vertical slice, (s) above steady state water level for a partially submerged slope
$v$	depth below wall top
$V$	vertical force acting at the foundation underside
$v^2/(2g)$	fluid kinetic energy height
$V_p$	velocity of particle sedimentation in water
$v_{p,h}$	peak horizontal ground velocity
$v_{t,l,avr}$	wave velocity, (t) transversal, (l) longitudinal, (avr) averaged
$W$	equivalent block weight or of displaced flow mass
$w$	width of a foundation (& structure)
$w_d$	width of a vibrating drum

$W_e$	mass of explosive
$W_f$	width of a tectonic fault area
$W_s(')$	total weight of a vertical slice (above steady state water level), ('submerged weight of part of a vertical slice below steady state water level
$W_z$	saturated weight of part of a vertical slice below steady state water level
$x, r$	horizontal, slant distance
$x_i$	distance from impact
$x_r$	distance along the ground surface from a roller
$y_{rz}$	lever arms of the horizontal components of external and inertial forces respectively with respect to the centre of a trial circular slip surface with the radius R
$z$	elevation of fluid above a reference datum, height of truncated part of a cone
$z_I$	pile settlement
$\Delta E_a$	dynamic increment of active soil lateral force
$\Delta M_\theta$	second moment of inertia of trapped mass of soil beneath a foundation in rotation when the Poisson's ratio >1/3
$\Delta_s$	equivalent horizontal displacement of ground surface, (s) differential horizontal soil displacement along tunnel height
$\Delta_w \Delta t^{-1}$	peak particle velocity
$\Delta \sigma_{v,z}$	additional vertical stress at a depth z due to foundation load
$H_\omega$	horizontal harmonic force
$\alpha_p$	ground cohesion mobilization factor along pile shaft
$\alpha_{(s)}$	angle of inclination to the horizontal of an equivalent block and soil cohesion mobilisation factor (s) the base of a vertical slice
$\beta$	angle of rotation of pile cap, angle of inclination to the horizontal of the interface between slip and toe surfaces along slope
$\beta_t$	tuning ratio
$\delta_b$	friction angle between soil and pile cap in coarse grained soil (silt, sand, gravel), angle of inclination to the horizontal of the toe of a slip surfaces along slope, (b) between wall back and soil
$\delta_\phi$	friction angle between ground and pile shaft
$\phi_{(I)}$	soil friction angle, (I) in static condition
$\gamma_{s,w}$	unit weight of soil (s) and water (w)
$\gamma_{(d)}$	(average) shear strain (over pile length), soil unit weight, (d) dry
$\eta_{aw}$	absolute viscosity of water
$\eta_w$	inclination to the horizontal of soil surface at the back of a wall (positive upwards)
$\lambda$	A mean annual rate of exceedance of an earthquake magnitude
$\mu$	shear modulus of the Earth's crust
$\nu$	Poisson's ratio

$\phi$	back of wall inclination to the vertical (positive from back to front)
$\theta$	angle of inclination to the horizontal of the slip surfaces along slope, rotation of the structure and its foundation, rotation of a wall/column of rectangular tunnel
$\rho$	ground unit density
$\sigma'$	effective axial stress
$\sigma'_m$	mean principal effective stress
$\sigma'_n$	axial stress acting on the sliding surface along slope
$\sigma_3$	confining effective pressure
$\sigma_v(\cdot)$	stress, v –vertical, ( $\cdot$ ) – effective, r – radial, t – tangential
$\tau_{(hv),max}$	soil shear strength (hv) in horizontal to vertical plane, (max) maximum
$\tau/\sigma'_v$	stress ratio
$\omega_{(d,o)}$	circular frequency
$\xi$	damping ratio
$\psi$	angle of pile inclination to the vertical, also between horizontal and the gravitational accelerations

# **Chapter 1**

## **Introduction**

### **1.1 Scope**

Engineers prefer to use codes for design of structures subjected to cyclic and dynamic loads. However, design codes are very brief concerning the seismic response of underground structures (foundations, tunnels, pipelines) and when they provide recommendations on the best practice these recommendations are limited to usual types of structures (buildings) and ground conditions. The users of British Standards are aware that compliance with them does not necessarily confer immunity from relevant statutory and legal requirements. Often engineers need to seek advice and help from specialists in soil dynamics. Because the issues in soil dynamics are rather complex, the specialist use simple considerations and methods not least for checking of the results of more complex analyses. Hence, engineers can use simple considerations and methods for assessment of severity of a problem before engaging specialists for solution of the problem.

The aim of this volume is to provide information on the basic mechanisms and factors affecting the behaviour of ground and buried structures in cyclic conditions in order to help engineering judgement. The analyses are based on well known engineering principles and methods that are familiar to many readers. The accuracy and precision of the simple analyses are demonstrated for actual case histories instead of using numerical analyses and laboratory testing, which have their disadvantages such as complexity, high cost and long duration. The equations provided in this volume are suitable for hand calculations.

### **1.2 Codes and Standards**

#### ***1.2.1 National***

Increasing globalization and sharing of information has led to the gradual replacement of many national codes by international ones, generally supported by country-specific provisions where deemed necessary. The national codes are usually subject oriented concerning the effects of earthquakes, machinery, construction, mining and

transport industries. The national codes or annexes to international codes usually contain location specific data such as the levels of earthquake excitation, allowable noise and vibration limits and references to other relevant national legislations.

Examples of rather comprehensive national codes are American and European standards available for soil dynamic testing (ASTM D3999, 4015, 4428, 5777, 7128, 7400) and design in seismic condition (IBC 2009, EN 1998-1, 5). National codes exist concerning ground and structural vibration issues (e.g. ANSI S2.47, S3.18 and 3.29, US DOT-293630-1, BS 5228-2, 6472, 7385-2, DIN 4024-1 and 2, 4150-3, 45669-1, 45672-1, AS 2187.2, OENORM S9020, CSA Z107.54, SS 460 48 66, NS 8141, TS 10354 according to Skipp, 1998, and others).

### ***1.2.2 International***

The International Standards Organization (ISO), with the headquarters in Geneva, published a number of standards related to the issues of ground and structural vibrations and their effects on humans and structures (e.g. ISO 2631/1 to 3, 4866, 6897, 8041, 8569, 9996, 10811-1 and 2, 10815, 14837-1, 23469 etc.). The international standards will replace national standards when the level of local development and treatments of code subjects become acceptable to the users.

## **1.3 Existing Methods**

### ***1.3.1 Using Graphs***

When the major factors that affect an event do not exceed three then the effects of the factors on the results of an event can be plotted on a graph in two-dimensions. Frequent plots include:

- ground acceleration/velocity/displacement attenuation relationships
- Fourier and response spectral acceleration/velocity/displacement relationships
- mean annual rate of exceedance of earthquake magnitudes
- boundaries between liquefied and non-liquefied sandy soil
- soil stiffness and damping ratio change with strain
- cyclic stress ratio effect on the number of cycles to failure
- amplification factor change with the tuning ratio

#### ***1.3.1.1 Examples of Attenuation Relationships for Peak Ground Motion and Permanent Co-seismic Displacement***

Ambraseys et al. (2005) proposed the following relation between the peak horizontal ground acceleration  $a_{ph}$  in  $\text{m/s}^2$ , the earthquake moment magnitude  $M_w$ , and the minimal distance  $d$  from the location of interest to the surface projection of a

fault (or epicentral distance where the location of the causative fault has not been reported):

$$\log_{10}(a_{p,h}) = 2.522 - 0.142 \cdot M_w + (-3.184 + 0.314 \cdot M_w) \cdot \log_{10}\sqrt{d^2 + 7.6^2} + S + F, \quad (1.1)$$

where  $S = 0.137$  for soft soil sites (with the transversal wave velocity range between 180 and 360 m/s to a depth of 30 m),  $S = 0.05$  for stiff soil sites (with the transversal wave velocity range between 360 and 750 m/s to a depth of 30 m) and 0 otherwise,  $F = -0.084$  for normal and strike-slip faulting earthquakes,  $F_T = 0.062$  for reverse (thrust) faulting earthquakes,  $F = -0.044$  for unspecified faulting earthquakes and 0 otherwise. The standard deviation is 0.222–0.022  $M_w$ . One standard deviation is added when it is expected that the effect of one of the following factors may increase the peak acceleration above the average value.

- Rupture directivity and fling step near tectonic faults
- Confining and focusing by sediment basin edges
- Topographic amplification by ridges and canyons
- Wave bouncing from Moho surface (the Earth's crust and mantle boundary)

The average peak horizontal accelerations of rock and soft soil from unspecified faulting earthquakes are shown in Fig. 1.1.

According to Fig. 1.1, the average peak horizontal acceleration of soft soil sites can reach  $7.7 \text{ m/s}^2$  while on rock  $5.6 \text{ m/s}^2$  for the moment magnitude  $M_w = 8$  indicating the importance of local soil amplification of bedrock acceleration.

Akkar and Bommer (2007) proposed the following attenuation relationship between the peak horizontal ground velocity  $v_{p,h}$  in cm/s, the earthquake moment

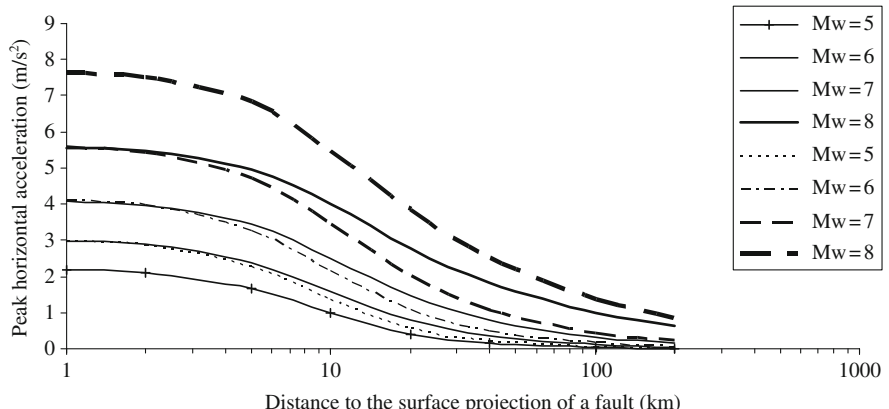


**Fig. 1.1** The average peak horizontal accelerations of rock (continuous lines) and soft soil sites (dashed lines) from unspecified faulting according to Equation (1.1)

magnitude  $M_w$ , and the minimal distance  $d$  from the location of interest to the surface projection of the fault (or the epicentral distance where the location of the causative fault has not been reported)

$$\log_{10}(v_{p,h}) = -1.26 + 1.103 \cdot M_w - 0.085 \cdot M_w^2 + (-3.103 + 0.327 \cdot M_w) \cdot$$

$$\log_{10}\sqrt{d^2 + 5.5^2} + S + F, \quad (1.2)$$

where  $S = 0.266$  for soft soil sites (with the transversal wave velocity range between 180 and 360 m/s to a depth of 30 m),  $S = 0.079$  for stiff soil sites (with the transversal wave velocity range between 360 and 750 m/s to a depth of 30 m) and 0 otherwise,  $F = -0.083$  for normal and strike-slip faulting earthquakes,  $F = 0.0116$  for reverse (thrust) faulting earthquakes and 0 otherwise. The standard deviation is  $0.344 - 0.04 M_w$ . One standard deviation is added when it is expected that the effect of one of the following factors may increase the peak acceleration above the average value.

- Rupture directivity and fling step near tectonic faults
- Confining and focusing by sediment basin edges
- Topographic amplification by ridges and canyons
- Wave bouncing from Moho surface (the Earth's crust and mantle boundary)

The average peak horizontal velocities of rock and soft soil from unspecified faulting earthquakes are shown in Fig. 1.2.

Figure 1.2 indicates that the average peak horizontal velocity of soft soil sites can reach 97 cm/s while on rock 59 cm/s for the moment magnitude  $M_w = 8$  indicating the importance of local soil amplification of bedrock velocity.

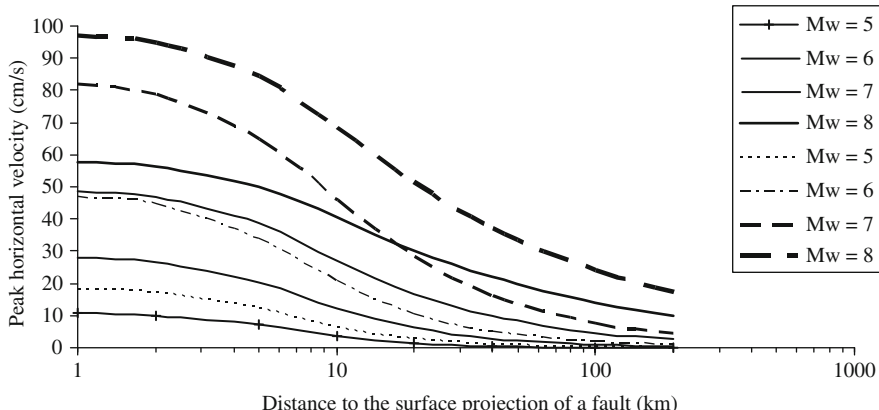


**Fig. 1.2** The average peak horizontal velocity of rock (*continuous lines*) and soft soil sites (*dashed lines*) from unspecified faulting according to Equation (1.2)

Bommer and Elnashai (1999) proposed the following attenuation relation between peak horizontal ground displacement  $d_{p,h}$  in cm, the surface wave magnitude  $M_s$ , and the minimal distance  $d$  to the surface projection of the fault (or epicentral distance where the location of the causative fault has not been reported):

$$\log_{10}(d_{p,h}) = -1.757 + 0.526 \cdot M_s - 1.135 \cdot \log_{10}\sqrt{d^2 + 3.5^2} + S + 0.32 \cdot P, \quad (1.3)$$

where,  $S = 0.114$  for soft soil sites (with the transversal wave velocity range between 180 and 360 m/s to a depth of 30 m),  $S = 0.217$  for stiff soil sites (with the transversal wave velocity range between 360 and 750 m/s to a depth of 30 m) and 0 otherwise,  $P$  is a variable that takes a value of 0 for mean peak displacement and 1 for 84-percentile values of exceedance of the mean peak displacement. One standard deviation is added when it is expected that the effect of one of the following factors may increase the peak acceleration above the average value.

- Rupture directivity and fling step near tectonic faults
- Confining and focusing by sediment basin edges
- Topographic amplification by ridges and canyons
- Wave bouncing from Moho surface (the Earth's crust and mantle boundary)

Based on the above equation, the average peak horizontal displacements for rock and soft soil are shown in Fig. 1.3.

According to Fig. 1.3, the average peak horizontal displacement of soft soil sites can reach 108 cm while on rock 65 cm for the surface wave magnitude  $M_s = 8$  indicating the importance of local soil amplification of bedrock displacement.

Ambraseys and Srbulov (1994, 1995), among others, provided the attenuation relationships of co-seismic permanent displacements depending on earthquake

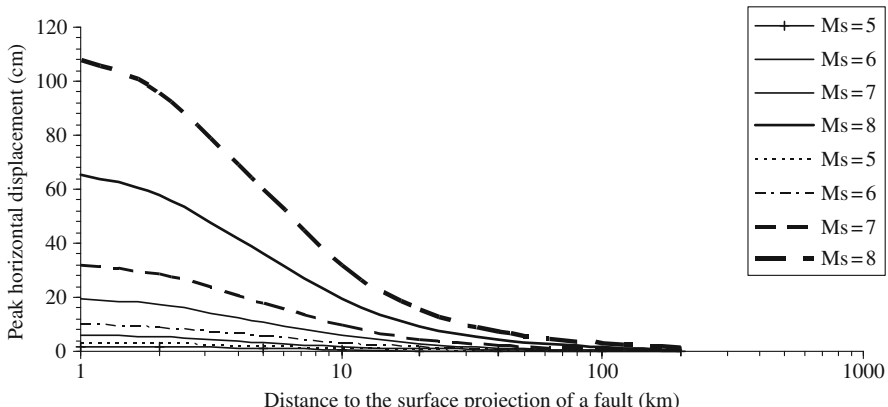


**Fig. 1.3** The average peak horizontal displacement of rock (continuous lines) and soft soil sites (dashed lines) from unspecified faulting according to Equation (1.3)

magnitude, earthquake source distance and the ratio between the critical acceleration for slope instability and the peak horizontal acceleration of ground. The attenuation relationships have been derived using least square regression performed on the permanent ground displacements, which are calculated using double integration in time of the difference between the base acceleration and the critical acceleration. The following assumptions and limitations apply:

- Constant critical acceleration ratio is independent on the amount and rate of sliding.
- Earthquake surface wave magnitude  $M_s$  range 5 to 7.7.
- Earthquake source distances to 50 km.
- Acceleration records caused by thrust (46%), normal (26%) and strike slip (29%) faults (Fig. 2.5) with the mean depth of the events  $10 \pm 4$  km.
- One-way horizontal component of displacement only for slopes. Down slope displacement is calculated by dividing the horizontal component with  $\cos\bar{\alpha}$ ,  $\bar{\alpha}$  is inclination to the horizontal of the equivalent block.
- Horizontal ground acceleration was considered only.

The attenuation relationship for one-way (down slope only) permanent horizontal component of displacements on sloping ground is according to Ambraseys and Srbulov (1994, 1995)

$$\log_{10}(u_1) = -2.41 + 0.47 \cdot M_s - 0.01 \cdot r_f + \log_{10} \left( \frac{\left[ 1 - \left( k_c / k_p \right) \right]^{2.64}}{\left( k_c / k_p \right)^{1.02}} \right) + 0.58 \cdot p, \quad (1.4)$$

and for two-way displacement on level ground is

$$\log_{10}(u_2) = -2.07 + 0.47 \cdot M_s - 0.012 \cdot r_f + \log_{10} \left( 1 - k_c / k_p \right)^{2.91} + 0.6 \cdot p, \quad (1.5)$$

where  $u_{1,2}$  are in cm,  $r_f = (h_f^2 + d_f^2)^{0.5}$ ,  $h_f$  is the hypocentral depth,  $d_f$  is the source distance,  $k_c$  is the ratio between the critical horizontal acceleration at which the factor of safety of slope stability is 1 and the gravitational acceleration,  $k_p$  is the ratio between the peak horizontal ground acceleration and the gravitational acceleration,  $p$  is the number of standard deviations. The results of these relationships are shown in Fig. 1.4 for three earthquake magnitudes and three source-to-site distances.

### 1.3.1.2 Examples of Fourier Spectra and Response Spectral Acceleration, Velocity and Displacement Relationships

Jean Baptise Joseph, baron de Fourier observed first in 1822 that any periodic function can be represented by a series of sinusoidal and co sinusoidal waves (forming orthogonal pairs) with different phases and amplitudes, which are harmonically related. A plot of Fourier amplitudes versus frequency is called a Fourier amplitude

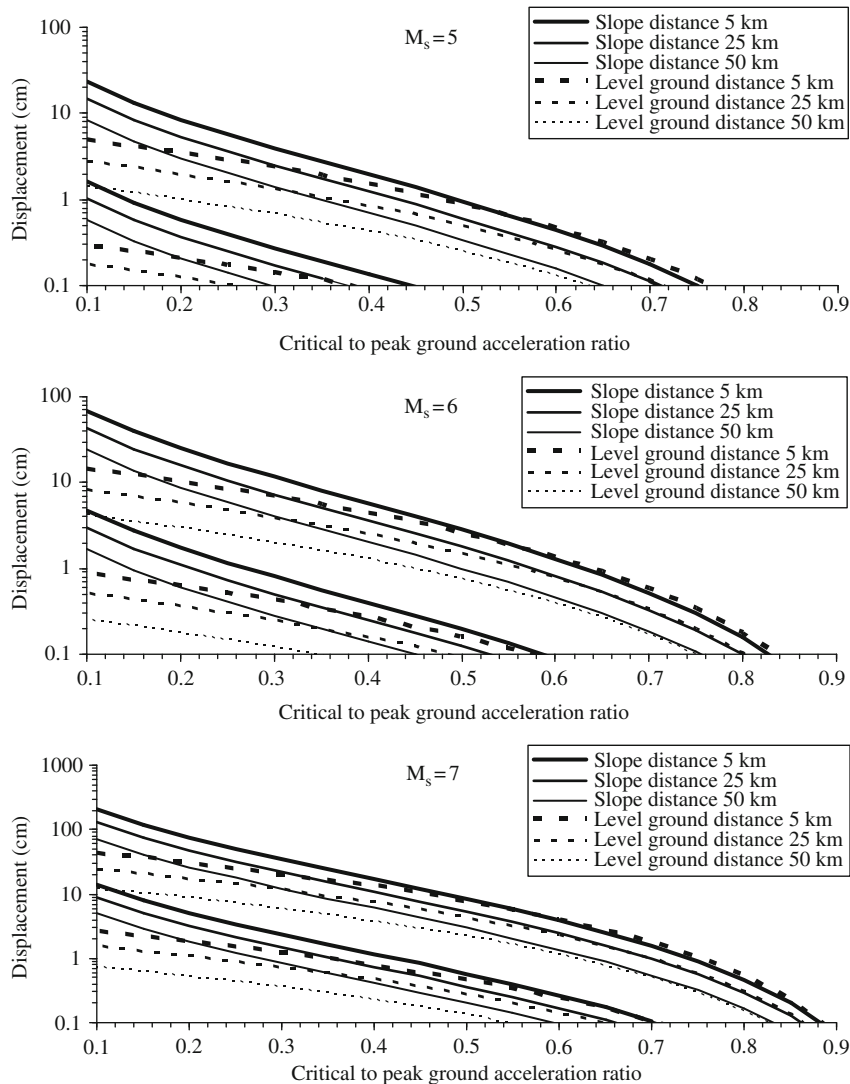


**Fig. 1.4** Average  $\pm$  one standard deviation of co-seismic displacements of slopes and level ground according to Equations (1.4) and (1.5)

spectrum. The peak value of the spectrum is used to determine the predominant frequency of free vibration of ground.

Response spectra are graphs showing maximum response (peak acceleration, velocity or displacement) of a series of elastic single degree of freedom oscillators (SDOFO) on a rigid base to the ground vibration time histories as a function of the natural periods (or frequencies) of vibration of the oscillators for a given amount

of material damping. SDOFO can oscillate in one mode only and its behaviour is described in details by Kramer (1996) among others.

The response spectra are used to determine the response of a structure with known period of vibration to the base excitation. Examples of the spectra for a time history of acceleration shown in Fig. 1.5 are shown in Figs. 1.6 and 1.7.

The calculations of Fourier and response spectra can be performed using Excel workbooks provided on <http://extras.springer.com/2010> as the appendices to the book by Srbulov (2010).

### 1.3.1.3 Example of Mean Annual Rate of Exceedance of Earthquake Magnitudes

Gutenberg and Richter (1944) gathered data for the earthquakes in southern California over a period of many years and divided the number of exceedance of each magnitude by the length of the time period to define a mean annual rate of exceedance  $\lambda$  of an earthquake magnitude. The reciprocal value of the annual rate of

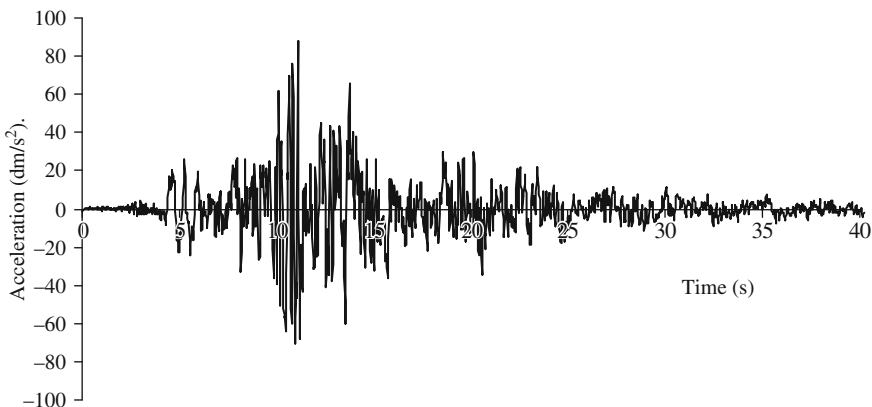


**Fig. 1.5** Example acceleration time history

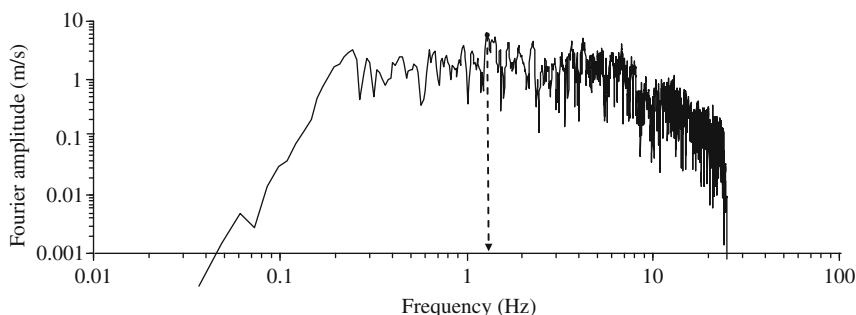


**Fig. 1.6** Fourier amplitude spectrum of the time history shown in Fig. 1.5

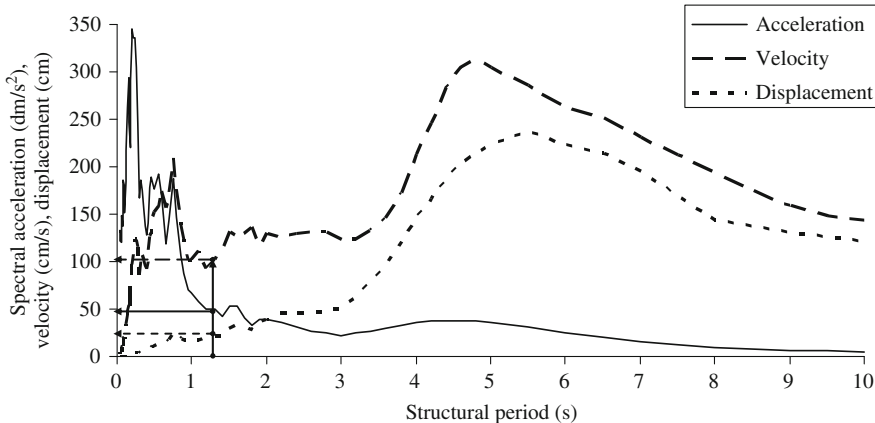


**Fig. 1.7** Elastic response spectra of acceleration, velocity and displacement for 5% of the critical damping for different structural periods and the time history shown in Fig. 1.5

exceedance for a particular magnitude is commonly referred to as the return period of earthquakes exceeding that magnitude. The example of Gutenberg–Richter relationship is based on data by Ambraseys and Sarma (1999) for the 1018 earthquakes from Iran (26° to 40° North and 44° to 64° East) with the range of surface wave magnitudes from 4.5 to 7.4 over the period of 79 years (1900 to 1979). Figure 1.8 depicts a mean annual rate of exceedance versus the surface wave magnitudes obtained by Ambraseys and Sarma (1999).

$$\begin{aligned} \log_{10}(\lambda) &= 4.7 - 0.8 \cdot M_s \quad 4.5 \leq M_s \leq 7.1 \\ \log_{10}(\lambda) &= 11.27 - 1.72 \cdot M_s \quad 7.1 \leq M_s \leq 7.4, \end{aligned} \quad (1.6)$$

where  $M_s$  is the surface wave magnitude based on the amplitude of Rayleigh waves with a period of about 20 s.

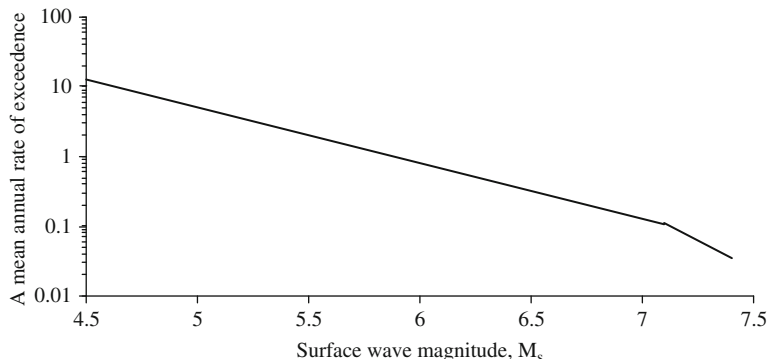


**Fig. 1.8** A mean annual rate of exceedance of Iranian earthquakes in the period 1900–1979

### 1.3.1.4 Example of Boundaries Between Liquefied and Non-liquefied Sandy Soil

Empirical procedures for analysis of potential of liquefaction of sandy soil mainly follow the work of Seed et al. (1985). The procedures are based on:

- a cyclic stress ratio  $\tau/\sigma'_v$ ,
- normalized blow count ( $N_1$ )<sub>60</sub> from the standard penetration tests (SPT),
- an empirical chart obtained from the past case histories.

According to Seed and Idriss (1971), the cyclic stress ratio, for magnitude  $M = 7.5$  earthquakes, is calculated according to the following formula for effective overburden pressure of 100 kPa

$$\frac{\tau}{\sigma'_v} = 0.65 \cdot \frac{a_{p,h}}{g} \cdot \frac{\sigma_v}{\sigma'_v} \cdot r_d , \quad (1.7)$$

where  $\tau$  is the shear stress caused by an earthquake,  $a_{p,h}$  is the peak horizontal ground acceleration,  $g$  is the gravitational acceleration,  $\sigma_v$  and  $\sigma'_v$  are the total and effective overburden pressure,  $r_d$  is a stress factor with depth. Different proposals exist for the stress factor with depth  $r_d$  because of its large scatter (e.g. Cetin et al., 2004). EN 1998-5 (2004) adopts  $r_d = 1$ .

A measured SPT blow count  $N$  can be normalized to an overburden pressure of 100 kPa according to Liao and Whitman (1986), and can be corrected to an energy ratio of 60% (the average ratio of the actual energy  $E_m$  delivered by hammer to the theoretical free-fall energy  $E_{ff}$ ) and is denoted ( $N_1$ )<sub>60</sub>.

$$(N_1)_60 = N_{SPT} \cdot \sqrt{\frac{100}{\sigma'_v}} \cdot \frac{E_m}{0.6 \cdot E_{ff}}, \quad \sigma'_v \text{ is in kPa}$$

$$0.5 < \sqrt{\frac{100}{\sigma'_v}} < 2, \quad (\text{EN 1998 - 5 : 2004}), \quad (1.8)$$

$$N'_{SPT} = 0.75 \cdot N_{SPT} \text{ at depths} \leq 3m, \quad (\text{EN 1998 - 5 : 2004})$$

where  $\sigma'_v$  is the effective overburden pressure at the depth where  $N$  is recorded from SPT's blow count. Other corrections to  $N$  are applied, such as for the bore-hole diameter, rod length and sampler type (e.g. Skempton, 1986; Cetin et al., 2004).

Boundaries between liquefiable and non-liquefiable (silty) sand are published by NCEER and are periodically updated in the light of experience (Youd and Idriss, 2001). The boundaries are shown in Fig. 1.9 for earthquake magnitude  $M = 7.5$ , effective overburden pressure of 100 kPa, nearly horizontal ground surface and depths to about 20 m below the ground surface.

Different magnitude scaling factors are used (e.g. Cetin et al., 2004). EN 1998-5 (2004) uses the magnitude correction, i.e. divider of the right hand side of Equation (1.7), suggested by Ambraseys (1988) as shown in Table 1.1.

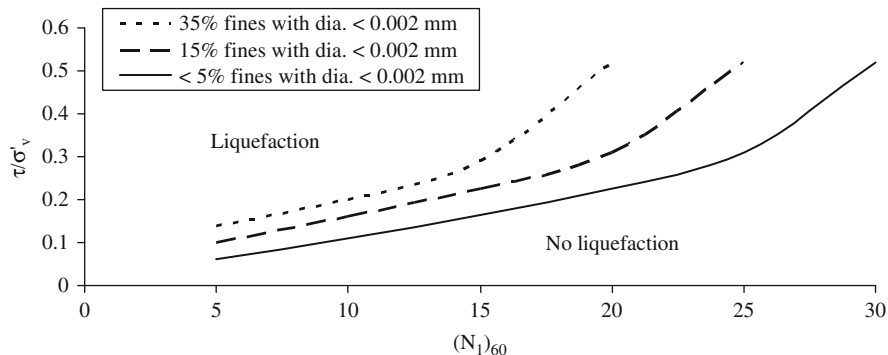


**Fig. 1.9** Boundaries between liquefaction prone and resistant soil depending on applied shear stress ratio ( $\tau/\sigma'_v$ ) for earthquake magnitude  $M = 7.5$ , effective overburden pressure 100 kPa and nearly horizontal ground surface (based on EN 1998-5, 2004)

**Table 1.1** Magnitude correction factors (dividers of the right hand side of Equation (1.7) according to Ambraseys (1988) and EN 1998-5 (2004)

Magnitude $M_s$	5.5	6.0	6.5	7.0	8.0
The correction factor	2.86	2.20	1.69	1.30	0.67

### 1.3.1.5 Examples of Soil Stiffness and Damping Ratio Change with Strain

Laboratory tests have shown that soil stiffness and damping (energy dissipation) is influenced by cyclic strain amplitude, density and acting mean principal effective stress of coarse grained soil, plasticity index and over consolidation ratio of fine grained soil, and number of loading cycles (e.g. Seed and Idriss, 1970, Hardin and Drnevich, 1972, Vucetic and Dobry, 1991, Ishibashi, 1992, etc.). Examples of soil shear modulus and damping ratio dependence on shear strain, soil plasticity index and mean effective confining pressure are shown on Fig. 1.10.

### 1.3.1.6 Example of Cyclic Stress Ratio Effect on the Number of Cycles to Failure

Soil shear strength in cyclic condition depends on number of cycles, cyclic stress or strain amplitude and for fine grained soil on frequency due to the rate effect. An example of shear strain (change in initial right angle) and effective stress (total less pore water pressure) change with a number of cycles is shown in Fig. 1.11.

When cyclic tests are repeated for a number of cyclic stress ratios during stress controlled tests then graphs showing the effect of cyclic stress ratios on a number of cycles at failure can be drawn as shown in Fig. 1.12.

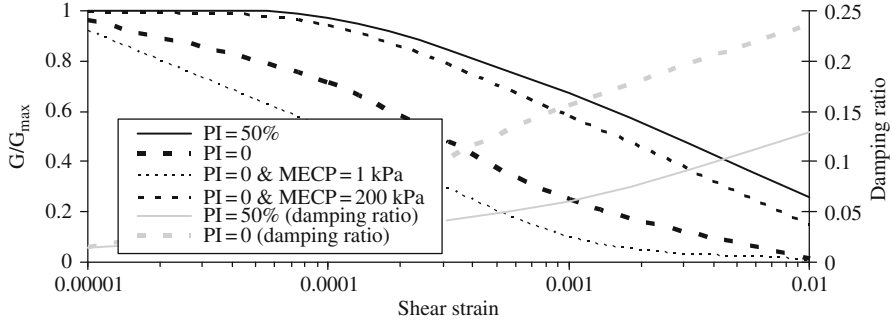


**Fig. 1.10** Dependence of shear modulus and damping ratio on shear strain, soil plasticity index (PI, %) (thick lines from Vucetic and Dobry, 1991) and mean effective confining pressure (MECP) for non-plastic soil (thin lines from Ishibashi, 1992)

### 1.3.1.7 Example of Amplification Factor Change with the Tuning Ratio

The horizontal motion of a single degree of freedom oscillator (SDOFO) to base shaking in horizontal direction is described by the following equation of motion based on the Newton's second law of motion

$$m \cdot d^2u/dt^2 + c \cdot du/dt + k \cdot u = -m \cdot d^2u_b/dt^2, \quad (1.9)$$

where  $m$  is the mass,  $c$  is the coefficient of viscous damping,  $k$  is the coefficient of elastic damping,  $u$  is the amplitude of horizontal displacement of SDOFO,  $u_b$  is the amplitude of base horizontal displacements. The amplification factor for harmonic motion of a SDOFO (e.g. Clough and Penzien, 1993) is:

$$\begin{aligned} \frac{d^2u/dt^2}{d^2u_b/dt^2} &= \sqrt{\frac{1 + (2\beta_t\xi)^2}{(1 - \beta_t^2)^2 + (2\beta_t\xi)^2}} \\ \xi &= \frac{c}{2 \cdot \sqrt{k \cdot m}}, \\ \beta_t &= \frac{\omega_d}{\omega_o} \end{aligned} \quad (1.10)$$

where  $\beta_t$  is the tuning ratio,  $\omega_d$  is the circular frequency of an input motion,  $\omega_o$  is the circular frequency of the output motion =  $k^{1/2}m^{-1/2}$ ,  $\xi$  is the damping ratio as a portion of the critical damping, which prevents oscillations. The amplification factor for different damping ratios and tuning factors are shown in Fig. 1.13.

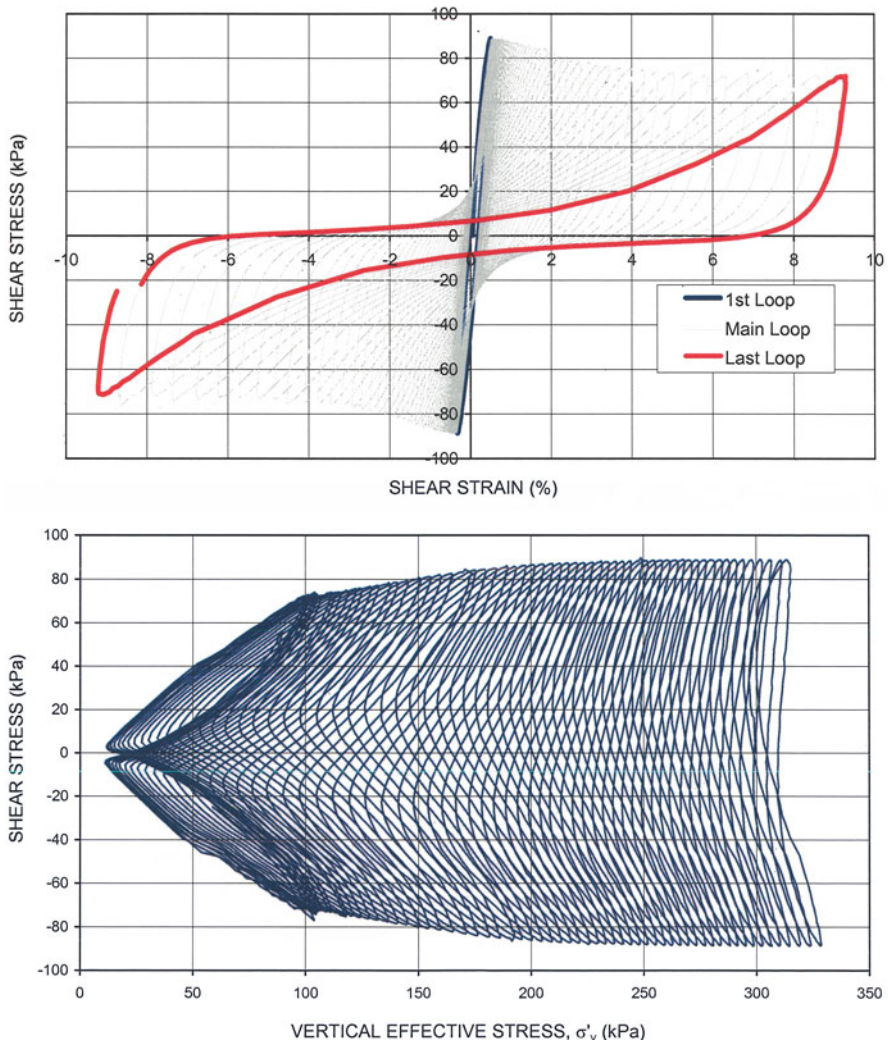


**Fig. 1.11** Example of change in shear strain and vertical effective stress acting on a sample of silt during stress controlled simple shear test

### 1.3.2 Using Formulas

Engineering codes prefer specifying formulas in addition to graphs and tables for engineering use. The use of formulas is limited to simple cases. However, the use of formulas is simple and convenient for parametric analyses to investigate the effect of influential parameters on the result.

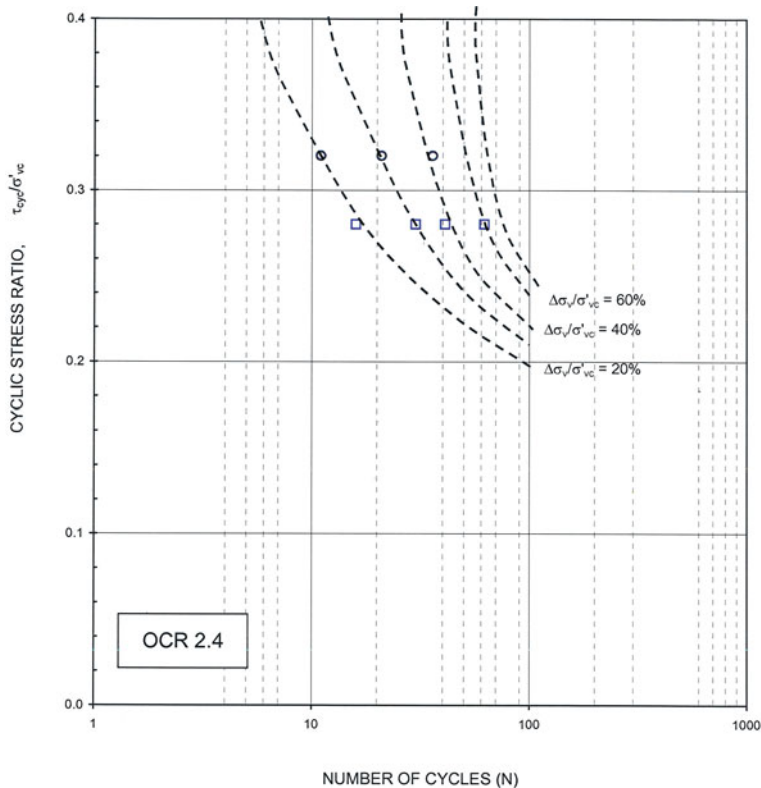


**Fig. 1.12** Example of relationships between cyclic stress ratio acting on a sample of silt and the number of cycles to failure during stress controlled simple shear tests

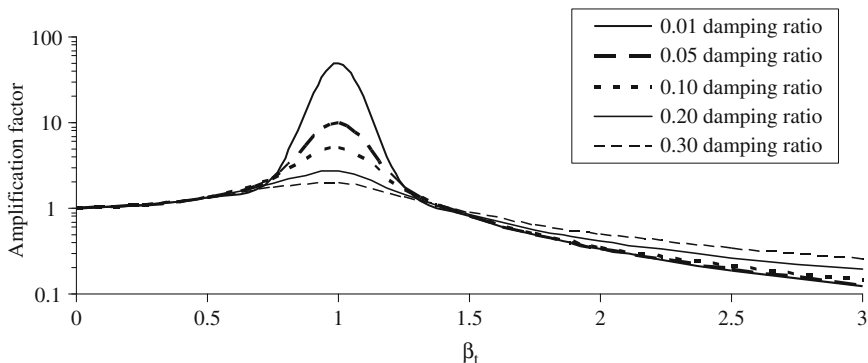


**Fig. 1.13** Amplification factor dependence on the tuning ratio

### 1.3.2.1 Example for Soil Wave Velocity from the Results of Standard Penetration Tests

A number of formulas exist for calculation of transversal wave velocity based on the results of field tests and index soil properties. For example, Japan Road Association (2002) allows the use of the following formulas for transversal wave velocity  $v_t$  in m/s:

$$\begin{aligned} v_t &= 100 \cdot N_{SPT}^{1/3}, & 1 \leq N_{SPT} \leq 25 \text{ in clay,} \\ v_t &= 80 \cdot N_{SPT}^{1/3}, & 1 \leq N \leq 50 \text{ in sand} \end{aligned}, \quad (1.11)$$

where  $N_{SPT}$  is the number of blow counts of the standard penetration test (e.g. ASTM D1586, EN 1997-2). The longitudinal wave velocity  $v_l$  can be calculated from the formula:

$$v_l = v_t \cdot \sqrt{\frac{2 - 2 \cdot \nu}{1 - 2 \cdot \nu}}, \quad (1.12)$$

where  $\nu$  is Poisson's ratio (between axial deformations in two perpendicular directions under load in one direction).

### 1.3.2.2 Examples for Maximum Soil Shear Modulus and Its Ratio

A number of formulas exist for calculation of the maximum shear modulus  $G_{max} = \rho v_t^2$ , where  $\rho$  is soil unit density and  $v_t$  is transversal wave velocity. Well known is the empirical relationship according to Seed and Idriss (1970).

$$G_{max} = 1000 \cdot K \cdot \sigma'_m^{0.5}, \quad (1.13)$$

where  $K$  is a constant dependent on soil relative density  $D_r$ ,  $K = 0.586 + 16.5D_r$  for  $30 \leq D_r \leq 90$ ,  $\sigma'_m$  is the mean principal effective stress ( $\text{lb ft}^{-2}$ ).

Laboratory test data suggest that  $G_{max}$  can be expressed as:

$$G_{max} = 625 \cdot F(e) \cdot OCR^k \cdot p_a^{1-n} \cdot \sigma'_m^n, \quad (1.14)$$

where  $F(e) = (0.3 + 0.7e^2)^{-1}$ , according to Hardin (1978),  $F(e) = e^{-1.3}$  according to Jamiolkowski et al. (1991),  $e$  is void ratio,  $OCR$  is the over consolidation ratio,  $p_a$  is atmospheric pressure in the units of  $\sigma'_m$  that is the mean principal effective stress, the stress exponent  $n$  is often taken equal to 0.5, the exponent  $k = -0.00004PI^2 + 0.0095PI + 0.0014$ , for  $0 \leq PI \leq 100$  and  $k = 0.5$  for  $PI > 100$ ,  $PI$  is soil plasticity index in percent.

Lin et al. (2000) performed a test program with measurements of transversal wave velocity by the down-hole method and large-scale dynamic triaxial tests and resonant-column tests of gravelly deposit from Taichung area of Taiwan. They found that the shear modulus ratio  $G/G_{max}$  of the gravelly cobble deposits does not decrease

below a value of about 0.5 for shear strain greater than  $10^{-4}$ , in contrast to sandy soil. They suggested the following relationship for  $G_{\max}$ :

$$G_{\max} = 305 \cdot \exp(0.0025 \cdot \sigma_3'), \quad (1.15)$$

where  $\sigma_3'$  is confining effective pressure in kPa and  $G_{\max}$  is in MPa.

Ishibashi and Zhang (1993) proposed the following relationship between shear modulus  $G$  and its maximum value  $G_{\max}$  for fine grained soil:

$$\begin{aligned} G/G_{\max} &= K \cdot \sigma'_m^m \\ K &= 0.5 \cdot \left\{ 1 + \tanh \left[ \ln \left( \frac{0.000102 + n}{\gamma} \right)^{0.492} \right] \right\} \\ m &= 0.272 \cdot \left\{ 1 - \tanh \left[ \ln \left( \frac{0.000556}{\gamma} \right)^{0.4} \right] \right\} \cdot \exp(-0.0145 \cdot PI^{1.3}), \\ n &= \begin{cases} 0 & \text{for } PI = 0 \\ 3.37 \times 10^{-6} \cdot PI^{4.404} & \text{for } 0 < PI \leq 15 \\ 7.0 \times 10^{-7} \cdot PI^{1.976} & \text{for } 15 < PI \leq 70 \\ 2.7 \times 10^{-5} \cdot PI^{1.115} & \text{for } PI > 70 \end{cases} \end{aligned} \quad (1.16)$$

where  $\sigma'_m$  is the mean principal effective stress,  $\gamma$  is shear strain,  $PI$  is soil plasticity index in percent.

### 1.3.2.3 Examples for Amplitudes of Vibration of a Horizontal Soil Layer

For a uniform isotropic soil layer overlying rigid bedrock subjected to a harmonic horizontal motion, the ratio of the amplitudes of at depth acceleration  $a_{\text{peak,depth}}$  divided by the surface  $a_{\text{peak,surface}}$  is (e.g. Kramer, 1996);

$$\frac{a_{\text{peak,surface}}}{a_{\text{peak,depth}}} = \frac{1}{\sqrt{\cos^2(\omega \cdot H/v_t) + [\xi \cdot (\omega \cdot H/v_t)]^2}}, \quad (1.17)$$

where  $\omega$  is the circular frequency of ground shaking,  $H$  is the layer thickness,  $v_t$  is transversal wave velocity and  $\xi$  is damping ratio.

Srbulov (2003) used the formula for the circular frequency  $\omega_n$  and period  $T_n$  of the  $n_m^{\text{th}}$  mode of free vibration of an infinite soil layer, with constant soil properties over an interval of shear strain, to back analyze the ratio between peak surface and at depth acceleration.

$$\omega_n = \frac{2 \cdot \pi \cdot (2 \cdot n_m - 1)}{4 \cdot H} \cdot \sqrt{\frac{G}{\rho}},$$

$$T_n = \frac{2 \cdot \pi}{\omega_n},$$
(1.18)

where  $H$  is soil layer thickness,  $G$  is shear modulus,  $\rho$  is unit soil density. The results indicated that the peak acceleration occurred in the first vibration mode in majority of the cases analyzed but that the peak ground acceleration could occur in other vibration modes up to the 6th mode. The amplitudes of first three vibration modes of a horizontal soil layer are shown in Fig. 1.14.

#### 1.3.2.4 Examples for Stiffness of Embedded and Piled Foundation

Wolf (1994), for example, summarised the following static stiffness and viscous damping coefficients shown in Table 1.2. Static stiffness coefficient is the ratio between applied force and caused displacement and viscous damping coefficient is the ratio between applied force and caused velocity of movement.

#### 1.3.2.5 Example for Kinematic Soil-Pile Interaction

Nikolaou et al. (2001) suggested the following formula obtained by data fitting for bending moment  $M$  in a pile due to kinematic soil pile interaction caused by different pile and soil stiffness

$$M \cong 0.042 \cdot a_{p,h} \cdot \rho_1 \cdot H_1 \cdot d^3 \cdot \left(\frac{L}{d}\right)^{0.30} \cdot \left(\frac{E_p}{E_1}\right)^{0.65} \cdot \left(\frac{v_2}{v_1}\right)^{0.50},$$
(1.19)

where  $a_{p,h}$  is the peak horizontal acceleration at the soil surface in the free field,  $\rho_1$  is unit density of top soil layer,  $H_1$  is the thickness of the top soil layer,  $L$  is pile length,  $d$  is pile diameter,  $E_p$  is pile Young modulus,  $E_1$  is Young modulus of top soil later,  $v_{2,1}$  are transversal wave velocities of the bottom and top soil layer respectively.

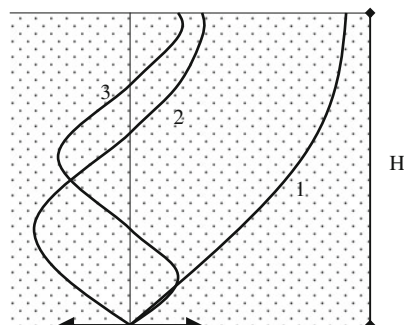


**Fig. 1.14** Normalised horizontal displacements at a time instant for the first three modes of vibration of a horizontal layer

**Table 1.2** Static stiffness and viscous coefficients for embedded (equivalent) cylindrical foundations and piles (Wolf, 1994)

Case	Embedded static stiffness, $K$	Embedded coefficient, $c_0$	Pile static stiffness, $K$
Horizontal	$\frac{8 \cdot G \cdot r_o}{2-\nu} \cdot \left(1 + \frac{e}{r_o}\right)$	$0.68 + 0.57 \cdot \sqrt{\frac{e}{r_o}}$	$2 \cdot r_o \cdot E \cdot \left(\frac{E_p}{E}\right)^{0.21}$
Vertical	$\frac{4 \cdot G \cdot r_o}{1-\nu} \cdot \left(1 + 0.54 \cdot \frac{e}{r_o}\right)$	$0.8 + 0.35 \cdot \frac{e}{r_o}$	$3.8 \cdot r_o \cdot E \cdot \left(\frac{l}{2 \cdot r_o}\right)^{0.67}$
Rocking	$\frac{8 \cdot G \cdot r_o^3}{3 \cdot (1-\nu)} \cdot \left[1 + 2.3 \cdot \frac{e}{r_o} + 0.58 \cdot \left(\frac{e}{r_o}\right)^3\right]$	$0.15631 \cdot \frac{e}{r_o}$	$1.2 \cdot r_o^3 \cdot E \cdot \left(\frac{E_p}{E}\right)^{0.75}$

*Notes:*  $G$  – soil shear modulus,  $\nu$  is soil Poisson's ratio,  $e$  is embedment depth,  $r_o$  is the radius of (equivalent) cylinder,  $E$  is soil Young modulus,  $E_p$  is pile Young modulus,  $l$  is a half thickness of a soil layer. The viscous damping coefficient  $C = r_o v_t^{-1} c_0$  of a dashpot,  $v_t$  is soil transversal wave velocity

### 1.3.3 Using Computer Software

A large number of commercial computer software exists based on boundary/finite/discrete elements and finite difference methods. The software considers parts of a domain and the connections between them together with the fulfilment of boundary and initial conditions. Besides frequent lack of knowledge concerning boundary and initial conditions, which can be minimised by using distant and transmitting boundaries, the major problem is specifying and verifying correct numerical model of complex soil behaviour in cyclic condition. Possible problems with procedure convergence and solution uniqueness can be overcome by using appropriate methods. However, chaotic behaviour in non-linear dynamics is caused by physical and not numerical reasons and cannot be avoided. Baker and Gollub (1992), among others, state that two conditions are sufficient to cause chaotic motion:

1. the system has at least three independent variables
2. the variables are coupled by non-linear relationships.

Examples of phase diagrams (plot of velocity versus displacement amplitudes) for a chaotic and harmonic motion are shown in Fig. 1.15.

An example of computed displacement vectors by finite elements method used to analyse the vibration of a compressor on rubber bearings and piled foundation is shown in Fig. 1.16.

### 1.3.4 Using Small Scale Physical Models

The models can be tested either under actual gravitational field ( $1g$ ) using shaking tables when model mass is large or under up to 200 times larger than the gravitational acceleration when model mass is a few tones. Modern apparatus include

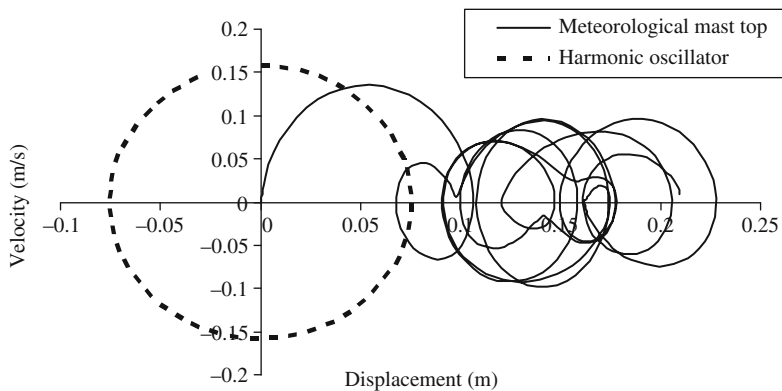


**Fig. 1.15** Examples of phase diagrams of calculated chaotic motion of a meteorological mast under wave and wind actions and of a harmonic oscillator

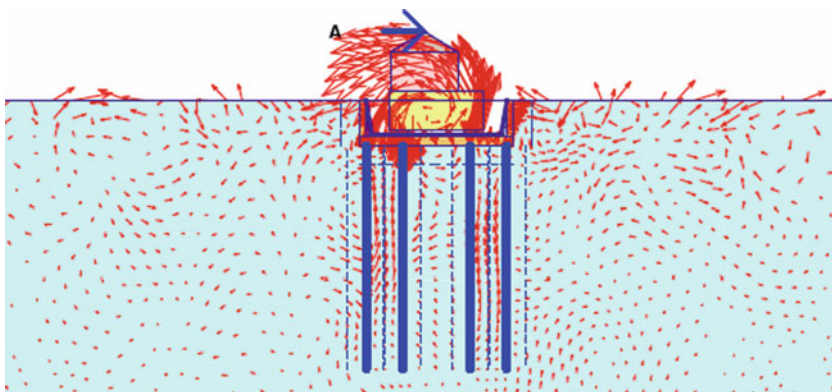


**Fig. 1.16** An example of computed displacement vectors by finite elements method used to analyse the vibration in a cross section of a compressor on rubber bearings and piled foundation

electronics and robotic machinery; hence they are complex, time consuming and costly and are, therefore, reserved mainly for research and special structures or ground conditions. Example sizes of a shaking table and geotechnical centrifuge apparatus are shown in Figs. 1.17 and 1.18. More details on centrifuge modelling is provided by Taylor (1994), among others.

### 1.3.5 Using Large Scale Prototypes

Besides unintended failures during earthquakes or damages of actual structures by construction, transport and mining activities, large scale testing of undamaged prototypes in cyclic condition is not frequent. The exceptions are standardized high-strain dynamic (STATNAMIC) testing of piles (ASTM D4945) and measurements

**Fig. 1.17** An example of a shaking table apparatus (adapted from [peer.berkeley.edu/news/1999july/geotech.html](http://peer.berkeley.edu/news/1999july/geotech.html))

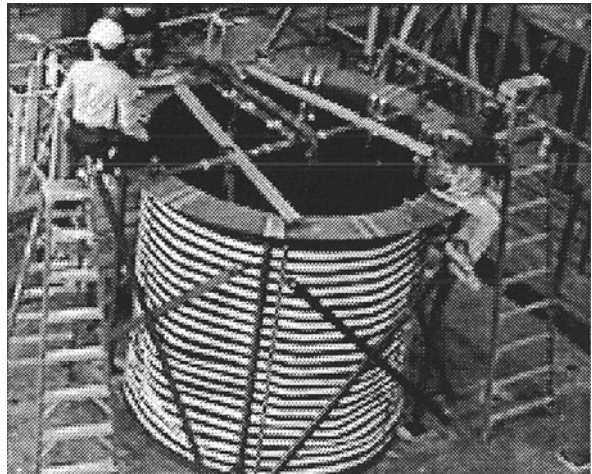


**Fig. 1.18** An example of a geotechnical centrifuge with a 9 m radius and 4.5 t model to accelerate to 50 g (adapted from [peer.berkeley.edu/news/1999july/geotech.html](http://peer.berkeley.edu/news/1999july/geotech.html))

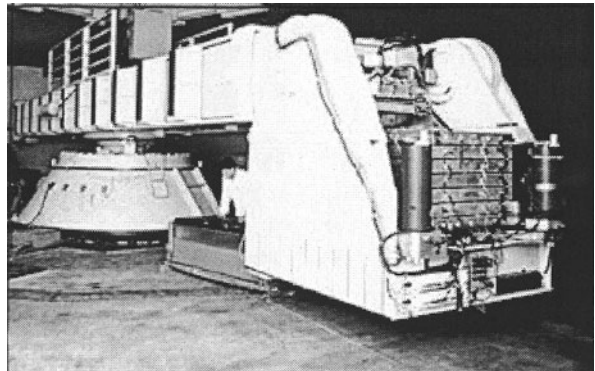


**Fig. 1.19** Setup for a weight dropping trial used to measure peak particle velocities with distance



of peak particle velocity/acceleration (and time histories of vibration) caused by falling weight or vibration sources (machine, train, pile driving, blasting). Figure 1.19 illustrates a setup used in a weight dropping trial to measure peak particle velocities with distance.

## 1.4 General Comments on Simple Analyses

### 1.4.1 Application and Users

Simple analyses are intended for obtaining better insight into the significance of main parameters affecting a problem, for assessing of severity of a problem and for rough check of the results of more complex methods. They may serve as final considerations if their results indicate that there is no need for more detailed and complex analyses. Simple analyses should be considered as rough tools to obtain results when resources, time and cost are limited such as for preliminary and concept designs, and similar situations.

The users of simple analyses should know the limitations and accuracy of the methods and be knowledgeable in the subject and exercise sound engineering judgement when using the results.

### 1.4.2 Input Data and Time Involved

Simple analyses require minimum of input data (which should be reliable and accurate as much as possible) and minimum of time for their implementation without use of computers. However, the user must always make a judgment about the applicability of simplified analyses with respect to a considered problem and avoid over simplification as well as unjustified increase in complexity if available input data are not reliable.

### 1.4.3 Cost and Risks

The cost of using simple analyses is minimal as no software or hardware is required. Possible risk is over confidence of a user who may not have sufficient knowledge and experience in practice to judge about the applicability and usefulness of the results and about limitations of simple analyses.

## 1.5 Summary

The simple analyses are useful for practicing engineers, and for both specialists and novices in the field. The analyses do not require use of computers or testing equipment. The key requirements for use of simple analyses are:

1. Understanding of a problem
2. Having an idea about possible range of the outcomes.
3. Know limitations of the method used.

## References

- Akkar S, Bommer JJ (2007) Empirical prediction for peak ground velocity derived from strong-motion records from Europe and the Middle East. *Bull Seismol Soc Am* 97:511–530
- Ambraseys NN (1988) Engineering seismology. *Earthquake Eng Struct Dyn* 17:1–105
- Ambraseys NN, Sarma SK (1999) The assessment of total seismic moment. *J Earthquake Eng* 3:439–462
- Ambraseys NN, Srbulov M (1994) Attenuation of earthquake induced ground displacements. *Earthquake Eng Struct Dyn* 23:467–487
- Ambraseys NN, Srbulov M (1995) Earthquake induced displacements of slopes. *Soil Dyn Earthquake Eng* 14:59–71
- Ambraseys NN, Douglas J, Sarma SK, Smit PM (2005) Equations for the estimation of strong ground motions from shallow crustal earthquakes using data from Europe and the Middle East: horizontal peak ground acceleration and spectral accelerations. *Bull Earthquake Eng* 3:1–53
- ANSI S2.47 (1990) Vibration of buildings – guidelines for the measurement of vibrations and evaluation of their effects on buildings. American National Standards Institute, Acoustical Society of America, New York, NY, Secretariat for Committees 51, 52 and 53
- ANSI S3.18 (1979) Guide for the evaluation of human exposure to whole-body vibrations. American National Standards Institute, Acoustical Society of America, New York, NY, Secretariat for Committees 51, 52 and 53
- ANSI S3.29 (1983) Guide to the evaluation of human exposure to vibration in buildings. American National Standards Institute, Acoustical Society of America, New York, NY, Secretariat for Committees 51, 52 and 53
- AS 2187.2 (2005) Explosives – storage and use, part 2: use of explosives. Council of Standards Australia
- ASTM D1586 Standard test method for standard penetration test (SPT) and split-barrel sampling of soils. Annual Book of ASTM Standards. American National Standards Institute
- ASTM D3999-91 Standard test methods for the determination of the modulus and damping properties of soils using the cyclic triaxial apparatus. Annual Book of ASTM Standards 04.08, American Society for Testing and Materials
- ASTM D4015-92 Standard test method for modulus and damping of soils by the resonant-column method. Annual Book of ASTM Standards 04.08, American Society for Testing and Materials
- ASTM D4428/D 4428 M-00 Standard test methods for crosshole seismic testing. Annual Book of ASTM Standards 04.08, American Society for Testing and Materials
- ASTM D4945-08 Standard test method for high-strain dynamic testing of piles. Annual Book of ASTM Standards 04.08, American Society for Testing and Materials
- ASTM D5777-00 Standard guide for using the seismic refraction method for subsurface investigation. Annual Book of ASTM Standards 04.08, American Society for Testing and Materials
- ASTM D7128-05 Standard guide for using the seismic-reflection method for shallow subsurface investigation. Annual Book of ASTM Standards, American Society for Testing and Materials
- ASTM D7400-08 Standard test methods for downhole seismic testing. Annual Book of ASTM Standards, American Society for Testing and Materials
- Baker GL, Gollub JP (1992) Chaotic dynamics, an introduction. Cambridge University Press, Cambridge, UK
- Bommer JJ, Elnashai AS (1999) Displacement spectra for seismic design. *J Earthquake Eng* 3:1–32
- BS 5228-2 (2009) Code of practice for noise and vibration control on construction and open sites – part 2: vibration. British Standards Institution

- BS 6472 (1992) Guide to evaluation of human exposure to vibration in buildings (1 Hz to 80 Hz). British Standards Institution
- BS 7385-2 (1993) Evaluation and measurement for vibration in buildings, part 2: guide to damage levels from ground borne vibration. British Standard Institution
- Cetin KO, Seed RB, Kiureghian AD, Tokimatsu K, Harder LH Jr, Kayen RE, Moss RES (2004) Standard penetration test-based probabilistic and deterministic assessment of seismic soil liquefaction potential. ASCE J Geotechn Geoenviron Eng 130:1314–1340
- Clough RW, Penzien J (1993) Dynamics of structures, 2nd edn. McGraw Hill, New York, NY
- CSA Z107.54-M85 (R2001) Procedure for measurement of sound and vibration due to blasting operations. Canadian Standards Association, Canada
- DIN 4024-1 (1988) Maschinenfundamente; Elastische Stützkonstruktionen für Maschinen mit rotierenden Massen. Deutsche Industries Norm
- DIN 4024-2 (1991) Maschinenfundamente; Steife (starre) Stützkonstruktionen für Maschinen mit periodischer Erregung. Deutsche Industries Norm
- DIN 4150-3 (1999) Erschütterungen im Bauwesen – Teil 3: Einwirkungen auf bauliche Anlage Norm Ausgabe, Deutsch, Deutsche Industries Norm
- DIN 45669-1 (1995) Messung von Schwingungssimmissionen; Teil 1: Schwingungsmesser; Anforderungen, Prüfung. Deutsche Industries Norm
- DIN 45672-1 (1991) Schwingungsmessungen in der Umgebung von Schienenverkehrswegen; Teil 1: Messverfahren. Deutsche Industries Norm
- EN 1997-2 (2007) Eurocode 7 – geotechnical design, part 2: ground investigation and testing. European Committee for Standardization, Brussels
- EN 1998-1 (2004) Eurocode 8 – design of structures for earthquake resistance, part 1: general rules, seismic actions and rules for buildings. European Committee for Standardization, Brussels
- EN 1998-5 (2004) Eurocode 8 – design of structures for earthquake resistance, part 5: foundations, retaining structures and geotechnical aspects. European Committee for Standardization, Brussels
- Gutenberg B, Richter CF (1944) Frequency of earthquakes in California. Bull Seismol Soc Am 34:1985–1988
- Hardin BO (1978) The nature of stress-strain behaviour of soils. In: Proceedings of earthquake engineering and soil dynamics symposium, vol 1, ASCE, Pasadena, CA, pp 3–89
- Hardin BO, Drnevich VP (1972) Shear modulus and damping in soil: design equations and curves. ASCE J Soil Mech Foundations Div 98:667–692
- IBC (2009) International Building Code. International Code Council, Washington, DC
- Ishibashi I (1992) Discussion to: Effect of soil plasticity on cyclic response, by M. Vucetic and R. Dobry. ASCE J Geotechn Eng 118(5):830–832
- Ishibashi I, Zhang X (1993) Unified dynamic shear moduli and damping ratios of sand and clay. Soils Foundations 33(1):182–191
- ISO 2631/2 (1989) Evaluation of human exposure to whole body vibration, part 2: continuous and shock induced vibration in buildings (1–8 Hz). International Organization for Standardization, Geneva
- ISO 2631/3 (1995) Evaluation of human exposure to whole body vibration, part 3: evaluation of exposure to whole body z-axis vertical vibration in frequency range 0.1–1.63 Hz. International Organization for Standardization, Geneva
- ISO 4866 (1990) Evaluation and measurement for vibration in buildings. Part 1: guide for measurement of vibrations and evaluation of their effects on buildings. International Organization for Standardization, Geneva
- ISO 6897 (1994) Guidelines for the evaluation of the response of occupants of fixed structures, especially buildings and off-shore structures to low frequency horizontal motion (0.063 to 1 Hz). International Organization for Standardization, Geneva
- ISO 8041 (1990) Human response to vibration – measuring instrumentation. International Organization for Standardization, Geneva

- ISO 8569 (1996) Mechanical vibration and shock measurement and evaluation of shock and vibration effects on sensitive equipment in buildings. International Organization for Standardization, Geneva
- ISO 9996 (1996) Mechanical vibration – disturbance to human activity and performance; classification. International Organization for Standardization, Geneva
- ISO 10811-1 (2000) Mechanical vibration and shock – vibration and shock in buildings with sensitive equipment – part 1: measurement and evaluation. International Organization for Standardization, Geneva
- ISO 10811-2 (2000) Mechanical vibration and shock – vibration and shock in buildings with sensitive equipment – part 2: classification. International Organization for Standardization, Geneva
- ISO 10815 (1996) Mechanical vibration – measurement of vibration generated internally in railway tunnels by the passage of trains. International Organization for Standardization, Geneva
- ISO 14837-1 (2005) Mechanical vibration – ground-borne noise and vibration arising from rail systems – part 1: general guidance. International Organization for Standardization, Geneva
- ISO 23469 (2005) Bases for design of structures – seismic actions for designing geotechnical works. International Organization for Standardization, Geneva
- Jamiolkowski M, Leroueil S, LoPriesti DCF (1991) Theme lecture: Design parameters from theory to practice. In: Proceedings Geo-Coast '91, Yokohama, Japan, pp 1–41
- Japan Road Association (2002) Specifications for highway bridges, part V: seismic design. PWRI, Japan
- Kramer SL (1996) Geotechnical earthquake engineering. Prentice Hall, Upper Saddle River, NJ
- Liao SSC, Whitman RV (1986) Overburden correction factors for SPT in sand. ASCE J Geotechn Eng 112:373–377
- Lin SY, Lin PS, Luo H-S, Juag CH (2000) Shear modulus and damping ratio characteristics of gravely deposits. Canad Geotechn J 37:638–651
- Nikolaou S, Mylonakis G, Gazetas G, Tazoh T (2001) Kinematic pile bending during earthquakes: analysis and field measurements. Geotechnique 51(5):425–440
- NS 8141 (1993) Vibrasjoner og støt – Måling av svingehastighet og beregning av veilegende grenseverdier for å unngå skade på byggverk. Standard Norge
- OENORM S9020 (1986) Bauwerkserschütterungen; Sprengerschütterungen und vergleichbare impulsförmige Immissionen. Nationale Festlegungen, Austria
- Seed HB, Idriss IM (1970) Soil modules and damping factors for dynamic response analyses. Report EERC 70-10, Earthquake Engineering Research Center, University of California, Berkeley, CA
- Seed HB, Idriss IM (1971) Simplified procedure for evaluating soil liquefaction potential. ASCE J Soil Mech Foundation Div 107:1249–1274
- Seed HB, Tokimatsu K, Harder LF, Chung RM (1985) Influence of SPT procedures in soil liquefaction resistance evaluations. ASCE J Geotechn Eng 111:1425–1445
- Skempton AW (1986) Standard penetration test procedures and the effects in sands of overburden pressure, relative density, particle size, aging and over consolidation. Geotechnique 36:425–447
- Skipp BO (1998) Ground vibration – codes and standards. In: Skipp BO (ed) Ground dynamics and man-made processes. The Institution of Civil Engineers, United Kingdom, 29–41
- Srbulov M (2003) An estimation of the ratio between horizontal peak accelerations at the ground surface and at depth. Eur Earthquake Eng XVII(1):59–67
- Srbulov M (2010) Ground vibration engineering – simplified analyses with case studies and examples. Springer, New York, NY
- SS 460 48 66 (1991) Vibration och stöt – Riktvärden för sprängningsinducerade vibrationer i byggnader Fastställd. Swedish Standard Institute
- Taylor RN (ed) (1994) Geotechnical centrifuge technology. Blackie Academic & Professional, UK
- TS 10354 (1992) Air blast and ground vibration in mining. Turkish Standard Institute
- US DOT-293630-1 (1998) High-speed ground transportation noise and vibration impact assessment. U.S. Department of Transportation, Office of Railroad Development, Washington, DC

- Vucetic M, Dobry R (1991) Effect of soil plasticity on cyclic response. ASCE J Geotechn Eng 117(1):89–107
- Wolf JP (1994) Foundation vibration analysis using simple physical models. PTR Prentice Hall, Upper saddle River, NJ
- Youd TL, Idriss IM (2001) Liquefaction resistance of soil. Summary report from the 1996 NCEER and 1998 NCEER/NSF workshop on evaluation of liquefaction resistance of soils. ASCE J Geotechn Geoenviron Eng 127:297–313

# **Chapter 2**

## **Main Ground Motion Sources and Properties**

### **2.1 Introduction**

Earthquakes and their effects represent the greatest and most frequent influential factor for ground and structural damage. Less damaging and frequent factor of structural damage and effect on people and processes are the industrial activities.

Scope of this chapter is to point to and briefly describe the main ground motion sources and their properties that are considered in the following chapters of this volume.

### **2.2 Earthquakes**

Earthquakes are caused most frequently by quick slip over tectonic faults but also by volcano activity, large landslides, large cave collapse, atomic explosions and large meteorite impact. Earthquakes are chaotic in nature (e.g. Goltz, 1998; Scholz, 1990) and the prediction of their sizes and return periods are uncertain. Known factors that affect seismic hazard at a location are:

- earthquake magnitude (various types exist based on recorded maximum amplitude of ground waves or tectonic fault area, slip and rock stiffness)
- the source to site distance (epicentral between a site and Earth's surface projection of an earthquake hypothetical centre at depth or to the surface of tectonic fault that caused an earthquake)
- rate of occurrence (return period)
- duration of ground shaking (i.e. number of pulses above a threshold level of acceleration)
- source and wave path (fault types shown in Fig. 2.5 and rupture directivity and fling step effect i.e. strong ground motion in the perpendicular and the same direction of rupture propagation of a tectonic fault)
- sediment basin edge and depth (seismic wave focusing by basin edges as optic lenses do to light rays and the edge confining effect as throwing a yo-yo ball against a wall)

- local soil layers (amplification of small and attenuation of strong acceleration)
- topography (ridges and canyons seismic wave amplitude amplification)
- space and time clustering (seismic gaps i.e. periods of minimal seismic activity in space and time)
- seismic wave bounce from the Moho surface (which is the boundary between Earth's crust and mantle)

Detail description of the effects of each individual factor is provided in specialized literature (e.g. Stewart et al., 2001). A brief summary and treatment of the effects of factors are provided by Srbulov (2008), among others.

### 2.2.1 Earthquake Magnitude

Earthquake magnitude is a major factor that affects earthquake hazards at a location. Dependence of earthquake magnitude on the causative fault area and the average slip of fault enabled establishment of empirical correlations between the fault parameters and earthquake magnitude. Wells and Coppersmith (1994) provided empirical relationships between the moment magnitude  $M_w$  (in the range 6–7), the surface rupture length  $L_r$  (km), the fault rupture area  $A_{\text{fault}}$  ( $\text{km}^2$ ), and the maximum surface displacement  $D_s$  (m) for different fault types. The ratio between fault area and its length gives an indication of its depth below the thickness of non-seismogenic zone (0–5 km).

$$\begin{aligned}
 M_w &= 5.16 + 1.12 \cdot \log L_{r,\text{strike-slip}} \pm 0.28 \cdot n_d \\
 M_w &= 5.00 + 1.22 \cdot \log L_{r,\text{reverse}} \pm 0.28 \cdot n_d \\
 M_w &= 4.86 + 1.32 \cdot \log L_{r,\text{normal}} \pm 0.34 \cdot n_d \\
 M_w &= 5.08 + 1.16 \cdot \log L_{r,\text{all}} \pm 0.28 \cdot n_d \\
 M_w &= 3.98 + 1.02 \cdot \log A_{\text{strike-slip}} \pm 0.23 \cdot n_d \\
 M_w &= 4.33 + 0.90 \cdot \log A_{\text{reverse}} \pm 0.25 \cdot n_d \\
 M_w &= 3.93 + 1.02 \cdot \log A_{\text{normal}} \pm 0.25 \cdot n_d \\
 M_w &= 4.07 + 0.98 \cdot \log A_{\text{all}} \pm 0.24 \cdot n_d \\
 M_w &= 6.81 + 0.78 \cdot \log D_{s,\text{strike-slip}} \pm 0.29 \cdot n_d \\
 M_w &= 6.52 + 0.44 \cdot \log D_{s,\text{reverse}} \pm 0.52 \cdot n_d \\
 M_w &= 6.61 + 0.71 \cdot \log D_{s,\text{normal}} \pm 0.34 \cdot n_d \\
 M_w &= 6.69 + 0.74 \cdot \log D_{s,\text{all}} \pm 0.40 \cdot n_d
 \end{aligned}, \tag{2.1}$$

where  $n_d$  is the number of standard deviations according to Wells and Coppersmith (1994). Field studies of fault rupture length and the maximum surface displacement are important for inference of the sizes of past earthquakes. A number of other studies have been performed for different regions, e.g. for the Eastern Mediterranean region by Ambraseys and Jackson (1998).

Ambraseys (1990), for example, derived the following relationships between various common earthquake magnitude scales:

$$\begin{aligned} 0.77 \cdot m_b - 0.64 \cdot M_L &= 0.73 \\ 0.86 \cdot m_b - 0.49 \cdot M_s &= 1.94, \\ 0.80 \cdot M_L - 0.60 \cdot M_s &= 1.04 \end{aligned} \quad (2.2)$$

where  $m_b$  is body wave magnitude,  $M_L$  is local magnitude,  $M_s$  is surface wave magnitude.

Chen and Chen (1989) provided the following relationships between  $\log_{10}(M_o)$  and the surface wave magnitude  $M_s$  that is based on the logarithm of maximum amplitude of Rayleigh waves with a period of about 20 s. The seismic moment  $M_o = L_f W_f S_f \mu$ , where  $L_f$  and  $W_f$  are the length and width of a tectonic fault area,  $S_f$  is the average slip on the fault during an earthquake in metres (which is typically about  $5 \times 10^{-5} L_f$  for intraplate earthquakes, Scholz et al., 1986),  $\mu$  is shear modulus of the Earth's crust. The total seismic energy released at the hypocentre during an earthquake is also estimated in Joules (J) as  $\log E = 11.8 + 1.5M_s$  (Gutenberg and Richter, 1956). The energy released by the 1960 Chilean earthquake with magnitude 9.5 could be of the order of  $10^{19}$  J (Johnston, 1990).

$$\begin{aligned} \log_{10}(M_o) &= M_s + 12.2 \text{ for } M_s \leq 6.4 \\ \log_{10}(M_o) &= 1.5 \cdot M_s + 9.0 \text{ for } 6.4 < M_s \leq 7.8 \\ \log_{10}(M_o) &= 3.0 \cdot M_s - 2.7 \text{ for } 7.8 < M_s \leq 8.5 \end{aligned} \quad (2.3)$$

When  $\log_{10}(M_o) = 1.5M_w + 10.7$  by Hans and Kanamori (1979) is replaced into Equation (1.3), it is possible to obtain the correlation between the moment magnitude  $M_w$  and the surface wave magnitude  $M_s$  and then from Equation (1.2) between  $M_s$ , the local magnitude  $M_L$  (better known as Richter magnitude that is based on logarithm of the maximum amplitude from a Wood-Anderson seismometer located 100 km from the epicentre of the earthquake) and the body magnitude  $m_b$  that is based on the logarithm of amplitude of longitudinal body waves with period of 1 s.

### 2.2.2 Principal Earthquake Hazards

The hazards are:

- severity and repeatability of ground shaking at a location causing inertial forces
- ground deformation and failure
- soil liquefaction
- ground surface rupture by tectonic fault
- tsunamis
- structural failures: (a) caused by ground failure, (b) causing ground failure, (c) caused by interaction between a structure and ground shaking
- rupture of pipelines, cables, and lifelines; consequences include gas explosion, lack of water supply for fire fighting, lack of access to help casualties etc.

While the inertial forces always occur, tsunamis are relatively rare.

### 2.2.2.1 Severity and Repeatability of Ground Shaking

Severity and repeatability of ground shaking is frequently expressed in terms of peak horizontal ground acceleration for a specified return period in years or for a percentage of probability of exceedance within a period of interest.

Amplitudes of ground acceleration in both the horizontal and vertical direction could exceed the gravitational acceleration, the predominant period of ground acceleration can vary in the range from 0.15 s on rock to 0.8 s on loose to medium dense cohesionless soil or soft to firm cohesive soil (e.g. EN 1998-1, 2004), and the acceleration duration can vary from a few seconds for small earthquake magnitudes and rock sites to several tens of seconds for large earthquake magnitudes and soft soil sites.

Examples of sources containing information on severity and repeatability of ground shaking are:

- Global seismic hazard map produced by the global seismic hazard assessment program (GSHAP, 1999) (<http://www.seismo.ethz.ch/GSHAP/>)
- European-Mediterranean seismic hazard map produced by European Seismological Commission (2003) (<http://wija.ija.csic.es/gt/earthquakes/>)
- Eurocode 8: Design of structures for earthquake resistance, Part 1: General rules, seismic actions and rules for buildings (2004)
- Uniform Building Code (1997), now replaced by the International Building Code (2009)
- Building Center of Japan: The seismic code: guidelines for structural calculations
- The United States Geological Survey – USGS ([http://nsmp.wr.usgs.gov/nsmn\\_eqdata.html](http://nsmp.wr.usgs.gov/nsmn_eqdata.html) for time histories of ground motion and <http://wwwneic.cr.usgs.gov/neis/epic/epic.html> for earthquake data)
- The Pacific Earthquake Engineering Research Center – PEER (<http://peer.berkeley.edu/smcat/>)
- The National Geophysical Data Center – NGDC (<http://www.ngdc.noaa.gov/nndc/struts/form?t=101650&s=1&d=1>)
- European Earthquake Data Base (at <http://www.isesd.cv.ic.ac.uk/>)
- Kyoshin Network K-NET (at <http://www.k-net.bosai.go.jp/>)
- National seismic codes (<http://www.iaee.or.jp/>)

Older publications and seismic codes contain information on earthquake intensity rather than magnitude. The intensity is qualitative description of the effects of earthquakes at a particular location depending on damage caused to structures and ground and human reaction. In case that no other information is available at a location, then the peak horizontal ground acceleration can be estimated based on earthquake intensity as shown in Fig. 2.1.

### 2.2.2.2 Ground Deformation and Failure

Earthquakes can trigger all types of slope failures, from disrupted slides and falls to coherent slides and lateral spreads, Fig. 2.2.

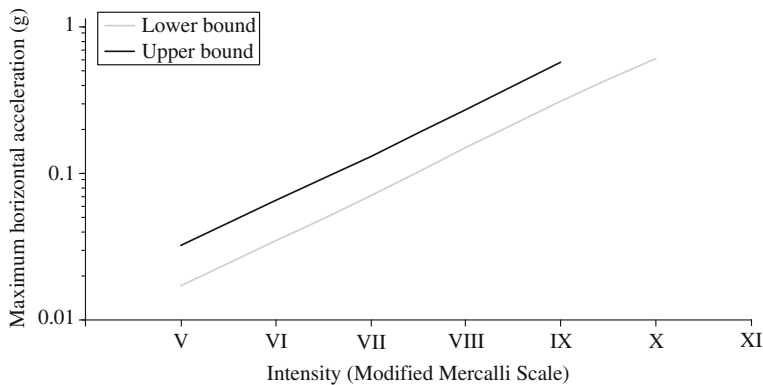


**Fig. 2.1** Relationship between maximum horizontal acceleration and earthquake intensity (MIL-HDBK, 1997)

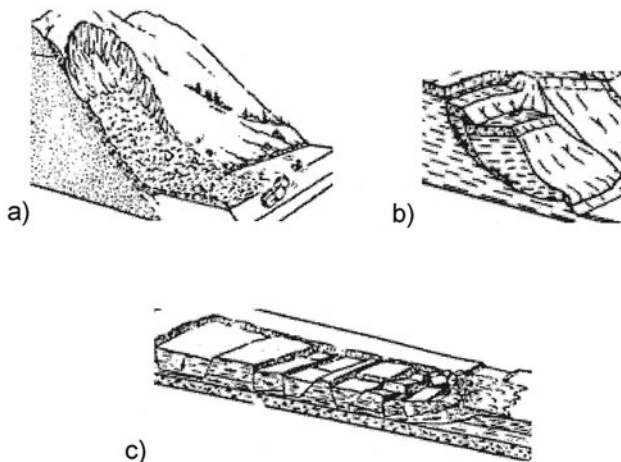


**Fig. 2.2** Some types of slope failures: (a) disrupted landslide, (b) coherent landslide, (c) lateral spread (adapted from TRBNAS, 1978)

Slope failures are identified by anomalous topography, including arcuate or linear scarps, backward-rotated masses, benched or hummocky topography, bulging toes, and ponded or deranged drainage. Unusual vegetation type or age also is common. Submarine failures can be identified with the aid of marine remote-sensing techniques. However, slope failures can also be caused by other factors such as rainfall, erosion at the toe, loading at the crest, weathering, tectonics, ground water level change and artesian pressures.

Keefer (1984) studied the effects of 40 historical earthquakes on slope failures and the results of his finding are given in Table 2.1. Table 2.1 shows that earthquake

**Table 2.1** Types, frequency and minimum triggering magnitudes of earthquakes to cause slope failures

Type of slope failure	Frequency of occurrence during earthquakes	Minimum triggering earthquake magnitude $M_L$
Rock falls, disrupted soil slides	Very frequently	4.0
Rock slides		4.0
Soil lateral spreads	Frequently	5.0
Soil slumps, soil block slides		4.5
Soil avalanches		6.5
Soil falls	Moderately frequently	4.0
Rapid soil flows, rock slumps		5.0
Sub aqueous landslides	Uncommon	5.0
Slow earth flows		5.0
Rock block slides		5.0
Rock avalanches		6.0

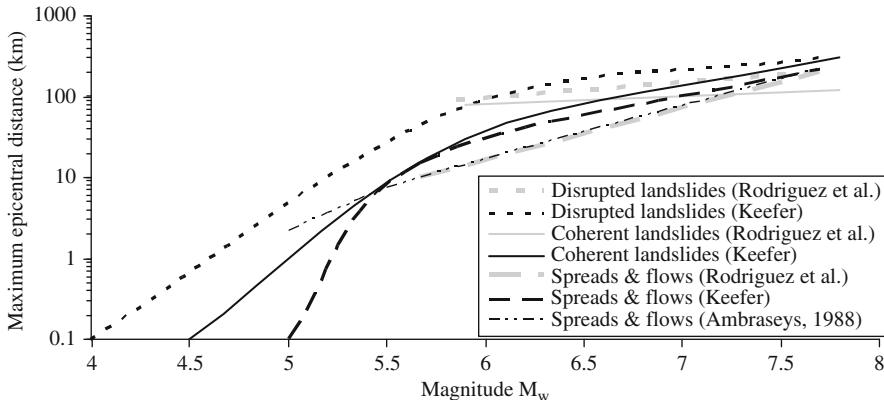


**Fig. 2.3** The maximum epicentral distances to various slope failures dependent on earthquake moment magnitudes  $M_w$

magnitudes less than 4.0 are of no engineering significance and that slope failures occur more frequently in non-cohesive materials.

Keefer (1984) and Rodriguez et al. (1999) plotted the graph of the combinations of earthquake magnitudes and fault distances at which different types of landslides occurred. A combined graph is shown in Fig. 2.3 from which it follows that no slope failures are expected beyond 120 km epicentral distance even from earthquakes with magnitudes up to 8 and that disrupted landslides are more prone to earthquake effects than coherent landslides, spreads and flows.

### 2.2.2.3 Soil Liquefaction

Earthquakes can cause liquefaction of saturated granular soil in loose to medium dense state with prevented drainage, but other causes of liquefaction exist too.

**Fig. 2.4** An aerial view of sand volcano caused by sand liquefaction (adapted from <http://sciblogs.co.nz/the-atavism/2010/09/05/what-happened-under-canterbury-yesterday-morning/>)



Obermeier (1996) noted that, among other factors causing liquefaction are rapid sedimentation and loading, artesian conditions, slumping, chemical weathering and periglacial environment. He also describes the effect of soil liquefaction observed when a low permeability layer exists over liquefied soil. If the ground surface of the cap layer is slightly inclined then the top layer exhibits cracks, uneven surface due to differential settlement and some lateral movement. If the ground surface of the cap layer is nearly horizontal and the thickness of the top layer is less than 10 m then sand volcanoes, shown in Fig. 2.4, can be formed facilitated by the existence of previous desiccation cracks, rotten tree roots and channels burrowed by animals. The expelled sandy soil spreads around and forms a layer. When such layers are buried by new deposits, they leave a permanent record of the past event. If sand volcanoes are prevented by greater thickness of the overlaying layer or tree roots provide sufficient reinforcement to hold the top layer intact then sills (intrusions) are formed within upper sandy layers.

#### 2.2.2.4 Ground Surface Rupture by Tectonic Fault

Structures should not be located across known active tectonic faults because their large movements will cause failure of the structure. There is no unique definition of fault activity. Commonly, it has been accepted that active faults caused disruption of strata during the last 10,000 years (Holocene age), 100,000 years (from late Pleistocene age) or even Quaternary age deposits covering the last about two million years.

Geomorphic changes arise due to tectonic fault rupture of the Earth's surface or by warping or folding of surfaces because of fault movement. Geomorphic changes can also be caused by climate changes (glaciation for example), weathering and erosion/deposition processes, volcanism, tsunamis, slope failures etc.

- The primary geomorphic indicator of paleoearthquakes on **normal faults** (Fig. 2.5a) is a fault scarp. Normal fault scarps vary from mountain front thousands of meters high cut in bedrock, to decimetre scale scarples that displace

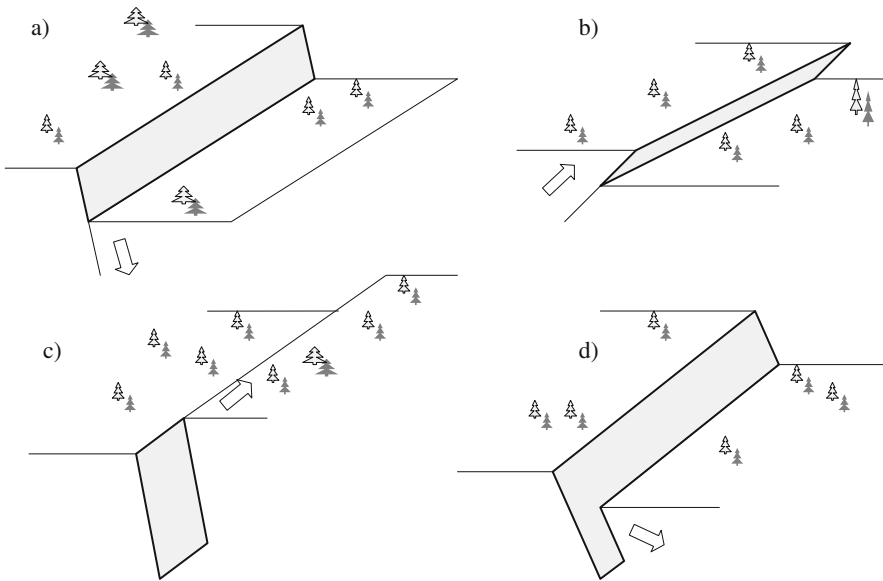


**Fig. 2.5** Types of tectonic fault movements: (a) normal, (b) reverse, (c) strike-slip, (d) oblique

Quaternary alluvium and colluviums (Stewart and Hancock, 1990). Overlaps, step-overs and gaps are common in normal fault surface ruptures. Range-front morphology can be controlled by factors other than uplift rate, such as climate, lithology and tectonic structure (McCalpin, 1996).

- The primary geomorphic indicators of paleoearthquakes on **reverse (thrust) faults** (Fig. 2.5b) are surface displacements around the faults (frequently bifurcated towards the surface), growth of surface folds and changes in the elevation of the land surface. Convergent tectonic plate margins are the largest and most widespread compressional tectonic environments. Local compressional tectonic environments are found at restraining bends or stopovers along transform and strike-slip faults, along transpressive strike-slip faults, in fold and thrust belts in some back arc regions and some in continental interiors. Two types of secondary faults are associated with thrust faults. The crest of active surface anticlines are commonly cut by normal faults and grabens that trend along the fold crest parallel to the fold axis. Sudden bending of thick-bedded sequences of sediments is often accompanied by slip along bedding planes in the fold limbs. This slip generates slip faults that are rooted in the axis of folds and extend through the fold limbs (e.g. Carver and McCalpin, 1996).
- **Strike-slip faults** (Fig. 2.5c) produce characteristic landforms including linear valleys, offset of deflected streams, shutter ridges, sag ponds, pressure ridges, benches, scarps and small horsts and grabens (Keller, 1986). In many cases the fault trace is composed of a wide zone of alternating tension gashes (extensional) and mole tracks (compressional) that trend obliquely with respect to overall fault strike.

But tectonic faults can also create underground barriers for oil reservoirs and preferential paths for ground streams.

### 2.2.2.5 Tsunamis

Tsunamis are water waves generated by impulsive geological phenomena such as earthquakes, landslides, and volcanic eruptions. Although the waves may have very small amplitude in the open ocean (less than a meter), where their wavelength makes them unnoticeable except to sensitive ocean-bottom pressure sensors, the slowing down of such waves in shallow water near coastlines leads to a dramatic increase in amplitude and shortening of their wavelength and eventual breaking. This process is known as shoaling. (e.g. Ambraseys and Synolakis, 2010).

## 2.3 Industry

Ground vibrations can be caused by various reasons but this volume is only dealing with the types of vibrations caused by the industry.

### 2.3.1 Transport

High speed trains are capable of causing soil peak particle velocity of 60 mm/s at the vibration frequency of 14 Hz (e.g. Bahrekazemi, 2004), which means the peak particle acceleration of  $60 \times 2 \times \pi \times 14 \times 1000^{-1} \sim 5.3 \text{ m/s}^2$  or  $0.53g$ . The total duration of the vibration due to a high speed train passage is between 2 and 5 s. The energy (load times settlement) applied on the ballast under rail slipper from each axle of a high speed train carriage is of the order of 0.6 kJ.

Measured peak particle velocities from road traffic was less than 10 mm/s on soft to medium stiff clay with the vibration frequency range from about 10 to 20 Hz (e.g. Barneich, 1985). However, the peak particle velocity caused by heavy construction vehicles on poorly maintained roads with pot holes can reach more than 100 mm/s (e.g. Srbulov, 2010). The pulse duration is less than a second. The energy released at the impact could be up to about 5 kJ.

### 2.3.2 Construction and Demolition

Pile driving could cause soil peak particle velocities in vicinity of a pile being driven up to almost 1 m/s (e.g. Wiss, 1981) but more frequently of the order of 100 mm/s. The soil acceleration corresponding to the peak velocity of 1 m/s at the frequency of 20 Hz in soft soil is  $1 \times 2 \times \pi \times 20 = 125 \text{ m/s}^2 \sim 12.5g$ . The energy per blow (force times fall height) of impact hammers can reach about 45 MJ. Averaged hammer efficiency is about 40% of the maximum energy of a hammer. The waste is caused by friction and plastic deformation within materials of the helmet and cushion used at pile heads to protect pile from damage. Also most of the energy

that goes into the ground from a pile is used for plastic deformation required to penetrate the pile. Only a small fraction of energy causes ground vibration, under normal circumstances.

Vibratory rollers can cause soil peak particle velocities in the vicinity of the order of 50 mm/s at frequency of about 30 Hz (e.g. Hiller and Crabb, 2000) i.e. the peak particle acceleration of  $50 \times 2 \times \pi \times 30 \times 1000^{-1} = 9.4 \text{ m/s}^2 \sim 1g$ . The maximum vibration energy (force times maximum vibration amplitude) released at a roller-soil interface could be about 1 kJ.

Demolition of structures and particularly cooling towers could cause soil peak particle velocity of more than 1 m/s in the vicinity of the structure (e.g. Eldred and Skipp, 1998) but rather not more than 100 mm/s at the distance greater than 10 m (e.g. Dowding, 2000). The energy on impact could have been 137.5 MJ.

### **2.3.3 Blasting in Construction and Mining**

Measured peak particle velocities caused by bench blasting in quarries could exceed 250 mm/s at distances of 25 m and with frequencies of 45 Hz (e.g. Kahriman, 2004) so that the peak particle acceleration exceeds  $250 \times 2 \times \pi \times 45 \times 1000^{-1} \sim 70 \text{ m/s}^2 \sim 7g$ . The energy released by the blast is proportional to the product of a half of explosive mass and the square of detonation velocity, which can be of the order of 5 km/s for a slurry type explosive or about 4.2 km/s for ANFO, for example.

## **2.4 Summary**

Earthquakes are the strongest and most frequent reason for ground and structural damage and failure with ground shaking reaching the peak horizontal ground acceleration up to about the acceleration of gravity for the predominant frequencies between about 1 and 10 Hz and the peak velocities of up to about 1 m/s.

Although ground vibration caused by the industry can reach the peak acceleration of more than ten times the gravitational acceleration and the peak velocities of 1 m/s, the amount of damage caused by such vibration is smaller than the one caused by earthquakes because of smaller amount of energy released by the industrial processes than earthquakes with smaller frequencies (longer periods) of vibrations. However, large number of cycles caused by the industry can cause fatigue of all materials.

The resonance effect, which occurs when the frequency (period) of free vibration of a source and the recipient are nearly the same, must be avoided in all cases in order to avoid damage and failure of structures and ground.

## **References**

- Ambraseys NN (1990) Uniform magnitude re-evaluation of European earthquakes associated with strong motion records. *Earthquake Eng Struct Dyn* 19:1020

- Ambraseys NN, Jackson JA (1998) Faulting associated with historical and recent earthquakes in the Eastern Mediterranean region. *Geophys J Int* 133:390–406
- Ambraseys NN, Synolakis C (2010) Tsunami catalogues for the Eastern Mediterranean, revisited. *J Earthquake Eng* 1(3):309–330
- Bahrekazemi M (2004) Train-induced ground vibration and its prediction. PhD thesis, Division of Soil and Rock Mechanics, Department of Civil and Architectural Engineering, Royal Institute of Technology, Stockholm
- Barneich JA (1985) Vehicle induced ground motion. In: Gazetas G, Selig ET (eds) *Vibration problems in geotechnical engineering*. Proceedings of ASCE Convention, Detroit, MI, pp 187–202
- Carver GA, McCalpin JP (1996) Paleoseismology of compressional tectonic environments. In: McCalpin JP (ed) *Paleoseismology*. Academic, New York, NY, pp 183–270
- Chen P, Chen H (1989) Scaling law and its applications to earthquake statistical relations. *Tectonophysics* 166:53–72
- Dowding CH (2000) Construction vibration. Reprinted 1996 version. Prentice Hall, Upper Saddle River, NJ
- Eldred PJL, Skipp BP (1998) Vibration on impact. In: Skipp BO (ed) *Ground dynamics and man-made processes*. The Institution of Civil Engineers, United Kingdom
- EN 1998-1 (2004) Eurocode 8 – design of structures for earthquake resistance, part 1: general rules, seismic actions and rules for buildings. European Committee for Standardization, Brussels
- Goltz C (1998) Fractal and chaotic properties of earthquakes (lecture notes in earth science). Springer, Berlin
- Gutenberg B, Richter CF (1956) Earthquake magnitude: intensity, energy and acceleration. *Bull Seismol Soc Am* 46:104–145
- Hans T, Kanamori H (1979) A moment magnitude scale. *J Geophys Res* 84:2348–2340
- Hiller DM, Crabb GI (2000) Ground borne vibration caused by mechanised construction works. Transport Research Laboratory report 429, United Kingdom
- IBC (2009) International Building Code. International Code Council
- Johnston AC (1990) An earthquake strength scale for the media and the public. *Earthquakes Volcanoes* 22(5):241–216
- Kahriman A (2004) Analysis of parameters of ground vibration produced from bench blasting at a limestone quarry. *Soil Dyn Earthquake Eng* 24:887–892
- Keefer DK (1984) Landslides caused by earthquakes. *Bull Geol Soc Am* 95:406–421
- Keller EA (1986) Investigation of active tectonics; use of surficial earth processes. In: Wallace RE (ed) *Active tectonics: studies in geophysics*. National Academic Press, Washington, DC, pp 136–147
- McCalpin J (1996) *Paleoseismology*. Academic, New York, NY
- MIL-HDBK (1997) Soil dynamics and special design aspects. U.S. Department of Defence Handbook 1007/3
- Obermeier SF (1996) Using liquefaction induced features for paleoseismic analyses. In: McCalpin (ed) *Paleoseismology*. Academic, New York, NY, pp 331–396
- Rodriguez CE, Bommer JJ, Chandler RJ (1999) Earthquake-induced landslides: 1980–1997. *Soil Dyn Earthquake Eng* 18:325–346
- Scholz CH (1990) *The mechanics of earthquakes and faulting*. Cambridge University Press, Cambridge
- Scholz CH, Aviles C, Wesnousky S (1986) Scaling differences between large intraplate and interplate earthquakes. *Bull Seismol Soc Am* 76:65–70
- Srbulov M (2008) *Geotechnical earthquake engineering – simplified analyses with case studies and examples*. Springer, New York, NY
- Srbulov M (2010) *Ground vibration engineering – simplified analyses with case studies and examples*. Springer, New York, NY
- Stewart IS, Hancock PL (1990) What is a faulty scarp? *Episodes* 13:256–263

- Stewart JP, Chiou S-J, Bray JD, Graves RW, Somerville PG, Abrahamson NA (2001) Ground motion evaluation procedures for performance based design. Pacific Earthquake Engineering Research Centre, College of Engineering, University of California, Berkeley PEER report 2001/09, [http://peer.berkeley.edu/publications/peer\\_reports/reports\\_2001/reports\\_2001.html](http://peer.berkeley.edu/publications/peer_reports/reports_2001/reports_2001.html)
- TRBNAS (1978) Landslides – analysis and control. In: Schuster RL, Krizek RJ (eds) Special Report 176. Transportation Research Board, National Academy of Science, Washington, DC, Poster
- Wells DL, Coppersmith KJ (1994) New empirical relationships among magnitude, rupture length, rupture width, rupture area, and surface displacement. Bull Seismol Soc Am 84:974–1002
- Wiss JF (1981) Construction vibrations: state of the art. ASCE J Geotechn Div 94(9):167–181

# Chapter 3

## Typical Ground Motions, Recording, Ground Investigations and Testing

### 3.1 Introduction

Ground motions are recorded (a) for quantitative assessments of their effects on structures, processes and people, (b) for checking of predicted values, (c) when required by legislations and in other cases.

Ground investigation is performed to decrease the risk that exist when ground condition is unknown, to enable more accurate predictions of ground response, when required by legislations.

The aim of this chapter is to provide an overview of the main types and effects of ground waves, the instruments and recording used in practice, processing of the records, site investigations and laboratory testing of soil samples in soil dynamics.

### 3.2 Main Ground Wave Types and Effects

#### 3.2.1 Main Types

**Body waves** (i.e. waves at depth) originate from deep vibration sources such as earthquakes and mine blasting. Two types of body waves exist – longitudinal and transversal.

- **Longitudinal waves** propagate in direction of the particle movement and are caused by axial stresses
- **Transversal waves** propagate perpendicular to direction of the particle movement and are caused by shear stresses

Longitudinal waves travel faster than the transversal waves but their amplitudes are smaller so is their effect. The ratio between velocities of the longitudinal  $v_l$  and transversal  $v_t$  waves in an elastic solid is (e.g. Kramer, 1996)

$$\frac{v_l}{v_t} = \sqrt{\frac{2 - 2 \cdot \nu}{1 - 2 \cdot \nu}}, \quad (3.1)$$

where  $\nu$  is Poisson's ratio  $< 0.5$ . For Poisson's ratio of 0.5, which is characteristic for fully saturated soft to firm clay in undrained condition (when there is no time for excess pore water pressure caused by wave propagation to dissipate), the velocity  $v_l$  would be infinite according to Equation (3.1), which is not realistic because Equation (3.1) is applicable to elastic solids with Poisson's ratio less than 0.5.

**Surface (i.e. near surface) waves** originate from shallow vibration sources such as transport and construction activities. Two types of surface waves are of engineering significance

- **Rayleigh waves** are similar to water ripples except that ground particles move in opposite direction in the case of Rayleigh waves unlike water waves, Fig. 3.1c.

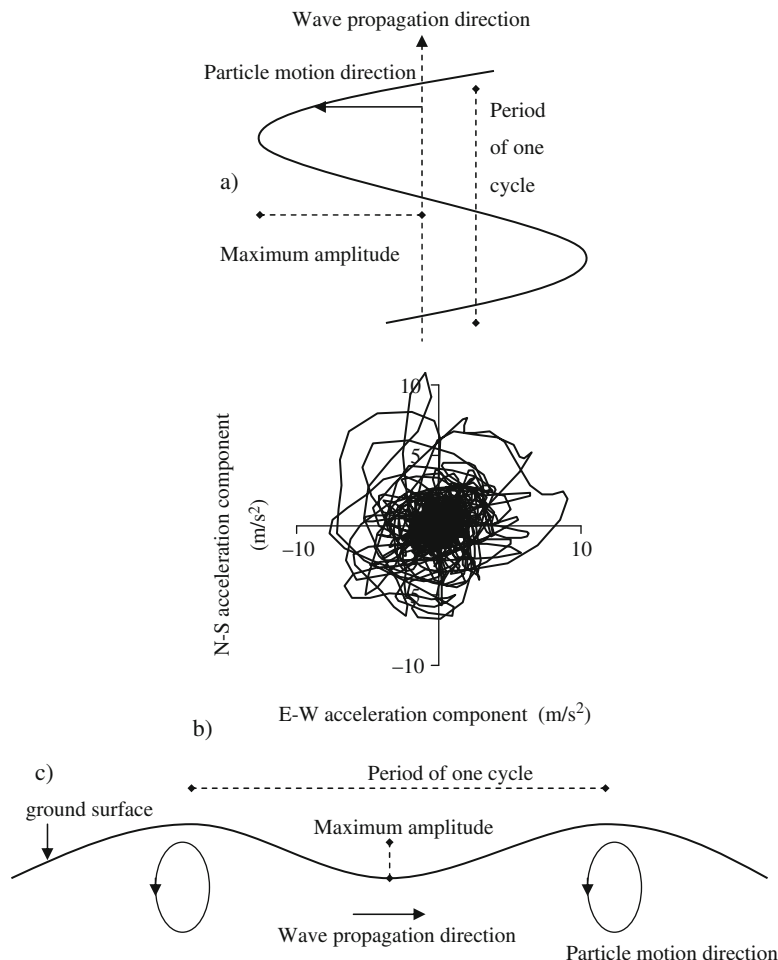


**Fig. 3.1** Sketches of (a) sinusoidal shape of vertically propagating transversal body wave, (b) horizontal ground surface accelerations in time caused by an earthquake, (c) sinusoidal shape of horizontally propagating near ground surface Rayleigh wave

The Rayleigh wave velocity is similar to, but slightly lower than the transversal wave velocity. The minimum horizontal distance  $r_f$  at which Rayleigh waves appear at the surface from body waves is (e.g. Kramer, 1996)

$$r_f = \frac{D_s}{\sqrt{\left(\frac{v_l}{v_r}\right)^2 - 1}}, \quad (3.2)$$

where  $D_s$  is the depth of a vibration source,  $v_l$  and  $v_r$  are velocities of the longitudinal and Rayleigh wave respectively.

- **Love waves** can develop if a ground layer with lower body wave velocity exists under the ground surface. Love waves propagate near ground surface in the horizontal direction similar to a snake movement due to multiple reflections of horizontal body transversal waves that are trapped within the subsurface layer. Love wave velocity range from the transversal wave velocity of the half space to the transversal wave velocity of the subsurface layer (e.g. Kramer, 1996).

Figure 3.1 show sketches of main parameters of transversal and Rayleigh waves i.e. amplitudes, period and number of cycles.

### 3.2.2 Main Effects

Particle motions causes decrease and increase of distances between them and, therefore, strains (change of length per distance) and stresses (ratio between acting force and area). Kramer (1996) for axial stresses and Timoshenko and Goodier (1970) for shear stresses have showed that axial strain  $\varepsilon$  is equal to the ratio between axial peak particle velocity  $PPV_a$  and longitudinal wave velocity  $v_l$  in one directional motion,  $\varepsilon = PPV_a * v_l^{-1}$ , and that shear strain  $\gamma$  is equal to the ratio between transversal peak particle velocity  $PPV_t$  and the transversal wave velocity  $v_t$  in one directional motion,  $\gamma = PPV_t * v_t^{-1}$ . Axial stress  $\sigma$  is equal to the product of soil unit density  $\rho$ , axial peak particle velocity  $PPV_a$  and longitudinal wave velocity  $v_l$ ,  $\sigma = \rho * PPV_a * v_l$ , and shear stress  $\tau$  is equal to the product of soil unit density  $\rho$ , transversal peak particle velocity  $PPV_t$  and the transversal wave velocity  $v_t$  in one directional motion,  $\tau = \rho * PPV_t * v_t$ . In three dimensional motion, sums of derivatives of various componential stresses equal componential inertial forces.

## 3.3 Instruments and Recording

An essential part of a measuring instrument is its transducer (sensor), which converts the amplitude of particle motion into an electrical signal. The main characteristics of transducers are (e.g. Dowding, 2000):

- Sensitivity i.e. the ratio between transducer's electrical outputs to its mechanical excitations for transducers, which do not require an energy source for their operation, or output voltage per unit of measurement per unit of input voltage for passive transducers, which require an energy source for their operation.
- Cross-axis or transverse sensitivity is the sensitivity to motion in a direction perpendicular to the direction of measurement.
- Resolution is the smallest change in mechanical input that produces a recordable change in the electric output.
- Frequency range over which the electrical output is constant with a constant mechanical input.
- Phase shift is the time delay between the mechanical input and the electrical output of the instrument.
- Calibration requirements are the allowable variations in electrical output with constant amplitude input when there are changes in frequency range of the input, change in environment, amplitude of the input, or time.
- Environmental sensitivity describes the response of a transducer to humidity, temperature, or acoustic changes.
- Mass and size of a transducer are important when available space is limited.

Lucca (2003), for example, mentions the following problems arising from the limited applicability of transducer:

- Decoupling may happen when the coil inside of the magnetic field of a geophone moves enough to disrupt the magnetic field and so exceeds the operational limits of the transducer when used for close-in monitoring near sources, such as pile driving and blasting. It also happens if instruments is not firmly attached to the base and moves more than it.
- Aliasing occurs whenever a signal from a transducer is not sampled at greater than twice the maximum frequency of the signal, which in effects means a sort of filtering of high frequencies and truncation of the maximum amplitudes of the vibration. To measure the amplitude correctly at high frequencies, the sample rate must be at least four to five times greater than the frequency of monitored vibration. Frequencies in the extreme near field can be as high as 6000 Hz. Although this signal attenuates quickly, it can still involve many hundreds of hertz within 6 m of a blast. This will cause exceeding of the operational limits of many commercial geophones and will generate erroneous data.

The measurement systems also need an accurate method of storing data, adequate storage space, and transmitting data to a location where they can be analysed. Some systems download data by mobile phone at regular intervals. Others have to be visited on site. Bormann (2002) highlighted one important property of vibration data acquisition and processing

- High signal to noise ratio to avoid sometimes complete masking of ground vibration caused by a particular vibration source by environmental noise.

### 3.3.1 Geophones

Geophone consists of a permanent magnet, coils, top and bottom springs, steel casing and cable connector. An example of a geophone casing with cable connector is shown in Fig. 3.2.

The output from a velocity transducer (geophone) is generated by a coil moving through a permanent magnetic field. The voltage induced in the coil is directly proportional to the relative velocity between the coil and the magnetic field. The voltage output is usually high enough so that amplification is not required even if using long connecting cables. Basic geophone data are provided by the manufacturer together with the calibration certificates. Geophones may need to be re-calibrated periodically either by the manufacturer or the user. To ensure data integrity, all components of data acquisition system need to be calibrated before use. Signal amplifiers, filters, analogue to digital converters and recorders are calibrated by the manufacturers. The user need to check operational limits of equipment and expire date of the calibration before use.

**Method of fixation of transducers** to their bases is an important issue in ground vibration measurement. Individual transducers are usually screwed into three orthogonal faces of a metal cube to create triaxial array with one vertical and two horizontal components (e.g. Hiller and Crabb, 2000; ISO 4866, 1990). The arrays are then screwed on to say 200 mm long stainless steel spikes driven fully into ground. Where necessary, any loose soil or vegetation is removed before the spikes are driven. If geophones are to remain in place for a long time and in order to minimize coupling distortion, they are buried to a depth at least three times the main dimension of the mounting unit. Each excavation is backfilled with the excavated soil hand-tamped around the array to ensure good coupling with the ground and to minimise the risk of disturbance. ISO 4866 (1990) states that, alternatively,



**Fig. 3.2** An example of uniaxial geophone casing about 30 mm high and 25 mm wide with cable connector at the top

transducers can be fixed to a rigid surface plate (for example a well-bedded paving slab).

The number of locations at which vibration measurements could be made simultaneously is restricted by the data acquisition system. Typically, geophones are positioned as close as practicable to a vibration source and then at distances oriented radially from the source depending on the source energy output. It is important to avoid decoupling and aliasing effects (Section 3.1), which are possible near blasting location and near driven piles. Lucca (2003) states that “If a seismograph is set up in an area where there are multitude of surfaces and structures, the interaction of the vibration waves with each other, surfaces and structures may cause the seismograph readings to be erroneous and not representative of the actual peak particle velocities affecting the structure”.

### 3.3.2 Accelerometers

Although measurement of particle velocity by geophones directly yield ground stress as a product of ground unit density, particle velocity and wave propagation velocity, and ground strain as the ratio between particle velocity and wave propagation velocity (e.g. Dowding, 2000), geophone properties may not be suitable for the measurements in near field of high energy vibration sources.

Accelerometers are used for vibrations with amplitudes or frequencies outside the operating limits of geophones. Accelerometers have a range of  $\pm 50$  times the gravitational acceleration and a near linear response proportional to acceleration from about 1 Hz to 10 kHz, but are not suitable for low-frequency measurements when the outputs are integrated to obtain velocity. Further disadvantages of the accelerometers are that they require a power supply and are more susceptible to backgrounds noise than geophones (e.g. Hiller and Crabb, 2000). Bormann (2002) states “*However, the latest generation accelerometers are nearly as sensitive as standard short-period (SP) seismometers and also have a large dynamic range. Consequently, for most traditional short period networks, accelerometers would work just as well as 1-Hz SP seismometers although the latter are cheaper. In terms of signal processing, there is no difference in using a seismometer or an accelerometer.*”

A number of different types of accelerometers are available.

- **Servo (or force balance) accelerometers** use a suspended mass to which a displacement transducer is attached. When accelerometer housing is accelerated, the signal produced by the relative displacement between the housing and accelerometer mass is used to generate a restoring force that pushes the mass back towards its equilibrium position. The restoring force is proportional to the acceleration and can be measured electronically. Servo accelerometers can provide very good accuracy over the range of frequencies of greatest interest in earthquake engineering (e.g. Kramer, 1996). An example of a three componential force balance accelerometer casing is shown in Fig. 3.3.

**Fig. 3.3** An example of a three component force balance accelerometer casing about 6 cm high and 13 cm diameter



- **Piezoresistive accelerometers** use piezoresistive strain gauges. The strain gauges are solid state silicon resistors, which electrical resistance changes in proportion to applied stress and are small, a few centimetres. The upper limit of the frequency range is a few thousands hertz. They require an external power supply (e.g. Dowding, 2000). An example of a piezoresistive accelerometer casing is shown in Fig. 3.4.
- **Piezoelectric accelerometers** use the property of certain crystals to produce a voltage difference between their faces when deformed or subjected to a force. The accelerometer can work in compression or shear. The compression transducers are sensitive to the environment. The shear transducers are less affected by temperature changes, are lighter and have wider frequency response (e.g. Dowding, 2000). Examples of uniaxial piezoelectric accelerometer casings are shown in Fig. 3.5.
- **Micro machined differential electric capacitive sensors** are claimed to offer a lower noise floor and significantly better stability performance over time and over temperature than piezoresistive accelerometers. The change of the sensor element capacity with acceleration is detected and transformed into voltage by a

**Fig. 3.4** An example of a uniaxial piezoresistive accelerometer casing about 15 mm in diameter and 25 mm high

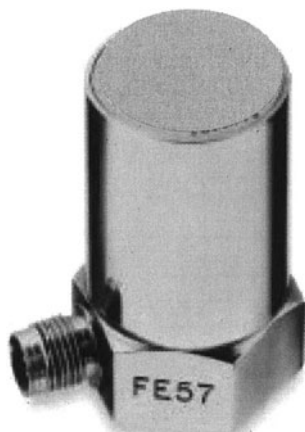


**Fig. 3.5** An example of uniaxial piezoelectric accelerometer casings a few millimetres large

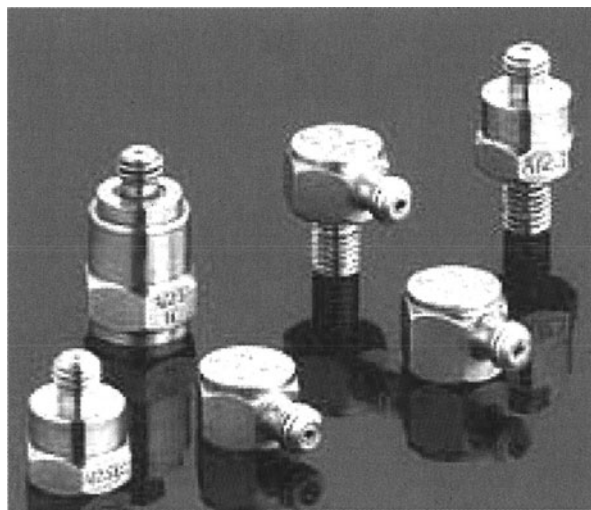
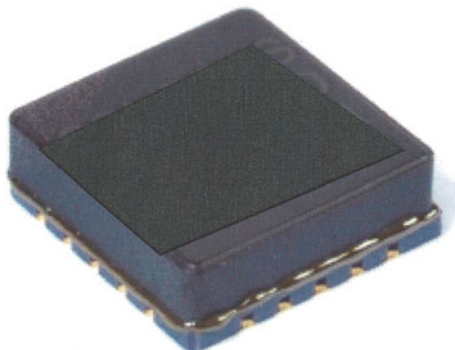


**Fig. 3.6** An example of a micro machine capacitive acceleration sensor about 10 mm wide



converter, which includes an amplifier and an additional integrator that forms an electronic feedback circuit. An example of a uniaxial micro machine capacitive acceleration sensor is shown in Fig. 3.6.

Besides sensors and accelerometer casing, an important component of an accelerometer is an accurate clock, particularly when more than one component of motion is measured or when the ground motion at different locations are compared. Modern instruments maintain time accuracy by synchronizing on daily bases with radio time signals transmitted by a standard time service or recording such signals along with the ground motion data. Universal Coordinated Time (i.e. Greenwich Mean Time) is used as a common worldwide basis (Kramer, 1996). Some micro machined sensors are also supplied with Global Positioning System receiver.

## 3.4 Processing of Records

Processing of vibration records is necessary because the visual inspection of a time history only reveals maximum amplitude and duration but not influences of potential noise caused by the recoding system/process and/or background (environment) and not the predominant frequency. Besides that, vibration records may contain various errors. Corrections of two basic errors are described in this section. Douglas (2003), for example, listed types of possible non-basic errors in strong-motion records, Table 3.1, are: insufficient digitizer resolution, S-wave trigger, insufficient sampling rate, multiple baselines, spikes, early termination, and amplitude clipping.

These types of non-standard errors are shown in Fig. 3.7.

### 3.4.1 Filtering

There are a number of reasons for filtering of high (and low) frequencies that may be contained within a vibration record. The following description is based on Bommer (1992) and others.

**Table 3.1** Types of non-basic errors in strong motion records (from Douglas, 2003)

Error type	Comments
Insufficient digitizer resolution	Digital instruments with a low bit range can cause recording of a few levels of amplitudes only resulting in a step like record. The resolution of the instrument can be calculated as $2A_f(2n_b)^{-1}$ , where $A_f$ is the instrument's amplitude range, $n_b$ is the A/D converter bit range (usually between 10 and 24 bits). The peak ground acceleration (PGA) from instruments with low digitizer resolution is within $\pm r/2$ of the true PGA. The lack of sufficient bit range introduces high and low frequency noise into the recorded ground vibration
S-wave trigger	Analogue instruments start recording once triggered by acceleration above a trigger level (say 0.001g). Digital instruments record continuously but could loose the initial part of a record if their pre-event memory is too short
Insufficient sampling rate	This error causes missing sections of data points
Multiple baselines	Records from analogue instruments that were digitized in sections, which are not spliced together well
Spikes	These can be corrected by either removing the suspect point(s) or reducing the amplitude of the spike after examining original record
Early termination	Records from both analogue and digital instruments may exhibit lack of film or memory or instrument malfunction
Amplitude clipping	Occurs when instrument measuring range is exceeded by amplitudes of ground vibration

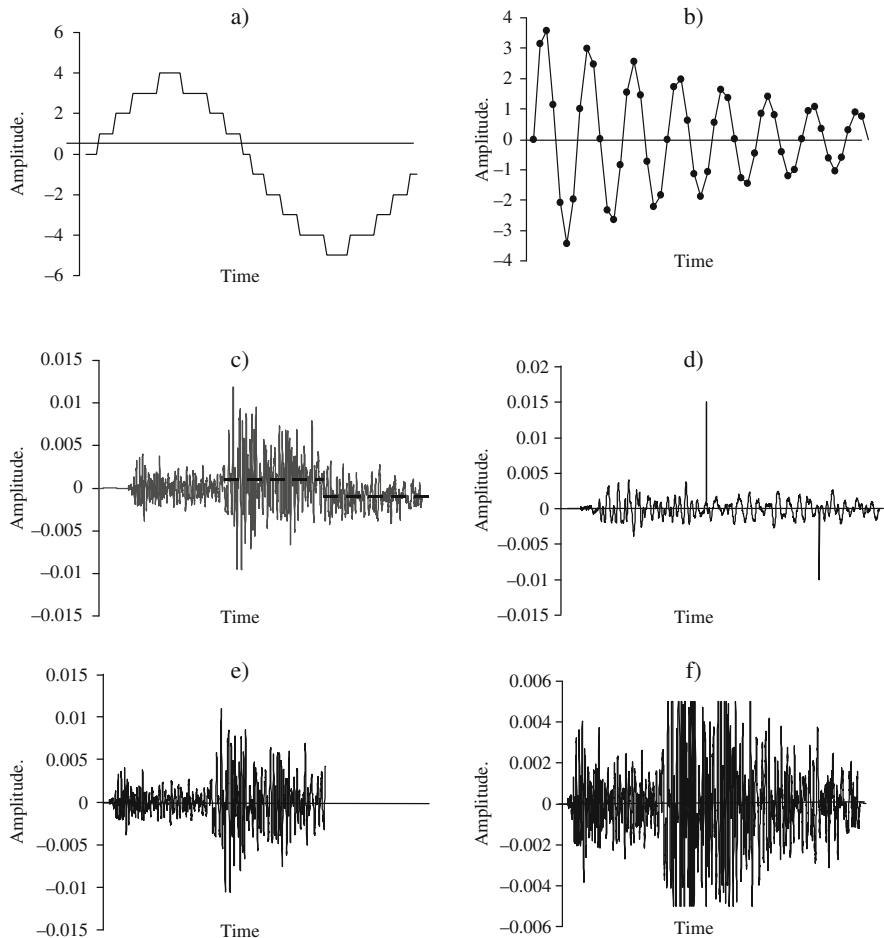


**Fig. 3.7** Examples of problems in vibration records caused by: (a) insufficient instrument resolution, (b) insufficient sampling rate, (c) multiple base lines, (d) spikes, (e) early termination, (f) amplitude clipping

- Vibration record may contain background noise together with the signal from vibration source, which vibration is intended to be monitored. Filters modify the recorded data to preserve information of importance but remove data where the noise to signal ratio is too high, usually at low and high frequencies within a vibration record. In filtering extreme parts of a record, both the noise and the true signal are lost.
- Low-pass (anti-aliasing) filter is used to ensure that, for all activities, the Nyquist frequency was well in excess of the frequencies anticipated, so that all wave forms were accurately recorded (e.g. Hiller and Crab, 2000). Nyquist frequency is inversely proportional to twice the time interval at which vibration amplitudes

are recorded. For example, for the analogue signal from a geophone sampled at approximately 2 kHz (0.0005 s time interval), a low-pass filtering is performed for frequencies above 800 Hz (e.g. Hiller and Crab, 2000).

High frequency noise is removed using filters. Analogue type filters within measuring instruments are no longer in use because they automatically filter useful information as well. Numerical filtering is used in frequency domain. For this reason, vibration records in time domain are transferred into frequency domain using fast Fourier transform (FFT), Fig. 3.8.

The filter is applied by multiplication of the amplitudes of FFT and the filtered vibration record is recovered using the inverse transform. Alternatively, the impulse response of a filter can be found in time domain and applied to the vibration record in time domain by convolution.

An ideal numerical filter function would transmit required frequencies and attenuate completely all unwanted frequencies in a record of ground vibration. This, however, is not achievable due to limitations of the Fourier analysis. A transition between wanted and unwanted frequencies requires having two (step-like) values at the same frequency. This cannot be expressed by a Fourier series. To overcome this problem, a transition zone or ramp is introduced between narrow ranges of frequencies. Such a filter also is not perfectly realisable due to Gibb's effect in which the Fourier representation of a function always overshoots the true value at a point of discontinuity. The effects of these limitations is to allow spectral leakage, thus Fourier amplitude spectrum (FAS) of a filtered signal divided by the FAS of the original signal would produce a rippled function. The extent of the ripples is largely dependent on the width of the transition zone. To some extent the ripples can be reduced by widening the transition zone. Various filters developed represent different attempts to overcome some of these difficulties and to achieve greater efficiency in terms of computing time. None of them is perfect.

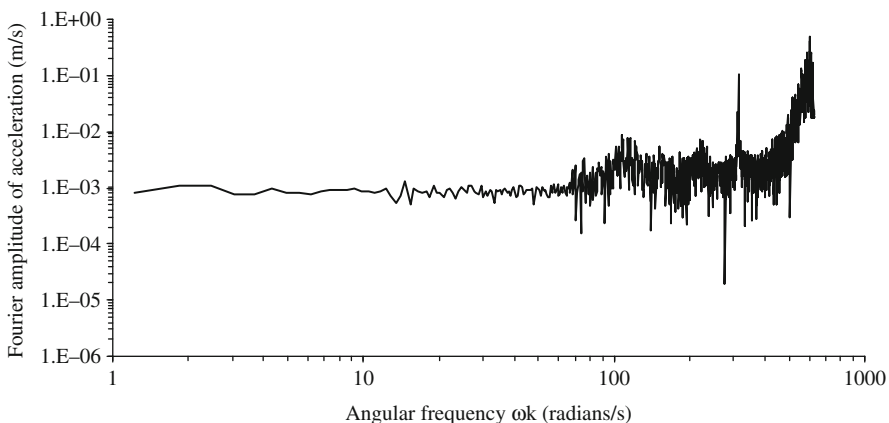


**Fig. 3.8** Amplitudes of a discrete Fourier series in frequency domain

The choice of the cut-off frequencies is made by the user performing the adjustment. A low frequency cut-off has a significant effect on the processed vibration record, since although of small amplitude, the duration of each wave can be large, and when integrated in time to obtain velocity and displacement can strongly influence their time histories. The high frequency cut-off has little influence since the waves are both of small amplitude and short duration. The high frequency limit is effectively controlled by the Nyquist frequency. It is inappropriate to apply filters to records of short duration. The reason is that for the filter to be effective it must modify the low frequency end of the FAS, with the first frequencies corresponding to  $T_r^{-1}$ ,  $2T_r^{-1}$ , etc., where  $T_r$  is the record duration. If a vibration record has duration of say 2 s, then it means filtering out frequencies of 1/2, 2/2, etc. Hz, which represent periods of 0.5, 1, etc. s that may form part of the signal. Therefore, such filtering creates distortion of the record.

Srbulov (2010) provides an example of a filtered record together with an Excel work book used on <http://extras.springer.com/2010>.

### 3.4.2 Baseline Correction

The baseline correction of short vibration records consists of finding a function that approximates the long period offset from the time axis (baseline error) of a vibration record, Fig. 3.9.

The error could be caused by digitization of an analogue record or other reasons. If uncorrected, the base line error may cause erroneous values of ground velocity and displacement when they are integrated in time from an acceleration record.

The best fit of the record average values (baseline) is then subtracted from the record considered to produce desirable adjustment. Different criteria may be used to define the best fit. Sometimes, the least square approach is used i.e. minimization of the sum of squared differences between uncorrected and corrected record. In other cases it may be required to achieve zero end velocity. The baseline correction can

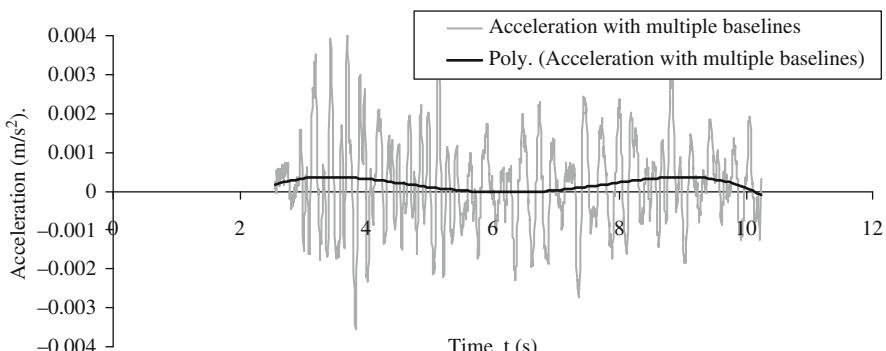


**Fig. 3.9** Fourth order polynomial fitted by Microsoft Excel to an acceleration record

provide reasonable results for the records of short duration. Depending on the shape of the record average values, different functions can be considered from linear to polynomial of higher order and other functions.

Srbulov (2010) provides an example of a vase line corrected record together with an Excel work book used on <http://extras.springer.com/2010>.

## 3.5 Site Investigation

Data on ground profile, ground water level and ground classification properties should always be available even if attenuation relationships of ground vibration are used from literature in order to be able to assess the relevance of use of empirical data. Field non-intrusive (geophysical) methods need to be supplemented by field intrusive methods (boreholes) in order to achieve greater accuracy and uniqueness in the interpretation of the results. Also, field intrusive methods may require their supplement by laboratory testing in order to be able to determine ground properties in the conditions different from the existing ground conditions, for example at increased shear strains and stresses. Laboratory testing of a limited number of samples represent only a tiny part of the whole mass and a representative number of samples should be obtained and tested. Sampling and testing of ground should achieve:

- **Minimum sample disturbance** and preservation of in situ stresses, moisture content and ambient temperature as much as possible.
- **Uniform stress and strain distribution** within specimen during testing and ability to control or measure boundary stresses and strain.
- **Stress path** similar to the expected stress path in the field because some soil properties are stress path dependent.
- **Consistency and repeatability** of the results obtained from the same test conditions.

One method of soil investigation and testing is not sufficient to provide data on all necessary ground properties and ground conditions.

### 3.5.1 Surface (Non-intrusive)

AASHTO (2009), for example, summarizes advantage and disadvantages of geophysical surveying. The **advantages** are summarized as follows:

- Non-intrusive methods are beneficial when conventional drilling, testing and sampling are difficult, for example in deposits of gravel and talus, or where potentially contaminated subsurface soil may occur.

- Geophysical testing covers a relatively large area and can be used to optimize the locations and types of in-situ testing and sampling. Geophysical methods are particularly well suited to projects with large longitudinal extent compared to lateral extent, for example paths between vibration sources and the recipients.
- Geophysics assesses the properties of ground at very small strain, of the order of  $10^{-5}$ , thus providing information on ground elastic properties.
- Geophysical methods are relatively inexpensive when considering cost relative to the large areas over which information can be obtained.

Some of the **disadvantages** of geophysical methods include:

- Most methods work best for situations in which there is a large difference in stiffness or conductivity between adjacent ground layers.
- It is difficult to develop good stratigraphic profiling if the general stratigraphy consists of hard material over soft material or resistive material over conductive material.
- Results are generally interpreted qualitatively and, therefore, only experienced geophysicist that is familiar with the particular testing method can obtain useful results.
- Specialized equipment is required (compared to more conventional subsurface exploration tools).
- Since evaluation is performed at very low strain, information regarding ultimate strength for evaluation of strength limit states is only obtained by correlation, which may be difficult if ground classification properties are only inferred.

### 3.5.1.1 Geophysical Refraction

The method is standardized (e.g. ASTM D5777). Geophysical refraction is usually used to define depths (typically to 30 m but possibly to  $\sim 300$  m) of subsurface layers (usually maximum four) and ground water level as well as to determine the velocity of longitudinal wave propagation through subsurface layers. Longitudinal waves are used because they travel fastest through ground and are the first to arrive at a receiver but determination of velocity of transversal waves is possible by geophysical refraction.

The method is based on measurement of travel time of longitudinal wave propagation from a source (hammer blow, weight drop, and explosive charge – more expensive) to a receiver (geophone) on the ground surface, Fig. 3.10.

When a longitudinal wave travelling from the source reaches an interface between two materials of different wave propagation velocities, the wave is refracted according to Snell's law. When the angle of incidence equals the critical angle at the interface, the refracted wave moves along the interface between two materials, this interface is referred to as a refractor. From plotted times of arrival of a longitudinal wave at different distances of geophones it is possible to calculate both the

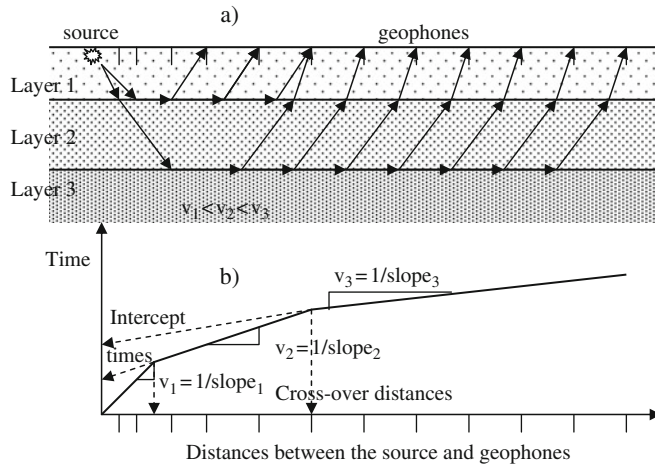


**Fig. 3.10** (a) Refracted wave paths, (b) time-distance plot for three horizontal layers

velocity of wave propagation from the slope(s) of the polygon and the depths of the refractor(s), from intercept times and crossover distances.

The calculation formulas are based on the following assumptions:

- The boundaries between layers are planes that are either horizontal or dipping at a constant angle.
- There is no ground surface undulations.
- Each layer is homogeneous and isotropic (with the same properties in any direction).
- The wave velocity increases with depth.
- Intermediate layers must have sufficient velocity contrast, thickness and lateral extent to be detected.

Ground layers can be inclined and therefore measurements in two opposite directions are used. The velocity obtained for the refractor from either of these two measurements alone is the apparent velocity of the refractor. Both, forward and back measurements are necessary to calculate the true wave velocity and the dip of layers unless other data indicate a horizontal layering.

The error of calculation of layer depth increases as the angle of dip of the layer increases. If a layer has wave velocity lower than the velocity of the layer above it (velocity reversal exists) then the lower wave velocity layer cannot be detected. The computed depths of deeper layers are greater than the actual depths. For irregular layer interfaces other methods exist to calculate layer profiles such as the common reciprocal method. For lateral variation in wave velocity within a layer, thin intermediate velocity layers and velocity inversion, the generalized reciprocal method is used (e.g. ASTM D5777). Calculation methods can be developed for anisotropic soil, but for simplicity are not usually used.

The geophysical refraction method is sensitive to ground vibrations from various sources such as:

- Ambient sources of noise involve ground vibration due to wind, water movements (e.g. wave break on a beach, fluid movement in pipelines), natural micro seismicity or rain drops on geophones.
- Geologic sources of noise include lateral and vertical variations in wave velocity (e.g. presence of large boulders).
- Cultural sources of noise include vibration due to movement of the personnel conducting measurements, vehicles, construction activity, etc.

### 3.5.1.2 Geophysical Reflection

The method is standardized (e.g. ASTM D7128-05). It is most frequently used for determination of wave propagation velocity and thickness of subsurface layers on a large scale for very deep stratigraphy and rarely for shallow soil layers. The test and its interpretation are conceptually very simple. The test is performed by using an impulse to cause usually longitudinal wave at the surface and measuring the arrival time of direct and reflected wave at a receiver on the surface, Fig. 3.11.

Wave velocity is calculated from direct wave and layer thickness from reflected wave assuming that wave velocity propagation is isotropic (equal in two perpendicular directions). In the case of inclined layer boundary, the layer thickness and its inclination can be determined using two receivers of which one is placed at the source (e.g. Kramer, 1996).

More than one layer can be detected and their wave velocities determined by the method. The problem arises when the times of direct and reflected wave coincide (due to wide pulse width) and also when layers have low velocities. Difficulty with resolution increases with increased source to receiver distance. Therefore, this method uses much smaller source to geophone distances in comparison with geophysical refraction, which may require a source to geophone distance of up to five times the depth of investigation. McDowell et al. (2002), for example, stated that “Attempts to use higher frequency sources (giving shorter wavelengths) to improve

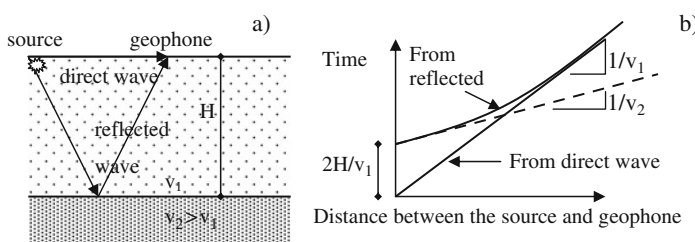


**Fig. 3.11** (a) Reflected and direct wave paths, (b) time-distance plot for direct and reflected wave

*the basic resolution of the method have been inhibited by lack of penetration of the pulse, caused by greater attenuation of the vibration energy in the near surface layers. Even when adequate penetration and resolution of the geological structure has been achieved, it may not be possible to observe the geophysical signal if the environmental noise is excessive.”*

### 3.5.2 Deep (Intrusive)

#### 3.5.2.1 Geophysical Down-Hole

The method is standardised (e.g. ASTM D7400-08). It can be performed in a single borehole when a vibration source is located on the ground surface and a single receiver moved to different depths or a number of receivers are fixed at different depths in the borehole, Fig. 3.12.

From a plot of measured travel time of longitudinal or transversal waves versus depth, ground wave propagation velocity at a depth is obtained from the slope of the plot (e.g. Kramer, 1996).

In a version called up-hole test, a movable energy source is located in borehole with a single receiver on the ground surface close to the borehole. However, transversal waves can be generated much more easily when the source is on the ground surface and, therefore, down-hole test is more frequently used. The down-hole test allows detection of layers that can be undetected in geophysical refraction survey. Also, it provides ground wave velocity in the vertical direction, which may be different from velocities in the horizontal and slant direction in anisotropic soil. Kramer (1996), for example, mentions potential difficulties with down/up-hole test and their interpretation as:

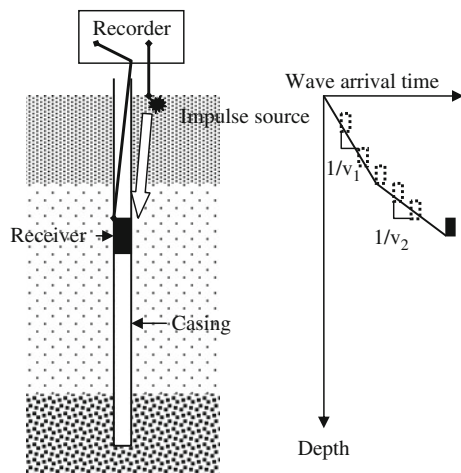


**Fig. 3.12** (a) Cross section of a seismic down-hole test, (b) travel-time versus depth graph

- Soil disturbance by drilling equipment.
- The use of casing and borehole fluid for borehole stabilisation.
- Insufficient or excessively large impulse source.
- Background noise effects.
- Groundwater level effect.
- The effects of material and radiation damping on waveforms can make identification of transversal wave arrivals difficult at depth greater than 30–60 m.

### 3.5.2.2 Geophysical Cross-Hole

The method is standardized (e.g. ASTM D4428/D4428M-00). The method is used for determination of velocity of longitudinal and transversal ground waves propagating horizontally through primarily soil layers, in the absence of rock. Minimum two but preferably three boreholes are used in line spaced at 3 m apart, in order to minimize chance that the arrival of refracted rather than direct waves is recorded, Fig. 3.13.

When a higher velocity horizontal layer exists near the level of the source and receivers then the recorded wave amplitude may be the result of a refracted wave propagated through the higher velocity layer. ASTM D4428/D4428M-00, for example, provide example calculations for this case. PVC pipe or aluminium casing is grouted in boreholes and three-directional receivers (geophones or accelerometers) must be fixed firmly to them. Impulsive source used can be explosive charge, hammer or air gun.

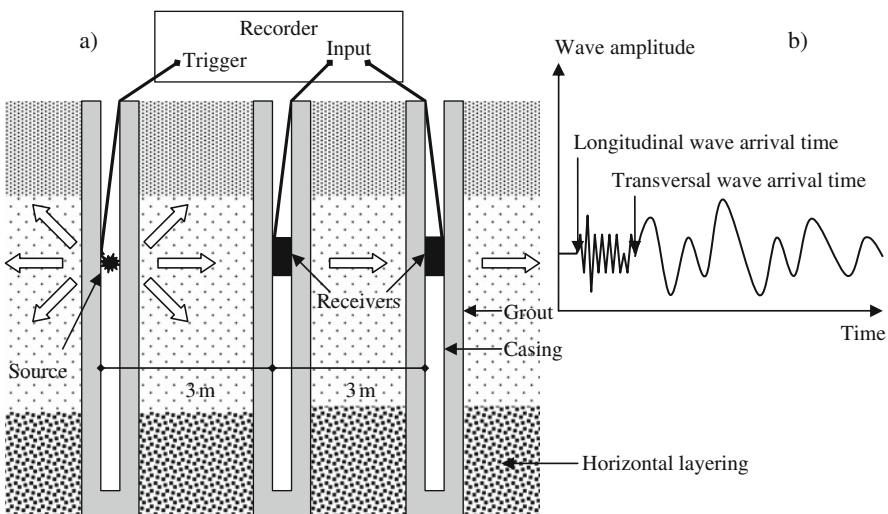


**Fig. 3.13** (a) Cross section of the test setup, (b) recorded wave amplitudes from a reversible impulse source

The cross-hole test allows detection of layers that can be undetected in geo-physical refraction survey. Also, it provides ground wave velocity in the horizontal direction, which may be different from velocities in the vertical and slant direction in anisotropic soil. The test results (i.e. measured times of incoming waves at the receivers) may be affected by borehole deviation and therefore a survey must be conducted to establish true horizontal distances between boreholes, particularly at depths greater than 15–20 m. Wave amplitude attenuation measurements from cross-hole tests performed in at least three boreholes has been used to obtain material damping ratios at small strain (e.g. Kramer, 1996). Boreholes are used not only for measurements of ground wave propagation velocity and detecting of ground layering but also for taking samples for laboratory testing and performing of in situ tests. An in-situ test called standard penetration test (SPT) (e.g. ASTM D1586-08a, EN 1997-2, 2007) is performed in boreholes world wide and routinely. Japan Road Association (2002), for example, provides expressions for assessment of soil transversal velocity based on the average blow count  $N_i$  of SPT in a soil layer:

$$\begin{aligned} \text{For cohesive soil layer : } v_t &= 100 \cdot N_i^{1/3}, \quad 1 \leq N_i \leq 25 \\ \text{For sandy soil layer : } v_t &= 80 \cdot N_i^{1/3}, \quad 1 \leq N_i \leq 50 \end{aligned} \quad (3.3)$$

### 3.5.2.3 Geophysical Cone

It is an addition to the electric piezo-cone (e.g. ASTM D5778-95, EN 1997-2, 2007) and is described by Lunne et al. (2001), Fig. 3.14.

As standard cone (35.7 mm diameter i.e.  $10 \text{ cm}^2$  cross sectional area and  $60^\circ$  apex angle) can be used for soil classification and identification of ground layering,

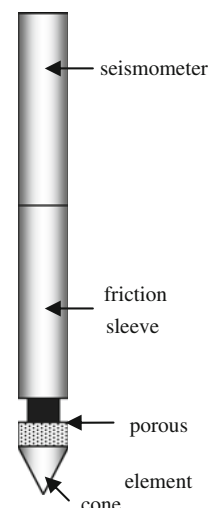


**Fig. 3.14** Sketch of an electric piezo seismic cone

geophysical cone can be used instead of geophysical down-hole test or as an addition to them because the use of piezo-cone is fast (penetration speed  $2\pm0.5$  cm/s) and may be cheaper. Its use is limited by the availability at a site and depth of penetration that can be achieved with pushing in force of up to 200 kN, depending of vehicle on which the cone is mounted.

Miniature velocity meter is usually placed above a piezo-cone unit. Other necessary equipment includes a memory oscilloscope and an impulse source, which is capable of generating high frequency waves, located on the ground surface (at less than 1 m from the cone push-in rod). Except this downward wave propagation setup, a version was used involving two geophysical cones in parallel, one as a source and the other as a receiver, similar to geophysical cross-hole test described in Section 6.3.2. In such a setup, the verticality of the cone rods is important. Both longitudinal and transversal waves can be generated on the ground surface. The measurements are usually performed at 1 m interval during a brief break in a continuous penetration. The use of two receivers 0.5 or 1 m apart can improve the quality of the recorded data by eliminating problems related to triggering times.

Pushing in of cone penetrometer into ground causes inevitably formation of a zone of remoulded ground and large strain deformation around the cone rod. The extent of this zone is relatively small in comparison with the whole source to receiver distance passing through undisturbed ground.

## 3.6 Laboratory Testing of Soil Samples

These tests are used when ground vibration induced stress and strain states are expected to be different from the existing states within ground. For example, pile driving, soil compaction and blasting are expected to induce large strains in the vicinity of the sources in comparison with small strain (less than  $10^{-6}$ ) induced by propagation of ground waves during field testing. Large strains are associated with ground failure and, therefore, laboratory tests are really necessary only for investigation of ultimate equilibrium condition and not for considerations of serviceability criteria. The order of description of various laboratory tests corresponds to the frequency of their use.

### 3.6.1 Shear Strength

Cyclic shear strength can be measured using either simple shear or triaxial cyclic tests but the simple shear is simpler and cheaper and resembles more closely actual horizontal ground motion due to propagation of vertical shear waves.

### 3.6.1.1 Simple Shear Test

The test and its typical results are described by Finn (1985), for example. Cyclic simple shear apparatus is used frequently for testing of potential to liquefaction of saturated sandy soil. It approximates closely usual assumptions introduced by Seed and Idriss (1967) that:

- Seismic excitation is due primarily to transversal waves propagating vertically.
- Level ground conditions may be approximated by horizontal layers with uniform properties.

The apparatus is also used for the investigation of degradation of the strength and stiffness of saturated clay in cyclic condition. Cyclic simple shear test consists of applying a cyclic force or displacement to a top or bottom surface of thin ground specimen, with width to height ratio in excess of 5 preferably. Constant cyclic force/displacement amplitude is used when an equivalent number of significant stress cycles concept (Seed et al., 1975) is considered. Time histories of irregular cyclic force/displacement amplitudes and in two directions may be applied as well (e.g. Ishihara and Nagase, 1985). The first simple shear test apparatus (Fig. 3.15) was developed by Roscoe (1953) for static testing of soil. It was adapted to cyclic loading conditions first by Peacock and Seed (1968). The apparatus development follows recognition of the deficiencies of direct shear test device, in which a ground specimen is enclosed within rigid metal box that is split in the middle and is capable of shearing the specimen along a distinct shear zone.

The Roscoe apparatus uses a specimen of rectangular cross-section and generates simple shear (change of shape by distortion) under plane strain conditions in the case when constant volume is maintained so that no displacement occurs in direction perpendicular to the direction of shearing.

The slipping required to accommodate the change in side plate length violates an ideal boundary condition for simple shear at the ends as complementary shear stresses cannot be developed. The shear stresses that occur during slip are indeterminate so to ensure controlled conditions during a test these frictional shear stresses should be reduced as much as possible, ideally to zero by lubricating the side plates. Other simple shear devices exist; the Norwegian Geotechnical Institute uses a wire-reinforced membrane around a cylindrical specimen while the Swedish

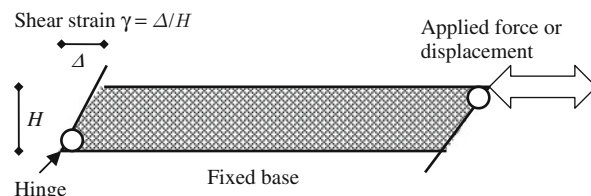


**Fig. 3.15** Sketch of cross section through Roscoe simple shear apparatus

Geotechnical Institute uses a series of stacked rings (e.g. Kramer, 1996). When shared in these devices, the specimen does not maintain plane strain conditions (Finn, 1985). In Roscoe apparatus, essentially uniform simple shear conditions can be induced in most parts of a specimen particularly at small strain. Around the boundaries and near the ends, narrow zones of smaller than average shear strain exist.

From the shear modulus  $G_{\text{secant}}$  obtained from the test results, it is possible to back calculate transversal wave velocity at a particular strain level as a square root of the ratio between the shear modulus at that strain level and soil unit density. A damping ratio is also calculated. Ishihara and Nagase (1985) summarized the effects of multidirectional and irregular loading on the tests results as follows:

- The maximum ratio of shear stress to the initial confining stress at 3–5% shear strain in the multidirectional loading test is about 1.5 times the cyclic stress ratio necessary to cause the same range of shear strain in unidirectional uniform loading test for loose sand (with density of 45% of the maximum value) and for medium dense sand (with density of 75% of the maximum value) and 0.9 times the stress ratio in unidirectional uniform loading test for dense sand (with density of 95% of the maximum value). In other words, loose and medium dense sand are more difficult and dense sand more easily disturbed by multidirectional than unidirectional uniform loading shaking.

While the effects of multi-directivity of loading are not influenced significantly by sand density, the effects of load irregularity are manifested to a varying degree depending on sand density.

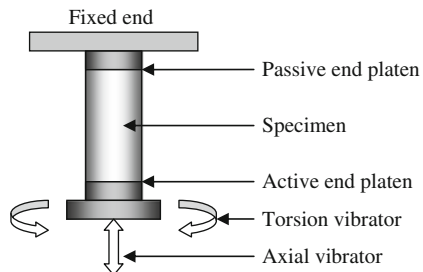
### **3.6.2 Stiffness**

No single test exist that can be applied to the whole range of strain from small values of  $10^{-6}$  to the strain at failure of several percent. Therefore, more than one test types are combined.

#### **3.6.2.1 Resonant Column**

The test is standardized (e.g. ASTM D4015 – 92). The test consists of vibrating a cylindrical specimen in torsion to determine shear modulus and damping ratio or in axial direction to determine axial modulus and damping ratio at the resonance frequency between the excitation and the system vibration. The specimen diameter could vary from 33 mm onwards and the height to diameter ratio should not be less than 2 or more than 7 except when applied axial stress is greater than confining stress in which case the ratio shall not be greater than 3. Nevertheless, non-uniform stress condition will exist in torsion. Different types of apparatus exist. Skoglund et al. (1976), for example, compared the results obtained by six different investigators and found that the differences in shear and axial modulus ranged from -19% to +32% of

**Fig. 3.16** Schematic of a resonant column test with fixed top end without triaxial chamber and loading piston



the average value. No systematic or consistent differences could be associated with different types of apparatus used. A variant of test schematic with fixed top end and movable bottom end is shown in Fig. 3.16 without a triaxial chamber and loading piston.

Test can be performed at different strain but it is considered to be non-destructive when strain amplitude of vibration is less than  $10^{-4}$  rad. Details of calculation of modulus and damping ratio depend on the apparatus used. Clayton et al. (2009), for example, investigated the effects of apparatus stiffness and mass, and specimen fixity, on the results obtained from Stokoe apparatus with free top end. They showed that the stiffness of the drive head and the mass of the apparatus base can both have a significant effect on the results obtained when stiff specimens are tested in addition to issues concerning connectivity between the specimen, the apparatus base and the top cap.

### 3.6.3 Shear Strength and Stiffness

Cyclic triaxial test is standardized (e.g. ASTM D3999-91). The cyclic triaxial test consists of applying either a cyclic axial stress of fixed magnitude (load control) or cyclic axial deformation (displacement control) on a cylindrical soil specimen enclosed in a triaxial pressure cell. The specimen diameter could vary from 38 to 300 mm and the height to diameter ratio should not be less than 2 in order to minimize non-uniform stress conditions within the test specimen, which are imposed by the specimen end platens, Fig. 3.17.

Although the test is used for strain level to about 0.5%, loose sand/soft clay tend to experience bulging in the middle of the specimen and dense sand/stiff clay tend to develop a distinct inclined shear zone, which cause a highly non-uniform distribution of strain within the specimen. Local measurements of strain are performed sometimes on the specimen side within the cell particularly when the specimen response at small strain is investigated. Such measurements are not standardized and are performed by specialized soil testing laboratories (e.g. Jardine et al., 1985; Burland, 1989; Tatsuoka et al., 1997). Such specialized tests are more expensive but also the cost of cyclic triaxial test is about ten times greater than the cost of static triaxial test.

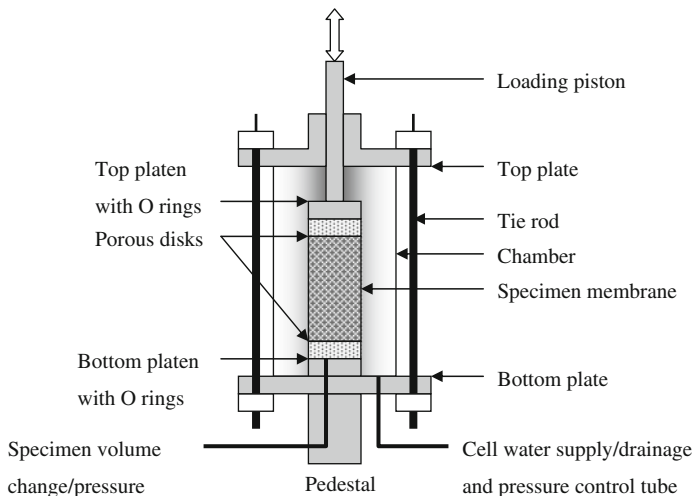


**Fig. 3.17** Sketch of cross section through triaxial pressure cell and cylindrical specimen

The cylindrical specimens have been obtained from nearly vertical boreholes and therefore the test simulates best the effects of propagation of nearly vertical longitudinal waves. The test results are plotted as a graph of axial stress versus axial strain. From the secant axial modulus obtained from the ratio between axial stress and strain, it is possible to back calculate longitudinal wave velocity at a particular strain level as a square root of the ratio between the axial modulus at that strain level and soil unit density. A damping ratio is also calculated. Other features of the test are:

- A 90° change in the direction of the major principal stress occurs during the two halves of the loading cycle. If cyclic deviator (axial less radial) stress is smaller than the deviator stress during consolidation, no stress reversal occurs.
- The maximum cyclic axial stress that can be applied to the specimen is equal to the effective confining pressure (cell pressure less the excess pore water pressure within the specimen).
- Different methods of preparing specimen from disturbed soil sample may result in significantly different cyclic behaviour.
- Membrane compliance effect cannot be simply accounted for in the test procedure or in interpretation of test results. Changes in pore water pressure can cause changes in membrane penetration in specimens of coarse cohesionless soils. These changes can significantly influence the test results.
- Degree of specimen saturation can significantly affect the axial stiffness and consequently the longitudinal wave velocity inferred from the axial stiffness particularly at near saturation state. For saturated soil the longitudinal wave velocity correspond to about 1500 m/s, i.e. longitudinal wave velocity propagation

through water, and for degree of saturation of less than about 99%, the longitudinal wave velocity corresponds to the wave velocity through dry soil (e.g. Gazetas, 1991).

The results of tests performed on specimens in axi-symmetric strain condition in cyclic triaxial apparatus and in plane strain condition in cyclic simple shear apparatus may be different. For testing of liquefaction potential, for example, the results from triaxial tests should be multiplied by a factor of about 0.7 (Seed, 1979). For static condition however, greater angle of friction of sand is measured in plane strain condition than in triaxial condition (e.g. Cornforth, 1964). Townsend (1978), for example, summarized factors affecting cyclic triaxial strength of cohesionless soil. Similar effects are expected on the soil stiffness and wave velocity.

### **3.6.4 Soil Permeability**

Coefficient of soil permeability of water, defined as the quantity of flow through unit area of soil under a unit pressure gradient, and volumetric compressibility have a major influence on dissipation and generation of excess pore water pressure during earthquakes.

Soil permeability of water depends on many factors of which soil grain sizes (fine or coarse), soil porosity and degree of saturation are the most influential ones. Fine grained soil, of low porosity and partially saturated has smaller permeability to water than coarse, porous and fully saturated soil (e.g. Das, 1985).

Water permeability can be determined by field water pumping tests performed in boreholes to avoid problems with samples disturbance, size and orientation. Field permeability tests are standardized (e.g. ASTM 6391, EN 1997-2, 2007). Their primary advantages are that the soil is not disturbed, and that the field tests can also provide information to validate inferences about soil layering. However, they have several disadvantages. They generally measure horizontal permeability, which can be several times larger than the vertical permeability values that may be directly relevant to post-seismic analysis. Also, they provide permeability at ambient confining stress and not increased stresses during strong ground motion (although water pumping from borehole causes a decrease of ground water level and an increase of in-situ effective stress). Another difficulty in field testing is that a smear zone formed along borehole wall may affect the test results unless wash boring or bore-hole washing is performed. Additional problem could appear in layered fine and coarse grained soil if fine grains suspended in water within a borehole move towards more permeable coarser grained soil and form so called filter cake, which apparently decreases permeability of coarser grained soil.

Soil coefficient of water permeability is not usually measured in cyclic conditions but soil porosity change in cyclic conditions will result in the change of permeability.

### 3.7 Summary

The type and locations of instruments used for vibration measurement depend not only on properties of a vibration source but also on the properties of measuring instrument.

- Velocity measurement transducers (sensors) termed geophones are used in the frequency range that is greater than the natural frequency of vibration of a velocity sensor, which is approximately from about 0.1–100 Hz in the case of so called short period sensors. Short period sensors are relatively stable in a broad range of temperatures and do not require power supply unless having electronically extended frequency range. Geophones are used at larger distances from high energy sources such as arising from pile driving and blasting to avoid decoupling (out of range) and aliasing (signal smoothing) effects.
- Acceleration measurement transducers (sensors) termed accelerometers are used in the frequency range that is smaller than the natural frequency of vibration of acceleration sensor, which is approximately a few tens of Hz unless being electronically extended to a few kHz. Accelerometers require power supply and are more susceptible to background (environmental) noise than geophones, which are cheaper. Modern electronic miniature vibration sensors operate at a wider range of frequencies and amplitudes than conventional type accelerometers and geophones.

Besides right choice of instrument type and their location, method of fixation of transducers to their bases is an important issue in ground vibration measurement. No slippage or separation of an instrument from its base must be allowed even in the case of very severe ground motion in the near field of blasting, which frequency could reach thousands of Hertz and amplitudes of several gravitational accelerations.

Data on ground profile, ground water level and ground classification properties should always be available even if attenuation relationships of ground vibration are used from literature in order to be able to assess the relevance of use of empirical data. For better understanding and prediction of ground vibration, ground profile and properties can be inferred using a number of methods:

- Field non-intrusive methods are relatively fast and inexpensive but the results are unreliable when stiffer layers overly softer layers and need knowledge of ground profile. Geophysical (seismic) methods are applied at small strain, while large strain exists in vicinity of pile driving, soil compaction or blasting.
- Field intrusive methods are more expensive and time consuming than non-intrusive methods but may be applied when stiffer layers overly softer layers. The electric piezo and geophysical cone penetration test is capable of replacing drilling of borehole and performing geophysical testing in them but is limited by the depth of cone penetration.

- Laboratory testing is applicable at large strain and higher ambient stresses than strain and stress existing in the field when using geophysical (seismic) methods.

Ground investigations should be used to establish relationships between ground damping versus strain, ground wave velocity or stiffness versus strain, Poisson's ratio and unit density at least for the ground layers close to ground surface.

## References

- AASHTO (2009) Guide specifications for LRFD Seismic Bridge Design. American Association of State Highway and Transportation Officials
- ASTM D6391-99 Standard test method for field measurement of hydraulic conductivity limits of porous materials using two stages of infiltration from a borehole. Annual Book of ASTM Standards 04.08, American Society for Testing and Materials
- ASTM D1586 Standard test method for standard penetration test (SPT) and split-barrel sampling of soils. Annual Book of ASTM Standards. American National Standards Institute
- ASTM D3999-91 Standard test methods for the determination of the modulus and damping properties of soils using the cyclic triaxial apparatus. Annual Book of ASTM Standards 04.08, American Society for Testing and Materials
- ASTM D4015-92 Standard test method for modulus and damping of soils by the resonant-column method. Annual Book of ASTM Standards 04.08, American Society for Testing and Materials
- ASTM D4428/D4428M-00 Standard test methods for crosshole seismic testing. Annual Book of ASTM Standards 04.08, American Society for Testing and Materials
- ASTM D5777-00 Standard guide for using the seismic refraction method for subsurface investigation. Annual Book of ASTM Standards 04.08, American Society for Testing and Materials
- ASTM D5778-07 Standard test method for electronic friction cone and piezocone penetration testing of soils. Annual Book of ASTM Standards 04.08, American Society for Testing and Materials
- ASTM D7128-05 Standard guide for using the seismic-reflection method for shallow subsurface investigation. Annual Book of ASTM Standards, American Society for Testing and Materials
- ASTM D7400-08 Standard test methods for downhole seismic testing. Annual Book of ASTM Standards, American Society for Testing and Materials
- Bommer J (1992) The recording, interpretation and use of earthquake strong-motion. Internal report. Imperial College of Science, Technology and Medicine, London, UK
- Bormann P (ed) (2002) New manual of seismological observatory practice. GeoForschungsZentrum, Potsdam
- Burland JB (1989) Small is beautiful – the stiffness of soils at small strains. Canad Geotechn J 26:499–516
- Clayton CRI, Priest JA, Bui M, Zervos A, Kim SG (2009) The Stokoe resonant column apparatus: effects of stiffness, mass and specimen fixity. Geotechnique 59(5):429–437
- Cornforth DH (1964) Some experiments on the influence of strain conditions on the strength of sand. Geotechnique 16(2):143–167
- Das BM (1985) Advanced soil mechanics. McGraw-Hill, Singapore
- Douglas J (2003) What is a poor quality strong-motion record? Bull Earthquake Eng 1:141–156
- Dowding CH (2000) Construction vibration. Reprinted 1996 version. Prentice Hall, Upper Saddle River, NJ
- EN 1997-2 (2007) Eurocode 7 – geotechnical design, part 2: ground investigation and testing. European Committee for Standardization, Brussels
- Finn WDL (1985) Aspects of constant volume cyclic simple shear. In: Khosla V (ed) Advances in the art of testing soils under cyclic conditions. Proceedings of geotechnical engineering division of ASCE convention, Detroit, MI, pp 74–98

- Gazetas G (1991) Foundation vibrations. In: Fang H-Y (ed) Foundation engineering handbook, 2nd edn. Chapman & Hall, London, pp 553–593
- Hiller DM, Crabb GI (2000) Ground borne vibration caused by mechanised construction works. Transport Research Laboratory report 429, United Kingdom
- Ishihara K, Nagase H (1985) Multi-directional irregular loading tests on sand. In: Khosla V (ed) Advances in the art of testing soils under cyclic conditions. Proceedings of geotechnical engineering division of ASCE convention, Detroit, MI, pp 99–119
- ISO 4866 (1990) Evaluation and measurement for vibration in buildings. Part 1: guide for measurement of vibrations and evaluation of their effects on buildings. International Organization for Standardization
- Japan Road Association (2002) Specifications for highway bridges, part V: seismic design. PWRI, Japan
- Jardine RJ, Fourier AB, Maswoswse J, Burland JB (1985) Field and laboratory measurements of soil stiffness. In: Proceedings of the 11th international conference on soil mechanics and foundation engineering, vol 2, San Francisco, CA, pp 511–514
- Kramer SL (1996) Geotechnical earthquake engineering. Prentice Hall, Upper Saddle River, NJ
- Lucca FJ (2003) Tight construction blasting: ground vibration basics, monitoring, and prediction. Terra Dinamica L.L.C, Granby, Connecticut, USA
- Lunne T, Robertson PK, Powell JJM (2001) Cone penetration testing in geotechnical practice. Spon Press, London
- McDowell PW, Barker RD, Butcher AP, Culshaw MG, Jackson PD, McCann DM, Skip BO, Matthews SL, Arthur JCR (2002) Geophysics in engineering investigations. Report C562 of Construction Industry Research and Information Association, London, UK
- Peacock WH, Seed HB (1968) Sand liquefaction under cyclic loading simple shear conditions. ASCE J Soil Mech Foundations Div 94(SM3):689–708
- Roscoe KH (1953) An apparatus for the application of simple shear to soil samples. In: Proceedings of the 3rd international conference on soil mechanics, vol 1, Zurich, pp 186–191
- Seed HB (1979) Soil liquefaction and cyclic mobility evaluation for level ground during earthquakes. ASCE J Geotechn Eng Div 105(GT2):201–255
- Seed HB, Idriss IM (1967) Analysis of soil liquefaction: Niigata earthquake. ASCE J Soil Mech Foundations Div 93(SM3):83–108
- Seed HB, Lee KL, Idriss IM, Makdisi F (1975) Dynamic analysis of the slides in the Lower San Fernando Dam during the earthquake of February 9, 1971. ASCE J Geotechn Eng Div 101(GT9):889–911
- Skoglund GR, Marcuson WF 3rd, Cunny RW (1976) Evaluation of resonant column test devices. ASCE J Geotechn Eng Div 11:1147–1158
- Srbulov M (2010) Ground vibration engineering – simplified analyses with case studies and examples. Springer, New York, NY
- Tatsuoka F, Jardine RJ, Presti DLo, Benedetto HDi, Kodaka T (1997) Theme lecture: characterizing the pre-failure deformation properties of geomaterials. In: Proceedings of the 14th international conference on soil mechanics and foundation engineering, Hambourg, Germany, vol 4, pp 2129–2133
- Timoshenko SP, Goodier JN (1970) Theory of elasticity, 3rd edn. McGraw-Hill, New York, NY
- Townsend FC (1978) A review of factors affecting cyclic triaxial tests. Special Technical Publication 654, ASTM, pp 356–358

# Chapter 4

## Soil Properties Used in Simple Analyses

### 4.1 Introduction

Soil is a complex system of grains of different shapes, sizes and minerals as well as voids filled with water and/or air. Soil is heterogeneous, anisotropic and inelastic medium with its properties dependent on previous loading history, state of stress and its path in static condition. In cyclic condition, soil properties can also depend on the amplitude, number of cycles and even frequency of loading if fine grained.

The scope of this chapter is to describe the soil properties used in simple analyses and how they can be determined from routine tests and site investigation methods.

### 4.2 Shear Strength and Stiffness

#### 4.2.1 Non-cohesive Soil

##### 4.2.1.1 Shear Strength in Static Condition

Peck et al. (1974) provided an approximate empirical graph for estimation of an effective soil friction angle  $\phi_1$  as a function of the standard penetration test blow count  $N_{SPT}$ . Their graph can be approximated by the following formula.

$$\phi_1 = 30 + \frac{10}{35} \cdot (N_{SPT} - 10), \quad 10 < N_{SPT} < 40 \quad (4.1)$$

Terzaghi and Peck (1948) suggested a qualitative relationship between the number of SPT blow count  $N_{SPT}$  and soil relative density  $D_r$ , which when expressed in numerical terms is shown in Fig. 4.1.

From the relationship between  $D_r$  and void ratio  $e$

$$D_r = \frac{e_{\max} - e}{e_{\max} - e_{\min}}, \quad (4.2)$$

follows that

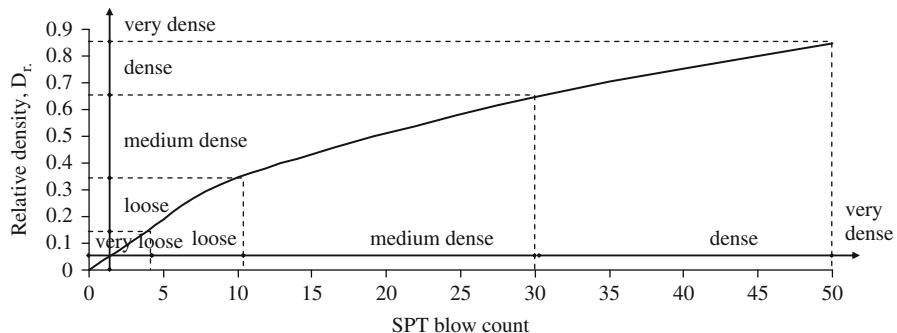


Fig. 4.1 Relative densities versus SPT blow count N

$$e = e_{\max} - D_r \cdot (e_{\max} - e_{\min}), \quad (4.3)$$

where  $e_{\max}$  can be determined from ASTM D4253 and  $e_{\min}$  from ASTM D4254, for example. Soil porosity  $n$  is defined as the ratio between the volume of voids in soil and the total volume of soil and voids. It is related to void ratio  $e$ ; which is the ratio between the volume of voids and the volume of solids

$$n = \frac{e}{e + 1} \quad (4.4)$$

According to the results of Bjerrum et al. (1961),  $\phi_1$  in static conditions can be obtained from the following formula, which does not take account of grain shape, mineral type, inter-granular friction, or relative density that have major influences on friction angle.

$$\phi_1 = 12 + \sqrt{27^2 - \left[ \frac{27}{11.5} \cdot (n \cdot 100 - 36) \right]^2} \quad (4.5)$$

$0.36 < n < 0.475$

The value of  $\phi_1$  from Equation (4.5) can be used to check slope stability in static condition when other data are not available. It should be noted that on submergence or rapid fill in saturated condition of soil within slopes, the buoyancy or overburden increase affect both the magnitude and direction of the principal stresses acting on such soil, which in turn can cause a decrease of soil volume and built up of excess pore water pressure when drainage is prevented and ultimately to soil liquefaction. Therefore, not only the friction angle from Equations (4.1) and (4.5) but also built up of excess pore water pressure in submerged or rapidly filled soil in saturated condition with prevented drainage needs to be considered for slope stability analyses.

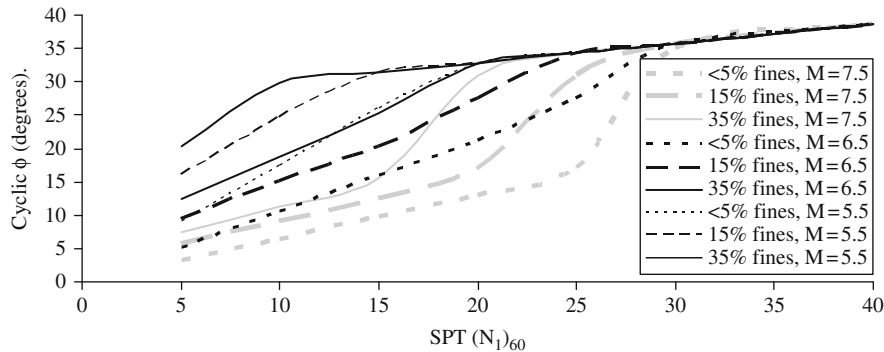


**Fig. 4.2** Friction angle of sandy soil in cyclic loading for earthquake magnitudes 5.5, 6.5 and 7.5 and normalised ( $N_1$ )<sub>60</sub> from [Equation 1.8](#)

#### 4.2.1.2 Shear Strength in Cyclic Condition and for Pseudo-Static Analyses

Soil shear strength  $\tau_{\max}$  is equal to the product of acting effective axial stress  $\sigma'$  and tan of soil friction angle  $\phi$  i.e.  $\tau_{\max} = \sigma' \tan \phi$  so that  $\tau_{\max}/\sigma' = \tan \phi$ . The chart for soil friction angle in cyclic condition in Fig. 4.2 follows from the empirical chart in EN 1998-5 (2004) showing boundary curves for stress ratios  $\tau_{\max}/\sigma'$  at onset of liquefaction as functions of normalized blow counts of standard penetration test for earthquake magnitude 7.5 and level ground. For other earthquake magnitudes, the correction coefficients from EN 1998-5 (2004) are applied, [Fig. 6.4](#).

For normalised blow count of standard penetration test exceeding the maximum values shown in Fig. 4.2, friction angle in static condition  $\phi_1$  can be used.

#### 4.2.1.3 Stiffness

At small strain ( $< 10^{-6}$ ), maximum Young modulus  $E_{\max} = \rho v_l^2$  and maximum shear modulus  $G_{\max} = \rho v_t^2$ ,  $\rho$  is soil unit density,  $v_l$  and  $v_t$  are longitudinal and transversal wave velocities respectively. The velocities are measured in the field using geophysical methods or geophysical cone. When such data are not available then the formulas in [Section 1.3.2.2](#) can be used.

At large strain (also number of cycles and cyclic amplitudes), soil stiffness decreases from the maximum value. Decrease of soil stiffness causes change of ground motion, which in turn affects strain amplitude and soil stiffness so that a recursive relationship exists. To help with this situation, EN 1998-5 (2004) provides a table of average soil damping ratios and average reduction factors ( $\pm$  one standard deviation) for shear modulus G within 20 m depth dependence on peak horizontal ground acceleration, [Fig. 4.3](#), for soil with average transversal velocity not exceeding 360 m/s, a shallow water table and plasticity index PI  $\leq 40\%$ . For stiffer soil profiles and deeper water table the reduction and the range of variations should be reduced.

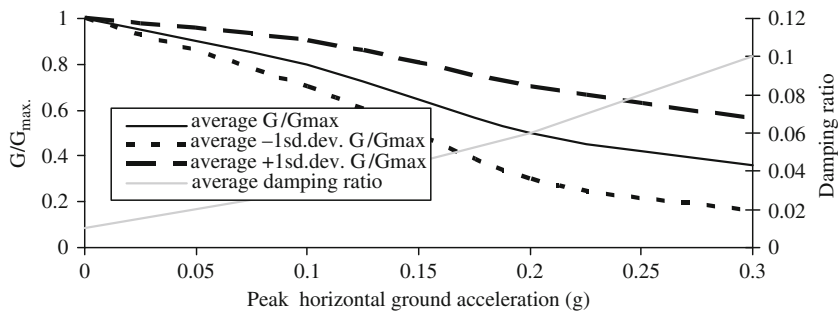


**Fig. 4.3** Average soil damping ratio and average reduction factors ( $\pm$  one standard deviation) for shear modulus  $G$  within 20 m depth (EN 1998-5, 2004)

If instead of peak horizontal ground acceleration  $a_{p,h}$ , peak ground velocity  $v_{p,h}$  or displacement  $d_{p,h}$  are known then  $a_{p,h} = \omega v_{p,h} = \omega^2 d_{p,h}$ , where circular frequency  $\omega = 2\pi f$ ,  $f$  is frequency of ground vibration.

## 4.2.2 Cohesive Soil

### 4.2.2.1 Shear Strength in Static Condition

Shear strength of fine grained soil (fine silt and clay) in static condition,  $c_u \sim (0.11 + 0.37PI) \sigma'_v OCR^{0.8}$ , where  $\sigma'_v$  is effective overburden pressure and  $OCR$  is the over consolidation ratio, which may be caused by removal of past overburden but also desiccation, cementation and ageing , and secondary compression. Skempton (1957) proposed the correlation between  $c_u$  and  $PI$  for normally consolidated clay and Wroth and Houlsby (1985) between  $c_u$  and  $OCR$ .

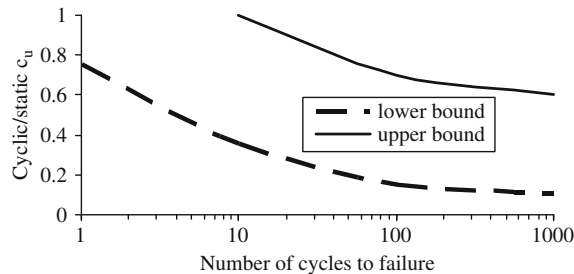
At large displacement, soil with plasticity index  $PI > 0.25$  can develop residual shear strength corresponding to the frictional angle range from  $5^\circ$  to  $15^\circ$  even at large rates of shear (e.g. Tika et al., 1996).

### 4.2.2.2 Shear Strength in Cyclic Condition

Shear strength  $c_u$  of fine grained soil (fine silt and clay) in cyclic condition decreases with the increase of number of cycles (Fig. 4.4), similarly to the shear strength of coarse grained soil. However, unlike slight rate of shear dependence of shear strength of sand (e.g. Hungr and Morgenstern, 1984),  $c_u$  depends on the rate of shear possibly because of viscosity of water films bonded electro-chemically to fine grains. The boundaries in Fig. 4.4 are from Lee and Focht (1976).

The net effect of  $c_u$  reduction with the increase of number of cycles and  $c_u$  increase due to rate effect frequently cancel each other except in the case of very soft clay (the lower bound in Fig. 4.4) and sensitive clay in Norway and Canada, which can exhibit flow type slope failures like liquefied sand.

**Fig. 4.4** General characteristics of variation of undrained shear strength with number of cycles to failure



#### 4.2.2.3 Stiffness

The comments made in Section 4.2.1.2 also apply to cohesive soil.

### 4.3 Permeability

This property is not used by the simple methods described in this volume.

### 4.4 Summary

The simple analyses do not require more soil parameters than simple static analyses used in practice. The following data are necessary for the simple dynamic analyses:

- Fines content and standard penetration test blow count in coarse grained soil (coarse silt, sand, gravel) to a depth of 20 m
- Plasticity index and over consolidation ratio of fine grained soil (clay and fine silt)
- Earthquake magnitude and peak horizontal ground acceleration

The following data should be gathered whenever feasible and particularly for unusual soil such as peat, carbonate sand, sabkha, quick clay, residual soil, tailings, fly ash in ponds, etc.:

- Soil unit density
- Transversal wave velocity of soil layers to a depth of interest by a geophysical method
- Shear strength of soil by cyclic simple shear test in laboratory
- Soil stiffness and damping ratio dependence on shear strain by resonant column test in laboratory
- Poisson's ratio of soil from transversal and longitudinal wave velocities
- Earthquake return period, site to source distance, causative tectonic fault type and extent

- Topographic and geological data
- Records of ground behaviour during past earthquakes (slope failures, tectonic fault surface rupture)

## References

- ASTM D4253 – Standard test method for maximum index density and unit weight of soils using a vibratory table. Annual Book of ASTM Standards 04.08, American Society for Testing and Materials
- ASTM D4254 – Standard test method for minimum index density and unit weight of soils and calculation of relative density. Annual Book of ASTM Standards 04.08, American Society for Testing and Materials
- Bjerrum L, Krinstad S, Kummeneje O (1961) The shear strength of fine sand. In: Fifth international conference on soil mechanics and foundation engineering, vol 1, Paris, pp 29–37
- EN 1998-5 (2004) Eurocode 8 – design of structures for earthquake resistance, part 5: foundations, retaining structures and geotechnical aspects. European Committee for Standardization, Brussels
- Hungr O, Morgenstern NR (1984) High velocity ring shear test on sand. *Geotechnique* 34:415–421
- Lee KL, Focht JA (1976) Strength of clay subjected to cyclic loading. *Marine Georesources and Geotechnology* 1(3):165–168
- Peck RB, Hanson WE, Thornburn TH (1974) Foundation engineering, 2nd edn. Wiley, New York, NY
- Skempton AW (1957) Discussion: further data on c/p ratio in normally consolidated clay. In: Proceedings of the Institution of Civil Engineers, vol 7, London, UK, pp 305–307
- Terzaghi K, Peck RB (1948) Soil mechanics in engineering practice. Wiley, New York, NY
- Tika TE, Vaughan PR, Lemos LJ (1996) Fast shearing of pre-existing shear zones in soil. *Geotechnique* 46(2):197–233
- Wroth CP, Housby GT (1985) Soil mechanics – property characterization and analysis procedures. Keynote lecture. In: Proceedings of the 11th international conference on soil mechanics and foundation engineering, San Francisco, CA, pp 1–55

# Chapter 5

## Fast Sliding of Non-liquefied Soil

### 5.1 Introduction

Fast slope failures are important because they frequently leave no time available for their remediation or even escape of people. Several types of fast slope failures occur, such as:

- Slides on single or multiple surfaces
- Rock falls and rolls
- Soil and rock avalanches, debris run-outs and fast spreads
- Soil flows

The scope of this chapter is to summarize briefly the main mechanism and factors affecting slides, the existing methods used for their analyses, and to present a simple analysis and its assumptions with implementation to five case histories in order to assess the accuracy and usefulness of the simple analyses in routine engineering practice. The simple analyses of rock falls, soil and rock avalanches, debris run-outs and fast spreads are considered by Srbulov (2008) using Excel workbooks. Soil flows are considered in [Chapter 6](#) of this volume. The emphasis is on the use of simple key equations for assessment of parameters of landslide motion for the case histories considered.

### 5.2 Mechanism and Factors

Ambraseys and Srbulov (1995) considered two stages of slope sliding.

In the first, **co-seismic**, stage gravity and inertial forces can generate a new failure surface or activate a pre-existing slip plane along which slope displacements occur. Co-seismic sliding is usually small due to short periods of earthquake pulses and their frequent reversal. The main factors affecting co-seismic stage are:

- Ground acceleration i.e. inertia forces, which are dependent on earthquake magnitude, source to site distance and on local ground conditions and type of tectonic fault.
- Critical acceleration, which is dependant on slope geometry and undrained shear strength of soil along slip surface

The second, **post-seismic**, stage follows if the first stage caused soil shear strength to decrease to a residual value below the peak strength or excess pore water pressure generated by earthquake caused decrease of the peak shear strength to a value that is not sufficient to maintain the static equilibrium of a slope. The permanent sliding caused by the effect of gravity only can be large and fast causing a slide to overshoot the location where it would have attained a stable position had the driving inertia forces been zero so that the factor of safety against sliding is greater than zero in the final resting position. The main factors affecting post-seismic movements are:

- Slope geometry
- Shear strength of soil in undrained condition including rate of share effect

The third stage, involves **consolidation and creep** in soft and loose soil with excess pore water pressure dissipation and redistribution and grains better packing in time. Also, if deep open cracks caused by ground movement are filled with surface or ground water it could trigger further sliding.

## 5.3 Existing Methods

### 5.3.1 Co-seismic Stage

Newmark's (1965) sliding block method is frequently used for analyses of permanent co-seismic displacements. The use of Newmark's (1965) sliding block method for a number of ground acceleration records is summarised in Equation (1.4) and shown in Fig. 1.4 from Ambraseys and Srbulov (1995). The method essentially consists of double integration in time of the difference between ground and the critical acceleration, which corresponds to the maximum shear resistance of soil to sliding, Fig. 5.1. The critical acceleration need not be constant in time but could change if soil shear strength is displacement and rate of share dependent and/or slope changes its geometry with large displacements.

### 5.3.2 Post-seismic Stage

Ambraseys and Srbulov (1995) two-block method for post-seismic displacements is largely used because of its simplicity and it has an analytical solution (closed

**Fig. 5.1** An example of permanent co-seismic displacement from double integration in time of the relative acceleration

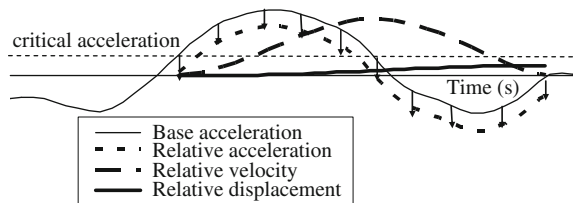
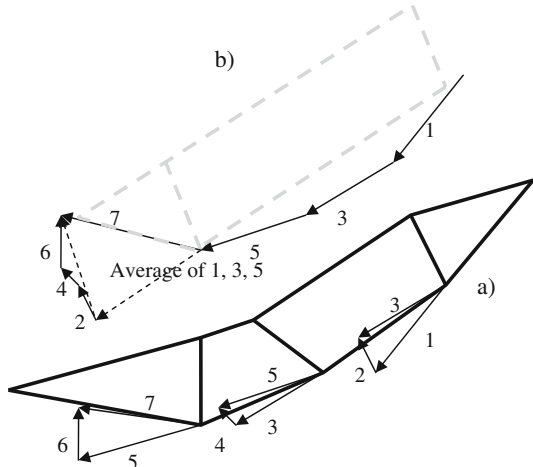


**Fig. 5.2** (a) Multi blocks for a concave slip surface, (b) equivalent two blocks with similar mass, length and thickness



form) when soil shear strength is constant and when the interface between two blocks divides the angle between the slip surface and the toe into two equal parts. LESSLOSS (2007) project describes analyses using multiple block method and other numerical methods. Multi blocks can be replaced by equivalent two block case as indicated in Fig. 5.2. The displacement vectors at the bases need not be parallel with the bases of wedges when soil volumetric change (expansion/contraction) occurs on shearing (in dense/loose sand i.e. stiff/soft clay).

## 5.4 Simple Model for Post-seismic Stage

The model consists of two prismatic blocks which slide on two basal planes with the interface between two blocks dividing the angle between the slope and the toe into two equal parts so that an analytical solution is possible. In this case, the amount of sliding down a slope equals the amount of sliding along the toe.

Ambraseys and Srbulov (1995) method determines the angle of inclination of the interface so that the factor of safety in static condition is minimal but this requires the use of a numerical procedure for analyses of block sliding instead of simple formulas. The calculations for a number of cases indicate that the differences between

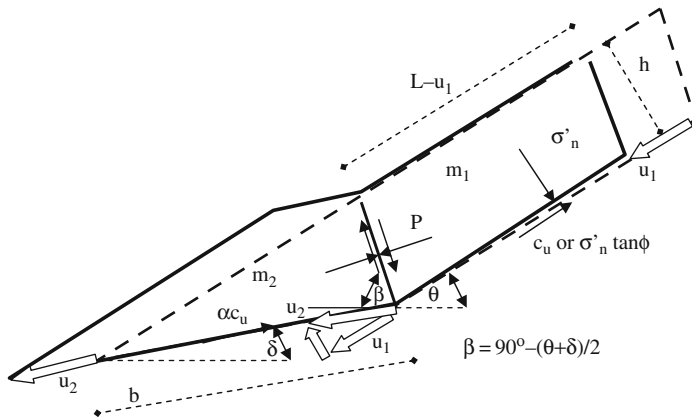


**Fig. 5.3** Notation used with the two-block method

the results of the numerical and analytical methods are of the order of difference that can be caused by natural variation in soil properties or inaccuracy connected with assumed soil properties. The notations used with the derivation of the equations of motions are shown in Fig. 5.3.

The two equations of motions of contiguous slope and toe masses due to the effect of gravity alone are:

$$m_1 \cdot d^2 u_1 / dt^2 = m_1 \cdot g \cdot \sin \theta - c_u \cdot (L - u_1) + P \cdot \cos(90^\circ - \beta - \theta) + \frac{c_u \cdot h}{\tan(\beta + \theta)} \quad (5.1)$$

$$m_2 \cdot d^2 u_2 / dt^2 = m_2 \cdot g \cdot \sin \delta - \alpha \cdot c_u \cdot (b + u_2) + P \cdot \cos(90^\circ - \beta - \delta) - c_u \cdot h \cdot \frac{\cos(\beta + \delta)}{\sin(\beta + \theta)} \quad , \quad (5.2)$$

where the second derivative of displacement  $u$  in time represents acceleration,  $g$  is the gravitational acceleration,  $c_u$  is undrained shear strength of fine grained soil or  $\sigma'_n \tan \phi$  in coarse grained soil,  $\sigma'_n$  is axial stress acting on the sliding surface along slope,  $\phi$  is the friction angle of coarse grained soil,  $\alpha$  is coefficient of proportion of  $c_u$  along the toe and the slope,  $P$  is the axial force acting on the interface. In coarse grained soil, it is assumed for simplicity that the shear strengths along the sliding surface, interface and toe are the same. The angles of inclination to the horizontal of the slip surfaces along slope, toe and interface are  $\theta$ ,  $\delta$ ,  $\beta$  respectively. It is assumed that during sliding the total mass ( $m_1 + m_2$ ), the shear strength ( $c_u$ ,  $\alpha c_u$  or  $\sigma'_n * \tan \phi$ ) and the angle  $\beta = 90^\circ - 0.5(\theta + \delta)$  remains constant. The initial width of the toe is  $b = h^*[\sin(\theta - \delta)]^{-1}$ ,  $h$  is the thickness of the block on slope. At the beginning of motion, the displacements and velocities are zero and the initial factor of safety against sliding is less than one.

The condition of mass conservation and  $\beta = 90^\circ - 0.5(\theta + \delta)$  implies that:

$$\begin{aligned} m_1 &= \rho \cdot h \cdot (L - u_1) \\ m_2 &= \rho \cdot h \cdot \left( \frac{b}{2} + u_2 \right) \\ u_1 &= u_2 \end{aligned} \quad (5.3)$$

From Equations (5.2) and (5.3) it follows that the axial interface force P is:

$$P = \frac{\rho \cdot h \cdot \left( \frac{b}{2} + u_1 \right) \cdot \left( \frac{d^2 u_1}{dt^2} - g \cdot \sin \delta \right) + c_u \cdot [\alpha \cdot (b + u_1) + h \cdot \tan(\frac{\theta-\delta}{2})]}{\cos(\frac{\theta-\delta}{2})} \quad (5.4)$$

Substituting Equation (5.4) into Equation (5.1), it becomes for  $u_1 < L$ :

$$\begin{aligned} \frac{d^2 u_1}{dt^2} &= \frac{[c_u \cdot (1 - \alpha) - \rho \cdot h \cdot g \cdot (\sin \theta - \sin \delta)] \cdot u_1}{\rho \cdot h \cdot \left( L + \frac{b}{2} \right)} \\ &+ \frac{\rho \cdot h \cdot g \cdot \left( L \cdot \sin \theta + \frac{b}{2} \cdot \sin \delta \right) - c_u \cdot [L + \alpha \cdot b + 2 \cdot h \cdot \tan(\frac{\theta-\delta}{2})]}{\rho \cdot h \cdot \left( L + \frac{b}{2} \right)} \end{aligned} \quad (5.5)$$

**The factor of safety F during and at the end of sliding** is the ratio between resisting and driving forces.

$$F = \frac{c_u \cdot [L - u_1 + \alpha \cdot (b + u_1) + 2 \cdot h \cdot \tan(\frac{\theta-\delta}{2})]}{\rho \cdot g \cdot h \cdot [(L - u_1) \cdot \sin \theta + (\frac{b}{2} + u_1) \cdot \sin \delta]} \quad (5.6)$$

The **initial factor of safety  $F_o$**  < 1 at time  $t = 0$  when  $u_1 = 0$  is:

$$F_o = \frac{c_u \cdot [L + \alpha \cdot b + 2 \cdot h \cdot \tan(\frac{\theta-\delta}{2})]}{\rho \cdot g \cdot h \cdot [L \cdot \sin \theta + (\frac{b}{2}) \cdot \sin \delta]}, \quad (5.7)$$

which is used to simplify the solution of Equation (5.5) for block acceleration in time:

$$\begin{aligned} \frac{d^2 u_1}{dt^2} &= \frac{(1 - F_o) \cdot g \cdot \left( L \cdot \sin \theta + \frac{b}{2} \cdot \sin \delta \right)}{\left( L + \frac{b}{2} \right)} \\ &\cdot \cos \left( t \cdot \sqrt{\frac{g \cdot (\sin \theta - \sin \delta) + c_u \cdot (\alpha - 1)}{L + \frac{b}{2}}} \right) \end{aligned} \quad (5.8)$$

The block velocity in time is:

$$\frac{du_1}{dt} = \frac{(1 - F_o) \cdot g \cdot \sqrt{\rho \cdot h} \cdot \left( L \cdot \sin \theta + \frac{b}{2} \cdot \sin \delta \right)}{\sqrt{[\rho \cdot g \cdot h \cdot (\sin \theta - \sin \delta) + c_u \cdot (\alpha - 1)] \cdot \left( L + \frac{b}{2} \right)}} \cdot \sin \left( t \cdot \sqrt{\frac{g \cdot (\sin \theta - \sin \delta) + c_u \cdot (\alpha - 1)}{L + \frac{b}{2}}} \right) \quad (5.9)$$

The block displacement in time is:

$$u_1 = \frac{(1 - F_o) \cdot \rho \cdot g \cdot h \cdot \left( L \cdot \sin \theta + \frac{b}{2} \cdot \sin \delta \right)}{\rho \cdot g \cdot h \cdot (\sin \theta - \sin \delta) + c_u \cdot (\alpha - 1)} \cdot \sin \left( t \cdot \sqrt{\frac{g \cdot (\sin \theta - \sin \delta) + c_u \cdot (\alpha - 1)}{L + \frac{b}{2}}} \right) \quad (5.10)$$

**Duration of sliding** in seconds until the movement stops is:

$$T = \pi \cdot \sqrt{\frac{\rho \cdot h \cdot \left( L + \frac{b}{2} \right)}{\rho \cdot g \cdot h \cdot (\sin \theta - \sin \delta) + c_u \cdot (\alpha - 1)}} \quad (5.11)$$

The **maximum slip** at time T is:

$$u_{\max} = \frac{2 \cdot \rho \cdot h \cdot g \cdot (1 - F_o) \cdot \left( L \cdot \sin \theta + \frac{b}{2} \cdot \sin \delta \right)}{\rho \cdot g \cdot h \cdot (\sin \theta - \sin \delta) + c_u \cdot (\alpha - 1)} \quad (5.12)$$

The **maximum velocity and acceleration** of sliding are:

$$\begin{aligned} \left( \frac{du_1}{dt} \right)_{\max} &= \frac{\pi \cdot u_{\max}}{2 \cdot T} \\ \left( \frac{d^2u_1}{dt^2} \right)_{\max} &= \frac{\pi^2 \cdot u_{\max}}{2 \cdot T^2} \end{aligned} \quad (5.13)$$

## 5.5 Case Histories

It is intended to demonstrate that the key equations in Section 5.4 can be used for both planar and convex shaped slip surfaces with sufficient accuracy in comparison with the results of numerical analyses performed using Excel spreadsheet provided by Srbulov (2008).

### 5.5.1 Maidipo Slide in China

The slide occurred in a natural slope of mudstone, siltstone and shale at Maidipo, a cross section of which is shown in Fig. 5.4, with maximum displacement along the slope of 69 m that is inferred based on the topography.

There is no indication of pre-existing shear surfaces, except that the slide occurred along the joints in rock. The water level in the slope is not known, and from the brief description of the site it is assumed that the slope was dry. Zhongyou (1984) reconstructed the sequence of sliding, and suggested that the slip occurred in four stages, deduced from the fact that the slide material came to rest in four blocks. He estimated that the whole sliding sequence lasted 2 min and the peak velocity of the first block was about 28 m/s. The slide was probably triggered by the erosion or submergence of its toe and softening of the mudstones. This may led to a progressive loss of the toe support and the failure.

Assuming that the strength properties of the toe and slope materials were the same ( $\alpha = 1$ ), that  $\delta = 0$  and  $\gamma = 22 \text{ kN/m}^3$ ,  $\sigma'_n = 22 \times 12.5 = 275 \text{ kPa}$ ,  $\phi = 15^\circ$  (the largest residual value for plasticity index  $>0.25$ ),  $c_u \sim 275 \times \tan 15^\circ = 74 \text{ kPa}$ , which results in the initial factor of safety against sliding  $F_o = 0.66$  for  $\beta = 73.5^\circ$ . The calculated duration  $T$  of the sliding according the sliding blocks model was 4.4 s. The calculated maximum displacement, velocity and acceleration of the motion are 62.5 m, 22.3 m/s and 1.62 of the gravitational acceleration respectively, and the final factor of safety  $F_f = 2.04$ .

Ambraseys and Srbulov (1995) used a non-linear numerical procedure to match the slip of 69 m inferred from the topography and assumed  $\phi = 17.2^\circ$ . The calculated  $\beta = 102^\circ$ ,  $F_o = 0.6$ ,  $F_f = 2.4$ ,  $T = 12.7$  s, the maximum velocity and acceleration of 8.5 m/s and 0.24 of the gravitational acceleration respectively. The minimum  $c = 48.4 \text{ kPa}$  for  $F_o = 1$ .

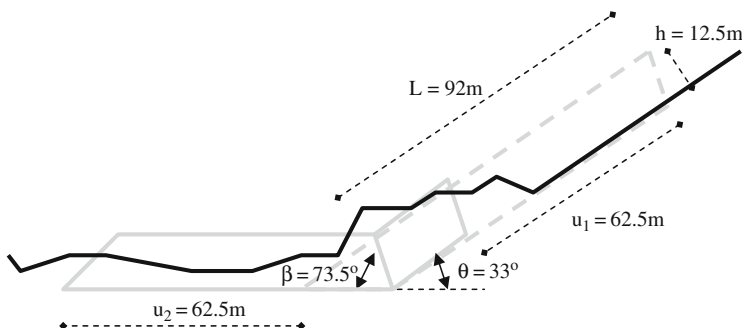


**Fig. 5.4** Sketch of the cross section of the Maidipo slide

### 5.5.2 Catak Slide in Turkey

Genc (1993) concluded that there were several factors that triggered the Catak landslide, including the presence of faults and joints in deeply weathered marls, shales, tuffities, limestone and basalts. Also, the natural slope was over steepened by the Macka river incision, and the removal of material at the toe by road works on the Trabzon-Erzurum highway along with prolonged heavy rainfall exacerbated by a spring may have acted as the triggering mechanism for the mass movement. The speed of the slide is not known, but it was such that it crushed a coffee house and vehicles parked alongside the highway at the base of the hill, burying at least 66 people, including the operator of a road grader who was trying to remove material that had fallen onto the road during earlier slip movements. Sketch of the cross section of the Catak slide is shown in Fig. 5.5.

Because of the saturation of the slope, total strength analysis and an undrained strength of the slope material are used. The computation performed using the closed form solution with  $\beta = 71^\circ$ ,  $\delta = 0$ ,  $\gamma = 20 \text{ kN/m}^3$ ,  $\sigma'_n = 20 \times 20 = 400 \text{ kPa}$ . Assuming  $\alpha = 1$ ,  $c_u = 0.3 \times 400 = 120 \text{ kPa}$ , the corresponding initial factor of safety  $F_o = 0.58$ . For  $u_{\max} = 206 \text{ m}$ , the final factor of safety  $F_f = 3.6$ . The duration of sliding  $T = 20.7 \text{ s}$  and the maximum velocity and acceleration  $15.7 \text{ m/s}$  and  $0.24$  of the gravitational acceleration respectively.

Ambroseys and Srbulov (1995) used a nonlinear numerical procedure to calculate the critical interface angle  $\beta = 97.5^\circ$  for the minimal initial factor of safety  $F_o = 0.8$ . The minimum  $c = 203 \text{ kPa}$  for  $F_o = 1$ . For the maximum displacement  $u_{\max} = 142 \text{ m}$  inferred from the topography, they calculated that  $c_u = 162 \text{ kPa}$  with the final factor of safety  $F_f = 1.44$ . The duration of sliding  $T = 23.2 \text{ s}$ , and the maximum velocity and acceleration of the mass are  $9.6 \text{ m/s}$  and  $0.15$  of the gravitational acceleration respectively.

### 5.5.3 Usoy Slide in Tajikistan

Gaziev (1984) described the landslide, which involved about  $2 \text{ km}^3$  of rock in the Pamirs during the strong earthquake of 1911 ( $M_s = 7.4$ ). According to Gaziev

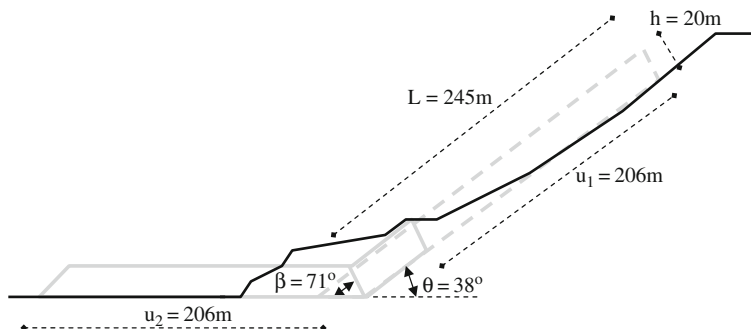


**Fig. 5.5** Sketch of the cross section of the Catak slide

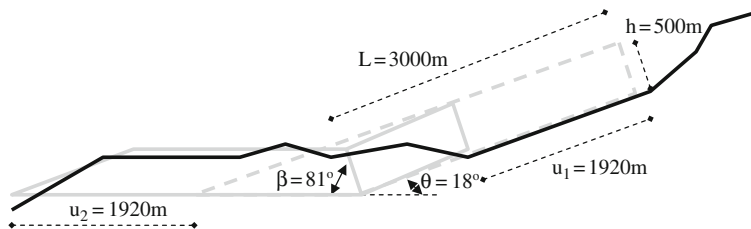


**Fig. 5.6** Sketch of the cross section of the Usoy slide

(1984), the sedimentary rock in which the slide occurred was crushed into rock flour. There are no data about piezometric level within the slide. A cross section through the slide is shown in Fig. 5.6.

For assume  $\beta = 81^\circ$ ,  $\alpha = 1$ ,  $\delta = 0$ ,  $\sigma'_n = 500 \times 24 = 12,000$  kPa,  $\phi = 7.5^\circ$ ,  $c_u \sim 12,000 \times \tan 7.5^\circ = 1580$  kPa,  $F_o = 0.68$ ,  $u_{\max} = 1920$  m, the slide duration  $T = 111.4$  s, the maximum velocity and acceleration are 27.1 m/s and 0.078 of the gravitational acceleration respectively. The final factor of safety  $F_f = 1.9$ .

Ambraseys and Srbulov (1995) matched the inferred slide of 2050 m based on the topography with assumed  $\phi = 9^\circ$ , to calculate  $\beta = 119^\circ$  for the minimum  $F_o = 0.67$ . The minimum  $c = 838$  kPa for  $F_o = 1$ . The calculated sliding time  $T = 107$  s, the maximum velocity and acceleration are 30 m/s and 0.09 of the gravitational acceleration respectively. The final factor of safety  $F_f = 2.0$ .

#### 5.5.4 Vajont Slide in Italy

Crosta et al. (2007) stated that *the major attention to the initial movements observed at the Vajont site was partially due to the event that took place on March 22, 1959 at the Pontesei water reservoir tens of kilometres from Vajont site*. The lake level was lowered about 30 m because of the observed movement close to the left abutment of the dam when 5 million cubic metres of landslide caused a water wave about 18 m high above the lake level that killed one person on the opposite valley side. The 400 m long and 47 m thick landslide moved on a failure surface inclined at 5° to the horizontal.

In 1963, approximately 275 million of cubic metres of rock slid into the reservoir following a lowering of its water level for 10 m to about two thirds of the maximum depth. The slide area involved about  $2 \text{ km}^2$ , moved laterally about 360 m and 140 m upward on the opposite valley side, at an estimated velocity of 20 to 30 m/s and with duration of about 50 s causing an earthquake that lasted up to 97 s. The water wave eroded trees and soil on the opposite side of the valley to a maximum elevation of 235 m above the reservoir level. The water wave above the dam crest was over 100 m, destroyed five villages and about 2943 persons were killed and many others were injured. The velocity of water above the dam crest was about  $(2 \times 9.81 \times 100)^{1/2} = 4.5$  m/s.

Numerous two dimensional limit equilibrium back analyses required friction angles for slide stability in the range from  $7^\circ$  to  $28^\circ$ . Slow torsional shear tests

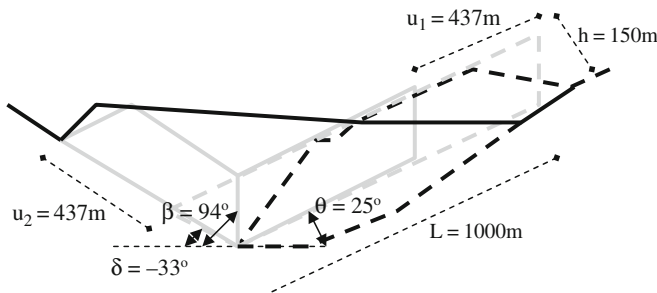


**Fig. 5.7** Sketch of the cross section of the Vajont slide

resulted in the peak and residual friction angles of the clay at the location of  $30^\circ$  and  $5^\circ$  respectively. Fast shear tests resulted in the values of the residual friction angles in the range from  $4^\circ$  to  $10^\circ$ . A cross section through the slide is shown in Fig. 5.7.

For an averaged  $\theta = 25^\circ$ ,  $\delta = -33^\circ$ ,  $\beta = 94^\circ$ , assumed  $\alpha = 1$ ,  $\sigma'_n = 150 \times 25 = 3750\text{ kPa}$ ,  $\phi = 7^\circ$ ,  $c_u = 3750 \times \tan 7^\circ = 460\text{ kPa}$ ,  $F_o = 0.44$ ,  $u_{\max} = 436.8\text{ m}$  and duration  $T = 33.8\text{ s}$ , the maximum velocity and acceleration are  $20.3\text{ m/s}$  and  $0.19$  of the gravitational acceleration respectively. The final factor of safety  $F_f = -3.43$ , so a slide back occurred from the maximum elevation reached during the initial slip.

Ambraseys and Srbulov (1995) non-linear numeric method with assumed  $\phi = 10^\circ$ , resulted in  $\beta = 110^\circ$  for the minimum  $F_o = 0.55$ . The minimum  $c = 512\text{ kPa}$  for  $F_o = 1$ . The calculated sliding time  $T = 34\text{ s}$ , the maximum displacement, velocity and acceleration are  $359.5\text{ m}$ ,  $16.5\text{ m/s}$  and  $0.15$  of the gravitational acceleration respectively. The final factor of safety  $F_f = 17.2$ .

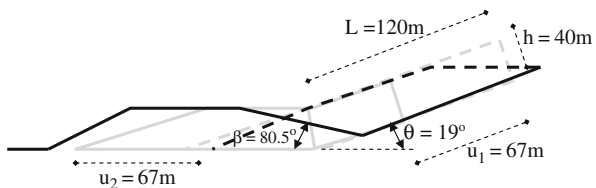
### 5.5.5 Higashi Takezawa Slide in Japan

Gerolymos and Gazetas (2007) described about  $300\text{ m}$  wide,  $250\text{ m}$  long, and  $40\text{ m}$  thick landslide that moved rapidly about  $100\text{ m}$  and involved about  $1.2$  millions of cubic metres of silt and dense silty sand formed by weathering of sandstone and siltstone. The terrace along the river and below the toe of the landslide consists of marine sand from the Tertiary period. The slide was triggered by the 2004 Niigata-Ken Chuetsu earthquake with the body wave magnitude  $M_w = 6.8$  following the heavy rainfall during the last three days before the earthquake. It was postulated that grain crushing may have induced liquefaction and apparent friction angle of  $3.3^\circ$ . A cross section of the slide is shown in Fig. 5.8.

For an averaged  $\theta = 19^\circ$ ,  $\delta = 0^\circ$ ,  $\beta = 80.5^\circ$ , assumed  $\alpha = 1$ ,  $\sigma'_n = 40 \times 20 = 800\text{ kPa}$ ,  $\phi = 5^\circ$ ,  $c_u = 800 \times \tan 5^\circ = 70\text{ kPa}$ ,  $F_o = 0.72$ ,  $u_{\max} = 67.2\text{ m}$  and duration  $T = 23.7\text{ s}$ , the maximum velocity and acceleration are  $4.4\text{ m/s}$  and  $0.06$  of the gravitational acceleration respectively. The final factor of safety  $F_f = 1.3$ .

Ambraseys and Srbulov (1995) non-linear numeric method with assumed  $\phi = 7^\circ$  (for  $5^\circ$ , the sliding exceeded the block initial length of  $120\text{ m}$ ), resulted in

**Fig. 5.8** Sketch of the cross section of the Higashi-Takezawa slide



$\beta = 120.2^\circ$  for the minimum  $F_o = 0.6$ . The minimum  $c = 55.8 \text{ kPa}$  for  $F_o = 1$ . The calculated sliding time  $T = 22.1 \text{ s}$ , the maximum displacement, velocity and acceleration are 96.9 m, 6.9 m/s and 0.09 of the gravitational acceleration respectively. The final factor of safety  $F_f = 2.85$ .

## 5.6 Discussion and Conclusions

The co-seismic permanent displacements of slopes are assessed using Newmark (1965) sliding block method. Equation (1.4) and Fig. 1.4 can be used for the assessment with the following input parameters:

- Earthquake magnitude
- Source to site distance
- Critical acceleration for the factor of safety against sliding of one
- Peak horizontal ground acceleration (e.g. according to Equation (1.1) and Fig. 1.1)

The post-seismic sliding of slopes under gravitational load only can be assessed using simple formulas such as:

- Equation (5.7) for the initial factor of safety against sliding, which must be less than one
- Equation (5.11) for duration of sliding
- Equation (5.12) for maximum sliding distance
- Equations (5.13) for maximum velocity and acceleration of sliding
- Equation (5.6) for the final factor of safety against sliding

Only a small number of input parameters are required for the assessment:

- Slide length and thickness
- Soil unit density above and the frictional angle or shear strength in undrained condition along slip surface
- The angles of inclination to the horizontal of slip surface and its toe

In many cases, the simple analysis can have sufficient accuracy not only for translational slides in cohesive and non-cohesive soil but also for slides of convex shapes.

## References

- Ambroseys NN, Srbulov M (1995) Earthquake induced displacements of slopes. *Soil Dyn Earthquake Eng* 14:59–71
- Crosta GB, Frattini P, Imposimato S, Roddeman D (2007) 2D and 3D numerical modelling of long run out landslides – the Vajont case study. In: Crosta GB, Frattini P (eds) Risk mitigation for earthquakes and landslides report 2007/01. <http://www.lessloss.org/main/index.php>
- Gaziev E (1984) Study of the Usoy landslide in Pamir. In: Proceedings of the 4th international symposium on landslides, vol 1, Toronto, Canada, pp 511–515
- Genc C (1993) Structural and geomorphological aspects of the Catak landslide, NE Turkey. *Q J Eng Geol* 26:99–108
- Gerolymos N, Gazetas G (2007) The case study of Highashi-Takezawa landslide, Japan (2004). In: Crosta GB, Frattini P (eds) Risk mitigation for earthquakes and landslides report 2007/01. <http://www.lessloss.org/main/index.php>
- LESSLOSS (2007) Landslides: from mapping to loss and risk estimation. In: Crosta GB, Frattini P (eds) Risk mitigation for earthquakes and landslides report 2007/01. <http://www.lessloss.org/main/index.php>
- Newmark NM (1965) Effect of earthquakes on dams and embankments. *Geotechnique* 15:139–160
- Srbulov M (2008) Geotechnical earthquake engineering – simplified analyses with case studies and examples. Springer, New York, NY
- Zhongyou L (1984) Examples of rapid landslides in semi rock strata. In: The 4th international symposium on landslides, vol 1, Toronto, Canada, pp 663–667

# Chapter 6

## Flow of Liquefied Sandy Soil

### 6.1 Introduction

Flows caused by liquefaction of sandy slopes and the effects on adjacent structures are among the most significant hazards caused by earthquakes. EN 1998-5 ([2004](#)) (and other publications world wide) specifies procedure for determination of liquefaction potential of sandy soil with horizontal or gently inclined surface using an empirical method but not for ground slopes during earthquakes.

For non-liquefied ground slopes, EN 1998-5 ([2004](#)) code allows that the stability verification may be carried out by means of simplified pseudo-static methods where the surface topography and soil stratigraphy do not present very abrupt irregularities. In modelling the behaviour of soil in cyclic conditions, it is important that the softening of soil stiffness with increasing strain and the effects of pore water pressure increase on soil shear strength is taken into account. A topographic amplification factor on slope acceleration can be taken into account according to informative annex A in the code. The horizontal seismic inertia force in pseudo-static analysis is taken proportional to a half of the peak horizontal acceleration along the slope. The vertical seismic force is either a half of the horizontal seismic inertia force, when vertical bedrock acceleration is greater than 60% of the horizontal acceleration, or one third of the horizontal force, when this is not the case.

The aim of this chapter is to summarize briefly: the main mechanism and factors affecting flow of liquefied sandy slopes, the main methods used for the analysis, to present simple considerations of liquefaction potential due to earthquakes and flow failures of slopes in sandy soil for fourteen case histories in order to indicate the accuracy and usefulness of the simple analyses in routine engineering practice. The chapter is based on a paper by Srbulov ([2010](#)) with kind permission of Patron Editore. The emphasis is on using simple models for the back analyses of the case histories considered.

## 6.2 Mechanism and Factors

When loose to medium dense fully saturated sandy soil is subjected to increase in excess pore water pressure without possibility of the pressure dissipation it may liquefy. Soil liquefaction could occur in static and cyclic condition. Soil liquefaction in seismic conditions depends mainly on:

- Soil density and fines content (According to Seed et al., 2003, liquefaction of sandy soil can occur when the corrected blow count of the standard penetration test ( $N_1$ )<sub>60</sub> is less than 30 for less than 5% fines, ( $N_1$ )<sub>60</sub> is less than 24 for 15% non-plastic fines and less than 21 for 35% non-plastic fines. Robertson and Wride, 1998, specified that liquefaction of sandy soil can occur when the corrected cone penetration test tip resistance  $q_{c1N}$  is less than 160 for fines content less than 5%. Andrus and Stokoe, 1998, specified that liquefaction of sandy soil can occur when transversal wave velocity is less than 210 m/s)
- Peak horizontal ground acceleration (which causes that the ratio between shear stress and effective axial stress is greater than 0.05)
- Earthquake magnitude (greater than about 5.5)
- Depth of deposit (data available mainly down to a depth of 20 m)

In static conditions, soil liquefaction depends mainly on (e.g. Obermeier, 1996):

- Rate of deposition and surcharging
- Artesian water pressure
- Amount of slope slumping and chemical weathering

Flow distance of liquefied slopes depends mainly on:

- Initial slope height (thickness of liquefied layer) and mass involved (greater values cause greater flow distance)
- Base inclination (greater inclination causes greater flow distance)
- Fines content (smaller content causes smaller flow distance)

## 6.3 Existing Methods

Unlike level ground, soil slopes are subjected to shear stresses caused by gravity forces. Ishihara (1993) suggested boundary lines between non-flow and flow conditions based on standard penetration test blow counts or cone penetration test resistances and effective overburden pressure.

Harder and Boulanger (1997) proposed a method to correct the cyclic stress ratio  $\tau/\sigma'$  for sand and Boulanger and Idriss (2007) for silt and clay in slopes with respect to level ground so that the empirical method for level grounds can be used for slopes. The scatter of the correction factors in their graphs is large and makes it difficult to develop engineering recommendations.

Olson (2001) considered motion of a sliding block on an assumed concave surface described by a third order polynomial to back analyse case histories of flow slides due to soil liquefaction. He found that the ratio between undrained shear strength of liquefied soil and effective overburden pressure varies in the range from 0.05 to 0.12, with an average of 0.09. Shear strength of coarse granular soil is usually represented by angle of friction instead of cohesion. In liquefied condition, effective overburden pressure is zero and hence soil shear strength in liquefied condition is zero by definition. Also, flow type failures are more fluid like rather than block like movements.

Srbulov (2005, 2008) considered simple rotating block for analysis of liquefaction potential and rolling block for analysis of flow type failures of slopes in sandy soil. Soil friction angle in cyclic condition is obtained by back analyses of the empirical data used for level ground. The rolling cylinder model exhibits high sensitivity to the model parameters, which is typical for chaotic motions.

A number of empirical relationships exist for determination of the path length of flow type failures. Hamada et al. (1986) proposed that the path length is proportional to the thickness of the liquefied layer and the larger of the ground surface slope angle or the slope angle of the lower boundary of the liquefied zone. Youd et al. (2002) provided an empirical attenuation relationship for flow distances based on:

- earthquake magnitude,
- modified earthquake source distance,
- ground slope inclination,
- cumulative thickness of saturated granular layers with the normalized standard penetration test blow count less than 15,
- average fines (particles less than 0.06 mm in diameter) content for the layers with the blow count less than 15,
- average grain size for the layers with the blow count less than 15.

## 6.4 Simple Models

### 6.4.1 Potential of Liquefaction of Soil Slopes

Duncan (1996), among others, reviewed properties of a number of methods that exist for pseudo-static analyses of slope stability against sliding using trial slip surfaces, Fig. 6.1.

Ambraseys and Menu (1988) argued that regardless of the method used, a trial slip surface can be represented by its equivalent block with the axial and transversal forces equal to the resultants of the axial and transversal forces acting along a trial slip surface, Fig. 6.2.

The stress ratio  $\tau/\sigma'$  due to horizontal acceleration  $a_h$  acting on soil above a trial slip surface and its equivalent sliding block can be calculated as

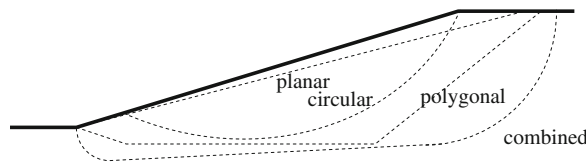


**Fig. 6.1** Cross section through types of potential slope slips surfaces

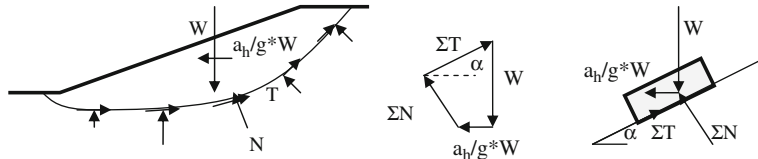


**Fig. 6.2** A potential slip surface with polygon of resultant forces and the equivalent sliding block

$$\frac{\tau}{\sigma'} = \frac{a_h/g \cdot W \cdot \cos \alpha}{\Sigma N'}, \quad (6.1)$$

when contribution of  $-a_h/g W \sin \alpha$  to  $\Sigma N'$  is ignored as relatively small value.

As

$$W = \Sigma T \cdot \sin \alpha + \Sigma N \cdot \cos \alpha$$

$$\Sigma T = \frac{\Sigma N' \cdot \tan \varphi}{F_s} \quad (6.2)$$

It follows that

$$\frac{\tau}{\sigma'} = \frac{a_h \cdot \cos \alpha}{g} \cdot \left( \frac{\tan \varphi}{F_s} + \frac{\Sigma N}{\Sigma N'} \cdot \cos \alpha \right), \quad (6.3)$$

where  $a_h$  is the horizontal acceleration acting above a trial slip surface = 0.5 the peak horizontal ground acceleration times the amplification factor,  $g$  is the gravitational acceleration,  $\alpha$  is inclination to the horizontal of an equivalent sliding block,  $\varphi$  is equivalent friction angle at the base of the sliding block,  $F_s$  is factor of safety of slope stability,  $\Sigma N/\Sigma N'$  is the ratio between total and effective resultant normal forces on a trial slip surface, which is proportional to the weight ratio  $\Sigma W/\Sigma W'$ .

Factor of safety of slope stability  $F_s$  i.e. critical horizontal acceleration  $a_{\text{critical}}$  for  $F_s = 1$  is usually calculated using limit equilibrium method. Many procedures based on limit equilibrium method exist. Computer program by Maksimovic (1988) is used for the calculations of  $F_s$  for different shapes of trial slip surfaces if actual slip surface is not known. An automatic search for a circular slip surface with minimum  $F_s$  can be used. The program calculates also the parameters  $\alpha$ ,  $\varphi$ ,  $\sigma'$  of the equivalent sliding block. Soil friction angle  $\phi_1$  in static condition is used for the calculation of  $F_s$  before onset of liquefaction because liquefied soil cannot transmit the horizontal acceleration and the level of transmitted acceleration throughout a partially liquefied slope is not known.

**Fig. 6.3** Boundaries between liquefied and non-liquefied soil for earthquake magnitude 7.5 from EN1998-5 (2004)

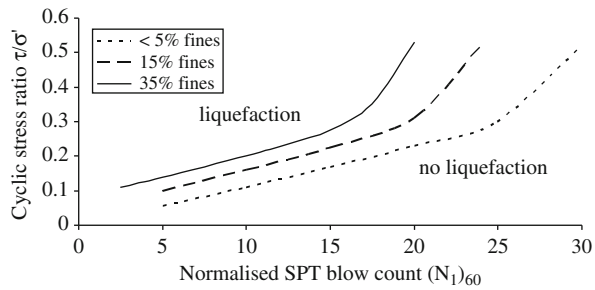
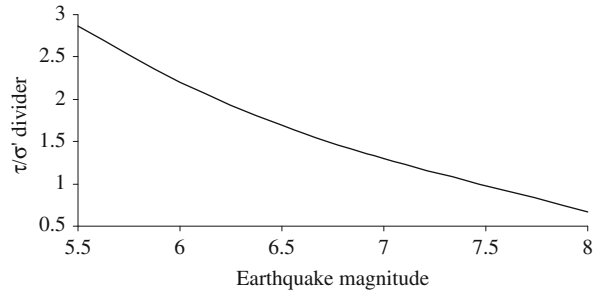


**Fig. 6.4** Divider of  $\tau/\sigma'$  for different earthquake magnitudes from EN1998-5 (2004), based on Ambraseys (1988)



From forces acting on sliding block in Fig. 6.2,  $\Sigma N = W \cos \alpha - a_h/g W \sin \alpha$ ,  $\Sigma T = W \sin \alpha + a_h/g W \cos \alpha$ , it is possible to define factor of safety  $F_s$  i.e. for calculated factor of safety  $F_s$  for a trial slip surface it is possible to calculate the angle  $\varphi$

$$\varphi = \arctan \left( F_s \cdot \frac{\tan \alpha + a_h/g}{1 - \tan \alpha \cdot a_h/g} \right) \quad (6.4)$$

The potential of liquefaction of a soil slope is then determined from the empirical chart used for level ground, as shown in Fig. 6.3 for earthquake magnitude 7.5 from EN 1998-5 (2004).

For earthquake magnitudes different from 7.5,  $\tau/\sigma'$  in Equation (6.3) should be divided by a factor shown in Fig. 6.4 from EN 1998-5 (2004) based on Ambraseys (1988).

## 6.4.2 Flow of Liquefied Slope

### 6.4.2.1 Extent

Bernoulli's equation for conservation of energy along a flow line of incompressible non-viscous fluid is used for the simple consideration of flow type failures of slopes

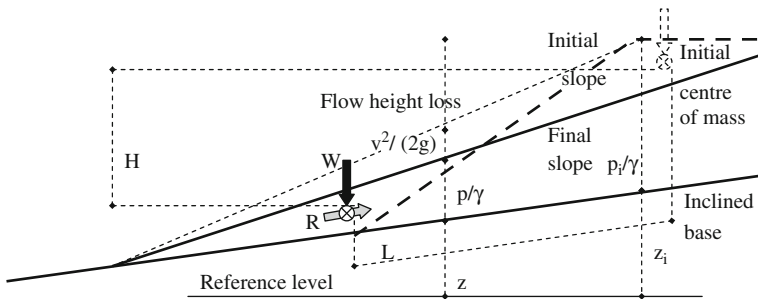


**Fig. 6.5** Sketch of cross section through failed slope with different energy heights

in sandy soil. Liquefied sandy soil has no shear strength by definition so it is non-viscous fluid. Flow of sandy soil is not conservative because it loses energy with sedimentation of particles along the flow path. Loss of energy also occurs when water flows around sharp edges due to formation of vortexes. Bernoulli's equation is applied in such cases by simulating energy loss using a coefficient that multiplies the kinetic energy of the flow. In the case of flow slides, the energy loss is considered as an additional term in Bernoulli's equation. Basic parameters are sketched in Fig. 6.5.

Bernoulli's equation with added energy loss in terms of energy heights is:

$$\frac{p}{\gamma} + z + \frac{v^2}{2 \cdot g} + \text{lost head} = \text{constant}, \quad (6.5)$$

where  $p/\gamma$  is so called pressure height,  $p$  is pressure,  $\gamma$  is unit weight of fluid,  $z$  is elevation above reference datum,  $v^2/(2g)^{-1}$  is the kinetic energy height,  $v$  is flow velocity,  $g$  is the gravitational acceleration. The constant in Equation (6.5) is calculated at the beginning of flow for the initial velocity and energy loss of zero, i.e. constant =  $p_i/\gamma + z_i$ . Of particular interest is the height drop of the centre of displaced soil mass  $H = R * L * W^{-1}$ , where  $R$  is the resistance force caused by sedimented particles in contact with the flow,  $L$  is flow path length of the centre of displaced soil mass,  $W$  is weight of displaced flow mass. The rate of lost head  $\beta = HL^{-1}$  will be back calculated from existing case histories with known final energy loss heights  $H$  and flow distances  $L$ . Tika et al. (1996) reported less than 1°C of temperature increase during fast shearing of clayey siltstone and claystone in ring shear apparatus, so the energy loss on heating is ignored for the calculation of the resistance  $R$ .

Equation (6.5) was derived for the condition of gravity load only. During earthquakes, horizontal inertia forces affect the magnitude and direction of the resultant of gravity and inertia forces. Liquefaction develops during earthquake and continues some time after it. Liquefied soil has no shear strength and cannot transfer horizontal inertial forces so the flow failure occurs under the effect of gravity only, for which Bernoulli's equation was derived.

### 6.4.2.2 Duration

The duration of flow can be estimated from sedimentation of soil particles in water. For simplicity, it is usually assumed that all sand particles are spheres and that the velocity  $V_p$  of particle sedimentation in water is described by Stokes law (e.g. Das, 1985)

$$V_p = \frac{\gamma_s - \gamma_w}{18 \cdot \eta_{aw}} \cdot D_{50}^2, \quad (6.6)$$

where  $\gamma_s$  and  $\gamma_w$  is unit weight of soil particle and water respectively ( $\text{N m}^{-3}$ ),  $\eta_{aw}$  is dynamic viscosity of water ( $\text{Nsm}^{-2}$ ),  $D_{50}$  is an average diameter of soil particles (m). The sedimentation time  $t$

$$t = \frac{p_i/\gamma}{V_p}, \quad (6.7)$$

where the height of sedimentation path  $p_i/\gamma$  is assumed equal to the initial thickness of liquefied layer because flow will not stop until soil particles from the top of flow settle down. At  $20^\circ\text{C}$ ,  $\eta_{aw} = 10^{-3} \text{ Nsm}^{-2}$ . At  $10^\circ\text{C}$ , the viscosity is 29.8% greater and at  $30^\circ\text{C}$  20.3% smaller than the viscosity at  $20^\circ\text{C}$ .

## 6.5 Case Histories

The simple method described in Section 6.4.1 is applied to a number of case histories in order to assess its usefulness in practice. The simple Equation (6.5) is applied to a number of case histories so that the rates of lost hydraulic heads are related to the amounts of fines and average particle diameters in order to find correlations between them and for an assessment of the importance of such influential factors.

### 6.5.1 Lower San Fernando Dam in California

The upstream slope of the 43 m high dam experienced a partial failure into the reservoir following the 1971 San Fernando earthquake with magnitude 6.6. Seed et al. (1973, 1975) and Lee et al. (1975) described initially the failure and its analysis. These studies concluded that liquefaction of the silty sand and sandy silt hydraulically filled in the upstream slope was the cause of the failure. Seismoscopes located on the abutment and crest of the dam recorded peak acceleration of  $0.55g$  and  $0.5g$  respectively. The seismoscope records also indicated that the slide occurred between 20 and 40 seconds after earthquake.

The average  $D_{50}$  and fines content of the liquefied fill are approximately 0.075 mm and 50% respectively. Olson (2001) selected representative  $(N_1)_{60}$  as 11.5 within boundaries between 5 and 15. For  $(N_1)_{60} = 11.5$ , it follows that  $\phi = 12^\circ$

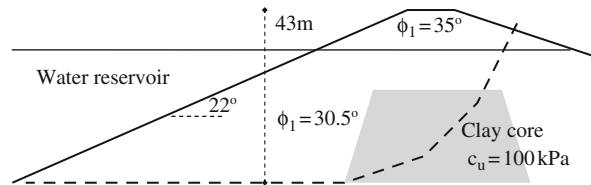


**Fig. 6.6** Cross section through the Lower Sand Fernando dam before failure and the slip surface analysed (dashed line)

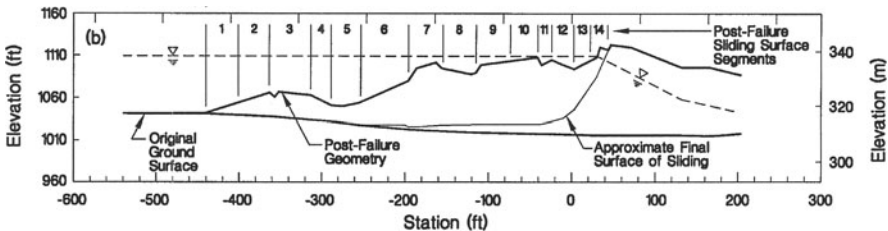


**Fig. 6.7** Cross section through the Lower Sand Fernando dam after failure (Olson, 2001)

for earthquake magnitude 7.5 and fines >35%. Using the correction factor for  $\tan\phi$  from Fig. 6.4 for earthquake magnitude of 6.6, it follows that  $\phi = 19^\circ$  in cyclic condition. For static condition,  $\phi_1 = 30.5^\circ$  for  $N = 11.5$ . The initial slope angle was  $22^\circ$ . For slope inclination less than  $30^\circ$ , Annex A of EN 1998-5 (2004) indicate an acceleration amplification factor along slope height of  $\geq 1.2$ , with at least 20% increase when a loose surface layer exists. For horizontal acceleration variation from  $0.55/(1.2 \times 1.2) = 0.38g$  at the base to  $0.55g$  at the crest and slope width variation from 84 m at the base to 20 m at the crest, an averaged horizontal acceleration is  $0.45g$  and  $a_h = 0.5 \times 0.45g = 0.225g$ . The vertical acceleration is  $1/3 \times 0.225g = 0.075g$ . The cross section, slip surface and the soil shear strength used are shown in Fig. 6.6.

The parameters estimated for the simple consideration of the flow are  $p_i/\gamma + z_i = 26$  m,  $H = 24$  m,  $L = 90$  m,  $W = 8500$  kN/m', based on Fig. 6.7.

### 6.5.2 Sheffield Dam in California

The earth dam had a maximum height of about 7.6 m over alluvial terrace deposits that were from 1.2 to 3 m thick. At the time of failure, the reservoir level was approximately 4.6–5.5 m deep (Seed et al., 1969). The slope inclination was about  $22^\circ$ . The 1925 earthquake had magnitude 6.3 at epicentral distance of about 10 km from the dam. Seed et al. (1969) estimated that the free field peak horizontal surface acceleration was about  $0.15g$ .

Based on examination of the failure mass, it seems that the downstream slope of the dam flowed over 60 m. Seed et al. (1969) concluded that the failure occurred due to liquefaction along the base of the dam. The soil involved was primarily silty

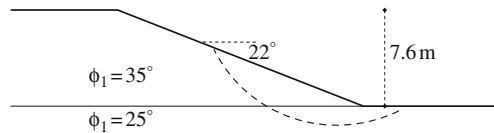


**Fig. 6.8** Cross section through downstream slope of the Sheffield dam before failure and the least stable slip surface analysed (dashed line)

sand to sandy silt with approximately 40% fines and approximate  $D_{50}$  of 0.1 mm. No penetration test results were available. Olson (2001) estimated  $(N_1)_{60}$  of about 4–6 while Seed (1987) and Seed and Harder (1990) estimated  $(N_1)_{60}$  in the range from 6 to 8. For  $(N_1)_{60} = 6$ , it follows that  $\phi = 9^\circ$  for earthquake magnitude 7.5 and fines >35%. Using the correction factor for  $\tan\phi$  from Fig. 6.4 for earthquake magnitude of 6.3, it follows that  $\phi = 16^\circ$  in cyclic condition. In static condition,  $\phi_1 = 25^\circ$  is assumed. For estimated averaged horizontal acceleration along the slope of  $1.1 \times 0.15 \times 1.2 = 0.19g$ ,  $a_h = 0.5 \times 0.19 = 0.095g$  and the vertical acceleration is about  $0.03g$ . The cross section, slip surface and the soil properties used are shown in Fig. 6.8.

The parameters estimated for the simple consideration of the flow are  $p_i/\gamma + z_i = 8$  m,  $H = 3$  m,  $L = 30$  m,  $W = 1200$  kN/m'.

### 6.5.3 Calaveras Dam in California

During dam construction using hydraulic fill for the core and interior portions of the slopes and un-compacted dumped fill for the rest of the slopes, over 600,000 m<sup>3</sup> from the upstream slope of the dam slid into the reservoir in 1918. The dam reached height of 61 m out of 73 m and the reservoir depth was about 23 m at the time of failure. The eyewitness described the failure as flow almost like water. Hazen (1920) explained the failure with reference to quicksand. The fines content was estimated at approximately 30% (Olson, 2001).

The parameters estimated for the simple consideration of the flow are  $p_i/\gamma + z_i = 60$  m,  $H = 30$  m,  $L = 200$  m,  $W = 60,000$  kN/m' based on Fig. 6.9.

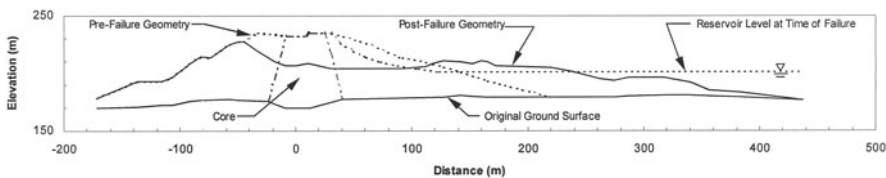


**Fig. 6.9** Cross section through the Calaveras dam (Olson, 2001)

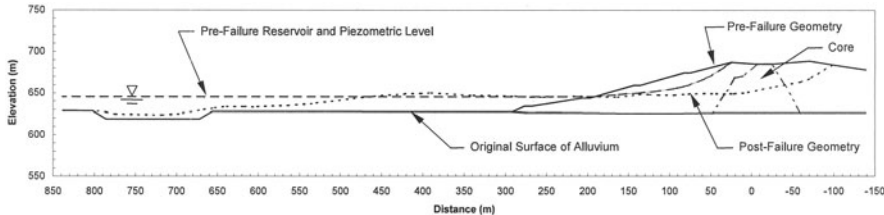


**Fig. 6.10** Cross section through Fort Peck dam (Olson, 2001)

#### 6.5.4 Fort Peck Dam in Montana – USA

The dam failed when it reached height of 62.8 m out of 76.3 m during hydraulic filling in 1938. The failure mass involved between 4 and 8 million  $\text{m}^3$  from the upstream slope. Casagrande (1965) provides detailed description of the failure. Olson (2001) stated that  $D_{50}$  of the fill varies in the range from 0.06 to 0.2 mm and that the fines content is about 55%.

The parameters estimated for the simple consideration of the flow are  $p_i/\gamma + z_i = 50 \text{ m}$ ,  $H = 30 \text{ m}$ ,  $L = 400 \text{ m}$ ,  $W = 100,000 \text{ kN/m}'$ , based on Fig. 6.10.

#### 6.5.5 North Dike of Wachusett Dam in Massachusetts – USA

Olson et al. (2000) described the failure and stability analyses of the North Dike of Wachusett Dam in details. The 3200 m long North Dike was constructed using controlled placement and compaction of the cut-off wall and core materials and uncontrolled fill method for the shells by dumping from horse-drawn carts. The upstream shell fill consists of sand to silty sand with some gravel. The upstream fill slope was 2H:1V including a bench 6 m wide at approximate elevation 117 m. Fill placement for the North Dike was completed in 1904, three years before the slope failure. In 1907, a slope failure occurred during initial filling of the reservoir along a 213 m long section of the North Dike. The failure was centered over the former river channel, where the dike height was 24.4 m, with the reservoir depth of 12.8 m.

The parameters estimated for the simple consideration of the flow are  $p_i/\gamma + z_i = 50 \text{ m}$ ,  $H = 30 \text{ m}$ ,  $L = 68 \text{ m}$ ,  $W = 5700 \text{ kN/m}'$ , based on Fig. 6.11.

#### 6.5.6 La Marquesa Dam in Chile

The 1985 central Chile earthquake with magnitude 7.8 caused the failure of two earth dams, La Marquesa and La Palma, located within approximately 80 km from the epicentre. The failures are described in detail by de Alba et al. (1987, 1988) and also discussed by Sully et al. (1995) and Castro (1995). De Alba et al. (1987) estimated the peak ground surface acceleration at the dam site of about 0.6g.

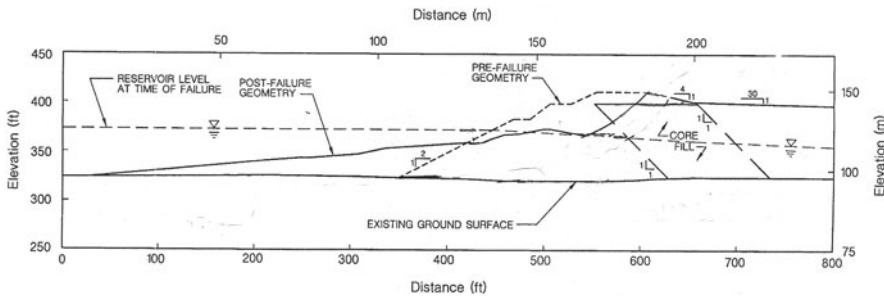


**Fig. 6.11** Cross section through north dike of Wachusett dam (adapted from Olson, 2001)

Large slides occurred in both the upstream and downstream slope of about 10 m high dam, but the upstream slope exhibited largest displacement when the reservoir level was about two thirds of the dam height. De Alba et al. (1987, 1988) proposed that liquefaction of the silty sand layer in the dam foundation caused the failure of the downstream and upstream slopes of the dam inclined at 35° and 25° to the horizontal respectively. The fines content of the silty sand layer was approximately 30% under the upstream slope and 20% under the downstream slope. Olson (2001) estimated the  $D_{50}$  of the layer about 0.15 mm based on the uniformity and fines content of the silty sand layer. The SPT blow counts measured under the upstream portion of the dam indicate  $(N_1)_{60}$  in the range from 4 to 6 and under the downstream portion of the dam in the range from 7 to 11. Castro (1995) argued that the failure of the downstream slope of the dam probably occurred in the silty and clayey sand in the lower portion of the downstream slope, which was also below pheatic surface with  $(N_1)_{60}$  of about 4 rather than in higher density foundation silty sand layer with  $(N_1)_{60}$  from 7 to 11.

Because the upstream slope exhibited flow type failure unlike the downstream slope of the dam, only the upstream slope is considered further. For the upstream slope angle less than 30° to the horizontal, the amplification factor according to Annex A of EN 1998-5 (2004) is 1.2. For the peak horizontal acceleration at the dam crest of  $1.2 \times 0.6 = 0.72g$  and  $0.6g$  at the bottom, averaged peak horizontal acceleration along the slope is  $0.66g$ ,  $a_h = 0.5 \times 0.66 = 0.33g$  and  $a_v = 0.11g$ . For  $(N_1)_{60} = 5$ , it follows that  $\phi = 7.5^\circ$  for earthquake magnitude 7.5 and fines  $\sim 35\%$ . Using the correction factor for  $\tan \phi$  from Fig. 6.4 for earthquake magnitude of 7.8, it follows that  $\phi = 5.6^\circ$  in the foundation layer in cyclic condition. In static condition,  $\phi_1 = 25^\circ$  is assumed. Within the upstream slope, soil friction angle in static condition was at least 35° in order to maintain factor of safety of 1.5. The  $N_{SPT}$  corresponding to  $\phi_1$  of 35° is 26.5 so it is unlikely that this soil exhibited strength reduction in cyclic condition. The cross section, slip surface and the soil properties used are shown in Fig. 6.12.

The parameters estimated for the simple consideration of the flow are  $p_i/\gamma + z_i = 10$  m,  $H = 5$  m,  $L = 18$  m,  $W = 400$  kN/m', based on Fig. 6.13.

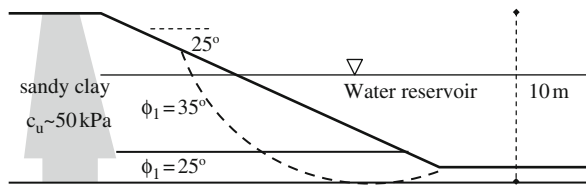


**Fig. 6.12** Cross section through upstream slope of the La Marquesa dam before failure and the least stable slip surface analysed (dashed line)

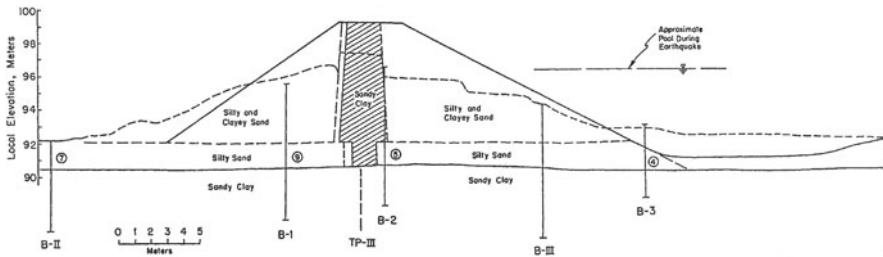


**Fig. 6.13** Cross section through La Marquesa dam (Olson, 2001)

### 6.5.7 La Palma Dam in Chile

The 1985 central Chile earthquake with magnitude 7.8 caused the failure of two earth dams, La Marquesa and La Palma, located within approximately 80 km from the epicentre. The failures are described in detail by de Alba et al. (1987, 1988) and also discussed by Jitno and Byrne (1995) and Castro (1995). De Alba et al. (1987) estimated the peak ground surface acceleration at the dam site of about 0.46g.

Based on the analyses performed by de Alba et al. (1987, 1988), it follows that liquefaction of the silty sand layer in the foundation caused the failure of the upstream slope of the 10 m high dam when the reservoir level was only about one third of the dam height. The upstream slope inclination to the horizontal was 27°. The fines content of the layer was approximately 15%. Olson (2001) estimated  $D_{50}$  of about 0.2 mm based on the uniformity and fines content of the silty sand layer. The SPT blow count recorded in the layer indicate  $(N_1)_{60}$  values in the range from 2 to 5.

For the upstream slope angle less than 30° to the horizontal, the amplification factor according to Annex A of EN 1998-5 (2004) is 1.2. For the peak horizontal acceleration at the dam crest of  $1.2 \times 0.46 = 0.55g$  and  $0.46g$  at the bottom, averaged peak horizontal acceleration along the slope is  $0.50g$ ,  $a_h = 0.5 \times 0.5 = 0.25g$  and  $a_v = 0.08g$ . For  $(N_1)_{60} = 3.5$ , it follows that  $\phi = 5^\circ$  for earthquake magnitude 7.5 and fines 15%. Using the correction factor for  $\tan\phi$  from Fig. 6.4 for earthquake magnitude of 7.8, it follows that  $\phi \sim 4^\circ$  in the foundation layer in cyclic condition. The silt and sandy silt layer below the top foundation layer had SPT blow count range from 6 to 10. For  $(N_1)_{60} = 8$ , it follows that  $\phi = 10^\circ$  for earthquake magnitude

**Fig. 6.14** Cross section through the upstream slope of La Palma dam before failure and the least stable slip surface analysed (dashed line)

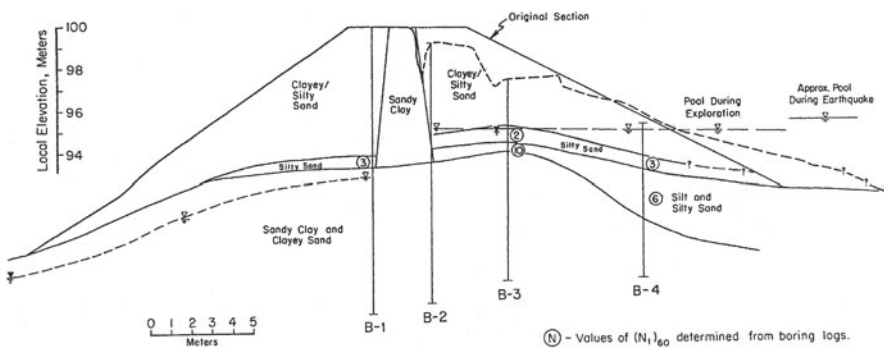
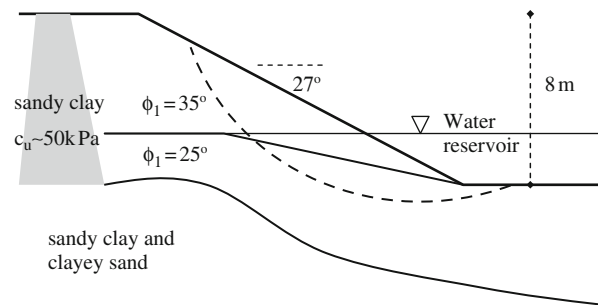


**Fig. 6.15** Cross section through La Palma dam (Olson, 2001)

7.5 and fines 35%. Using the correction factor for  $\tan\phi$  from Fig. 6.4 for earthquake magnitude of 7.8, it follows that  $\phi = 7.5^\circ$  in the layer below the top foundation layer in cyclic condition. In static condition,  $\phi_1 = 25^\circ$  is assumed. The cross section, slip surface and the soil properties used are shown in Fig. 6.14.

The parameters estimated for the simple consideration of the flow are  $p_i/\gamma + z_i = 8 \text{ m}$ ,  $H = 6 \text{ m}$ ,  $L = 15 \text{ m}$ ,  $W = 160 \text{ kN/m}'$ , based on Fig. 6.15.

### 6.5.8 Route 272 Embankment in Higashirekinai – Japan

The failure of a slope of embankment that is about 8 m high and with the slope inclined at about  $33^\circ$  to the horizontal was described by Sasaki et al. (1994). Sasaki et al. (1994) estimated the peak ground acceleration at the site to be greater than  $0.3g$ . The acceleration is caused by the 1993 Kishiro-Oki earthquake with magnitude 7.8.

The embankment is underlain by pumice bearing volcanic sand. As route 272 is very close to the Shibeche-cho embankment, Olson (2001) assumed that the foundation and fill conditions are similar. The fill was assumed to be silty sand with  $D_{50}$  in the range from 0.12 to 0.4 mm (an average  $\sim 0.2 \text{ mm}$ ) with the fines contents range from 12 to 35% (an average  $\sim 20\%$ ). The unit weight of soil is approximately

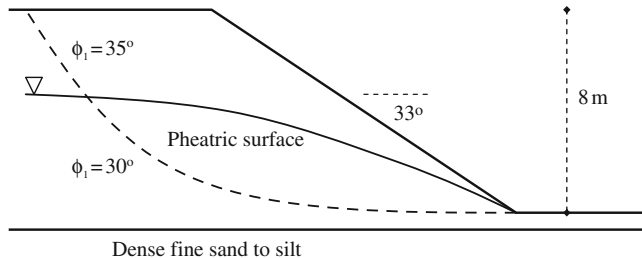


**Fig. 6.16** Cross section through the slope of the route 272 embankment before failure and the least stable slip surface analysed (dashed line)

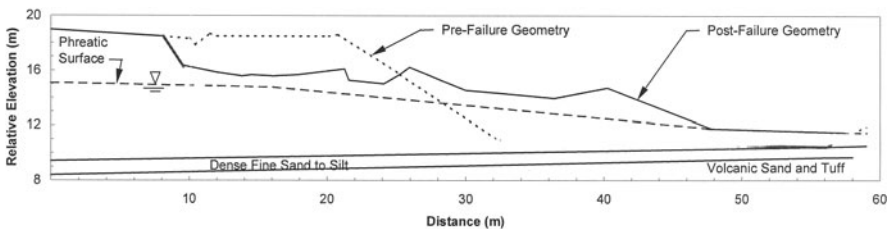


**Fig. 6.17** Cross section through the route 272 embankment (adapted from Olson, 2001)

16.5 kN/m<sup>3</sup>. The representative  $(N_1)_{60}$  value for the fill soil below the pheatic surface was in the range from 2 to 10 (an average  $\sim 6$ ).

For slope inclination greater than 30°, Annex A of EN 1998-5 (2004) recommends that the peak horizontal acceleration amplification factor at the crest is taken as 1.4 and that further 20% increase is applied if loose surface layer exist. The average horizontal acceleration of the slope was probably  $0.5*(1.4*1.2*0.3+0.3) = 0.4g$  so that  $a_h = 0.5*0.4 = 0.2g$  and  $a_v = 0.06g$ . For  $(N_1)_{60} = 6$ , it follows that  $\phi = 7^\circ$  for earthquake magnitude 7.5 and fines 20%. Using the correction factor for  $\tan\phi$  from Fig. 6.4 for earthquake magnitude of 7.8, it follows that  $\phi \sim 5^\circ$  of the fill in cyclic condition. In static condition,  $\phi_1 = 30^\circ$  is assumed. The cross section, slip surface and the soil properties used are shown in Fig. 6.16.

The parameters estimated for the simple consideration of the flow are  $p_i/\gamma + z_i = 7$  m,  $H = 3$  m,  $L = 20$  m,  $W = 700$  kN/m', based on Fig. 6.17.

### 6.5.9 Vlietepolder Deposit, Zeeland Province in Netherlands

In 1889, approximately 935,000 m<sup>3</sup> of bank and delta deposit were displaced and an area of 58,000 m<sup>2</sup> of land above the low water level disappeared, Koppejan et al. (1948). An average  $D_{50}$  of the deposit is approximately 0.12 mm with no fines according to Olson (2001).

The parameters estimated for the simple consideration of the flow are  $p_i/\gamma + z_i = 40$  m,  $H = 30$  m,  $L = 400$  m,  $W = 40,000$  kN/m', based on Fig. 6.18.

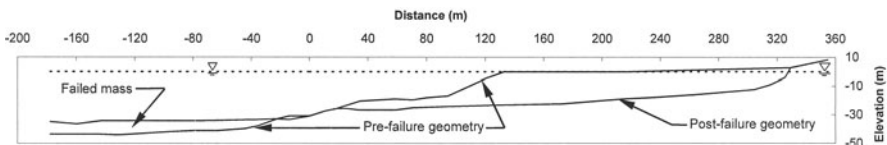


**Fig. 6.18** Cross section through Vlietepolder deposit – Zeeland province in Netherlands (Olson, 2001)

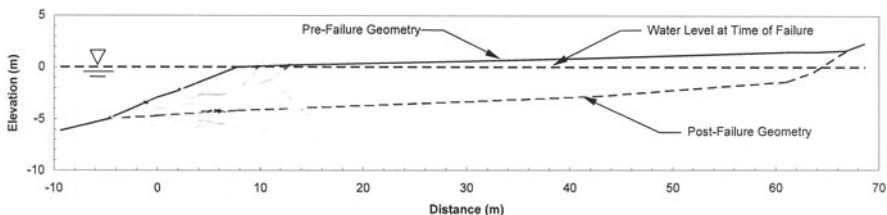


**Fig. 6.19** Cross section through the hydraulic fill at Helsinki harbour (Olson, 2001)

### 6.5.10 Helsinki Harbour Fill in Finland

In 1936, an extension to Helsinki harbour was constructed by placing hydraulically filled sand behind a rock berm, which was not completed and having a gap of 25 m until its final level. Approximately 6000 m<sup>3</sup> of sand flowed through the gap in the rock berm over a distance of 80–100 m into the harbour (Andersen and Bjerrum, 1968). The sand used as fill was obtained from a nearby borrow pit. No grain size distribution and fines content are available.

The parameters estimated for the simple consideration of the flow are  $p_i/\gamma + z_i = 7$  m,  $H = 5$  m,  $L = 90$  m,  $W = 1500$  kN/m', based on Fig. 6.19.

### 6.5.11 Lake Merced Bank in California

Ross (1968) investigated two slides involving approximately 244 m of shoreline, which occurred at a distance of 4–6.4 km from the centre of the rupture zone that was formed during the 1957 San Francisco earthquake with the magnitude  $M_L = 5.3$ . The majority of the failure occurred in fill soil, which was placed by end-dumping into the lake and possibly without any compaction. The slope of the embankment fill was about 30°. The peak acceleration at the site is not known. The recorded peak horizontal acceleration of bedrock approximately 11.2 km from the earthquake epicentre was 0.12g. The peak horizontal acceleration at the location of the slides could have been larger than 0.12g.

Ross (1968) reported on the results of site investigations in two boreholes performed after the slide. The fill is very uniform fine eolian sand with  $D_{50}$  and fines

content of approximately 0.21 mm and 1–4% respectively. No reliable measurements of penetration resistance were made in the fill. Olson (2001) estimated  $(N_1)_{60}$  approximately as 7.5 using a relative density of 40% typical of sand fill deposited through water and an average pre-failure vertical effective stress of 58.7 kPa. For  $(N_1)_{60} = 7.5$ , it follows that  $\phi = 5^\circ$  for earthquake magnitude 7.5 and fines <5%. Using the correction factor for  $\tan \phi$  from Fig. 6.4 for earthquake magnitude of 5.3, it follows that  $\phi = 15^\circ$  in cyclic condition. For static condition,  $\phi_1 = 30^\circ$  for  $N \sim 10$ . For average slope inclination less than  $30^\circ$ , Annex A of EN 1998-5 (2004) indicate an acceleration amplification factor along slope height of  $\geq 1.2$ , with at least 20% increase when a loose surface layer exists. For horizontal acceleration variation from  $0.15/(1.2 \cdot 1.2) = 0.10g$  at the base to  $0.15g$  at the crest, an averaged horizontal acceleration is  $0.12g$  and  $a_h = 0.5 \cdot 0.12g = 0.06g$ . The vertical acceleration is  $1/3 \cdot 0.06g = 0.02g$ . The cross section, slip surface and the soil shear strength used are shown in Fig. 6.20.

The parameters estimated for the simple consideration of the flow are  $p_i/\gamma + z_i = 15$  m,  $H = 5$  m,  $L = 13$  m,  $W = 1900$  kN/m', based on Fig. 6.21.

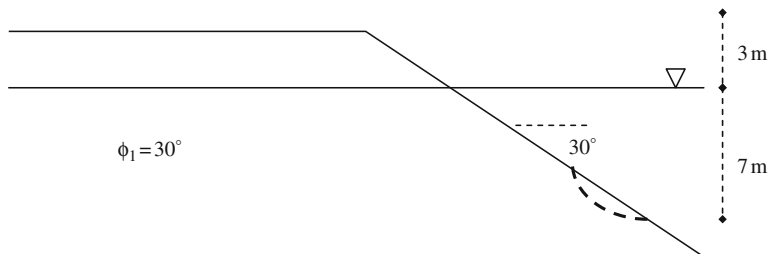


**Fig. 6.20** Cross section through the slope of lake Merced bank before failure and the least stable slip surface analysed (dashed line)

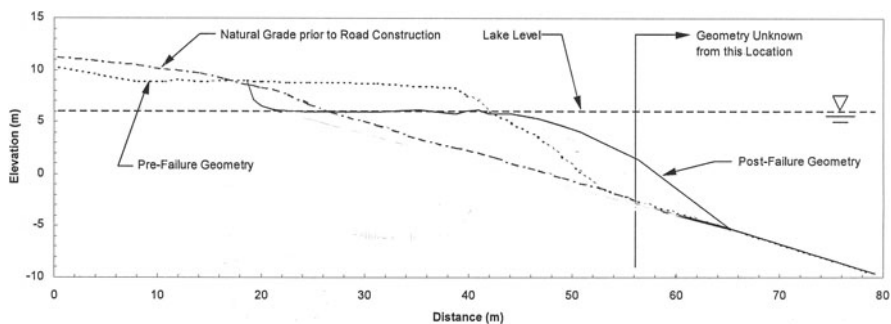


**Fig. 6.21** Cross section through lake Merced bank in California (Olson, 2001)

### 6.5.12 Hachiro-Gata Road Embankment in Akita – Japan

Ohya et al. (1985) described flow slide of the Hachiro-Gata embankment due to the 1983 Nihonkai-Chubu earthquake with magnitude 7.7 in Akita region of Japan. A peak ground acceleration of  $0.168g$  was measured in the town of Akita. The embankment was built of loose fine sand with approximate  $D_{50}$  of 0.2 mm and fines content between 10 and 20%. The representative  $(N_1)_{60}$  value is 4.4. Hence,  $\phi_1 \sim 30^\circ$  and  $\phi = 10^\circ$ . It is assumed for the calculations that  $a_h = 0.5 * 0.17g = 0.085g$ . The cross section, slip surface and the soil shear strength used are shown in Fig. 6.22.

The parameters estimated for the simple consideration of the flow are  $p_i/\gamma + z_i = 4$  m,  $H = 2$  m,  $L = 12$  m,  $W = 400$  kN/m', based on Fig. 6.23.

### 6.5.13 Lake Ackerman Road Embankment in Michigan – USA

Hryciw et al. (1990) describe liquefaction of hydraulically placed sand fill that was triggered by six 196 kN (22 t) trucks conducting a seismic reflection survey. The liquefaction resulted in a flow failure along a 91 m section of the embankment on Highway 24 in Michigan's Upper Peninsula. The failure created a 4.5 m wave that crossed the 122 wide lake Ackerman and destroyed a boat dock, which remains were strewn about 9 m onshore. The fill material used was sand end-dumped into the lake. Fill placed above the lake was moderately compacted. The average  $D_{50} = 0.4$  mm and the fines content 0%.

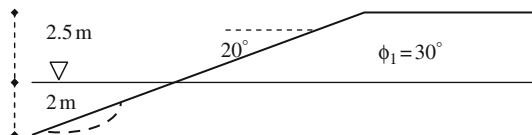


**Fig. 6.22** Cross section through the slope of Hachiro-Gata embankment before failure and the least stable slip surface analysed (dashed line)

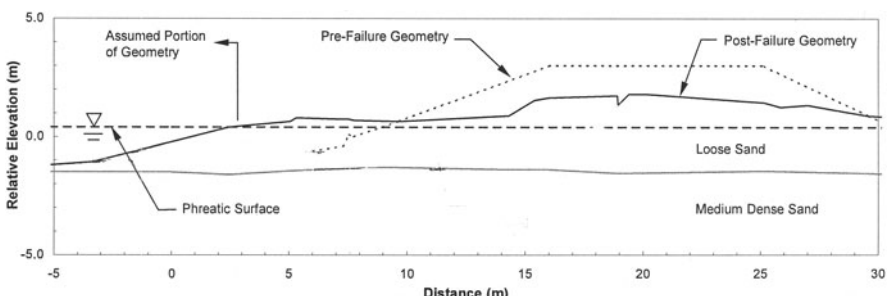


**Fig. 6.23** Cross section through Hachiro-Gata embankment in Japan (adapted from Olson, 2001)

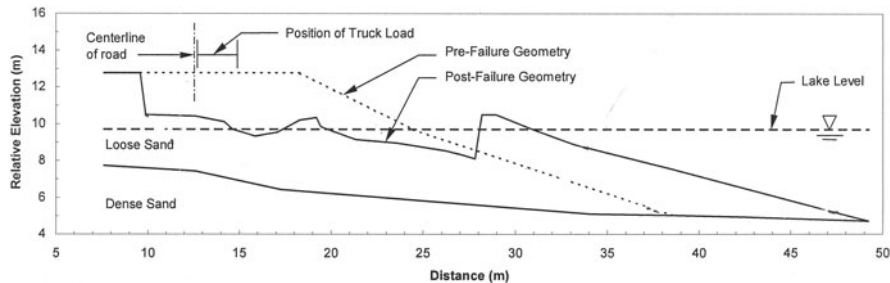


**Fig. 6.24** Cross section through Lake Ackerman embankment in Michigan-USA (adapted from Olson, 2001)

The parameters estimated for the simple consideration of the flow are  $p_i/\gamma + z_i = 8$  m,  $H = 4$  m,  $L = 19$  m,  $W = 300$  kN/m', based on Fig. 6.24.

### 6.5.14 Aberfan Coal Mine Waste in Wales – UK

Hutchinson (1986) described and analysed a fast spread of loose, cohesion-less coal mine waste at Aberfan in 1966. The spread developed in a 67 m high tip deposited on a hillside of about  $12^\circ$  inclination. The fast spread was preceded by a number of rotational slips and the removal of fines from its toe by seepage erosion. The spread travelled quickly in several “black waves” down slope about 275 m before division into a north and south lobe. The northern lobe was smaller and came to rest after a further travel of approximately 125 m, when its toe reached the low embankment of the old Glamorgan canal. The larger southern lobe reached this embankment after a further travel of about 150 m and had sufficient speed to override both this and the embankment of the dismantled railway, which were contiguous at that place, and to continue into the village of Aberfan for an additional 175 m, causing 144 deaths. The initial width of the spread run-out was 90 m and of the southern lobe about 130 m. The average thickness of the northern lobe was 1.2 m and of the southern lobe about 2 m. Estimated average speed of the spread, based on the account of eye-witnesses, was probably between 4.5 and 9 m/s and its maximum speed when it reached about 1 m high embankment between 11.2 and 13.5 m/s. The waste  $D_{50}$  varies in the range from 2 to 20 mm and the fines content from 2 to 22%.

The parameters estimated for the simple consideration of the flow are  $p_i/\gamma + z_i = 67$  m,  $H = 67$  m,  $L = 600$  m,  $W \sim 20,000$  kN/m'.

## 6.6 Discussion and Conclusions

The input data and the results of simple considerations of liquefaction potential of slopes due to earthquakes are given in Table 6.1 and of flow type failures in Table 6.2.

**Table 6.1** Summary of input data and the results of simple considerations of the liquefaction potential of slopes due to earthquakes

No	Slope	$a_h$ (g)	$F_s$	$\alpha$ (deg.)	$\varphi$ (deg.)	$\Sigma N / \Sigma N'$	$\tau/\sigma'$ Equation (6.3)	Corrected $\tau/\sigma'$ for $M = 7.5$
1	Lower San Fernando dam in California	0.225	0.89	9.3	33.8	1.9	0.6	0.37
2	Sheffield dam in California	0.09	1.12	20.8	25.5	1.2	0.13	0.07
6	La Marquesa dam in Chile	0.12	0.79	21.0	34.0	1.9	0.29	0.36
7	La Palma dam in Chile	0.12	0.74	24.8	35.5	1.5	0.26	0.32
8	Route 272 embankment in Higashiharekina – Japan	0.19	0.89	9.2	33.1	1.4	0.40	0.50
11	Lake Merced bank in California	0.06	0.83	29	34.5	2	0.13	0.05
12	Hachiro-Gata road embankment in Akita – Japan	0.085	1.14	18.7	26.7	2	0.19	0.21

**Table 6.2** Summary of input data and the results of simple considerations of the flow failures of slopes

No	Slope	$p_i/\gamma_i + z_i$ (m)	H (m)	L (m)	W (kN)	$R = H/L * W$ (kN)	$H/L = R/W(\beta)$	$D_{50}$ (mm)	Fines (%)	Time t (min)
1	Lower San Fernando dam in California	26	24	90	8500	2267	0.26	0.075	50	78
2	Sheffield dam in California	8	3	30	1200	120	0.1	0.1	40	5.5
3	Calaveras dam in California	60	30	200	60,000	9000	0.15	—	—	—
4	Fort Peck dam in Montana – USA	50	30	400	100,000	7500	0.075	0.13	55	97
5	North dike of Wachusetts dam in Massachusetts – USA	50	30	68	5700	2515	0.44	—	—	—
6	La Marquise dam in Chile	10	5	18	400	111	0.28	0.15	30	4
7	La Palma dam in Chile	8	6	15	160	64	0.4	0.2	15	2.8
8	Route 272 embankment in Higashiharekinai – Japan	7	3	20	700	105	0.15	0.2	20	1.4
9	Vlietpolder deposit, Zeeland province in Netherlands	40	30	400	40,000	2222	0.055	0.12	—	38
10	Helsinki harbour fill in Finland	7	5	90	1500	117	0.06	—	—	—
11	Lake Merced bank in California	15	5	13	1900	731	0.38	0.21	2	2
12	Hachiro-Gata road embankment in Akita – Japan	4	2	12	400	66.7	0.17	0.2	15	2
13	Lake Ackerman road embankment in Michigan – USA	6	4	19	300	63	0.21	0.4	0	0.5
14	Aberfan coal mine waste in Wales – UK	67	67	600	20,000	2233	0.11	2	10	0.3

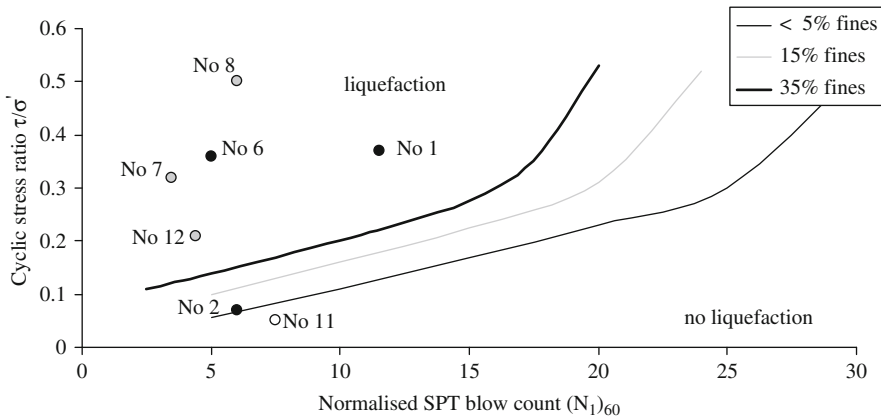


**Fig. 6.25** Cyclic stress ratios for the case histories considered and earthquake magnitude 7.5 (The numbers by the points refer to the numbers in Table 6.1)

The cyclic stress ratios from Table 6.1 are plotted in Fig. 6.25. In cases No 2 and 11, the calculated stress ratio is just below the border line of soil liquefaction for nearly horizontal ground. The reason for this maybe that the input data have been estimated and actual values could have been different.

Based on the available data and the results obtained using the simple consideration, the correlations between the rate  $\beta$  of flow energy decrease versus  $D_{50}$  and the fines contents from Table 6.2 are plotted in Fig. 6.26.

The scatter of the result is rather large. This is because of effect of other influential factors involved or inaccuracy of data assumed. The height loss in Equation (6.5) is simply calculated as the product between  $\beta$  from Fig. 6.26 and the horizontal distance along flow path. When the height loss of failed soil mass reaches its maximum value (the final centre of mass in Fig. 6.5) then the maximum flow distance is achieved.

The fact that the flow failures of liquefied soil are of limited extent instead very large indicates that the failed mass has some shear resistance. Following the flow failure at Calaveras dam, Hazen (1918) found it “surprising” that the failed mass (which had flowed over 200 m horizontally and approximately 30 m vertically) appeared “hard and solid” being highly resistant to the test piles that were driven to qualitatively evaluate the mass density. Hazen (1918) speculated that “*The condition of quick sand lasts only a few seconds until the surplus water can find its way out. When this happens, the grains again come to solid bearings and stability is restored*”. Terzaghi (1956) arguing against the idea of long distance turbidity flow offshore stated that “*both theory and experience showed that the water content of liquefied sediment would decrease as the stream of sediment advanced. If the gradient of the bed of the stream was very small, the stream would solidify within a relatively short distance from its source*”.

Dependence of the stress and force ratios on the model used is shown in Fig. 6.27 for the sliding block model used by Olson (2001) and the flow model considered in

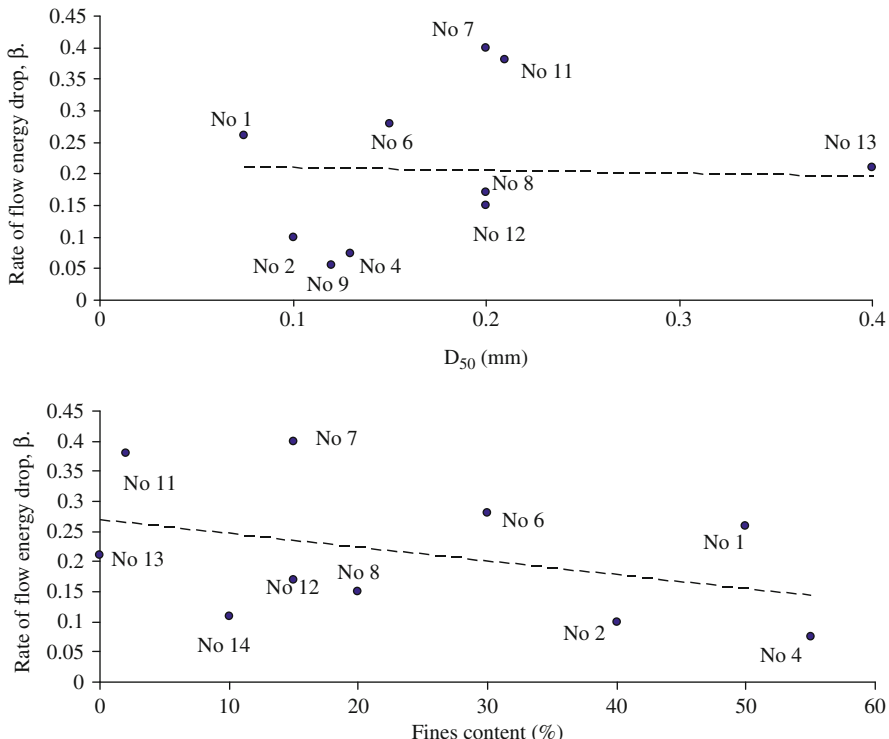
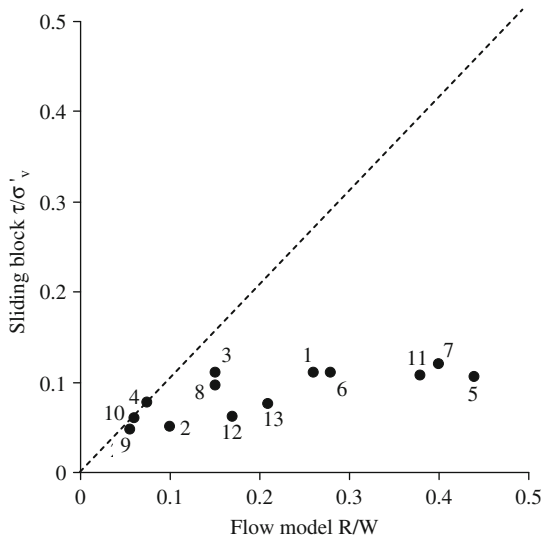


**Fig. 6.26** Relationships between the rate of flow energy drop versus average grain diameter  $D_{50}$  and fines contents from the considered case histories of flow failures (dashed lines represent averaged values, the numbers by the points refer to the numbers in Table 6.2)

this chapter. In liquefied condition, effective stress  $\sigma'_v$  is zero by definition. The shear to vertical effective stress ratios ( $\tau/\sigma'_v$ ) of liquefied soil derived by Olson (2001) are systematically smaller ( $<0.12$ ) than the resistant force to weight of flow mass ratios ( $R/W < 0.45$ ). The laboratory tests on soil samples in undrained condition provide only the lower bound values of soil shear strength because of prevented drainage unlike actual flows where drainage happens. Eckersley (1990) reported on the results of flowslides in 1 m high slope of coking coal. The flowslides were induced in the laboratory by slowly raising the water table. The liquefaction that occurred was a result of shear failure rather than the cause. Eckersley (1990) reported that  $\tau/\sigma'$  ratio at the end of movement was about 0.3. The fines content was less than 10%. For  $H = 0.5$  m and  $L = 2$  m at the end of flow,  $\beta = 0.25$ , which is in an excellent agreement with the data in Fig. 6.26.

Flow slides offshore can involve much larger masses and flow distances than the ones onshore. Dean (2010), for example, summarized the events following the 1929 Grand Banks earthquake with magnitude 7.2 and epicentre about 400 km south of Newfoundland. The earthquake occurred along two geological faults and triggered a submarine landslide that involved about  $200 \text{ km}^3$  of soil. The slide turned into

**Fig. 6.27** Correlation between the stress ratios ( $\tau/\sigma'_v$ ) of the sliding block model by Olson (2001) and the force ratios (R/W) calculated using the flow model (the numbers by the points refer to the numbers in Table 6.2)



turbidity current (presumably), which reached 100 km distance at estimated speed of about 6–100 km/h, breaking 12 submarine transatlantic telegraph cables. It caused a 15 m high tsunami that struck the coast 3 hours after the earthquake and reached the other side of the Atlantic Ocean. Srbulov (2003) argued against the postulated long distance mass travel caused by turbidity current and proposed that the long travel distance and cable destruction can be attributed to the propagation of near ground surface waves instead.

## References

- Ambraseys NN (1988) Engineering seismology. *Earthquake Eng Struct Dyn* 17:1–105
- Ambraseys NN, Menu JM (1988) Earthquake induced ground displacements. *Earthquake Eng Struct Dyn* 16:985–1006
- Andersen A, Bjerrum L (1968) Slides in sub aqueous slopes in loose sand and silt. *Norwegian Geotechn Inst Publ* 81:1–9
- Andrus RD, Stokoe KH (1998) Guidelines for evaluation of liquefaction resistance using shear wave velocity. In: Youd TI, Idriss IM (eds) Proceedings of the 1996 NCEER workshop on evaluation of liquefaction resistance of soils. Salt lake City, Utah, Report No. NCEER-97-0022
- Boulanger RW, Idriss IM (2007) Evaluation of cyclic softening in silt and clays. *ASCE J Geotechn Geoenviron Eng* 133:641–652
- Casagrande A (1965) Second Terzaghi lecture: the role of “calculated risk” in earthwork and foundation engineering. *ASCE J Soil Mech Foundations Div* 91(SM4):1–40
- Castro G (1995) Empirical methods in liquefaction evaluation. In: Proceedings of the 1st annual Leonardo Zeevaert international conference, Mexico City, Mexico, vol 1, pp 1–41
- Das BM (1985) Advanced soil mechanics. McGraw-Hill, Singapore
- De Alba P, Seed HB, Retamal E, Seed RB (1987) Residual strength of sand from dam failures in the Chilean earthquake of March 3, 1985. Earthquake Engineering Research Center Report No. UCB/EERC-87-11, University of California, Berkeley, CA

- De Alba PA, Seed HB, Retamal E, Seed RB (1988) Analyses of dam failures inn 1985 Chilean earthquake. ASCE J Geotechn Eng 114(2):1414–1434
- Dean ETR (2010) Offshore geotechnical engineering – principles and practice. Thomas Telford, London
- Duncan JM (1996) State of the art: limit equilibrium and finite element analysis of slopes. ASCE J Geotechn Eng 122:577–596
- Eckersley D (1990) Instrumented laboratory flowslides. Geotechnique XL(3):489–502
- EN 1998-5 (2004) Eurocode 8 – design of structures for earthquake resistance, part 5: foundations, retaining structures and geotechnical aspects. European Committee for Standardization, Brussels
- Hamada M, Yasuda S, Isoyama R, Emoto K (1986) Study on liquefaction induced permanent ground displacements. In: Report on the association for the development of earthquake prediction in Japan, Tokyo, Japan
- Harder LF Jr, Boulanger R (1997) Application of  $K\sigma$  and  $K\alpha$  correction factors. In: NCEER workshop on evaluation of liquefaction resistance of soils. Report NCEER-97-0022
- Hazen A (1918) A study of the slip in the Calaveras Dam. Eng News Record 81(26): 1158–1164
- Hazen A (1920) Hydraulic fill dams. Trans Am Soc Civil Eng 1458:1713–1821
- Hryciw RD, Vitton S, Thomann TG (1990) Liquefaction and flow failure during seismic exploration. ASCE J Geotechn Eng 116(2):1881–1899
- Hutchinson JN (1986) A sliding-consolidation model of for flow slides. Canad Geotechn J 23: 115–126
- Ishihara K (1993) Liquefaction and flow failure during earthquakes. Geotechnique 43(3):351–415
- Jitno H, Byrne PM (1995) Predicted and observed liquefaction response of Mochikoshi tailings dam. In: Proceeding of the 1st international conference on earthquake geotechnical engineering, vol 2, Tokyo, Japan, pp 1085–1090
- Koppejan AW, van Wamelen BM, Weinberg LJH (1948) Coastal flow slides in the Dutch province of Zeeland. In: Proceedings of the 2nd international conference of soil mechanics and foundation engineering, Rotterdam, Netherlands, pp 89–96
- Lee KL, Seed HB, Idriss IM, Makdisi FI (1975) Properties of soil in the San Fernando hydraulic fill dams. ASCE J Geotechn Eng Div 101(GT8):801–821
- Maksimovic M (1988) General slope stability package for micro computers. In: Proceedings of 6th international conference on numerical methods in geomechanics, vol 3, Innsbruck, pp 2145–2150
- Obermeier SF (1996) Using liquefaction induced features for paleoseismic analyses. In: McCalpin (ed) Paleoseismology. Academic, New York, NY, pp 331–396
- Ohya S, Iwasaki T, Wakamatsu M (1985) Comparative study of various penetration tests in ground that underwent liquefaction during the 1983 Nihon-Kai-Cjubu and 1964 Niigata earthquakes. In: Proceedings of workshop on in-situ testing methods for evaluation of soil liquefaction susceptibility, vol 1, San Francisco, CA, pp 5–88
- Olson SM (2001) Liquefaction analyses of level and sloping ground using field case histories and penetration resistance. PhD thesis, The Graduate College, University of Illinois at Urbana-Champaign ([http://www.geoengineer.org/onlinelibrary/paper\\_details.php?paperid=1530](http://www.geoengineer.org/onlinelibrary/paper_details.php?paperid=1530))
- Olson SM, Stark TD, Walton WH, Castro G (2000) Static liquefaction flow failure of the North Dike of Wachhusett Dam. ASCE J Geotechn Geoenvir Eng 126(12): 1184–1193
- Robertson PK, Wride CE (1998) Evaluating cyclic liquefaction potential using the cone penetration test. Canad Geotechn J 35:442–459
- Ross GA (1968) Case studies of soil stability problems resulting from earthquakes. PhD thesis, University of California, Berkeley, CA
- Sasaki Y, Oshiki H, Nishikawa J (1994) Embankment failure caused by the Kushiro-Oki earthquake of January 15, 1993. In: Proceedings of the 13th international conference on mechanics and foundation engineering, vol 1, New Delhi, India, pp 61–68

- Seed HB (1987) Design problems in soil liquefaction. ASCE J Eng Div 113(8):827–845
- Seed RB, Harder LF Jr (1990) SPT based analysis of cyclic pore pressure generation and undrained residual strength. In: Duncan JM (ed) Proceedings of H. Bolton Seed memorial symposium, vol 2. Bi-Tech Publishing, Richmond, BC, Canada, pp 351–376
- Seed HB, Lee KL, Idriss IM (1969) Analysis of Sheffield Dam failure. ASCE J Soil Mech Foundations Div 95(SM6):1453–1490
- Seed HB, Lee KL, Idriss IM, Makdisi F (1973) Analysis of the slides in the San Fernando Dam during the earthquake of Feb. 9 1971. Earthquake Engineering Research Center report 73-2, University of California, Berkeley, CA
- Seed HB, Lee KL, Idriss IM, Makdisi F (1975) Dynamic analysis of the slides in the Lower San Fernanndo Dam during the earthquake of February 9, 1971. ASCE J Geotechn Eng Div 101(GT9):889–911
- Seed RB, Cetin KO, Moss RES, Kammerer AM, Wu J, Pestana JM, Riemer MF, Sancio RB, Bray JD, Kayen RE, Faris A (2003) Recent advances in soil liquefaction engineering: a unified and consistent framework. In: Proceedings of the 26th annual ASCE Los Angeles geotechnical spring seminar, Keynote presentation, H.M.S. Queen Mary, Long Beach, CA, pp 1–71
- Srbulov M (2003) On the fast damage propagation through marine soil offshore Newfoundland following Grand Banks earthquake of 1929. Eur Earthquake Eng XVII(3):3–9
- Srbulov M (2005) Simple physical models of sand liquefaction and flow failures induced by earthquakes. Eur Earthquake Eng XIX(3):25–37
- Srbulov M (2008) Geotechnical earthquake engineering – simplified analyses with case studies and examples. Springer, New York, NY
- Srbulov M (2010) Simple consideration of liquefaction due to earthquakes and flow failures of slopes in sandy soil. Ingegneria Sismica XXVII(3):7–16
- Sully JP, Fernandez A, Zalzman S (1995) Back analysis of deformations for case histories involving flow type failures. In: Proceedings of the 3rd conference on recent advances in geotechnical earthquake engineering and soil dynamics, vol 1, St. Louis, MO, pp 499–502
- Terzaghi K (1956) Varieties of submarine slope failures. In: The 8th Texas conference on soil mechanics and foundation engineering, Austin, Texas, pp 41–55
- Tika TE, Vaughan PR, Lemos LJ (1996) Fast shearing of pre-existing shear zones in soil. Geotechnique 46(2):197–233
- Youd TL, Hansen CM, Bartlett SF (2002) Revised multilinear regression equations for prediction of lateral spread displacement. ASCE J Geotechn Geoenvir Eng 128:1007–1017

# Chapter 7

## Massive Retaining Walls

### 7.1 Introduction

Massive retaining walls use their own weight to transfer nearly horizontal lateral soil forces on the wall into nearly vertical forces on ground under the wall. Sketches of cross sections of massive retaining walls are shown in Fig. 7.1. The massive walls are also called gravity walls.

Most massive retaining walls performed well during earthquakes with exception of a few cases some of which are described in the case histories in Section 7.5.

When subjected to ground vibration from industrial sources, retaining walls without or with little lateral restraint near their tops may exhibit amplification of vibration between 3 and 5 according to BS 5228-2:2009. For slender masonry walls, BS 5228-2:2009 recommends the threshold limit of the peak particle velocity of 10 mm/s at the toe and 40 mm/s at the crest. Propressed or tied walls or massive walls can be subjected to values 50–100% greater than these limits according to the same standard. For continuous vibrations, the stated levels should be reduced by a factor of 1.5–2.5 according to BS 5228-2:2009.

The aim of this chapter is to describe the mechanism and factors influencing possible failure modes of massive retaining walls, the existing methods for analyses of their behaviour, simple model for calculation of lateral force during an earthquake, and the analyses of co-seismic and post-seismic slip of the wall if the factor of safety against sliding decreases below one during and after an earthquake. The emphasis is on the use of simple calculations of the stability of walls in the case histories considered.

### 7.2 Mechanism and Factors

The main factors affecting massive retaining wall failures are:

- Addition of loading/fill at the back
- Large water pressure difference between the front and the back due to prevented drainage

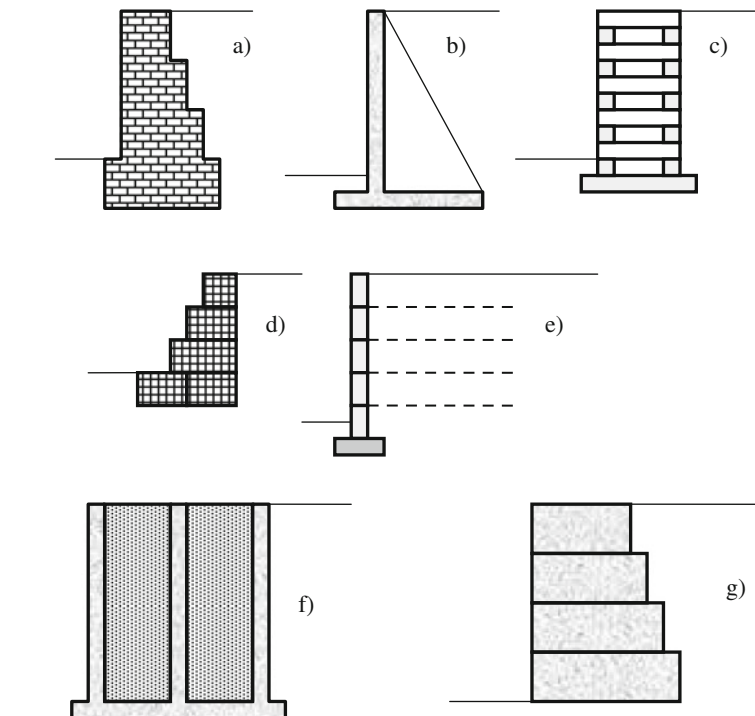


**Fig. 7.1** Sketches of cross sections of massive retaining walls (a) brick work, (b) reinforced concrete with counterforts that engage backfill mass (also called a cantilever or counterfort wall and is not treated as a massive wall), (c) crib, (d) gabion (metal mesh basket with rock fill), (e) reinforced soil with facing blocks, (f) caisson (or cellular cofferdam) filled with sand, (g) concrete blocks

- Earthquake acceleration
- Soil shear strength decrease in cyclic conditions
- Excavation in front of the wall
- Liquefaction and/or fluidization of ground in front of a wall, with collapse of the wall into it
- Liquefaction and/or fluidization of the backfill, increasing active force

Basic mechanisms of failures of massive retaining walls are shown in Fig. 7.2.

### 7.2.1 Bearing Capacity of Soil Under Wall Base

The calculation of soil lateral force during an earthquake is described in Sections 7.3.1 and 7.4.1. In case of ground vibration due to industrial activities, the lateral stress on a wall is proportional to the product of soil density, soil particle and wave velocities. If instead of soil velocity, soil acceleration is to be used as in the case of earthquake induced lateral force then soil acceleration is proportional to the product of ground velocity and  $2\pi f$ , where  $f$  is frequency of ground vibration.

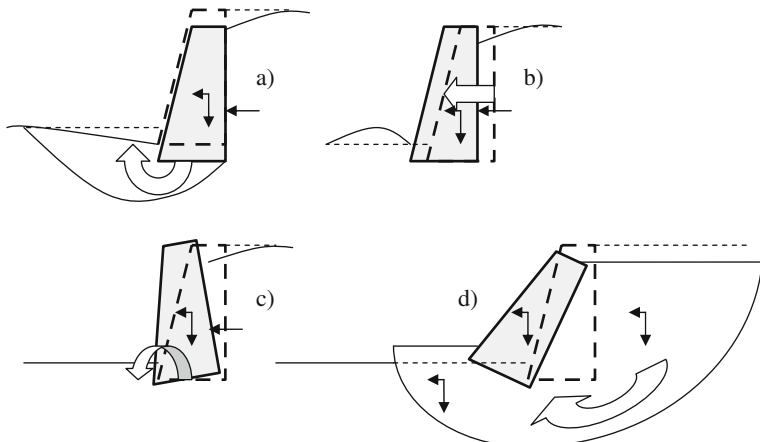


**Fig. 7.2** Failure mechanisms of massive retaining walls (a) base bearing, (b) sliding along toe, (c) overturning around external edge, (d) deep seated soil slip

Bearing capacity of soil under wall base is frequently calculated using empirical formulas defined for static conditions. The formulas are applicable for an averaged contact stress  $q_f$  over the effective foundation area, which is a part of physical foundation area with the resultant force in its centre. The eccentricity  $e$  of the resultant force from the centre of the physical foundation area  $e = M/R$ , where  $M$  is the resultant overturning moment and  $R$  is the perpendicular component of the resultant force at wall base. For a horizontal wall base, the reduced width is  $B' = B - 2M/R$ . The linear engineering beam theory states that the maximum eccentricity of  $R$  not to cause appearance of tensile stress i.e. uplift of one of the edges of wall toe is  $B/6$  so if the force  $R$  is located within the middle third part of  $B$ , the stresses acting on ground beneath a wall toe will be all compressive.

### 7.2.1.1 In Terms of Effective Stresses in Drained Conditions

According to the general bearing capacity equation, which was proposed by Meyerhof (1963) as a way to address issues in Terzaghi's earlier equation, the bearing stress  $q_f$  may be estimated as:

$$q_f = 0.5 \cdot \gamma \cdot B' \cdot N_\gamma \cdot s_\gamma \cdot i_\gamma \cdot d_\gamma \cdot b_\gamma \cdot g_\gamma + c' \cdot N_c \cdot s_c \cdot i_c \cdot d_c \cdot b_c \cdot g_c + \gamma \cdot D_f \cdot N_q \cdot s_q \cdot i_q \cdot d_q \cdot b_q \cdot g_q, \quad (7.1)$$

where  $\gamma$  is the bulk unit weight of soil beneath wall base or it is the submerged unit weight if the ground water level is at or above the soil surface,  $N$  are bearing capacity factors dependent on soil friction angle,  $s$  are foundation shape factors,  $i$  are factors for the resultant force inclination to wall base,  $d$  are factors dependent on wall base depth  $D_f$ ,  $b$  are base inclination factors,  $g$  are ground surface inclination factors,  $c'$  is soil cohesion. The factors according to different sources are given in Table 7.1.

**Table 7.1** Bearing capacity  $N$ , shape  $s$ , load inclination  $i$ , base depth  $d$ , base inclination  $b$  and ground surface inclination  $g$  factors for calculation of bearing capacity of shallow footings in terms of effective stresses in drained conditions

	EN 1997-1 (2004)	Hansen (1970)	API RP2A-WSD (2000)
$N_q$	$e^{\pi \tan \phi} \tan^2(45^\circ + \phi'/2)$	$e^{\pi \tan \phi} \tan^2(45^\circ + \phi'/2)$	$e^{\pi \tan \phi} \tan^2(45^\circ + \phi'/2)$
$N_y$	$2(N_q - 1) \tan \phi'$	$1.5(N_q - 1) \tan \phi'$	$2(N_q + 1) \tan \phi'$
$N_c$	$(N_q - 1) \cot \phi'$	$(N_q - 1) \cot \phi'$	$(N_q - 1) \cot \phi'$
$s_q$	$1 + B'/L' \sin \phi'$	$1 + B'/L' \sin \phi'$	$1 + B'/L' \sin \phi'$
$s_\gamma$	$1 - 0.3B'/L'$	$1 - 0.4B'/L'$	$1 - 0.4B'/L'$
$s_c$	$(s_q N_q - 1)/(N_q - 1)$	$0.2B'/L'$	$1 + B'/L' N_q / N_c$
$i_q$	$[1 - H/(V + A'c' \cot \phi')]^m$	$[1 - 0.5H/(V + A'c' \cot \phi')]^{5m}$	$[1 - G/(V + A'c' \cot \phi')]^{5m}$
$i_\gamma$	$[1 - H/(V + A'c' \cot \phi')]^{m+1}$	$[1 - 0.7H/(V + A'c' \cot \phi')]^{5(m+1)}$	$[1 - H/(V + A'c' \cot \phi')]^{m+1}$
$i_c$	$i_q - (1 - i_q)/(N_c \tan \phi')$	$0.5 - 0.5[1 - H/(A'c')]^{0.5}$	$i_q - (1 - i_q)/(N_c \tan \phi')$
$d_q$	–	$1 + 2 \tan \phi' (1 - \sin \phi')^2 D_f / B'$ for $D_f \leq B'$ $1 + 2 \tan \phi' (1 - \sin \phi')^2$ $\arctan(D_f/B') \text{ for } D_f > B'$	$1 + 2 \tan \phi' (1 - \sin \phi')^2 D_f / B'$
$d_\gamma$	–	1	1
$d_c$	–	$0.4D_f/B' \text{ for } D_f \leq B'$ $0.4D_f/B' \arctan(D_f/B') \text{ for } D_f > B'$	$d_q - (1 - d_q)/(N_c \tan \phi')$
$b_q$	$(1 - \alpha \tan \phi')^2$	$e^{-2\alpha \tan \phi'}$	$(1 - \alpha \tan \phi')^2$
$b_\gamma$	$(1 - \alpha \tan \phi')^2$	$e^{-2.7\alpha \tan \phi'}$	$(1 - \alpha \tan \phi')^2$
$b_c$	$b_q - (1 - b_q)/(N_c \tan \phi')$	$\alpha/2.565$	$b_q - (1 - b_q)/(N_c \tan \phi')$
$g_q$	–	$(1 - 0.5 \tan \beta)^5$	$(1 - \tan \beta)^2$
$g_\gamma$	–	$(1 - 0.5 \tan \beta)^5$	$(1 - \tan \beta)^2$
$g_c$	–	$\beta/2.565$	$g_q - (1 - g_q)/(N_c \tan \phi')$
$m$	$(2+B'/L')/(1+B'/L')$ for $H$ in $B'$ direction $(2+L'/B')/(1+L'/B')$ for $H$ in $L'$ direction	–	$(2+B'/L')/(1+B'/L')$ for $H$ in $B'$ direction $(2+L'/B')/(1+L'/B')$ for $H$ in $L'$ direction

Notes:  $H$ ,  $V$  are the resultant horizontal and vertical forces on loaded area

$\phi'$  is soil friction angle

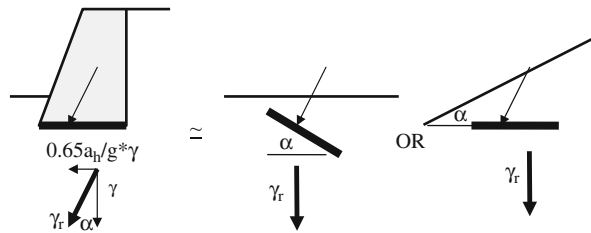
$\alpha, \beta$  are base and ground surface inclination to the horizontal in radians. Positive  $\alpha$  upwards in direction of  $H$  force, positive  $\beta$  downwards

$c'$  is soil cohesion

$A'$  is the effective foundation area =  $B' \times L'$

Equation (7.1) is derived for static condition and does not take into account inertial force in soil beneath foundation level. This effect can be estimated by considering apparent base or ground surface inclination for an angle necessary to rotate the resultant of inertial and gravitational force so that the resultant force acting on soil is vertical, Fig. 7.3. It should be mentioned that EN 1998-5 (2004) provides in its annex F an informative formula for the calculation of bearing capacity of shallow foundation in seismic condition.

**Fig. 7.3** Approximate consideration of the effect of earthquake forces acting on soil beneath a wall on its base bearing capacity as for an inclined base or inclined ground surface



### 7.2.1.2 In Terms of Total Stresses in Undrained Conditions

The ultimate bearing stress  $q_f$  is:

$$q_f = (\pi + 2) \cdot c_u \cdot s_c \cdot i_c \cdot b_c + \gamma \cdot D_f \text{ EN 1997 - 2 : 2004}$$

$$q_f = (\pi + 2) \cdot c_u \cdot (1 + s_c + d_c - i_c - b_c - g_c) + \gamma \cdot D_f \text{ Hansen (1970)} \quad (7.2)$$

$$q_f = (\pi + 2) \cdot c_u \cdot s_c \cdot i_c \cdot d_c \cdot b_c \cdot d_c + \gamma \cdot D_f \text{ API RP 2A - WSD (2000)}$$

The factors according to different sources are given in Table 7.2.

Equation (7.2) is derived for static condition and does not take into account inertial force in soil beneath foundation level. This effect can be estimated as described in the case of Equation (7.1), Fig. 7.3.

### 7.2.1.3 In Case of a Cohesionless Layer Over Soft Cohesive Layer

Punch through type failure may occur. If punch through type failure occurs, a shallow foundation can sink until the buoyancy force acting on the punched through

**Table 7.2** Shape  $s$ , load inclination  $i$ , base depth  $d$ , base inclination  $b$  and ground surface inclination  $g$  factors for calculation of bearing capacity of shallow footings in terms of total stresses in undrained conditions

	EN 1997-1 (2004)	Hansen (1970)	API RP2A-WSD (2000)
$s_c$	$1+0.2B'/L'$	$0.2B'/L'$	$1 + B'/L' / (\pi + 2)$
$i_c$	$0.5\{1 + [1 - H/(A'c_u)]^{0.5}\}$	$0.5 - 0.5[1 - H/(A'c')]^{0.5}$	$1 - mH/[A'c_u(\pi + 2)]$
$d_c$	—	$0.4D_f/B'$ for $D_f \leq B'$ $0.4D_f/B'\arctan(D_f/B')$ for $D_f > B'$	1
$b_c$	$1 - 2\alpha/(\pi + 2)$	$\alpha/2.565$	$1 - 2\alpha/(\pi + 2)$
$g_c$	—	$\beta/2.565$	$1 - 2\beta/(\pi + 2)$
$m$	—	—	$(2+B'/L')/(1+B'/L')$ for $H$ in $B'$ direction $(2+L'/B')/(1+L'/B')$ for $H$ in $L'$ direction

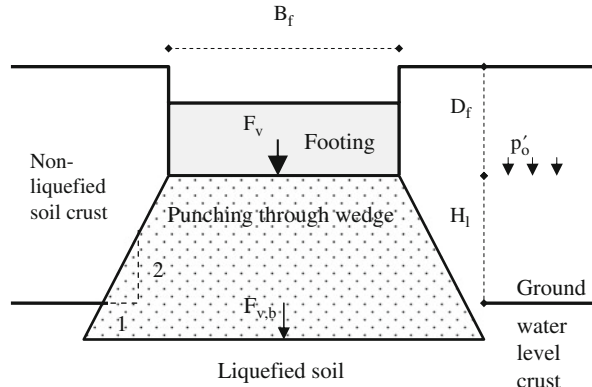
Notes:  $H$  is the resultant horizontal force on loaded area

$\alpha, \beta$  are base and ground surface inclination to the horizontal in radians. Positive  $\alpha$  upwards in direction of  $H$  force, positive  $\beta$  downwards

$c_u$  is soil cohesion

$A'$  is the effective foundation area =  $B' \times L'$

**Fig. 7.4** Punching through mode of failure into a soft sub-layer



wedge in Fig. 7.4 comes into equilibrium with the applied load. The vertical foundation capacity  $F_v$  in the case of punch through failure is (e.g. SNAME, 1997)

$$F_v = F_{v,b} - A_f \cdot H_l \cdot \gamma + 2 \cdot \frac{H_l}{B_f} (H_l \cdot \gamma + 2 \cdot p'_o) \cdot K_s \cdot \tan \phi \cdot A_f, \quad (7.3)$$

where  $F_{v,b}$  is determined assuming the foundation bears on the surface of the lower liquefied layer,  $A_f$  is foundation area,  $H_l$  is distance from a foundation level to the level of soft layer below,  $\gamma$  is unit weight of top soil,  $p'_o$  is effective overburden stress at the foundation depth,  $K_s$  is the coefficient of punching shear that is calculated from the equation  $K_s \cdot \tan \phi = \frac{3 \cdot c_u}{B_f \cdot \gamma}$ ,  $\phi$  is friction angle of top layer,  $c_u$  is undrained shear strength of soil in the bottom layer,  $B_f$  is diameter of an equivalent circular foundation and  $F_{v,b} = (c_u N_c + p') A_f$ , where  $N_c = 5.14$ ,  $p'$  effective overburden stress at the top of soft bottom layer.

### 7.2.2 Stability Against Sliding at Wall Base

The stability is expressed in terms of the factor of safety which is a ratio between resisting and driving forces. The resisting force is simply calculated as a sum of frictional capacity  $= N' \tan \phi'$ , where  $N'$  is the resultant perpendicular force on the wall base and  $\phi'$  is soil friction angle in terms of effective stresses in drained condition, and  $A' c'$ , where  $A'$  is effective base area  $= B' \times L'$  and  $c'$  is soil cohesion in terms of effective stresses in drained condition. In terms of total stresses in undrained conditions, the resisting force  $= A' c_u$ , where  $c_u$  is soil shear strength in terms of total stresses in undrained condition.

### 7.2.3 Stability Against Overturning Around the External Edge

The stability is expressed in terms of the factor of safety which is a ratio between resisting and driving rotational moments at the toe of a wall. The resisting moment is simply a sum of the products of lever arms by forces around the external edge, such

as due to self weight. The factor of safety against overturning around the external edge is defined in particular codes.

### 7.2.4 Stability Against Deep Seated Soil Slip

The factor of safety against sliding  $F_s$  can be calculated as for soil slopes using, for example, the routine method by Bishop (1955) for static conditions.

$$F_s = \frac{\sum [c' \cdot b_s + (W_s - u_w \cdot b_s) \cdot \tan \phi'] \cdot \frac{1}{\cos \alpha_s + \sin \alpha_s \cdot \frac{\tan \phi'}{F_s}}}{\sum (W_s \cdot \sin \alpha_s)}, \quad (7.4)$$

where  $c'$  is soil cohesion in terms of effective stresses in drained conditions,  $b_s$  is the width of a vertical slice into which a potential sliding mass is divided,  $W_s$  is the total weight of a vertical slice,  $u_w$  is pore water pressure at the base of a vertical slice,  $\phi'$  soil friction angle at the base of a vertical slice,  $\alpha_s$  is inclination to the horizontal of the base of a vertical slice. Equation (7.4) contains the factor of safety  $F_s$  implicitly and is solved iteratively. In case of partially submerged slopes,  $W_s$  represents a sum of slice weight above and below water table and  $u_w$  excess pore water pressure above steady state water level.

Equation (7.4) is derived for static condition and does not take into account inertial force in soil during an earthquake. This effect can be accounted for by considering apparent ground surface inclination for an angle necessary to rotate the resultant of inertial and gravitational force so that the resultant force acting on soil is vertical. Maksimovic (2008) suggests and extension of Equation (7.4) when external loads and inertial forces act on a soil mass.

$$\begin{aligned} F_s &= \frac{\sum [c' \cdot b_s + (R_v - u_s \cdot b_s) \cdot \tan \phi'] \cdot m_\alpha}{\sum (R_v \cdot \sin \alpha_s + M_x)} \\ R_v &= W_s + W_s' + R_y + p_s \cdot b_s + k_y \cdot (W_s + W_z), \\ M_x &= R_x \cdot y_r/R + k_x \cdot y_z \cdot (W_s + W_z)/R, \\ m_\alpha &= \frac{1}{\cos \alpha_s + \sin \alpha_s \cdot \tan \phi'/F_s}, \end{aligned} \quad (7.5)$$

where  $R_x$ ,  $R_y$  are the resultants of horizontal and vertical forces respectively (if any) acting on a vertical slice,  $u_s$  is pore water pressure above steady state water level for a partially submerged slope,  $p_s$  is line vertical load (if any) acting on a vertical slice,  $k_y$ ,  $k_x$  are the ratios between the vertical and horizontal inertial and the gravitational acceleration, which may vary along the slope height,  $W_s$  is the weight of part of a vertical slice above steady state water level,  $W_s'$  is the submerged weight of part of a vertical slice below steady state water level,  $W_z$  is the saturated weight of part of a vertical slice below steady state water level,  $y_r$ ,  $y_z$  are lever arms of the horizontal components of external and inertial forces respectively with respect to the centre of a trial circular slip surface with the radius  $R$ .

EN 1998-5 (2004) suggests that for pseudo-static analyses of slope stability  $k_x$  in the horizontal direction is taken equal to a half of the horizontal acceleration and  $k_y$  in the vertical direction as a half of  $k_x$  if the vertical acceleration is greater than 0.6 of the design bedrock horizontal acceleration and 0.33 of  $k_x$  if the vertical acceleration is smaller than 0.6 of the design bedrock horizontal acceleration. EN 1998-5 (2004) in informative annex A suggests for deep seated slips where the failure surface passes near to the base that *if pseudo-static method of analysis is used, the topographic effects may be neglected.*

The minimal required factors of safety against bearing, sliding and overturning type failures are defined in the codes.

## 7.3 Existing Methods

### 7.3.1 Empirical by Formulas

Okabe (1926) and Mononobe and Matsuo (1929) developed a pseudo-static analysis of seismic lateral earth forces on retaining structures, so-called Mononobe-Okabe (M-O) method. The M-O method is an extension of the static Coulomb (1776) theory of lateral earth pressures on retaining structures. It applies horizontal and vertical equivalent seismic forces to an active or passive rigid wedge in a dry cohesionless soil. No soil-structure interaction is considered, and soil strength degradation under cyclic loading must be assessed independently as soil input parameters. The lateral soil force acting on a retaining wall in seismic condition according to Mononobe-Okabe method may be estimated from:

$$\begin{aligned} E_a &= \frac{1}{2} \cdot K_a \cdot \gamma \cdot h_w^2 \cdot \cos \delta_b \\ K_a &= \frac{\cos^2(\phi - o - \psi)}{\cos \psi \cdot \cos^2 o \cdot \cos(\delta_b + o + \psi) \cdot \left[ 1 + \sqrt{\frac{\sin(\delta_b + \phi) \cdot \sin(\phi - \eta_w - \psi)}{\cos(\delta_b + o + \psi) \cdot \cos(\eta_w - o)}} \right]^2}, \\ \psi &= \arctan \left( \frac{a_h}{g} \right) \end{aligned} \quad (7.6)$$

where  $\gamma$  is unit weight of soil at the back of a wall,  $h_w$  is wall height,  $a_h$  is the horizontal acceleration (approximately 0.65 of the peak value for an equivalent harmonic motion),  $\delta_b$  is friction angle between wall back and soil,  $\phi$  is soil friction angle,  $o$  is the back of wall inclination to the vertical (positive from back to front), and  $\eta_w$  is inclination to the horizontal of soil surface at the back of a wall (positive upwards). When the difference  $\phi - \eta_w - \psi$  in Equation (7.6) becomes less than zero then the sine function becomes negative and the square root an imaginative number. This represents the condition when the slip of soil at the back of a wall occurs. However, retaining wall may have reserve resistance against sliding and can prevent slip of soil at the back of wall so that the lateral force can continue to build

up. EN 1998-5 (2004) in its normative annex E chooses to ignore the whole term in brackets [] in Equation (7.6) when  $\phi - \eta_w - \psi < 0$ .

The passive lateral soil force in front of a retaining wall in seismic condition is:

$$E_p = \frac{1}{2} \cdot K_p \cdot \gamma \cdot h_w^2 \cdot \cos \delta_b$$

$$K_p = \frac{\cos^2(\phi + o - \psi)}{\cos \psi \cdot \cos^2 o \cdot \cos(\delta_b - o + \psi) \cdot \left[ 1 - \sqrt{\frac{\sin(\delta_b + \phi) \cdot \sin(\phi + \eta_w - \psi)}{\cos(\delta_b - o + \psi) \cdot \cos(\eta_w - o)}} \right]^2}$$

$$\psi = \arctan \left( \frac{a_h}{g} \right)$$
(7.7)

Seed and Whitman (1970) performed a parametric study using M-O method to evaluate the effects of various input parameters on the magnitude of dynamic earth pressures. They observed that the maximum total earth pressure acting on a retaining wall can be divided into two components: the initial static pressure  $E_{as}$  and the dynamic increment  $\Delta E_a$  due to the base motion. They recommended that the dynamic increment acts at approximately 0.6 of wall height from its base. Towhata and Islam (1987) stated that total passive lateral force can also be divided into static and dynamic components in which case the dynamic component acts in the opposite direction of the static component.

The lateral soil forces on a retaining wall  $E_{as}$  and  $E_{ps}$  in static condition are calculated according to Coulomb (1776):

$$E_{as} = \frac{1}{2} \cdot K_{as} \cdot \gamma \cdot h_w^2 \cdot \cos \delta_b$$

$$K_{as} = \frac{\cos^2(\phi - o)}{\cos^2 o \cdot \cos(\delta_b + o) \cdot \left[ 1 + \sqrt{\frac{\sin(\delta_b + \phi) \cdot \sin(\phi - \eta_w)}{\cos(\delta_b + o) \cdot \cos(\eta_w - o)}} \right]^2},$$
(7.8)

$$E_{ps} = \frac{1}{2} \cdot K_{ps} \cdot \gamma \cdot h_w^2 \cdot \cos \delta_b$$

$$K_{ps} = \frac{\cos^2(\phi + o)}{\cos^2 o \cdot \cos(\delta_b - o) \cdot \left[ 1 + \sqrt{\frac{\sin(\delta_b + \phi) \cdot \sin(\phi + \eta_w)}{\cos(\delta_b - o) \cdot \cos(\eta_w - o)}} \right]^2},$$
(7.9)

where the same notation is used as in Equation (7.6). For  $\delta_b > 0$ , the assumption of a passive wedge with planar base in Equation (7.9) is not on the safe side for large  $\phi$  as the actual base of a passive wedge has a concave shape. Caquot and Kerisel (1948) provided values of  $K_{sp}$  using a shape of logarithmic spiral instead of planar shape.

The point of application of the M-O active and passive lateral force is assumed to be at one third above the base of the wall. The angles of inclination to the horizontal of a critical slip surface behind a wall are (Kramer, 1996):

- In seismic condition on active side

$$\phi - \psi + \arctan \left[ \frac{-\tan(\phi - \psi - \eta_w) + \sqrt{\tan(\phi - \psi - \eta_w) \cdot [\tan(\phi - \psi - \eta_w) + \cot(\phi - \psi - \phi)] \cdot [1 + \tan(\delta_b + \psi + o) \cdot \cot(\phi - \psi - o)]}}{1 + \{\tan(\delta_b + \psi + o) \cdot [\tan(\phi - \psi - \eta_w) + \cot(\phi - \psi - o)]\}} \right]$$

- In seismic condition on passive side

$$\psi - \phi + \arctan \left[ \frac{\tan(\phi + \psi + \eta_w) + \sqrt{\tan(\phi - \psi + \eta_w) \cdot [\tan(\phi - \psi + \eta_w) + \cot(\phi - \psi + o)] \cdot [1 + \tan(\delta_b + \psi + o) \cdot \cot(\phi - \psi + o)]}}{1 + \{\tan(\delta_b + \psi - o) \cdot [\tan(\phi - \psi + \eta_w) + \cot(\phi - \psi + o)]\}} \right]$$

- In static condition on active side

$$\phi + \arctan \left[ \frac{\tan(\phi - \eta_w) + \sqrt{\tan(\phi - \eta_w) \cdot [\tan(\phi - \eta_w) + \cot(\phi - o)] \cdot [1 + \tan(\delta_b + o) \cdot \cot(\phi - o)]}}{1 + \{\tan(\delta_b + o) \cdot [\tan(\phi - \eta_w) + \cot(\phi - o)]\}} \right]$$

- In static condition on passive side

(7.10)

$$-\phi + \arctan \left[ \frac{\tan(\phi + \eta_w) + \sqrt{\tan(\phi + \eta_w) \cdot [\tan(\phi + \eta_w) + \cot(\phi + o)] \cdot [1 + \tan(\delta_b - o) \cdot \cot(\phi + o)]}}{1 + \{\tan(\delta_b - o) \cdot [\tan(\phi + \eta_w) + \cot(\phi + o)]\}} \right]$$

For  $\sigma = \eta_w = 0$ , the angle of inclination to the horizontal of a critical slip surface in static condition on active side is  $45^\circ + \phi/2$  and on passive side  $45^\circ - \phi/2$ .

During the 1995 Hyogoken-Nanbu earthquake massive retaining walls such as masonry, non-reinforced concrete and leaning type were heavily damaged. Koseki et al. (1998) concluded that a horizontal acceleration coefficient based on a reduced value of the measured peak horizontal acceleration for 60–100% is appropriate for use with the M-O method.

Richards and Elms (1979) proposed that the seismic design of massive retaining walls is based on allowable permanent wall displacements. The permanent displacements are estimated similar to Newmark (1965) sliding block method for soil slopes.

Whitman and Liao (1985) identified shortcomings of the Richards and Elms (1979) method as: neglect of the dynamic response of the backfill, neglect of kinematic factors, neglect of tilting mechanism, neglect of vertical acceleration. Whitman and Liao (1985) combined different sources of uncertainty and defined a formula for permanent displacement of a rigid wall.

### 7.3.2 Numerical by Computer Software

Kramer (1996) mentioned a few rigorous two-dimensional finite element analyses that can predict permanent deformations. A rigorous analysis should be capable of accounting for nonlinear, inelastic, behaviour of soil and of the interfaces between soil and wall elements. Complex numerical methods require validation of their results, great expertise and can be expensive and time consuming.

Richards et al. (1999) used a simple kinematic method to predict the seismic earth pressure of cohesionless soil against retaining structures due to uniform horizontal ground acceleration. They used superposition of nonlinear horizontal soil displacement in the free field and linear wall displacement. They found that the seismic active thrust on the wall equals the total horizontal force from the free-field stress solution.

Zeng and Steedman (2000) considered rocking and sliding of rigid block model on a rigid foundation. They assumed that the soil behind the model behaves as a rigid plastic material, following the wall as it moves outward. The procedure was validated by data from centrifuge tests.

Kim et al. (2004) computed the dynamic force on the back of the wall by using the force components calculated from the equations given in Section 7.3.1 and the excess pore water pressure ratio ( $r_u$  = excess pore pressure in the back-fill over initial effective vertical stress), which is not easy to define for dynamic conditions. They verified the proposed model by comparing its results with those from series of shaking table tests.

Dakoulas and Gazetas (2008) back calculated earth and water pressures acting against the caisson quay walls at Kobe port during the 1995 Hyogoken-Nanbu earthquake using Pastor-Zienkiewich elasto-plastic constitutive model applied within FLAC software. Calculated excess pore water and initial mean effective stress ratio range is between 0.6 and 0.9 towards the end of ground shaking.

### 7.3.3 Experimental on Small Scale Models

Zeng and Steedman (2000) validated their method by data from centrifuge tests. Kim et al. (2004) used a series of shaking table tests for verification of their proposed model. Recently, Atik and Sitar (2009) reported on two sets of dynamic centrifuge model experiments performed to evaluate the magnitude and distribution of seismically induced lateral earth pressures on retaining structures and to study the seismic response of retaining wall-backfill systems. The results obtained from the centrifuge experiments were used to develop and calibrate a two-dimensional nonlinear finite element model built on the OpenSees platform. The finite element model was used to further study the seismic response of retaining wall-backfill systems and to evaluate the ability of numerical modelling in capturing the essential features of the seismic response observed in the centrifuge experiments.

The experimental results show that when the inertial force on the wall is at maximum the dynamic earth pressure increment is at minimum. The results of finite element modelling with denser soil showed that the seismic earth pressures decreased about 25–30% but this aspect requires further evaluation.

## 7.4 Simple Models and Assumptions

### 7.4.1 Dynamic Increment of Active Soil Lateral Force

Following Richards et al. (1999) idea, it is assumed in the simple model that the value of dynamic increment of active soil lateral force  $\Delta E_a$  in the horizontal direction for a vertical wall ( $\alpha = 0$ ) with horizontal soil surface in the back ( $\eta_w = 0$ ) is proportional to the sum (integral) of inertial forces acting on an active zone behind wall (Fig. 7.5) because the wall prevents free ground movements and is subjected to the ground forces.

$$\begin{aligned}\Delta E_a &= \int_0^{h_w} \rho \cdot a_h \cdot (h_w - v) \cdot \tan\left(45^\circ - \frac{\phi}{2} + \frac{\psi}{2}\right) dv \\ &= \int_0^{h_w} \frac{\partial \tau_{hv}}{dv} \cdot (h_w - v) \cdot \tan\left(45^\circ - \frac{\phi}{2} + \frac{\psi}{2}\right) dv \\ \tau_{hv} &= 0.65 \cdot \frac{a_{top}}{g} \cdot \sigma_v \\ \psi &= \arctan\left(\frac{0.65 \cdot a_{top}}{g}\right),\end{aligned}\quad (7.11)$$

where  $h_w$  is wall height above its base,  $a_h$  is the horizontal soil acceleration,  $\sigma_v$  is the total vertical stress in soil behind wall at depth  $v$  below wall top,  $\tau_{hv}$  is the average

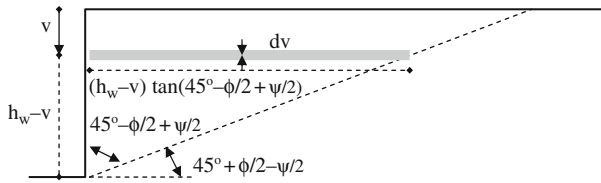


**Fig. 7.5** Sketch of a cross section through the active zone behind a wall

shear stress on a horizontal plane through soil behind wall at depth  $v$ ,  $\phi$  is soil friction angle in cyclic condition. The equation for  $\tau_{hv}$  is similar to [Equation \(1.6\)](#). When [Equation \(7.11\)](#) is solved

$$\Delta E_a = 0.65 \cdot a_{top} \cdot \rho \cdot \tan\left(45^\circ - \frac{\phi}{2} + \frac{\psi}{2}\right) \cdot \frac{h_w^2}{2} \quad (7.12)$$

The volume of ground mass involved in wall loading changes with direction of ground acceleration, towards or away from wall. [Equation \(7.12\)](#) considers an average active ground volume when ground acceleration changes sign. For layered and cohesive soil, an estimate of shear stress distribution along wall height can be obtained using SHAKE computer program.

The location of  $\Delta E_a$  force is at 2/3 of wall height from its base. The resultant of the static  $E_{as}$  and of dynamic increment  $\Delta E_a$  is located between 1/3 and 2/3 of wall height from its base depending on their relative values.

In the case of inclined soil surface at the back of a wall and/or inclined wall back side then the angle  $45^\circ - \phi/2 + \psi/2$  in [Equation \(7.12\)](#) should be replaced by the difference between  $90^\circ$  and the angle calculated from [Equation \(7.10\)](#).

#### 7.4.1.1 An Example

This example shows remarkable equality between the results of the two methods described in [Sections 7.3.1](#) and [7.4.1](#). The values of calculated  $E_a - E_{as}$  according to [Equations \(7.6\)](#) and [\(7.8\)](#) and  $\Delta E_a$  according to [Equation \(7.12\)](#) for  $h_w = 5$  m,  $\phi = 35^\circ$ ,  $\delta = 0$ ,  $\gamma = 20$  kN/m<sup>3</sup>,  $\rho = 2000$  kg/m<sup>3</sup>,  $\sigma = \eta_w = 0$ , for a range of  $a_{top}$  i.e.  $a_h$  multiplied by 0.65 is shown in [Fig. 7.6](#).

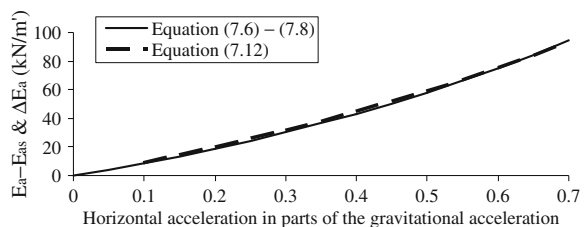


**Fig. 7.6** A comparison between the values of dynamic incremental lateral load on a wall based on different equations

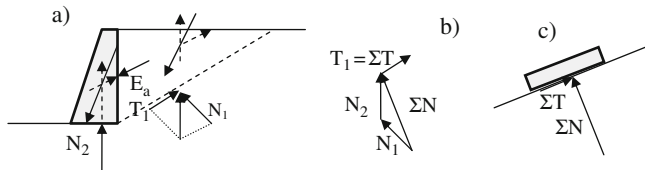


**Fig. 7.7** Sketch of (a) cross section through a massive wall with acting forces during an earthquake, (b) polygon of axial and transversal components of the forces on slip surfaces, (c) an equivalent block for co-seismic sliding

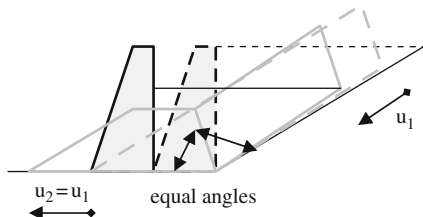
#### 7.4.2 Co-seismic Slip

When capacity against sliding at a wall base is exceeded during an earthquake then the wall will exhibit co-seismic slip. The amount of slip can be estimated using, for example, [Equation \(1.4\)](#) and [Fig. 1.4](#) based on Newmark ([1965](#)) sliding block method when the critical acceleration corresponding to the factor of safety of one against sliding, peak horizontal ground acceleration, earthquake magnitude, the hypocentral depth and the source to site distance are known or assumed. Sketches of the cross section through a wall, a polygon of components of forces acting on the slip surfaces and the equivalent block are shown in [Fig. 7.7](#).

#### 7.4.3 Post-seismic Slip

If the factor of safety against sliding of a wall is decreased below one during an earthquake and it remains below one after the earthquake then post-seismic slip will occur driven by gravity forces alone. The factor of safety decrease below one can be caused by build up of excesses pore water pressure in non-cohesive soil or decrease of shear strength to residual value in cohesive soil, for example, during an earthquake. Post-seismic slip is usually large and fast and can be analysed using the two block model described in [Section 5.4](#) for translational and equivalent slope slides. Sketch of the cross section through a wall and equivalent two sliding blocks are shown in [Fig. 7.8](#).

**Fig. 7.8** Sketch of the cross section through a massive wall and equivalent two blocks for post-seismic sliding



## 7.5 Case Histories

The case histories are considered to find if the results of the simple analyses are realistic and appropriate.

### 7.5.1 Quay Walls at Kobe Port in Japan

On 16 January 1995, Hyogoken-Nanbu earthquake of surface wave magnitude  $M_s = 6.9$  occurred in Hanshin area. In Kobe port, Inagaki et al. (1996) recorded the earthquake motion at the ground surface by a SMAC-B2 accelerometer. The corrected peak accelerations are  $5.25 \text{ m/s}^2$  in NW direction and  $2.30 \text{ m/s}^2$  in EN direction. The standard penetration test blow counts N at the recording station were obtained about two weeks after the earthquake and indicated N between 4 and 6 to 10 m depth with two exceptions of N = 1 at about 7.5 m depth. Liquefaction occurred around the recording station. The wave forms of the acceleration time histories in the horizontal direction indicate that the liquefaction occurred after 1.8 s from the beginning of the record.

Inagaki et al. (1996) described seaward displacements of the caisson walls of about 5 m maximum and 3 m average, settlement of about 2 m and tilt of about 4–5° and investigated the mechanism of deformation of the caisson walls by shake table tests. The shake table tests indicated that the excess pore water pressure in the replacement sand beneath the caisson did not reach 50% of the initial confining pressure. Both the shake table tests and the in-situ investigation by diving suggested that the mechanism of the deformation of the caisson is not only the sliding of the caisson during earthquake shaking but an overall deformation of the foundation soil beneath the caisson, which cross section is shown in Fig. 7.9.

The quay wall shown in Fig. 7.9 is founded on 4 m thick 10–200 kg stone rubble over about 17.5 m thick layer of filled sand. Stone backfill was placed next to the wall and decomposed granite (Masado) was used for landfill. The results of cyclic triaxial tests performed on samples of the landfill soil and replacement sand indicate these friction angles in cyclic condition equal to about  $10.2^\circ$  and  $11.3^\circ$  respectively (Inagaki et al., 1996). The test results are in good agreement with the cyclic soil friction angles shown in Fig. 4.2.

Although the caisson is 16.5 m high, the 2 m additional fill on top of it caused that the height  $h_w = 18.5 \text{ m}$  is used for soil lateral force calculation. At the beginning of earthquake, assumed soil and rock fill  $\phi = \delta_w = 35^\circ$ . Assumed unit weight of soil, caisson and rock fill  $\gamma = 20 \text{ kN/m}^3$  and in saturated condition  $\gamma' = 10 \text{ kN/m}^3$ . The total weight of the caisson and soil fill above it is assumed to be  $12*18.5*20 = 4440 \text{ kN/m}'$  and in submerged condition  $12*(4*20 + 14.5*10) = 2700 \text{ kN/m}'$ . Assumed inertial force acting on caisson mass is  $4440*0.65*5.25/9.81 = 1544 \text{ kN/m}'$ . Assumed resistance force to shearing at the base of the caisson is  $2700*\tan 35^\circ = 1890 \text{ kN/m}'$ . Assumed  $\psi = \arctan(0.65*5.25/9.81) = 19.2^\circ$ . In Equation (7.6),  $K_a = 0.61$  and soil lateral force in the horizontal direction  $E_a = 0.5*20*0.61*18.5^2*\cos 35^\circ = 1712 \text{ kN/m}'$ .

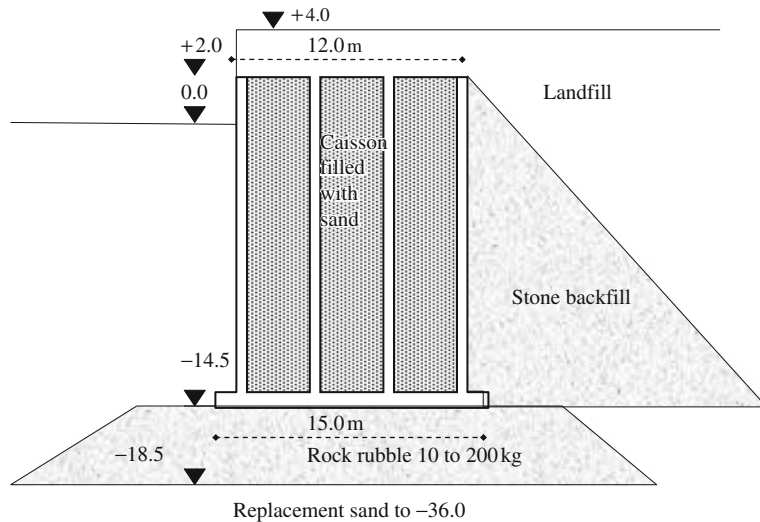


**Fig. 7.9** Cross section through the caisson in Kobe port

### 7.5.1.1 Bearing Capacity of the Replacement Sand Beneath the Caisson During the Earthquake

The bearing capacity of replacement sand at  $-18.5$  m level is calculated assuming that the loads at the base of the caisson are transferred through the rock rubble with an inclination of 2 vertical to 1 horizontal so that the width of the loaded area is  $15 + 4 = 19$  m. The vertical load from the caisson is  $2700 \text{ kN/m}'$  and from the rock rubble  $0.5 * (15 + 19) * 4 * 10 = 680 \text{ kN/m}'$ . From Equation (7.6),  $K_a = 0.61$  and for a depth of  $22.5$  m,  $E_a = 0.5 * 20 * 0.61 * 22.5^2 * 0.82 = 2532 \text{ kN/m}'$ . From Equation (7.7),  $K_p = 14.6$  and for the fill thickness of  $4$  m,  $E_p = 0.5 * 20 * 14.6 * 4^2 * 0.82 = 1915 \text{ kN/m}'$  so that net horizontal force is  $2532 - 1915 = 617 \text{ kN/m}'$ . The overturning moment is  $2532 * (9.25 + 2) + 1544 * (9.25 + 4) - 1915 * 4 / 2 = 45113 \text{ kNm/m}'$  so that the reduced width  $B' = 19 - 2 * 45, 113 / (2700 + 680) = -7 \text{ m}$ . The calculated resultant force is outside the loaded area and the bearing capacity was negligible if the inertial force acting on the caisson and the lateral active force on its back acted in phase. Another reason why the bearing failures did not happen can be short duration of inertial forces and their reversed direction.

### 7.5.1.2 Factor of Safety Against Sliding During the Earthquake and Co-seismic Slip

The factor of safety is the ratio between available resistance and driving forces i.e.  $1890 * (1544 + 1712)^{-1} = 0.58$ . The critical soil lateral force in the horizontal direction  $E_a = 1890 - 1544 = 346 \text{ kN/m}'$ . The corresponding  $K_a =$

$346^*(0.5^*20^*18.5^*0.82)^{-1} = 0.12$  which is smaller than  $K_{as} = 0.49$  in static condition. The caisson's stability in seismic condition was most likely checked using Mononobe-Okabe method but possibly using different friction angles of rock fill than  $35^\circ$  or smaller peak acceleration.

From Fig. 1.1, for earthquake magnitude 6.9 and the peak horizontal acceleration of  $5.25 \text{ m/s}^2$  it follows that the corresponding source to site distance is about 2.5 km on average for soft soil sites. From Fig. 1.4 and the critical to peak ground acceleration ratio of 0.1, it follows that the permanent co-seismic slip is about 0.5 m on average and about 1.9 m on average plus one standard deviation for slope distance to the earthquake source of 5 km. These co-seismic slips are much smaller than the observed horizontal displacements of the caissons so a significant post-seismic sliding most likely occurred.

#### 7.5.1.3 Factor of Safety Against Overturning Around the External Edge During the Earthquake

The factor of safety against overturning around the external edge i.e. the ratio between resisting and driving turning moments is for the horizontal soil lateral force of  $1712 \text{ kN/m}'$  at  $0.5^*18.5 = 9.25 \text{ m}$  above the base, for the caisson's inertial force of  $1544 \text{ kN/m}$  at  $18.5/2 = 9.25 \text{ m}$  above the base and for the weight of caisson and fill above it of  $2700 \text{ kN/m}$  at  $15/2 = 7.5 \text{ m}$  distance from the edge:  $2700^* 7.5^*(1712^*9.25 + 1544^*9.25)^{-1} = 0.67$ . Likely reasons why the caisson did not overturn could be short duration and alternating directions of inertia forces and/or out of phase action of the horizontal inertial force and the lateral active force on the caisson.

#### 7.5.1.4 Factor of Safety Against Deep Seated Slip After the Earthquake and Post-seismic Slip

The calculation is performed using computer software with an automatic search for the critical slip surface with minimum factor of safety (e.g. Maksimovic, 1988). The results are shown in Fig. 7.10.

For a manual calculation based on Equation (7.4) the results are shown in Table 7.3.

The factor of safety in post-seismic condition is smaller than one so post-seismic slip is considered according to Section 5.4. For two equivalent blocks with slip surface inclination to the horizontal  $\theta = 38^\circ$ , the base inclination to the horizontal  $\delta = -20^\circ$ , the interface angle inclination to the horizontal  $\beta = 81^\circ$ , assumed shear strength ratios at the base and slope  $\alpha = 1$ , effective axial stress on the slip surface  $\sigma'_n = 17.4 \times 10 = 174 \text{ kPa}$ , angle of landfill friction in (post) cyclic condition  $\phi = 11^\circ$ , an equivalent (undrained) shear strength  $c_u = 174 \times \tan(11^\circ) = 34 \text{ kPa}$ , the initial factor of safety of sliding stability  $F_o = 0.84$ , the maximum sliding  $u_{\max} = 5.6 \text{ m}$  and its duration  $T = 6.8 \text{ s}$ , the maximum velocity and acceleration of the post-seismic slip are  $1.3 \text{ m/s}$  and  $0.06$  of the gravitational acceleration respectively. The final factor of safety of slip stability  $F_f = 1.15$ . The

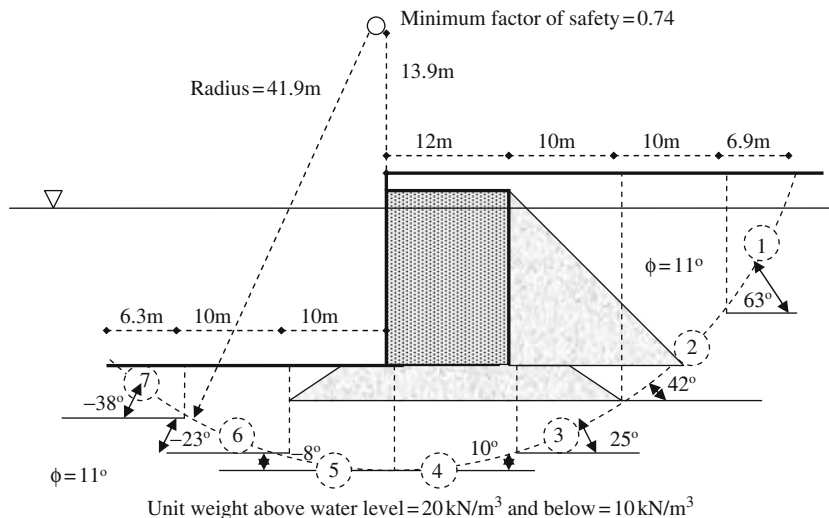


**Fig. 7.10** Cross section of the caisson in Kobe port and a circular slip surface with the minimum factor of safety against deep seated slip in post-seismic condition

**Table 7.3** Calculation of factor of safety  $F_s$  in post-seismic stage for a deep seated soil slip beneath the quay wall at Kobe port in Japan

Slice No	$W_s$ (kN)	$u_w$ (kPa)	$b_s$ (m)	$\alpha_s$ (degree)	$\frac{\sum(W_s - u_w b_s) \tan \phi (\cos \alpha_s + \sin \alpha_s \tan \phi F_s^{-1})}{\sum W_s \sin \alpha_s}$
1	600	0	6.9	63	170
2	2000	0	10	42	423
3	2800	0	10	25	535
4	3800	0	12	10	717
5	1000	0	10	-8	204
6	700	0	10	-23	166
7	200	0	6.3	-38	62
$\sum$	-	-	-	-	2277
$F_s$	-	-	-	-	0.72

horizontal component of the slip is  $5.6 \cdot \cos 38^\circ = 4.4$  m and the vertical component is  $5.6 \cdot \sin 38^\circ = 3.4$  m, which are not far away from the maximum observed horizontal displacement of up to 5 m and the settlement of 2 m. The geometries of two equivalent blocks are shown in Fig. 7.11.

### 7.5.2 Quay Wall at Kalamata Harbour in Greece

On 13 September 1986, an earthquake of surface wave magnitude  $M_s = 6.2$  occurred in the southern part of Peloponnesus. The epicentre of the main shock was located 12 km north of the port of Kalamata. The depth of the main shock was 8 km. The

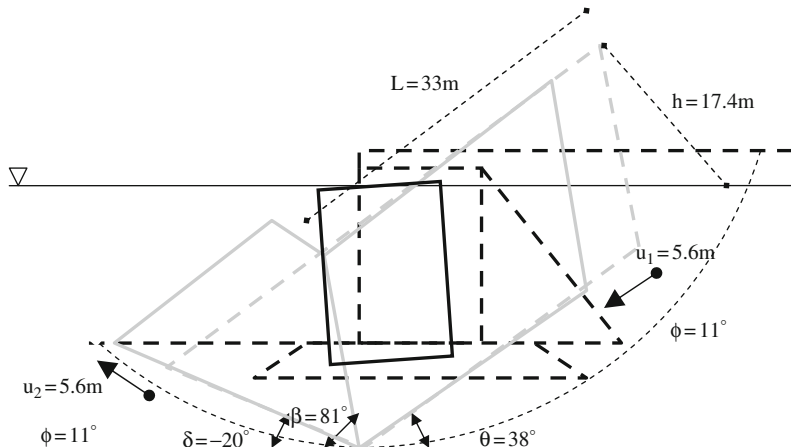


**Fig. 7.11** Cross section through two equivalent blocks used for the analysis of post-seismic sliding of the caisson in Kobe port

main shock was recorded by two SMA-1 accelerometers located at the basement of the 7 storey Prefecture Hall and the 2 storey Old P.T.T. Office. The peak horizontal accelerations recorded at the basement of the Prefecture Hall were 2.11 and  $2.91 \text{ m/s}^2$  and at the basement of the P.T.T. Office 2.35 and  $2.67 \text{ m/s}^2$  according to Pitilakis and Moutsakis (1989).

Pitilakis and Moutsakis (1989) described and analyzed by two dimensional finite elements the overall wall behaviour during the 1986 Kalamata earthquake. The quay wall was displaced horizontally about  $15 \pm 5 \text{ cm}$  and slightly rotated  $4^\circ\text{--}5^\circ$  seaward (Pitilakis and Moutsakis, 1989). They found that the calculated acceleration at the top of the wall was almost 30% larger than at its base, the behaviour of the wall was not governed by a rigid plastic movement, the wall and the neighbouring backfill acted in a very similar way during the seismic excitation and the vertical component of the ground motion had very little effect on the magnitude of the seismic pressure. A cross section of the wall is shown in Fig. 7.12.

The quay wall is founded through a 2.5–3.0 m thick layer of silty sand (SM) and gravelly sand (SG) on the silty sand formation (SM-ML). This formation covers a great part of the east costal area to a depth of 20 m. The standard penetration test (SPT) blow count varies from  $N = 20$  near its surface to more than 50 at depth (Pitilakis and Moutsakis, 1989). The upper formation is underlain by a gravelly sand formation (SG) which in turn lies on a marl formation at a depth of 60–70 m. The standard penetration test (SPT) blow count in the fill behind the wall varies from  $N = 5$  near the surface to  $N = 25$  at the bottom of the fill.

It is assumed that the total unit weight of the wall is  $24 \text{ kN/m}^3$  and in submerged condition  $14 \text{ kN/m}^3$ . It is assumed that the soil and fill unit weight above water level is  $20 \text{ kN/m}^3$  and below water level  $10 \text{ kN/m}^3$ . For silty sand, the standard penetration test blow count over 20 and earthquake magnitude over 6.5, the angle of friction is about  $35^\circ$ , according to Fig. 4.2. The same friction angle is assumed for wall soil

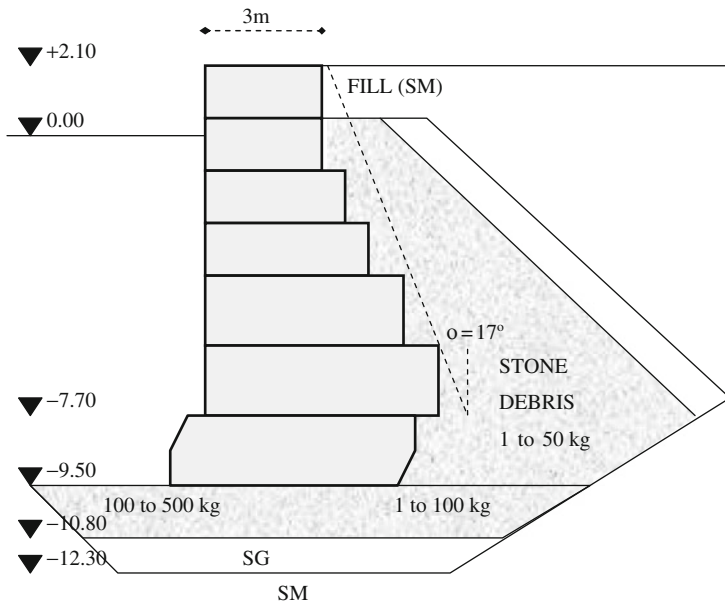


Fig. 7.12 Cross section of the Kalamata harbour quay wall

interface  $\delta_b$ . For the volume of wall of  $56 \text{ m}^3/\text{m}'$  it follows that its total weight is  $56*24 = 1344 \text{ kN/m}'$  and its partially submerged weight  $894 \text{ kN/m}'$ . The inertial force is  $1344*0.65*2.5/9.81 = 222 \text{ kN/m}'$ . The frictional resistance at the wall base is  $894 * \tan 35^\circ = 626 \text{ kN/m}'$ . In Equation (7.6), for back wall inclination to the vertical  $\theta = 17^\circ$  and the angle  $\psi = \arctan(0.65*2.5/9.81) = 9.4^\circ$ ,  $K_a = 0.60$  and soil lateral active force in the horizontal direction  $E_a = 0.5*20*0.60*11.6^2*\cos 35^\circ = 662 \text{ kN/m}'$ .

### 7.5.2.1 Bearing Capacity of Sandy Soil Beneath the Wall During the Earthquake

The bearing capacity of silty sand at  $-10.8 \text{ m}$  level is calculated assuming that the loads at the base of the wall are transferred through the rock fill with an inclination of 2 vertical to 1 horizontal so that the width of the loaded area is  $6.4 + 1.3 = 7.9 \text{ m}$ . The vertical load from the wall is  $894 \text{ kN/m}'$  and from the rock fill  $0.5*(6.4 + 7.9)*1.3*10 = 93 \text{ kN/m}'$ . For  $K_a = 0.60$  and for a depth of  $11.6 + 1.3 = 12.9 \text{ m}$ ,  $E_a = 0.5*20*0.60*12.9^2*0.82 = 819 \text{ kN/m}'$ . From Equation (7.7),  $K_p = 6.86$  and for the fill thickness of  $1.3 \text{ m}$ ,  $E_p = 0.5*20*6.86*1.3^2*0.82 = 95 \text{ kN/m}'$  so that net horizontal force is  $819 - 95 = 724 \text{ kN/m}'$ . The overturning moment is  $819*0.5*12.9 + 222*(0.5*11.6 + 1.3) - 95*0.5*1.3 = 6802 \text{ kNm/m}'$  so that the reduced width  $B' = 7.9 - 2*6802/(894 + 93) = -5.9 \text{ m}$ . The calculated resultant force is outside the loaded area and the bearing capacity was negligible if

the inertial force acting on the wall and the lateral active force on its back acted in phase. Another reason why the bearing failures did not happen can be short duration of inertial forces and their reversed direction.

#### **7.5.2.2 Factor of Safety Against Sliding During the Earthquake and Co-seismic Slip**

The factor of safety is the ratio between available resistance and driving forces i.e.  $626*(662 + 222)^{-1} = 0.71$ . The critical soil lateral force in the horizontal direction  $E_a = 626 - 222 = 404 \text{ kN/m'}$ . The corresponding  $K_a = 404*(0.5*20*11.6^2*0.82)^{-1} = 0.37$  which is smaller than  $K_{as} = 0.42$  in static condition. The wall's stability in seismic condition was most likely checked using Mononobe-Okabe method but possibly using different friction angles of rock fill than  $35^\circ$  or smaller peak acceleration.

From Fig. 1.4, for earthquake magnitude of 6.2, source to site distance of 12 km and for the critical to peak ground acceleration ratio of 0.1, it follows that the permanent co-seismic slip is about 0.2 m on average and about 0.5 m on average plus one standard deviation. The actual maximum co-seismic slip of up to 0.2 m is in agreement with estimated average slip.

#### **7.5.2.3 Factor of Safety Against Overturning Around the External Edge During the Earthquake**

The factor of safety against overturning around the external edge i.e. the ratio between resisting and driving turning moments is for the horizontal soil lateral force of  $662 \text{ kN/m'}$  at  $0.5*11.6 = 5.8 \text{ m}$  above the base, for the quay wall's inertial force of  $222 \text{ kN/m}$  at  $11.6/3*(6.4 + 2*3)/(6.4 + 3) = 5.1 \text{ m}$  above the base and for the weight of wall of  $894 \text{ kN/m}$  at  $[(3*11.6)*1.5 + 0.5*3.4*11.6*(3 + 0.33*6.4)]/56 = 2.74 \text{ m}$  distance from the edge:  $894*2.74*(662*5.8 + 222*5.1)^{-1} = 0.49$ . Likely reasons why the wall did not overturn could be short duration and alternating directions of inertia forces and/or out of phase action of the horizontal inertial force and the lateral active force on the wall.

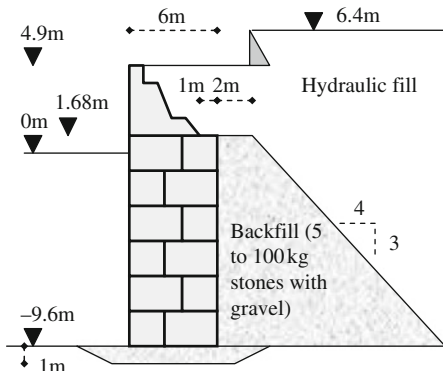
#### **7.5.2.4 Factor of Safety Against Deep Seated Slip After the Earthquake**

The calculation is performed using computer software with an automatic search for the critical slip surface with minimum factor of safety (e.g. Maksimovic, 1988). The calculated minimum factor of safety is 1.19 for a critical slip surface passing just under the back edge of the wall base. The calculation can be performed manually using Equation (7.5) and a table similar to the table given in Section 7.5.1.4.

### **7.5.3 Quay Wall at San Antonio Port in Chile**

Tsuchida et al. (1986) and Wyllie et al. (1986) described damage to the quay wall at San Antonio Port in Chile that is caused by the 3 March 1985 Chilean

**Fig. 7.13** Cross section through the quay wall at San Antonio Port in Chile



earthquake with magnitude  $M_s = 7.8$ , which induced peak horizontal ground surface acceleration of  $0.67g$ .

The wall is made of concrete blocks up to a height of 11.3 m with a top block 3.2 m high. The wall width is 6 m. The collapse of the wall happened over 60% of the wharf length (452 m) due to hydraulic backfill liquefaction during the earthquake. The backfill right behind the wall was made of 5–100 kg stones with gravel. The hydraulic fill comprises mainly fine to medium coarse sand with the standard penetration test blow count of between 15 and 19. The wall is founded over 1 m thick layer of 5–100 kg stones within sandstone formation. A cross section through the wall is shown in Fig. 7.13.

It is assumed that the friction angle of rock backfill and hydraulic fill was  $35^\circ$  at the beginning of earthquake. The liquefied hydraulic fill has no shear strength by definition of liquefaction. It is assumed that the total unit weight of concrete blocks was  $24 \text{ kN/m}^3$  and the submerged weight  $14 \text{ kN/m}^3$ . It is assumed that the total unit weight of fill is  $20 \text{ kN/m}^3$  and in submerged condition  $10 \text{ kN/m}^3$ . The total weight of the wall and the fill above it is assumed to be  $6*(11.3*24 + 3.2*20) = 011 \text{ kN/m}'$  and the submerged weight  $6*(11.3*14 + 3.2*20) = 1333 \text{ kN/m}'$ . The inertial force from the wall mass was assumed to be  $2011*0.65*0.67 = 876 \text{ kN/m}'$ . For assumed friction angle between wall base and the rock fill of  $35^\circ$ , it follows that the resisting force to sliding was  $1333*\tan 35^\circ = 933 \text{ kN/m}'$ . From Equation (7.6) and for  $\psi = \arctan(0.65*0.67) = 23.5^\circ$ , it follows that  $K_a = 0.48$  and for  $h_w = 14.5 \text{ m}$ ,  $E_a = 0.5*20*0.48*14.5^2*\cos 35^\circ = 828 \text{ kN/m}'$ .

### 7.5.3.1 Bearing Capacity of Rock Fill Under the Wall

The rock fill thickness is only 1 m above sandstone formation so that the bearing capacity should not have been a problem.

### 7.5.3.2 Factor of Safety Against Sliding During the Earthquake and Co-seismic Slip

The factor is a ratio between resisting and driving forces, i.e.  $933^*(876 + 828)^{-1} = 0.55$ . The critical horizontal force is  $933 - 876 = 57$  kN so that the wall stability may have been checked for a smaller peak ground acceleration than  $0.67g$ .

From Fig. 1.1, for earthquake magnitude of 7.8 and the peak ground acceleration of  $0.67g$ , the source to site distance could be about 10 km. From Equation (1.4), for earthquake magnitude of 7.8, the site to source distance of 10 km and for the critical to peak acceleration ratio of 0.1, it follows that the permanent displacement is about 1 m on average or about 4 m on average plus one standard deviation.

### 7.5.3.3 Factor of Safety Against Overturning Around the External Edge

The factor is a ratio between resisting and driving turning moments, i.e.  $1333^*6^*0.5^*(828^*14.5^*0.5 + 876^*14.5^*0.5)^{-1} = 0.33$ . Even if the inertial force on the wall mass and on the lateral force on the wall back were not in phase, the factor of safety was only  $1333^*6^*0.5^*(828^*14.5^*0.5)^{-1} = 0.55$  or  $1333^*6^*0.5^*(876^*14.5^*0.5)^{-1} = 0.63$ .

### 7.5.3.4 Factor of Safety Against Global Wall and Fill Failure and Slip in Post Seismic Condition

The calculation is performed using computer software with an automatic search for the critical slip surface with minimum factor of safety (e.g. Maksimovic, 1988). The calculated minimum factor of safety against slip just under the wall is 1.2. The calculation can be performed manually using Equation (7.5) and a table similar to the table given in Section 7.5.1.4.

The likely mechanism for the wall collapse was toppling type failure.

## 7.6 Discussion and Conclusions

The use of pseudo-static methods for checking of the factors of safety for bearing, sliding, overturning and global stability of massive walls during an earthquake is not realistic if the inertial force from wall mass and lateral active force on the wall back is assumed to act in phase based on the results obtained for the case histories analysed. Calculated factors of safety of wall stability could have been even smaller had the lateral force of water in hydrodynamic condition been decreased in front of the wall. The calculation of lateral soil force is performed using total soil weight although EN 1998-5 (2004) specifies that dynamically impervious soil has a coefficient of permeability of less than 0.5 mm/s and dynamically pervious soil greater than 0.5 mm/s. Soil permeability only affects build up or dissipation of excess pore water pressure because the amount of water leaving a unit volume of soil on one

side is replaced by the same amount of water entering on the other side so the mass and inertial forces are not affected.

The results from the centrifuge tests show that when the inertial force on the wall is at maximum the dynamic earth pressure increment is at minimum according to Atik and Sitar (2009). Other reasons why many massive walls survived earthquakes are short duration of earthquake pulses and their reverse direction.

The estimates of permanent co-seismic slip by Newmark (1965) sliding block method and post-seismic slip by Ambraseys and Srbulov (1995) two-block methods are realistic for the case histories analysed. This finding supports Richards and Elms (1979) proposal that the seismic design of massive retaining walls is based on allowable permanent wall displacements.

## References

- Ambraseys NN, Srbulov M (1995) Earthquake induced displacements of slopes. *Soil Dyn Earthquake Eng* 14:59–71
- API RP2A-WSD (2000) Recommended practice for planning, designing and constructing fixed offshore platforms – working stress design – 21st edition. American Petroleum Institute, Washington, DC
- Atik LA, Sitar N (2009) Experimental and analytical study of the seismic performance of retaining structures. Pacific Earthquake Engineering Research Centre report PEER 2008/104 [http://peer.berkeley.edu/publications/peer\\_reports/reports\\_2008/reports\\_2008.html](http://peer.berkeley.edu/publications/peer_reports/reports_2008/reports_2008.html)
- Bishop AW (1955) The use of slip circle for stability analysis. *Geotechnique* 5(1):7–17
- BS 5228-2 (2009) Code of practice for noise and vibration control on construction and open sites – part 2: vibration. British Standards Institution
- Caquot A, Kerisel J (1948) Tables for calculation of passive pressure, active pressure and bearing capacity of foundations. Gauthier-Vilars, Paris
- Coulomb CA (1776) Essai sur une application des regles des maximis et minimis a quelques problemes de statique relatifs a l'architecture. Memoires de l'Academie Royale pres Divers Savants
- Dakoulas P, Gazetas G (2008) Insight into seismic earth and water pressures against caisson quay walls. *Geotechnique* 58:95–111
- EN 1997-1 (2004) Eurocode 7 – geotechnical design, part 1: general rules. European Committee for Standardization, Brussels
- EN 1998-5 (2004) Eurocode 8 – design of structures for earthquake resistance, part 5: foundations, retaining structures and geotechnical aspects. European Committee for Standardization, Brussels
- Hansen JB (1970) A revised and extended formula for bearing capacity. Bulletin No. 28, Geoteknisk Institut, Akademiet for dde Tekniske Videnskaber, Copenhagen, Denmark
- Inagaki H, Iai S, Sugano T, Yamazaki H, Inatomi T (1996) Performance of caisson type quay walls at Kobe port. Soils and Foundations special issue, pp 119–136, Japanese Geotechnical Society Journal
- Kim SR, Kwon OS, Kim MM (2004) Evaluation of force components acting on gravity type walls during earthquakes. *Soil Dyn Earthquake Eng* 24:853–866
- Koseki J, Tatsuoka F, Munaf Y, Tateyama M, Kojima K (1998) A modified procedure to evaluate active earth pressure at high seismic loads. *Soils Foundations (Special issue on geotechnical aspects of the January 17, 1996 Hyogoken-Nambu earthquake)* 2:209–216
- Kramer SL (1996) Geotechnical earthquake engineering. Prentice Hall, Upper Saddle River, NJ
- Maksimovic M (1988) General slope stability package for micro computers. In: Proceedings of 6th international conference on numerical methods in geomechanics, vol 3, Innsbruck, pp 2145–2150

- Maksimovic M (2008) Mehanika tla. AGM knjiga, Belgrade
- Meyerhof GG (1963) Some recent research on the bearing capacity of foundations. Canadian Geotechnical Journal 1(1):16–26
- Mononobe N, Matsuo H (1929) On the determination of earth pressures during earthquakes. In: The World engineering congress, Tokyo, Japan
- Newmark NM (1965) Effect of earthquakes on dams and embankments. Geotechnique 15:139–160
- Okabe S (1926) General theory of earth pressures. J Jpn Soc Civil Eng 12:1
- Pitilakis K, Moutsakis A (1989) Seismic analysis and behaviour of gravity retaining walls – the case of Kalamata harbour quay wall. Soils Foundations 29:1–17
- Richards R, Elms D (1979) Seismic behaviour of gravity retaining walls. ASCE J Geotechn Eng 105:449–464
- Richards R, Huang C, Fishman KL (1999) Seismic earth pressure on retaining structures. ASCE J Geotechn Geoenvir Eng 25:771–778
- Seed HB, Whitman RV (1970) Design of earth retaining structures for dynamic loads. In: Proceedings of ASCE specialty conference, lateral stresses in the ground and design of earth retaining structures, Cornell University, Ithaca, New York, NY, pp 103–147
- SNAME (1997) Site specific assessment of mobile jack-up units, 1st edn (revision 1). The Society of Naval Architects and Marine Engineers, Jersey City, New Jersey, pp 61–69
- Towhata I, Islam S (1987) Prediction of lateral movement of anchored bulkheads induced by seismic liquefaction. Soils Foundations 27(4):138–147
- Tsuchida H, de La Fuente RH, Noda S, Valenzuela MG (1986) Damage to port facilities in Port of Valparaiso and Port of San Antonio by the March 3, 1985 earthquake in middle of Chile. In: Proceedings of 4th Jordanadas Chileanas de Sismología e Intemperie Antisísmica and international seminar on the Chielan March 3, 1985 earthquake, Santiago, Chile
- Whitman RV, Liao S (1985) Seismic design of retaining walls. Miscellaneous Paper GL-85-1, US Army Engineer Waterways Experimental Station, Vicksburg, MS
- Wyllie LA, Abrahamson N, Bolt B, Castro G, Durkin ME, Escalante L, Gates HJ, Luft R, McCormick D, Olson RS, Smith PD, Vallenás J (1986) The Chile earthquake of March 3, 1985. EERI, Earthquake Spectra 2(2):513
- Zeng X, Steedman RS (2000) Rotating block method for seismic displacement of gravity walls. ASCE J Geotechn Geoenvir Eng 126:709–717

# Chapter 8

## Slender Retaining Walls

### 8.1 Introduction

Slender retaining walls have emerged with developments in reinforced concrete and steel production as they use their flexural stiffness to transfer nearly horizontal active lateral soil forces on the wall into nearly horizontal passive forces onto the ground in front of wall. Sketches of cross sections of slender retaining walls are shown in Fig. 8.1. The walls are also called embedded.

Most of slender retaining walls performed well during earthquakes with exception of a few cases some of which are described in the case histories in Section 8.5.

When subjected to ground vibration from industrial sources, retaining walls without or with little lateral restraint near their tops may exhibit amplification of vibration between 3 and 5 according to BS 5228-2:2009. Propred or tied walls can be subjected to the threshold limit of the peak particle velocity up to 20 mm/s at the toe and 80 mm/s at the crest. For continuous vibrations, the stated levels should be reduced by a factor of 1.5–2.5 according to BS 5228-2:2009.

The aim of this chapter is to describe the mechanisms and factors influencing possible failure modes of slender retaining walls, the existing methods for analyses of their behaviour and a simple model for calculation of lateral force during an earthquake. The emphasis is on the use of simple analyses for the walls in the case histories considered.

### 8.2 Mechanism and Factors

Main factors affecting slender retaining wall failures are:

- Addition of loading/fill at the back
- Large water pressure difference between the front and the back due to prevented drainage
- Earthquake acceleration

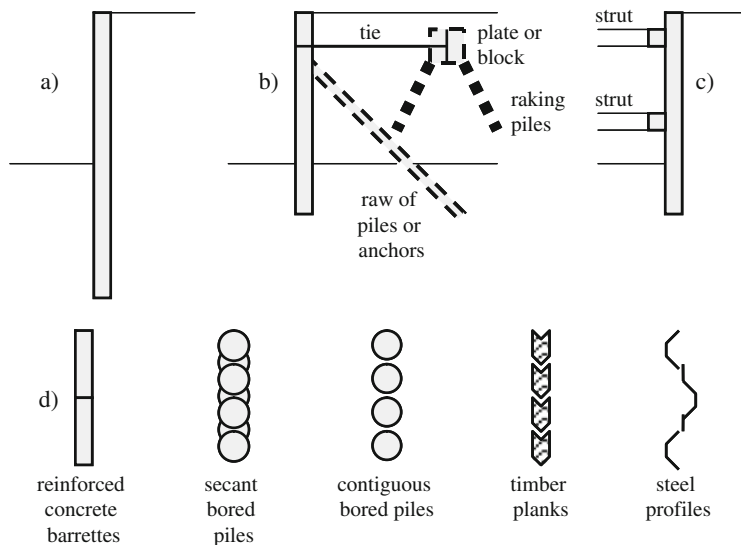


**Fig. 8.1** Sections through (a) cantilever, (b) anchored, (c) propped, (d) different materials for slender retaining walls

- Soil shear strength decrease in cyclic conditions
- Excavation in front of the wall
- Resonant response of wall, wall component, or wall/fill combination
- Liquefaction and /or fluidization of soil in front of wall
- Liquefaction and/or fluidization of backfill

Basic mechanisms of failures of slender retaining walls are shown in Fig. 8.2.

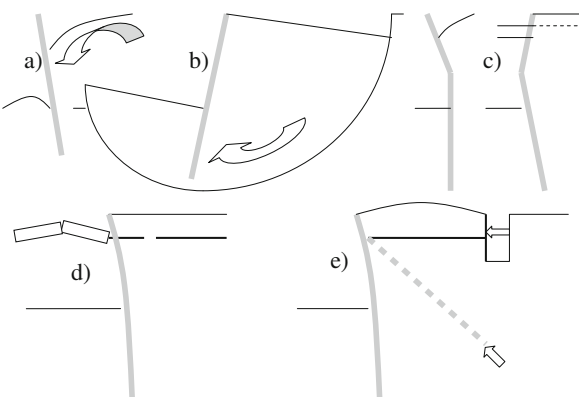


**Fig. 8.2** Types of failures of slender walls (a) forward rotational, (b) backward rotational, (c) flexural, (d) strut or tie break, (e) pull-out of tie or anchor

### **8.2.1 Stability Against Forward Rotation**

The stability is expressed in terms of the factor of safety which is a ratio between resisting and driving rotational moments acting on a wall. Driving moments are caused by lateral active force at the back of a wall and resisting moments are caused by lateral passive force in the front of a wall as well as by struts and ties if present.

### **8.2.2 Stability Against Backward Rotation**

The stability check is described in [Section 7.2.4](#).

### **8.2.3 Flexural Capacity**

The flexural capacity is checked by calculating the ratio between acting bending moment at a particular cross section of wall and the second moment of cross sectional area of a wall times a half of wall thickness. The calculated maximum bending stress must be smaller than allowable bending stress for wall material considered.

### **8.2.4 Capacity of Strut or Tie Against Break**

The capacity against break is calculated as the ratio between acting force and cross sectional area of a strut/tie, which must be smaller than allowable stress for strut/tie material considered. For struts in compression, capacity against buckling is also checked using Euler equation:

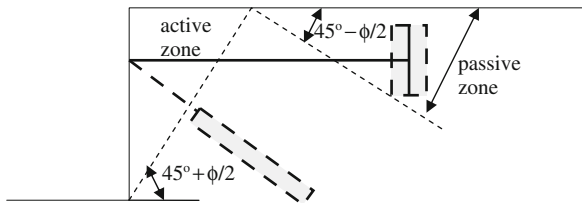
$$P_{critical} = \pi^2 \cdot \frac{E \cdot J}{l_k^2}, \quad (8.1)$$

where E is Young's modulus, J is the second moment of a cross sectional area,  $l_k$  is critical length, for both ends hinged = strut length, for one end hinged and the other with prevented rotation = 0.707 of strut length, for both ends with prevented rotation = 0.5 of strut length.

### **8.2.5 Pull Out Capacity of Tie or Anchor**

The capacity can be obtained from field pull out test or it can alternatively be estimated by applying soil mechanics theory. The theory provides acceptable location and dimensions of a tie plate/block within the passive zone to avoid its influence on the active zone behind wall. Figure 8.3 shows a cross section for the case of a wall with vertical back and the horizontal backfill. For inclined wall back and backfill, the angle of inclination of the passive and active zone can be calculated from

**Fig. 8.3** Acceptable location of a tie plate/block and anchor behind a wall with vertical back and the horizontal backfill to prevent the influence of the passive zone on the active zone behind wall



Equation (7.10). The actual passive zone has a concave surface so that the planar surface considered is on a safe side.

## 8.3 Existing Methods

### 8.3.1 Empirical by Formulas

The values and inclination of the active and passive lateral force on a retaining wall in pseudo static analyses can be calculated according to Section 7.3.1. Several methods exist for consideration of wall equilibrium, and bending moment distribution along its length. Burland et al. (1981) summarised and commented on the available methods, Fig. 8.4, as follows:

1. Gross lateral forces moment equilibrium uses a factor of safety  $F_p$  with respect to the total passive resistance of the toe and could be regarded as a load factor. Values of between 1.5 and 3 are usually used.
2. Net lateral force moment equilibrium uses a load factor of safety  $F_{np}$  of the moment of the net passive force. A value of 2 is normally adopted.
3. The method uses gross lateral forces moment equilibrium but multiplies the minimum embedment depth by a factor of safety  $F_d$ . A value of 1.7–1.2 is used for granular soil and 2–1.4 for undrained cohesive soil.

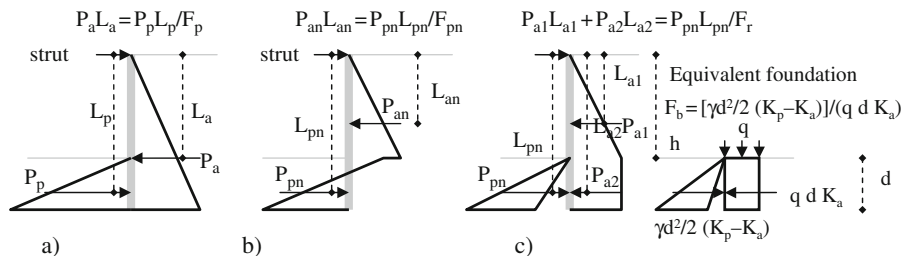


**Fig. 8.4** Different methods for consideration of slender wall equilibrium, (a) gross lateral force, (b) net lateral force, (c) bearing capacity analogy

4. The method determines the average shear strength required to achieve limiting equilibrium. The factors of safety  $F_s$  of available soil shear strength from 1.25 to 1.5 for soil friction angle and from 1.5 to 2 for soil cohesion are commonly used.

Burland et al. (1981) remarked that: *The use of both  $F_p$  and  $F_{np}$  can lead to very unsatisfactory results. There appears to be no logical or consistent relationship between  $F_p$  and  $F_s$  and its use can lead to very conservative values of wall penetration for drained conditions with  $\phi'$  less than 25° and for undrained conditions. With regard to  $F_{np}$ , its use with currently recommended values of about 2 leads to  $F_s$  generally less than 1.1 for both undrained and drained conditions. It should, therefore, only be used with great caution and with much higher values, which are compatible with acceptable values of  $F_s$ . For drained conditions in uniform ground, the use of  $F_d$  appears to be entirely satisfactory. However, it should not be used for undrained conditions or where the strength properties of ground vary significantly with depth.*

*The concept of factoring passive resistance of the toe of an embedded retaining wall is attractive in principle as the overall stability can be expressed as a single number. This is not the case for shear strength where the engineer may be faced with the possibility of a number of factors for strength and wall friction. Hence there are considerable benefits in developing a definition of factor of safety on passive resistance which and be shown to be logical and consistent.*

### 8.3.1.1 Simple Bearing Capacity Analogy

The analogy is sketched in Fig. 8.4c for frictional only soil above ground water level.

$$\begin{aligned}
 F_b &= \frac{0.5 \cdot \gamma \cdot d^2 \cdot (K_p - K_a)}{\gamma \cdot d \cdot K_a} \\
 F_r &= \frac{P_{pn} \cdot L_{pn}}{P_{a1} \cdot L_{a1} + P_{a2} \cdot L_{a2}} \\
 P_{pn} &= 0.5 \cdot \gamma \cdot d^2 \cdot (K_p - K_a) \\
 P_{a1} &= 0.5 \cdot \gamma \cdot h^2 \cdot K_a \\
 P_{a2} &= \gamma \cdot h \cdot K_a \cdot d \\
 L_{pn} &= h + \frac{2}{3} \cdot d \\
 L_{a1} &= \frac{2}{3} \cdot h \\
 L_{a2} &= h + 0.5 \cdot d
 \end{aligned} \tag{8.2}$$

where  $\gamma$  is soil unit weight,  $d$  is embedment depth,  $h$  is excavation depth in front of the wall

Burland et al. (1981) state for soil with cohesion  $c'$  and friction  $\phi'$  in terms of effective stresses:

$$\begin{aligned}
F_b &= \frac{0.5 \cdot \gamma \cdot d^2 \cdot (K_p - K_a) + 2 \cdot c' \cdot d \cdot (K_{ac} + K_{pc})}{\gamma \cdot h \cdot K_a \cdot d} \\
K_{ac} &= \sqrt{K_a}, K_{pc} = \sqrt{K_p} \\
F_r &= \frac{P_{pn1} \cdot L_{pn1} + P_{pn2} \cdot L_{pn2}}{P_{a1} \cdot L_{a1} + P_{a2} \cdot L_{a2}} \\
P_{n1} &= 0.5 \cdot \gamma \cdot d^2 \cdot (K_p - K_a) \\
P_{n2} &= 2 \cdot c' \cdot d \cdot (K_{pc} + K_{ac}) \\
P_{a1} &= 0.5 \cdot (K_a \cdot h \cdot \gamma - 2 \cdot c' \cdot K_{ac}) \cdot [h - 2 \cdot c' \cdot K_{ac}/(\gamma \cdot K_a)], \\
P_{a2} &= K_a \cdot h \cdot \gamma \cdot d \\
L_{pn1} &= h + \frac{2}{3} \cdot d \\
L_{pn2} &= h + 0.5 \cdot d \\
L_{a1} &= \frac{1}{3} \cdot [2 \cdot h - 2 \cdot c' \cdot K_{ac}/(\gamma \cdot K_a)] \\
L_{a2} &= h + 0.5 \cdot d
\end{aligned} \tag{8.3}$$

where  $\gamma$  is soil unit weight,  $d$  is embedment depth,  $h$  is excavation depth in front of the wall,  $c'$  is soil cohesion in terms of effective stresses,  $q$  is surcharge at the excavation level,  $K_{a,p}$  are coefficients of soil lateral active (a) and passive (p) pressures.

For cohesive soil in undrained conditions and in terms of total stresses:

$$\begin{aligned}
F_r &= \frac{4 \cdot c_u \cdot d \cdot L_{pn}}{0.5 \cdot (\gamma \cdot h - 2 \cdot c_u)^2 \cdot L_{a1}/\gamma + \gamma \cdot h \cdot d \cdot L_{a2}}, \gamma \cdot h \geq 2 \cdot c_u \text{ or ignore it} \\
L_{pn} &= h + 0.5 \cdot d \\
L_{a1} &= \frac{1}{3} \cdot (2 \cdot h - 2 \cdot c_u/\gamma) \\
L_{a2} &= h + 0.5 \cdot d
\end{aligned} \tag{8.4}$$

When surcharge (s) acts at the top and (p) at the excavation level in front of a wall:

$$\begin{aligned}
F_b &= \frac{p \cdot d \cdot (K_p - K_a) + 0.5 \cdot \gamma \cdot d^2 \cdot (K_p - K_a)}{(\gamma \cdot h - p) \cdot d \cdot K_a} \\
F_r &= \frac{P_{pn1} \cdot L_{pn1} + P_{pn2} \cdot L_{pn2}}{P_{a1} \cdot L_{a1} + P_{a2} \cdot L_{a2} + P_{a3} \cdot L_{a3}} \\
P_{pn1} &= 0.5 \cdot \gamma \cdot d^2 \cdot (K_p - K_a) \\
P_{pn2} &= p \cdot d \cdot (K_p - K_a) \\
P_{a1} &= s \cdot K_a \cdot h \\
P_{a2} &= 0.5 \cdot \gamma \cdot h^2 \cdot K_a \\
P_{a3} &= (s + \gamma \cdot h - p) \cdot d \cdot K_a \\
L_{pn1} &= h + \frac{2}{3} \cdot d \\
L_{pn2} &= h + 0.5 \cdot d \\
L_{a1} &= 0.5 \cdot h \\
L_{a2} &= \frac{2}{3} \cdot h \\
L_{a3} &= h + 0.5 \cdot d
\end{aligned} \tag{8.5}$$

For a **ground water level at depth  $j$  below the ground surface behind a wall**:

$$\begin{aligned}
 F_r &= \frac{P_{pn} \cdot L_{pn}}{P_{a1} \cdot L_{a1} + P_{a2} \cdot L_{a2} + P_{a3} \cdot L_{a3} + P_{w1} \cdot L_{w1} + P_{w2} \cdot L_{w2}} \\
 P_{pn} &= 0.5 \cdot d \cdot \left\{ (K_p - K_a) \cdot d \cdot \gamma - \frac{2 \cdot \gamma_w \cdot d}{2 \cdot d + h - j} \right. \\
 &\quad \left. \cdot [(K_p - K_a) \cdot (h + d - j) + K_a \cdot (h - j)] \right\} \\
 P_{a1} &= 0.5 \cdot \gamma \cdot j^2 \cdot K_a \\
 P_{a2} &= 0.5 \cdot (h - j) \cdot \gamma \cdot K_a \cdot \left[ j + h - \frac{2 \cdot \gamma_w \cdot (h - j) \cdot d}{\gamma \cdot (2 \cdot d + h - j)} \right] \\
 P_{a3} &= d \cdot \gamma \cdot K_a \cdot \left[ h - \frac{2 \cdot \gamma_w \cdot (h - j) \cdot d}{\gamma \cdot (2 \cdot d + h - j)} \right] \\
 L_{pn} &= h + \frac{2}{3} \cdot d \\
 L_{a1} &= \frac{2}{3} \cdot j \\
 L_{a2} &\sim 0.5 \cdot (j + h) \\
 L_{a3} &= h + 0.5 \cdot d
 \end{aligned} \tag{8.6}$$

For **walls without struts and in a basic case** like the one shown in Fig. 8.4c,

$$\begin{aligned}
 F_r &= \frac{P_{pn} \cdot L_{pn}}{P_{a1} \cdot L_{a1} + P_{a2} \cdot L_{a2}} \\
 P_{pn} &= 0.5 \cdot \gamma \cdot d^2 \cdot (K_p - K_a) \\
 P_{a1} &= 0.5 \cdot \gamma \cdot h^2 \cdot K_a \\
 P_{a2} &= \gamma \cdot h \cdot K_a \cdot d \\
 L_{pn} &= \frac{1}{3} \cdot d \\
 L_{a1} &= d + \frac{1}{3} \cdot h \\
 L_{a2} &= 0.5 \cdot d
 \end{aligned} \tag{8.7}$$

Water pressure, surcharges and cohesion may be included as in the case of a propped wall. The value of  $F_r$  between 1.5 and 2 would normally be appropriate according to Burland et al. (1981).

### 8.3.2 Numerical by Computer Software

Atik and Sitar (2009) summarise some of the analyses performed:

Siddharthan and Maragakis (1989) used finite element method for consideration of dynamic behaviour of flexural retaining walls supporting dry cohesionless soil. They used an incrementally elastic approach to model soil non-linear hysteretic behaviour and validated their model by comparing its results to recorded response from a dynamic centrifuge experiment. Siddharthan and Maragakis (1989)

concluded that bigger bending moments and smaller wall deflection occur for stiffer retaining walls supporting looser sandy backfill.

Veletsos and Younan (1997) considered flexural retaining walls supporting uniform linear viscous elastic material and observed that forces acting on flexural walls are much smaller than those acting on rigid ones.

Green et al. (2003) performed a series of nonlinear dynamic response analyses of a cantilever retaining wall using the FLAC and concluded that at small accelerations, the lateral soil forces were in agreement with the Mononobe-Okabe method. As acceleration increased, lateral soil forces were larger than those predicted by the M-O method.

Gazetas et al. (2004) performed a series of finite element analyses on several types of flexural walls subject to short duration of moderately strong excitations. They observed that “*as the degree of realism in the analysis increases, we can explain the frequently observed satisfactory performance of retaining systems during strong seismic shaking*”.

### **8.3.3 Experimental on Prototypes and Small Scale Models**

Chang et al. (1990) reported on successful field measurements of seismic lateral soil pressures on the embedded walls of the Lotung, Taiwan, quarter-scale reactor containment structure during several moderate size earthquakes. They found that measured seismic soil pressures were similar to or lower than estimates based on the M-O method.

Lew et al. (1995) described behaviour of four prestressed anchored piled walls in the Greater Los Angeles area during the 1994 Northridge earthquake with magnitude 6.7 that caused the acceleration of 0.2g and in some cases as large as 0.6g. The excavation depths were from 15 to 25 m in relatively stiff soil. Lew et al. (1995) reported that the measured deflections of these walls did not exceed 1 cm and that no significant damage was observed.

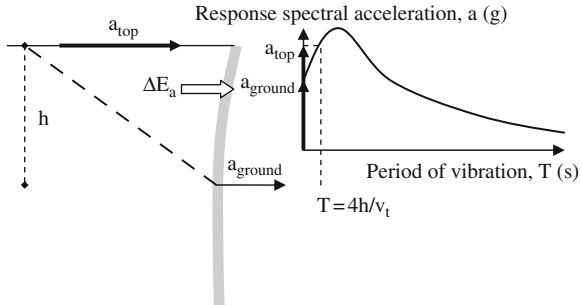
## **8.4 Simple Model and Assumptions**

### **8.4.1 Dynamic Increment of Active Soil Lateral Force**

The increment is calculated as described in Section 7.4.1. The only difference could be caused by the effect of fundamental period of vibration of soil retained by wall on the peak acceleration at the top  $a_{top}$  as sketched in Fig. 8.5, where  $v_t$  is an averaged transversal wave velocity along retained depth  $h$ .

Design acceleration response spectra are usually defined by seismic codes.

**Fig. 8.5** The effect of fundamental period of vibration  $T$  of retained soil on the peak horizontal acceleration  $a_{top}$  at the top and on the dynamic increment of active soil lateral force  $\Delta E_a$



## 8.5 Case Histories

Simple Equations (7.6) and (7.12) are used for the calculation of possible loads on the walls during earthquakes in order to assess the equation's accuracy and applicability in practice.

### 8.5.1 Embedded Wall of Cut and Cover Sepolia Station in Greece

The 1999 Parnitha earthquake in Greece with the earthquake magnitude  $M_s = 5.9$  caused measured peak ground surface acceleration of up to  $0.51g$  and rock outcrop acceleration of  $0.3g$  (Gazetas et al., 2005). The predominant period for the  $0.51g$  acceleration was  $0.15$  s and for the  $0.3g$  acceleration  $0.22$  s based on the peaks of response spectra.

At the station location, one accelerograph located at  $12.9$  m depth inside the station recorded the peak horizontal acceleration of  $0.24g$  and another instrument located approximately  $500$  m away from the station recorded the peak horizontal acceleration of  $0.36g$ . The predominant periods of vibrations were  $0.11$  and  $0.14$  s respectively with secondary period at  $0.26$  s based on the peak of the acceleration response spectra. A cross section through the station with reinforced concrete walls  $0.8$  m thick is shown in Fig. 8.6. The station suffered no damage during the earthquake.

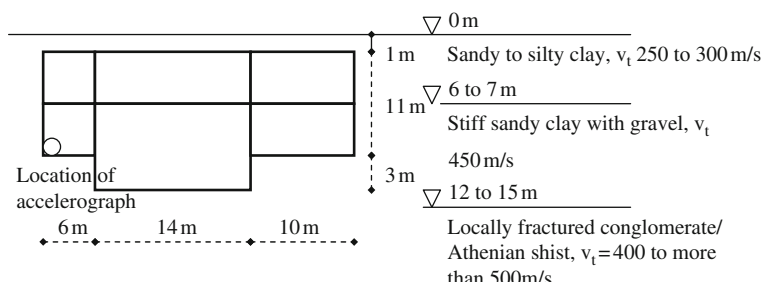


**Fig. 8.6** Sketch of a cross section through the Sapolia station in Greece and the ground profile

Based on the ground profile in Fig. 8.6, an averaged transversal wave velocity over 12 m depth is  $= 12*(3.5*(250)^{-1} + 4.5*(300)^{-1} + 4*(450)^{-1})^{-1} = 317 \text{ m/s}$ . The fundamental period of soil layer vibration over 12 m depth is  $4*12*(317)^{-1} = 0.15 \text{ s}$ . From the response spectra, the peak horizontal acceleration at the top  $a_{top}$  could have been about  $0.5g$ . Equation (7.6) is not applicable for  $\phi=0^\circ$  of clay in undrained condition during cyclic loading, i.e. because  $[\sin(0 - \psi)]^{1/2}$  is an imaginary number. From Equation (7.12),  $\Delta E_a = 0.65*0.5*9.81*2000*\tan(45^\circ - 0 + 9^\circ)*12^2/2*0.001 = 333 \text{ kN/m}^2$  for  $\psi = \arctan(0.65*0.5) = 18^\circ$ . For  $E_{as} = 0.5*20*12^2 - 2*40*12 = 480 \text{ kN/m}$  for assumed  $c_u = 40 \text{ kPa}$ , the total  $E_a = 333 + 480 = 813 \text{ kN/m}$ . The sum of horizontal axial stresses acting on the wall along a depth of 12 m based on the results of a two dimensional finite element model by Gazetas et al. (2005) is 539 kN/m, which is in a good agreement with the result of pseudo static analysis.

### 8.5.2 Anchored Wall at Kerameikos Station in Greece

The 23 m deep excavation was stabilised using 0.8 m diameter piles spaced at 1.8 m and 15 cm thick shotcrete (sprayed concrete), Fig. 8.7. Each pile was tied back by 5–7 anchors 12–24 m long with application of pre-stressed loading varying from 480 to 800 kN according to Gazetas et al. (2005). During excavation and anchoring, a substantial horizontal outward displacement of up to 9 cm of the wall was recorded. The retaining structure had not been designed against earthquake as it was supposed to be only temporary. No visible damage or permanent displacements of the wall was caused by the 1999 Parnitha earthquake in Greece except a few small cracks of the shotcrete, which could have existed before the earthquake (Gazetas et al., 2005).

Gazetas et al. (2005) analysed the wall behaviour during the earthquake using a two dimensional finite element model. Their model used transversal wave velocity of 135 m/s in top 7 m thick layer of alluvium sand and 280 m/s in the underlain 23 m thick soft Athenian shist. Their model considered rock outcrop peak horizontal

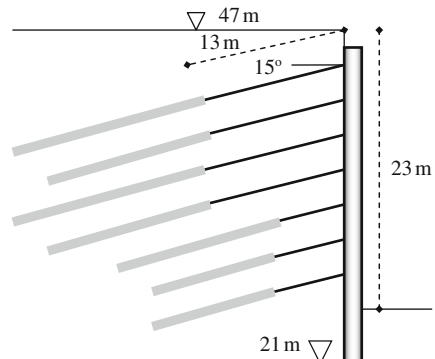


**Fig. 8.7** Sketch of a cross section through the Kerameikos station wall with pre-stressed anchors in Greece

acceleration of  $0.5g$  instead of recorded  $0.3g$  at a distance of less than 1 km. Their model provided peak horizontal acceleration at the top of the wall of  $0.56g$ . A summation of axial lateral stresses on the wall over 23 m depth in their model results in the lateral force of 426 kN/m, with the top 7 m contributing 127.5 kN/m and the bottom 3 m contributing 180 kN/m.

An averaged wave velocity over 23 m depth is  $23^*(7*(135)^{-1} + 16*(280)^{-1})^{-1} = 211$  m/s. The fundamental period of layer vibration over 23 m depth is  $4^*23^*(211) - 1 = 0.44$  s. For a peak horizontal acceleration of the acceleration record at Sepolia of  $0.36g$ , the response spectral acceleration at 0.44 s period is  $0.5g$ . For  $\psi = \arctan(0.65*0.5) = 18^\circ$  and Equation (7.6),  $K_a = 0.57$  and the lateral active soil force over depth of 7 m during the earthquake is  $E_a = 0.5^*20^*0.57^*72^*\cos 35^\circ = 229$  kN/m, which is greater than 127.5 kN/m according to Gazetas et al. (2005) model to 7 m depth. Athenian shist is weak rock with both cohesion and frictional angle so that Equation (7.6) does not apply. For assumed  $\phi = 40^\circ$  and  $c' = 100$  kPa, the lateral earth force in static condition is  $E_{as} = 0.5^*(23 - 7)^*[7^*24^*\tan^2(45^\circ - 40^\circ/2) - 2^*100^*\tan(45^\circ - 40^\circ/2)*7 + 23^*24^*\tan^2(45^\circ - 40^\circ/2) - 2^*100^*\tan(45^\circ - 40^\circ/2)]^*23 < 0$  so the cut is self supporting. From Equation (7.12),  $\Delta E_a = 0.65^*0.5^*9.81^*2000^*\tan(45^\circ - 20^\circ + 9^\circ)^*(23 - 7)^2/2^*0.001 = 29$  kN/m' for  $\psi = \arctan(0.65 * 0.5) = 18^\circ$ . The total lateral force is  $229 + 29 = 258$  kN/m according to the pseudo-static analysis, which is smaller than 426 kN/m' obtained by the finite element model. The reason for such discrepancy could be assumed ground properties.

### 8.5.3 Sheet Pile Quay Walls in Akita Port in Japan

Iai and Kameoka (1993) performed finite element analyses of earthquake induced damage of anchored sheet pile quay walls in Akita port in Japan. The damage was caused by the 1983 Nihonkai-Chubu earthquake with the magnitude  $M_J = 7.7$  that caused peak horizontal ground acceleration of  $0.24g$ .

The Ohama No. 2 wharf sheet pile wall suffered opening of a crack at about a mid height of the retained soil due to liquefaction of backfill. The horizontal displacement of the wall was about 2 m and the vertical displacement from 0.3 to 1.3 m. Ohama No. 1 wharf sheet pile wall with similar cross section as the No. 2 wall suffered no damage and no signs of liquefaction were evident at the location. A cross section through the No. 2 wall is shown in Fig. 8.8.

Liquefaction can occur during an earthquake after the peak ground acceleration has been passed. In the scenario before liquefaction, the imbalanced lateral water force in the front of the wall is calculated according to Westergaard (1931):

$$P_w = \frac{7}{12} \cdot \frac{a_h}{g} \cdot \gamma_w \cdot h^2, \quad (8.8)$$

where  $a_h$  is the horizontal acceleration,  $\gamma_w$  is unit weight of water or the liquid,  $h$  is depth of water or other liquid. In this case  $P_w = 7^*12^{-1}^*0.24^*9.8^*10^2 =$

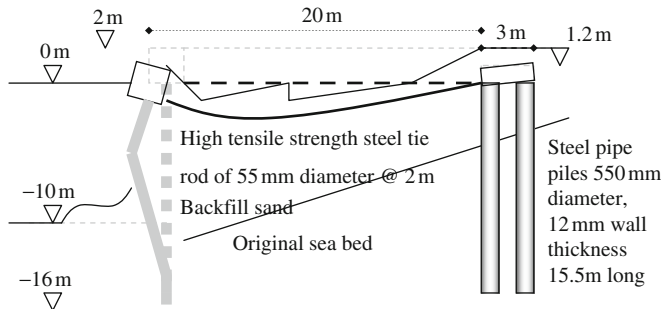


**Fig. 8.8** Sketch of a cross section through Ohama No. 2 wharf sheet pile quay wall at Akita port in Japan

137 kN/m. From Equation (7.6) and for  $\psi = \arctan(0.65*0.24) = 8.9^\circ$ ,  $\phi = 35^\circ$ ,  $\delta_b = 24^\circ$ ,  $K_a = 0.34$  and  $E_a = 0.5*20*0.34*12^2 * \cos 24^\circ = 447$  kN/m before liquefaction. The total lateral pressure is  $137+447 = 584$  kN/m before liquefaction. In post seismic condition and in the case of liquefaction, the unbalanced horizontal lateral force is about  $0.5*10*12^2 = 720$  kN/m, which is much greater than 584 kN/m before liquefaction so the wall failure most likely occurred after the earthquake due to liquefaction of backfilled sand.

## 8.6 Discussion and Conclusions

Slender retaining walls should behave very well during earthquakes due to their flexibility and ductility of the materials used for their construction. Soil liquefaction and softening behind, in front, below and around ties/anchors of the wall during and after earthquake must be avoided in order to avoid wall failures. It is difficult to compact back fill between wall ties or anchor/raking piles but the use of alternative techniques such as soil mixing or ground drains could help.

The use of pseudo static method for analyses of flexural walls in seismic condition may be adequate. The calculation of lateral soil force is performed using total soil weight although EN 1998-5 (2004) specifies that dynamically impervious soil has a coefficient of permeability of less than 0.5 mm/s and dynamically pervious soil greater than 0.5 mm/s. Soil permeability only affects build up or dissipation of excess pore water pressure because the amount of water leaving a unit volume of soil on one side is replaced by the same amount of water entering on the other side so the mass and inertial forces are not affected.

## References

- Atik LA, Sitar N (2009) Experimental and analytical study of the seismic performance of retaining structures. Pacific Earthquake Engineering Research Centre report PEER 2008/104 [http://peer.berkeley.edu/publications/peer\\_reports/reports\\_2008/reports\\_2008.html](http://peer.berkeley.edu/publications/peer_reports/reports_2008/reports_2008.html)
- BS 5228-2 (2009) Code of practice for noise and vibration control on construction and open sites – part 2: vibration. British Standards Institution
- Burland JB, Potts DM, Walsh NM (1981) The overall stability of free and propped embedded cantilever retaining wall. *Ground Eng ICE* 7:23–38
- Chang CY, Power MS, Mok CM, Tang YK, Tang HT (1990) Analysis of dynamic lateral earth pressures recorded on Lotung reactor containment model structure. In: Proceedings of the 4th U.S. national conference on earthquake engineering, Palm Springs, CA
- EN 1998-5 (2004) Eurocode 8 – design of structures for earthquake resistance, part 5: foundations, retaining structures and geotechnical aspects. European Committee for Standardization, Brussels
- Gazetas G, Psarropoulos PN, Anastasopoulos I, Gerolymos N (2004) Seismic behaviour of flexible retaining systems subjected to short-duration moderately strong excitation. *Soil Dyn Earthquake Eng* 24: 537–550
- Gazetas G, Gerolymos N, Anastasopoulos I (2005) Response of three Athens metro underground structures in the 1999 Parnitha earthquake. *Soil Dyn Earthquake Eng* 25:617–633
- Green RA, Olgun CG, Ebeling RM, Cameron WI (2003) Seismically induced lateral earth pressures on a cantilever retaining wall. In: Beavers J (ed) Proceedings of the 6th US conference and workshop on lifeline earthquake engineering. TCLEE Monograph No. 25. ASCE, Long Beach, CA, pp 946–955
- Iai S, Kameoka T (1993) Finite element analysis of earthquake induced damage of anchored sheet pile quay walls. *Soils Foundations* 33(1):71–91
- Lew M, Simantob E, Hudson ME (1995) Performance of shored earth retaining systems during the January 17, 1994, Northridge earthquake. In: Proceedings of the 3rd international conference on recent advances in geotechnical earthquake engineering and soil dynamics, St. Louis, MO, p 3
- Siddharthan R, Maragakis EM (1989) Performance of flexible retaining walls supporting dry cohesionless soils under cyclic loads. *Int J Numer Anal Methods Geomech* 13: 309–326
- Veletos AS, Younan AH (1997) Dynamic response of cantilever retaining walls. *J Geotechn Geoenviron Eng* 123(2):161–172
- Westergaard H (1931) Water pressure on dams during earthquakes. *Trans ASCE* 1835:418–433

# Chapter 9

## Shallow Foundations

### 9.1 Introduction

Shallow foundations transfer loads from structures into soil via the foundation undersides mainly and could be of pad, strip and raft shape. They are used when ground is firm or when loads are relatively small. The factors of safety for shallow foundations in static condition are usually high so that their performance in cyclic condition is usually satisfactory except in liquefiable and soft/loose soil in which case the build up of excess pore water pressure and reduction of soil strength to a small residual value could cause foundation failure and loss of serviceability as described in Section 9.5. Modern shallow foundations are made of (reinforced) concrete although older types were made of brick work or stone masonry, Fig. 9.1.

The aim of this chapter is to describe basic mechanism of behaviour and factors affecting such behaviour in cyclic condition, to provide a brief overview of existing methods for foundation analysis in cyclic condition, to present simplified analyses and to indicate their accuracy and applicability for a number of case histories. The emphasis is on the use of simple analyses for the case histories considered.

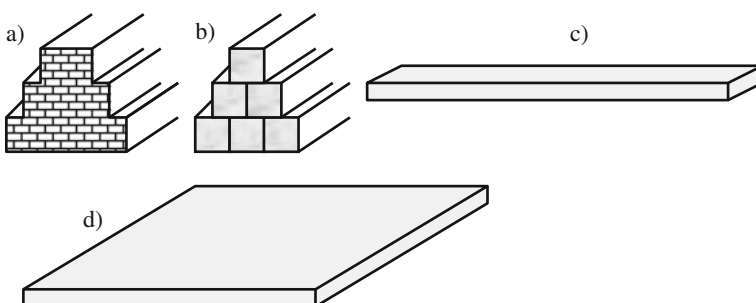


**Fig. 9.1** Sketches of shallow foundation types (a) cross section through a brick work strip foundation, (b) cross section through a stone masonry strip foundation, (c) three dimensional view of a reinforced concrete strip, (d) three dimensional view of a reinforced concrete raft (mat)

## 9.2 Mechanism and Factors

Main factors affecting foundation behaviour are:

- Applied load
- Foundation dimensions and type
- Soil properties
- Level of water
- Degree of compaction
- Structural versus soil stiffness, effect on load spreading among pads
- Possibilities of soil-structure interaction

Main mechanisms of behaviour are shown in [Fig. 7.2a–c](#) for massive retaining walls.

### ***9.2.1 Bearing Capacity of Soil Under Foundation***

The consideration is the same as described in [Section 7.2.1](#).

### ***9.2.2 Stability Against Sliding***

The consideration is the same as described in [Section 7.2.2](#).

### ***9.2.3 Stability Against Overturning***

The consideration is the same as described in [Section 7.2.3](#).

### ***9.2.4 Settlement During and After Earthquake***

The consideration is different from the case of static load. More details are given in Sections [9.3.1](#) and [9.4.3](#).

## 9.3 Existing Methods

### ***9.3.1 Empirical Using Formulas and Charts***

Classical pseudo static methods for the calculations of bearing capacity, sliding and overturning resistances are described in [Section 7.2](#).

Tokimatsu and Seed (1987) proposed a chart for estimation of volumetric strain after liquefaction of saturated sand in a magnitude 7.5 earthquake from the cyclic stress ratio and normalized standard penetration resistance ( $N_1$ )<sub>60</sub>. Large volumetric strain variation of 10 times is shown for the variation of ( $N_1$ )<sub>60</sub> from zero to 10 and 100 times for the variation of ( $N_1$ )<sub>60</sub> from zero to 20. Foundation settlement is obtained by summation of volumetric strain along depth of interest.

Ishihara and Yoshimine (1992) proposed a chart for estimating post liquefaction volumetric strain of sand without fines as a function of factor of safety against liquefaction or maximum shear strain. Large variations of the volumetric strain between 20 and 55% are predicted for the factor of safety against liquefaction of just less than one and the relative density of 30% (i.e. SPT's  $N$  of 3). Consequently, the accuracy of predicted additional foundation settlement may not be great.

Sarma and Chen (1995) considered seismic bearing capacity of shallow strip footings near sloping ground using the limit equilibrium method with composite sliding surfaces formed of linear and log-spiral parts. Sarma and Chen (1997) used the same method for deeper strip foundations.

### 9.3.2 Numerical Using Computers

Idriss et al. (1980) described finite element analyses for consideration of soil-structure interaction effects for nuclear power plants. Consideration of soil-structure interaction is also required for structures with massive or deep seated foundations, such as bridge piers, offshore caissons, and silos according to EN1998-5 (2004).

Gazetas et al. (2007) considered nonlinear response of shallow foundations under buildings to strong seismic excitation using elastic plastic constitutive soil model with the Mohr-Coulomb failure criterion and isotropic strain softening encoded in the ABAQUS finite element package. Foundation uplifting and soil plastic yielding are still not accepted concepts in engineering codes except in FEMA 356.

Templeton (2008) described finite element three dimensional analyses in seismic condition of the mat under Maleo Producer jackup on soft clay offshore. Jackups are mobile offshore oil platforms for shallow to medium depth water but are usually supported on spudcans instead of mats. The design earthquake loading was responsible for the need to perform complex numerical analyses in this case.

### 9.3.3 Experimental on Small Scale Models and Prototypes

Kishida et al. (1969) described the results of forced vibration tests and the observations of behaviour during earthquakes for different types of structures conducted to study soil structure interaction problems. Among other structures, an elevator tower in Mito city comprises 81 m high reinforced concrete structure with 22 storeys and 6.5 m deep reinforced concrete mat foundation 21 m wide and long. The foundation rests on a 10 m thick layer of dense gravel with clay over rock. Kishida et al. (1969) stated based on the results of forced vibration tests that damping ratios of

the foundation were 0.65% for the first (fundamental) period and 1.9% for the second vibration period. For recorded peak horizontal ground of about  $0.045g$  during an earthquake, the peak horizontal foundation acceleration was roughly 50% of the ground acceleration most likely because of kinematic interaction (ground wave filtering by the foundation with large stiffness) and inertial interaction (changing of vibration periods of ground motion by the massive structure).

Tajimi (1984) described the results of measurements and analyses of the fundamental periods of vibration of the foundation of a large scale shaking table. The foundation is 44.8 m wide and 90.9 m long in plan with varying depth from 21 m at the centre to 13 m at the edge, Fig. 9.2. The Fourier amplitude spectra of measured free vibration of the foundation exhibit the peak value at about 0.8 Hz in the longitudinal direction and 2.0 Hz in rocking. Ground profile at the location of the foundation contains gravel and sand to a depth of 48 m, silty clay to a depth of 78 m, sand and silt to a depth of 117 m, gravel to a depth of 181 m and weathered granite at greater depths. Distribution of transversal wave velocity with depth is given in Table 9.1.

For a depth approximately equal to the foundation length, the averaged transversal wave velocity is  $v_t = 117*(8*160^{-1} + 5*200^{-1} + 8*320^{-1} + 27*360^{-1} + 30*400^{-1} + 39*520^{-1})^{-1} = 360 \text{ m/s}$ . The fundamental period of horizontal vibrations of the layers is  $T = 4*117*360^{-1} = 1.3 \text{ s}$  and the frequency  $f = 1.3^{-1} = 0.77 \text{ Hz}$ , which is approximately equal to the measured free vibration of the foundation in longitudinal direction. Therefore, the zone of influence equalled approximately the foundation length in the direction of the foundation vibration.

Novak (1985) reviewed the results of field experiments conducted on vibrating foundations under harmonic excitation. He concluded that “*The agreement between the theory and experiments was found to be, on the whole, quite encouraging but some aspects of the theories available have to be refined. Vertical response amplitudes tend to be overestimated by theory which may be attributed primarily to redistribution of stresses in soil and its layering. Torsional response is predicted poorly; incorporation of slippage is needed. Embedment effects can be*

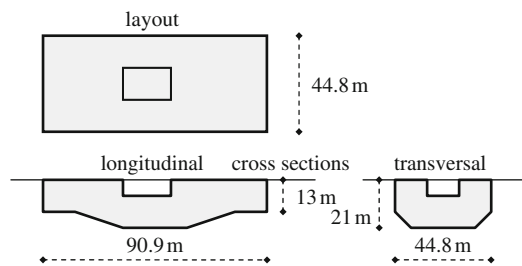


**Fig. 9.2** Schematic layout and cross sections of the foundation of a shaking table in Japan

**Table 9.1** Transversal wave velocity versus depth (from Tajimi, 1984)

Depth (m)	0–8	8–13	13–21	21–48	48–78	78–117	117–181	> 117
$v_t$ (m/s)	160	200	320	360	400	520	640	1160

*overestimated unless allowance is made for reducing of soil shear modulus towards ground surface and separation of footing sides from the soil."*

Yamagami and Hangai (1988) recorded and reported on behaviour of an embedded reinforced concrete tower at Chiba Experimental Station belonging to the Institute of Industrial Sciences, University of Tokyo. The tower is a 12.5 m long building comprising basement, ground floor and three floors above. The floor plan is hexagonal with 3 m side length and 5 m perpendicular distance between the sides. The foundation is located in a 5 m thick fill with transversal wave velocity of 140 m/s. The wave velocity of a 20 m thick soil layer below 5 m depth from the ground surface is 320 m/s. Thirteen three componential accelerometers are mounted in the tower and two at 1 and 40 m depth in the ground outside the tower. Soil pressure gauges are set on the side walls and floor slab of the basement. Yamagami and Hangai's (1988) findings refer to the 1987 earthquake with a magnitude 6.7 at an epicentral distance of 46 km (a focal depth of 58 km). The results of Yamagami and Hangai's (1988) indicate geometrical non-linear phenomenon caused by the separation of the structure from the ground and also the material non-linear behaviour at the peak horizontal ground accelerations of about 0.4g.

## 9.4 Simple Models and Assumptions

### 9.4.1 Earthquake Affected

If a dynamic analysis of shallow foundations of buildings and bridges is undertaken during an earthquake then the model shown in Fig. 9.3 can be used. It is not difficult to add horizontal force acting on the model of a gravity retaining wall from lateral earth pressures during an earthquake, for example.

From the second Newton's law of motion, the horizontal and rotational dynamic equilibrium equations in the centre of gravity of a rigid structure and its foundation are:

$$\begin{aligned} m \cdot \ddot{u} + m \cdot h \cdot \ddot{\theta} + P = 0 \\ (I + \Delta M_{\theta}) \cdot \ddot{\theta} + M - h \cdot P = 0 \end{aligned}, \quad (9.1)$$

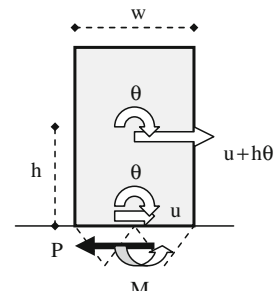


**Fig. 9.3** Discrete element model of a structure on its shallow foundation

where  $m$  is the mass of structure and its foundation,  $u$  is ground horizontal displacement i.e. its acceleration  $\ddot{u}$ ,  $h$  is the height of the centre of the mass,  $\theta$  is the rotation of the structure and its foundation,  $\ddot{\theta}$  is the rotational acceleration,  $P$  is the horizontal interaction force between soil and foundation,  $I$  is the polar moment of mass inertia around the centroid,  $\Delta M_\theta = 0.3\pi(v - 3^{-1})\rho r^5$  is the second moment of inertia of trapped mass of soil beneath the foundation in rotation when the Poisson's ratio  $v > 1/3$  according to Wolf (1994),  $r$  is the equivalent radius of foundation  $= (4J/\pi)^{1/4}$ ,  $J$  is the second moment of area of a foundation,  $M$  is the base reaction moment. Wolf (1994) considered this model for the analysis in time domain of earthquake caused motion using an explicit algorithm with a predictor-corrector scheme. He postulated that "*This rather simple discrete-element model with casual frictional element may well yield a better approximation of reality than a complicated 'rigorous' analysis by the boundary element method with non-casual linear-hysteretic damping or with some other sophisticated description of material damping*". Eliminating the force  $P$  from the above equations leads to the equation

$$\ddot{\theta} + \frac{M}{I_o} = -\frac{m \cdot h}{I_o} \cdot \ddot{u}, \quad (9.2)$$

where  $I_o = I + \Delta M_\theta + mh^2 = m^{*}12^{-1*}(w^2 + 16h^2) + \Delta M_\theta$ ,  $w$  and  $h$  are shown in Fig. 9.3. When properties of equivalent rotational spring and dashpot are used,  $M = K_\theta\theta + C_\theta\dot{\theta}$ ,  $K_\theta = 3\rho v^2 J/z$ ,  $z = r^2 \pi / 32(1-v)(v/v_t)^2$ ,  $C_\theta = \rho v J$ ,  $v = v_1$  for  $v < 1/3$  and  $v = 2v_t$  for  $1/3 < v < 1/2$  according to Wolf (1994), where  $v_l$  and  $v_t$  are the longitudinal and transversal wave velocities respectively. An irregular ground motion caused by earthquakes can be represented as an equivalent harmonic motion  $\ddot{u} = 0.65a_p \sin(2\pi ft)$ ,  $a_p$  is the peak horizontal ground acceleration defined in the National Annexes to EN 1998-1 (2004) for example,  $f = T^{-1}$ ,  $T$  is the period of the motion that corresponds to the peak in the acceleration response spectra (defined in EN 1998-1 (2004) for example). The use of EN 1998-1 (2004) is not obligatory in the U.K. except for structures with high consequences of failure and seismically unfavourable soil. When the values of  $M$  and  $\ddot{u}$  are replaced in the above equation it becomes an ordinary non homogeneous differential equation of the second order with constant coefficients:

$$\ddot{\theta} + \frac{C_\theta}{I_o} \cdot \dot{\theta} + \frac{K_\theta}{I_o} \cdot \theta = -\frac{m \cdot h \cdot 0.65 \cdot a_p}{I_o} \cdot \sin(\omega_o \cdot t), \quad (9.3)$$

which has a closed form solution (e.g. Giek and Giek, 1997) for under damped case ( $a < b$ ):

$$\theta = e^{-a \cdot t} \cdot [C_1 \cdot \sin(\omega \cdot t) + C_2 \cdot \cos(\omega \cdot t)] - \frac{A_o}{\sqrt{(b^2 - \omega_o^2)^2 + 4 \cdot a^2 \cdot \omega_o^2}} \cdot \sin \left( \omega_o \cdot t - \text{arc cot} \frac{b^2 - \omega_o^2}{2 \cdot a \cdot \omega_o} \right),$$

$$a = \frac{C_\theta}{2 \cdot I_o}, \quad b = \sqrt{\frac{K_\theta}{I_o}}, \quad \omega = \sqrt{b^2 - a^2}, \quad A_o = \frac{m \cdot h \cdot 0.65 \cdot a_p}{I_o}, \quad \omega_o = \frac{2 \cdot \pi}{T} \quad (9.4)$$

where  $T$  is the predominant period of base vibration caused by an earthquake.

When the initial conditions at  $t = 0$  are  $\theta = \dot{\theta} = 0$ ,

$$C_2 = \frac{-A_o}{\sqrt{(b^2 - \omega_o^2)^2 + 4 \cdot a^2 \cdot \omega_o^2}} \cdot \sin \left( \text{arc cot} \frac{b^2 - \omega_o^2}{2 \cdot a \cdot \omega_o} \right) \quad (9.5)$$

$$C_1 = \frac{a}{\omega} \cdot C_2 + \frac{A_o \cdot \omega_o / \omega}{\sqrt{(b^2 - \omega_o^2)^2 + 4 \cdot a^2 \cdot \omega_o^2}} \cos \left( \text{arc cot} \frac{b^2 - \omega_o^2}{2 \cdot a \cdot \omega_o} \right)$$

If force  $P$  exceeds the sliding resistance of soil under a foundation then permanent slip occurs. The amount of permanent slip can be calculated using the Newmark (1965) sliding block method. The method essentially consists of double integration in time of the difference between ground and the critical acceleration, which corresponds to the maximum shear resistance of soil to sliding, Fig. 5.1.

The permanent rotation of a shallow foundation and the structure it supports can be determined with analogy to the sliding block method. A rotating block model is shown in Fig. 9.4.

Critical horizontal acceleration at the onset of model rotation can be estimated from the following equations:

$$S_a \cdot \left( m \cdot h + \frac{I}{h} \right) = c_u \cdot \left( \frac{w}{2} \right)^2 \cdot \pi \cdot 1 \text{m in cohesive soil} \quad (9.6)$$

$$S_a \cdot \left( m \cdot h + \frac{I}{h} \right) = \sigma_v' \cdot \tan \phi \cdot \frac{\pi}{2} \cdot \frac{w}{2} \cdot 1 \text{m}^2 \text{ in purely frictional soil}$$

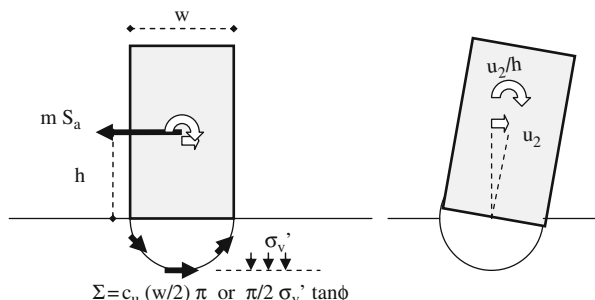


**Fig. 9.4** Rotating block model

where  $S_a$  is the horizontal structural acceleration,  $m$  is structural mass,  $h$  and  $w$  are the mass eccentricity (assumed at a half of the height) and width of building respectively,  $I$  is the polar moment of mass inertia around the centroid =  $12^{-1}m^*(w^2 + 4h^2)$ ,  $c_u$  is undrained shear strength of fine grained soil (clay and fine silt),  $\sigma_v'$  is the vertical effective stress at depth  $0.5w$  in purely frictional soil (coarse silt, sand, gravel),  $\pi/2$  is multiplying coefficient for assumed linear distribution between zero and  $\sigma_v'$  at a depth  $0.5w$ . When the structural acceleration  $S_a = a_g^*C$  then the ratio  $k_c$  between the critical horizontal ground acceleration  $a_g$  at which the factor of safety of foundation stability is 1 and the gravitational acceleration  $g$ :

$$k_c = \frac{c_u \cdot \left(\frac{w}{2}\right)^2 \cdot \pi \cdot 1m}{C \cdot g \cdot \left(m \cdot h + \frac{I}{h}\right)} \text{ in cohesive soil}, \quad (9.7)$$

$$k_c = \frac{\sigma_v' \cdot \tan \phi \cdot \frac{\pi}{2} \cdot \frac{w}{2} \cdot 1m^2}{C \cdot g \cdot \left(m \cdot h + \frac{I}{h}\right)} \text{ in purely frictional soil}$$

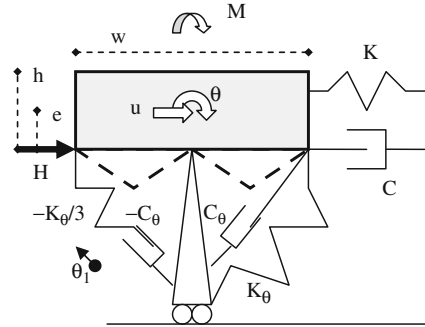
where the multiplying constant  $C$  of the horizontal ground acceleration  $a_g$  is obtained from design acceleration response spectrum (e.g. EN 1998-1, 2004) for the structural period of vibration equal to an inverted pendulum period of vibration. [Equation \(1.5\)](#) or [Fig. 1.4](#) can be used for estimation of permanent displacement  $u_2$  and subsequently permanent rotation  $u_2^*h^{-1}$  in radians.

Foundation stiffness and structural mass may cause so called kinematic and inertial interaction effects. Kinematic interaction between a shallow foundation and soil results in filtering of high frequency ground motion by stiff foundation according to the formula  $a_t = T^{-1}(v_t - v_{t-T_s})$  (e.g. Srbulov 2008, 2010), where  $a_t$  is foundation acceleration,  $T_s$  is the time necessary for a near surface seismic wave to pass along a foundation,  $v_t$  and  $v_{t-T_s}$  are the ground velocities at times  $t$  and  $t-T_s$ . The formula is applicable not only for near surface waves but also body waves because ground heterogeneity causes phase shift even in vertically propagating waves. The inertial interaction affects the period of foundation vibration in rocking as described in the section for deep foundation.

#### 9.4.2 Machinery Affected

Manufacturers specify what is allowable maximum amplitude of displacement or velocity and frequency range of vibration of a foundation under machinery (e.g. of rotating machinery such as compressors, turbines, pumps, fans). CP 2012-1 (1974) exists for foundations for reciprocating machinery, which generates biharmonic loads (e.g. steam engines, internal combustion engines, piston-type compressors

**Fig. 9.5** Discrete element model for coupled horizontal and rocking motion of a machine foundation



and pumps), with normal rotational frequency range from 5 to 25 Hz and when it is placed on a rigid block. Wolf (1994) considered a discrete element model of machine foundation in coupled horizontal and rocking motion, Fig. 9.5. It is not difficult to add a horizontal force varying in time from wave impact load on caisson breakwaters, for example.

Wolf (1994) introduced the physical discrete element model with an additional internal rotational degree of freedom  $\theta_1$  as an alternative to the recursive evaluation of the convolution integral. The model incorporates rigorously the convolution implicitly. The two rotational and one translational equation of motion require a predictor-corrector procedure for their solution. The analyses of motions of the caisson quay wall in Kobe port during the 1995 Hyogoken-Nanbu earthquake and Kalamata port block quay wall during the 1986 earthquake in Peloponnesus are performed by Srbulov (2008) using an Excel work sheet for the predictor-corrector procedure, for example.

Wolf (1994) formulated the rocking and horizontal equations of motions for harmonic rotational loading of circular frequency  $\omega$  as:

$$\begin{aligned} & [-\omega^2 \cdot (I + \Delta M_\theta) + S_\theta] \cdot \theta - S_\omega \cdot e \cdot u = M_\omega \\ & -\omega^2 \cdot m \cdot e \cdot \theta + [-\omega^2 \cdot m + S_\omega] \cdot u = H_\omega \end{aligned}, \quad (9.8)$$

where  $m$  is the mass of foundation,  $e$  is the eccentricity of  $m$  with respect to the underside,  $I = m/12(h^2 + w^2)$ ,  $\Delta M_\theta = 0.3\pi(v - 1/3)\rho r^5$  when  $1/3 < v \leq 1/2$  otherwise  $\Delta M_\theta = 0$ ,  $v$  is Poisson's ratio of soil,  $\rho$  is soil unit density,  $r$  is the equivalent radius of foundation  $= (4J/\pi)^{1/4}$ ,  $J$  is the second moment of area of a foundation,  $S_\omega = K_o^*(k_o + i^*b_o)$ ,  $K_o = r_o^*v_t^*A^*z_o^{-1}$ ,  $r_o = (A^*\pi^{-1})^{1/2}$ ,  $A$  is the foundation area,  $v_t$  is transversal wave velocity,  $z_o = r_o^*\pi^*8^{-1}(2 - v)$ ,  $b_o = \omega^*z^*v_t^{-1}$ ,  $k_o = 1 - \mu_o^*\pi^{-1}r_o^*z_o^{-1}b_o^2$ ,  $\mu_o = 2.4^*\pi^*(v - 3^{-1})$  for  $v > 1/3$  otherwise  $\mu_o = 0$ ,  $S_\theta = K_\theta^*(k_\theta + i^*b^*c_\theta)$ ,  $K_\theta = 3^*\rho^*v^2*\pi r^4 z^{-1}$ ,  $v = v_t$  for  $v \leq 1/3$  and  $v = 2^*v_t$  for  $1/3 < v \leq 1/2$ ,  $z = 9^*r^*\pi^*32^{-1}(1 - v)^*(v^*v_t^{-1})^2$ ,  $k_\theta = 1 - 4^*\mu^*3^{-1}\pi^{-1}r^*z^{-1}b_o^2 - 3^{-1}b_o^2(1 + b_o^2)^{-1}$ ,  $\mu = 0.3^*\pi^*(v - 3^{-1})$  for  $v > 1/3$  otherwise  $\mu = 0$ ,  $c_\theta = 3^{-1}b_o^2(1 + b_o^2)^{-1}$ . The solution of the above two linear equations of motions provides the values of  $u$  and  $\theta$  at any time depending on  $M_\omega$  and  $H_\omega$ .

When amplitudes and/or frequency of foundation vibration do not satisfy criteria set by the manufacturers of vibrating equipment then piled or base isolated or both foundations can be used. The base isolation is achieved by incorporation of elastomeric or lead rubber bearings or sliding friction pendulum under the foundation, by metallic, friction, viscoelastic, viscous fluid, tuned mass and liquid dampers in combination with base isolators or on their own. Detailed analytical and numerical analyses of motions of base isolated shallow foundations are provided by Srbulov (2010), for example.

### 9.4.3 Settlement Caused by Soil Vibration

Loose to medium dense coarse grained soil decreases its volume (becomes compact) when undergoes vibration due to its particles movement into the voids surrounding soil grains. Degree of soil compaction can be described by its relative density  $D_r$ , which is calculated using the formula (e.g. Das, 1985):

$$D_r = \frac{\gamma_{d(\max)}}{\gamma_d} \cdot \frac{\gamma_d - \gamma_{d(\min)}}{\gamma_{d(\max)} - \gamma_{d(\min)}}, \quad (9.9)$$

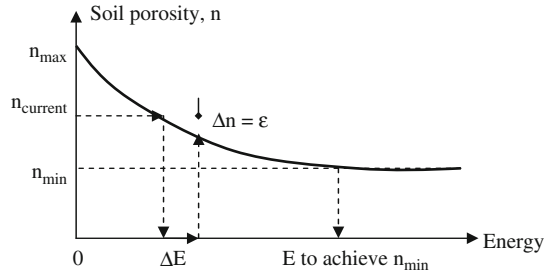
where maximum, minimum and natural soil dry density  $\gamma_d$  of coarse grained soil can be determined using, for example, ASTM D4914, D1556, D4253, D4254, BS 1377-2, BS 1377-4. Relative density can also be estimated from the results of field tests. For the standard penetration test blow count  $N_{SPT}$ , Terzaghi and Peck (1948), for example, suggested the classification shown in Fig. 4.1.

Lunne et al. (2001) provide graphs for estimation of relative density based on cone penetration tests. Relative density can be expressed as well in terms of void ratio  $e$ , i.e. the ratio between volume of voids and volume of solids within soil.

$$\begin{aligned} D_r &= \frac{e_{\max} - e}{e_{\max} - e_{\min}}, \\ e_{\min} &= \frac{G_s \cdot \gamma_w}{\gamma_{d(\max)}} - 1, \\ e_{\max} &= \frac{G_s \cdot \gamma_w}{\gamma_{d(\min)}} - 1 \end{aligned} \quad (9.10)$$

where  $G_s$  is the specific gravity of soil solids ( $\sim 2.65$ ) and  $\gamma_w$  is the unit weight of water  $9.81 \text{ kN/m}^3$ . Void ratio  $e$  is related to soil porosity  $n$  as  $e = n(1-n)^{-1}$ , or in turn  $n = e(1+e)^{-1}$ . Soil porosity  $n$  is defined as the ratio of the volume of voids (filled with air and water) to the total volume of soil. Decrease in soil porosity  $\Delta n$  is caused by decrease of voids in soil and is equal to the volumetric deformation  $\varepsilon_v$  of soil. For a unit area of soil,  $\varepsilon_v$  equals to the vertical strain  $\varepsilon$ , which when integrated along depth of interest equals to soil settlement. Ground vibration causes transmission of wave energy through soil under a foundation. The increase in energy  $\Delta E$  of soil at a depth beneath foundation can be calculated as a product of acting

**Fig. 9.6** Soil porosity versus compaction energy



total axial vertical stress times the active area under a foundation times the wave amplitude times the number of cycles. From a graph between soil porosity and the energy applied to achieve such porosity and calculated  $\Delta E$ , Fig. 9.6, it is possible to define  $\Delta n = \varepsilon$  and from it to calculate soil settlement caused by ground vibration as an integral of  $\varepsilon$  over depth of interest.

Acting axial vertical stress at a depth is a sum of the total overburden pressure caused by soil weight above that depth and the additional total vertical stress due to foundation load. The additional vertical stress  $\Delta\sigma_{v,z}$  at a depth  $z$  due to foundation load can be calculated either using Boussinesq (1885) formula or from a truncated cone. According to Boussinesq (1885):

$$\Delta\sigma_{v,z} = \frac{3 \cdot V \cdot z^3}{2 \cdot r^5} \quad (9.11)$$

$$r = \sqrt{z^2 + d_h^2}$$

where  $V$  is vertical force acting at the foundation underside,  $d_h$  is the horizontal distance between the location where the load  $V$  is acting and the location where the stress is calculated. A truncated cone (e.g. Wolf, 1994) is shown in Fig. 9.7.

According to Wolf (1994),

$$\frac{z_o}{r_o} = \frac{\pi}{4} \cdot (1 - \nu) \cdot \left( \frac{\nu}{\nu_f} \right)^2, \quad (9.12)$$

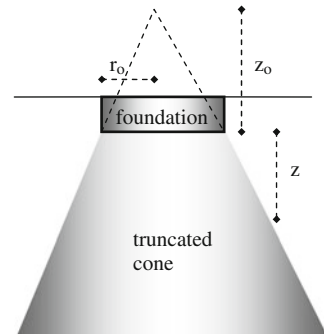


**Fig. 9.7** Truncated cone model

where  $\nu$  is Poisson's ratio,  $v$  is wave velocity, which is equal to the velocity of longitudinal waves  $v_l$  when  $\nu \leq 1/3$  and  $v = 2v_t$  when  $1/3 < \nu < 1/2$ , where  $v_t$  is transversal wave velocity. From the geometry of Fig. 9.7 it follows that

$$\begin{aligned} r &= r_o \cdot \left(1 + \frac{z}{z_o}\right) \\ \Delta\sigma_{v,z} &= \Delta\sigma_{v,z_o} \cdot \left(\frac{r_o}{r}\right)^2, \end{aligned} \quad (9.13)$$

where  $r_o$  is the radius of an equivalent disk,  $r_o = (A_f \pi^{-1})^{1/2}$ ,  $A_f$  is actual foundation area.

#### 9.4.3.1 Industrial Sources of Ground Vibration

Ground wave amplitude at the ground surface is calculated according to Equation (12.5) or (12.6) and estimated at a depth  $z$  from Fig. 9.8 for Rayleigh waves in the free field. For body waves, Equation (12.16) will provide wave velocity amplitude, from which the wave displacement amplitude can be calculated by dividing the velocity by  $2\pi f$ , where  $f$  is the frequency of vibration. The number of wave cycles depends on the number of cycles of a vibration source.

#### 9.4.3.2 Earthquakes

Attenuation relationships for the horizontal ground displacements are rarer than for the ground acceleration and for vertical ground displacements are even rarer. EN 1998-1 (2004) allows that design ground displacement is calculated from the formula:

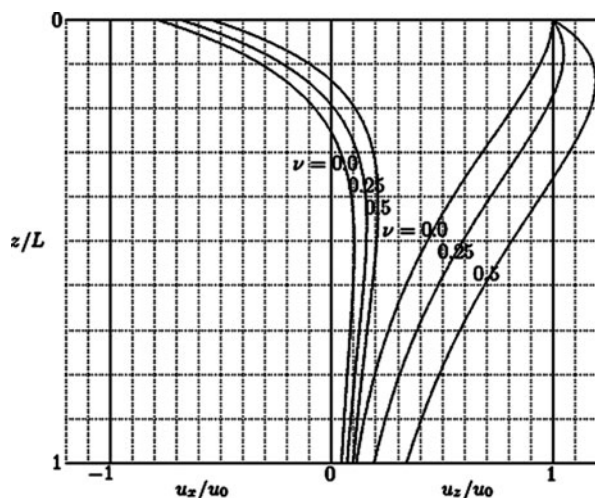


**Fig. 9.8** Rayleigh wave amplitude ratio change in the horizontal ( $u_x/u_0$ ) and the vertical direction ( $u_z/u_0$ ) with respect to the amplitude at the surface ( $u_0$ ) and the ratio  $z/L$  between depth ( $z$ ) and the wave length ( $L$ ) (Verruijt, 1994)

$$d_g = 0.025 \cdot a_g \cdot S \cdot T_C \cdot T_D, \quad (9.14)$$

where  $a_g$  is the design horizontal ground acceleration on type A ground (rock); for the vertical direction EN 1998-1 (2004) specifies that the vertical component is 0.9 of the horizontal component for earthquake surface wave magnitudes  $M_s \geq 5.5$  and 0.45 for  $M_s < 5.5$ ,  $S$  is ground type factor varying from 1 on rock to 1.4 on soil type E (surface alluvium layer with thickness varying between 5 and 20 m, underlain by stiffer material with  $v_t > 800$  m/s),  $T_C = 0.15$  s and  $T_D = 1$  s according to EN 1998-1 (2004) for vertical elastic response spectra.

Seed et al. (1975) developed the concept of an equivalent number of significant stress cycles to represent an irregular time history of shear stresses (caused by the horizontal ground accelerations) by a uniform series of harmonic stress cycles. The equivalent number of uniform stress cycles  $N_{eqv}$  was selected to cause pore pressure build-up equivalent to that of an actual shear stress time history at harmonic stress amplitude of 65% of the maximum actual shear stress (caused by the peak horizontal ground acceleration). Seed et al. (1975) data can be represented by a simple formula.

$$N_{eqv} = 0.0008 \cdot M_L^{4.88}, \quad (9.15)$$

where  $M_L$  is local earthquake magnitude.

Green and Terri (2005) examined the implications of using a high cycle fatigue hypothesis to compute the number of equivalent cycles for evaluating liquefaction by Seed et al. (1975) based on Palmgren – Miner cumulative damage hypothesis developed for metal fatigue evaluations in the elastic range of material behaviour. The results of a parametric study using a procedure that equates energy dissipated in soil subjected to earthquake motions show that the number of equivalent cycles varies as a function of earthquake magnitude, site-to-source distance and depth below ground level.

Hancock and Bommer (2004) reviewed, classified and compared various definitions of the effective number of cycle's concept. They found that measurement and hence predictions are particularly different for accelerograms with broad banded frequency content, which contain a significant number of non-zero crossing peaks. While the number of effective cycles depend on earthquake magnitude, its dependence on fault distance is small, approximately one cycle in 30 km. Fault rupture directivity effect has an important influence on the number of cycles in near-field ground motions. Based on data by Hancock and Bommer (2004), the number of effective acceleration cycles  $N_{cycles}$  can be expressed as:

$$N_{cycles} = 3 + \frac{7}{4} \cdot (M_W - 4) \pm (M_W - 3), \quad M_W > 4, \quad (9.16)$$

where  $M_W$  is earthquake moment magnitude. Sarma and Srbulov (1998) obtained similar results to Hancock and Bommer (2004). The number of equivalent cycles in Equation (9.15) represents the upper bound values.

## 9.5 Case Histories

The simple analyses are used for two cases of bearing failures of soil under foundations, the foundation vibration under machinery, the building settlement due to driving of adjacent piles and the settlement of a quay wall caused by an earthquake in order to demonstrate the applicability and accuracy of the analyses.

### 9.5.1 Kawagishi-cho Apartment Building Foundation Failure in Japan

Ishihara and Koga (1981) reported that the eight four story apartment buildings with approximate dimensions of 30 m by 8 m in the layout, which are constructed on reclaimed land, experienced severe settlement and various degrees of tilting of up to  $80^\circ$  from the vertical (Fig. 9.9) during the 1964 Niigata (Japan) earthquake with the magnitude  $M_w=7.5$ . The earthquake caused the peak surface acceleration of  $0.16g$  near the site. Ishihara and Koga (1981) noted that all the buildings tilted toward the sides of the buildings where the water tanks were placed on the roofs. The tilting of the buildings on shallow foundations occurred because of reduced shear strength of liquefied sand during the earthquake. Ishihara and Koga (1981) reported that the standard penetration test blow counts was about 4 and the cone penetration resistance less than 3 MPa at a depth range from about 2 to 4.5 m, in very loose sand of rather uniform gradation.

From Fig. 4.2, for SPT blow count of 4 and  $M_w = 7.5$ ,  $\phi = 3^\circ$  in cyclic condition. The equivalent width  $B' = 8.0 - 2*0.16*0.65*W*7.0/W \sim 6.5$  m for assumed height of the mass centroid at 7 m above the foundation level and the effective horizontal acceleration of  $0.65*0.16g$ . From Table 7.1, Hansen's (1970) factors for



**Fig. 9.9** Kawagishi-cho apartment buildings tilt in Japan (adapted from [www.ce.washington.edu/.../niigata/niigata.html](http://www.ce.washington.edu/.../niigata/niigata.html))

$c' = 0$  are:  $N_q = 1.3$ ,  $N_y = 0.02$ ,  $s_q = 1.0$ ,  $s_y = 0.9$ ,  $i_q = 0.76$ ,  $i_g = 0.68$ ,  $d_q = d_y = 1$ , the angle of an apparent increase of the ground surface inclination to the horizontal due to action of inertial force is  $\beta = \arctan(0.65*0.06) = 5.9^\circ$ ,  $g_q = (1 - 0.5 * \tan 5.9^\circ)^5 = 0.77 = g_y$ . From [Equation \(7.1\)](#) and for assumed  $\gamma = 10 \text{ kN/m}^3$  below the ground water level and  $\gamma = 20 \text{ kN/m}^3$  above the ground water level, and foundation depth of 1.0 m it follows:

$$q_f = 0.5 \cdot 10 \cdot 6.5 \cdot 0.02 \cdot 0.9 \cdot 0.68 \cdot 1 \cdot 1 \cdot 0.77 + 0 + 20 \cdot 1 \cdot 1.3 \cdot 1 \cdot 0.76 \cdot 1 \cdot 1 \cdot 0.77 \approx 15.5 \text{ kPa} \quad (9.17)$$

If each building floor contributed about 4 kPa then for four building floors the average pressure over the foundation area was 16 kPa, which is similar to the ultimate bearing pressure according to [Equation \(9.17\)](#). Therefore, large deformations are expected as they actually happened.

### 9.5.2 Terveler Building Foundation Failure in Adapazari – Turkey

Gazetas et al. ([2004](#)) summarised findings from a number of observers and analysed motion of a building with the height to width ratio of 2.1 and width  $\sim 7 \text{ m}$ , which severely tilted ([Fig. 9.10](#)) during the 1999 Izmit (Kocaeli) earthquake in Turkey with the magnitude  $M_w = 7.6$ .

The earthquake caused settlement, tilting and complete overturning of numerous buildings founded on sandy-silt and silty-sand layers with shear wave velocity of less than 60 m/s down to 15 m depth, so a consideration of soil structure interaction would have been required had the building been within European area according to EN 1998-5 ([2004](#)). The toppling was observed only for the buildings with height to width ratios greater than 1.8, provided that they were laterally free from other buildings on one of their sides. Ground acceleration was not recorded in the vicinity



**Fig. 9.10** Terveler (on the right side) and the adjacent building tilt in Adapazari – Turkey (adapted from <http://www.nibs.org/client/assets/files/bssc/Topic15-4-GeotechnicalEarthquakeEngineeringNotes.pdf>)

of the buildings but Gazetas et al. (2004) estimated that it could have been from 0.2 to  $0.3g \sim 2.5 \text{ m/s}^2$ . Unlike the Terveler building, the overturning of other buildings, continued slowly many hours after the earthquake.

The Adapazari overturning failures were not explained uniquely. An explanation is that the prevention of two-way swaying of buildings during the earthquake caused accumulation of one-way tilting and increased eccentricity of the building weight, which then contributed to the concentration of loads on and bearing type failures of shallow foundations and the toppling of the building during the earthquake. The slow toppling of the buildings in Adapazari other than Terveler building could be caused by excess pore water pressure redistribution away from the building layouts. The excess pore water pressure was generated during the earthquake. An analogue is the accumulation of large permanent displacement down slopes in comparison with smaller two-way permanent displacements of level ground during earthquakes. Also, delayed failures of soil slopes occur due to the excess pore water pressure redistribution in time (e.g. Ambraseys and Srbulov, 1995).

The fundamental period of vibration of the sandy-silt and silty-sand layer was about  $4*15/60 = 1 \text{ s}$ , so its vibration frequency was 1 Hz. Clause 4.3.3.2.2 of EN 1998-1 (2004) states that for building with height of up to 40 m an approximation of the vibration period on a rigid base =  $0.075*15^{3/4} = 0.57 \text{ s}$  for the moment resistant space concrete frame with height of 15 m.

The angle of rotation of the building during the earthquake is calculated using Equation (9.6). From Equation (1.12),  $v_l = 60*[(2 - 2*0.49)*(1 - 2*0.49)^{-1}]^{1/2} = 428.5 \text{ m/s}$  for assumed Poisson's ratio of 0.49. The second moment of the foundation area  $J = 15*7^3*12^{-1} = 428.75 \text{ m}^4$ , for assumed foundation length of 15 m and width of 7 m. The equivalent foundation radius  $r = (4*428.75*\pi^{-1})^{1/4} = 4.83 \text{ m}$ . The coefficient  $C_\theta = 1900*2*60*428.75 = 97,755,000 \text{ kg m}^2/\text{s}$ ,  $z = 4.83*9*\pi*32^{-1}*(1 - 0.49)^{*2^2} = 8.7 \text{ m}$ ,  $K_\theta = 3*1900*(2*60)^2*428.75*7.8^{-1} = 4,511,769,231 \text{ kg m}^2/\text{s}^2$ ,  $\Delta M_\theta = 0.3*\pi*(0.49 - 3^{-1})*1900*4.83^5 = 737,426 \text{ kg m}^2$ , building mass is estimated as  $m = 15*7*5*2400 = 1,260,000 \text{ kg}$ ,  $I_o = 1,260,000/12*[7^2 + 16*(15/2)^2] + 737,426 = 100,382,426 \text{ kg m}^2$ ,  $a = 97,755,000*(2*100,382,426)^{-1} = 0.49 \text{ s}^{-1}$ ,  $b = (4,511,769,231*100,382,426^{-1})^{1/2} = 6.7 \text{ s}^{-1}$ ,  $\omega = (6.7^2 - 0.49^2)^{1/2} = 6.7 \text{ radians/s}$  and the rotational period is  $2\pi*6.7^{-1} = 0.94 \text{ s}$ ,  $A_o = 1,260,000*(0.5*15)*0.65*2.5*100,382,426^{-1} = 0.15 \text{ s}^{-2}$ .

The fundamental period of rotation of a structure and its foundation (i.e. of an inverted pendulum) =  $2\pi*[I_o^*(K_\theta - m*g*2*h)^{-1}]^{1/2}$ ,  $I_o$  is mass moment of inertia of structure with respect to the top of foundation,  $k_\theta$  is foundation stiffness in rocking (= ratio between applied turning moment and foundation rotation in radians),  $g$  is the gravitational acceleration,  $h$  is the height of mass centroid above the foundation, i.e. =  $2\pi*\{1,260,000*12^{-1}*[7^2 + 16*(0.5*15)^2]*(4,511,769,231 - 1,260,000*9.81*2*0.5*15)^{-1}\}^{1/2} = 0.95 \text{ s}$ , which is very close to the fundamental period of vibration of 15 m thick soil layer beneath the building so a resonance occurs although the equivalent period of vibration of the structure and soil beneath  $T = (1^2 + 0.57^2 + 0.95^2)^{1/2} = 1.5 \text{ s}$ ,  $\omega_o = 2\pi*1^{-1}$

= 6.28 rad/s for the period of horizontal vibration of 1 s of the 15 m thick soil layer beneath the building,

$$C_2 = \frac{-0.15}{\sqrt{(6.7^2 - 6.28^2)^2 + 4 \cdot 0.49^2 \cdot 6.28^2}} \\ \cdot \sin \left( \text{arc cot} \frac{6.7^2 - 6.28^2}{2 \cdot 0.49 \cdot 6.28} \right) = -0.013$$

$$C_1 = \frac{0.49}{6.7} \cdot C_2 + \frac{0.15 \cdot 6.28 / 6.7}{\sqrt{(6.7^2 - 6.28^2)^2 + 4 \cdot 0.49^2 \cdot 6.28^2}} \\ \times \cos \left( \text{arc cot} \frac{6.7^2 - 6.28^2}{2 \cdot 0.49 \cdot 6.28} \right) = 0.010 \quad (9.18)$$

$$\theta = e^{-0.49 \cdot t} \cdot [-0.013 \cdot \sin(6.7 \cdot t) + 0.010 \cdot \cos(6.7 \cdot t)] \\ - 0.018 \cdot \sin(6.28 \cdot t - \text{arc cot } 0.885) \quad (9.19)$$

The maximum calculated angle of building rotation is 0.028 radians = 1.6°. The method cannot take into account an accumulation of building tilting when soil yielding occurs. The resonance condition that most likely occurred due to similar periods of the horizontal vibration of 15 m thick soil later beneath the building and the building rotational vibration period may be responsible for the building toppling.

For assumed  $c_u \sim 0.25 * 0.5 * 7 * 19^{2.0.8} \sim 30$  kPa and  $C = 1.5$  it follows from Equation (9.7) that  $k_c = 30 * (0.5 * 7)^2 * \pi * [1.5 * 9.81 * 1,260,000 * (0.5 * 15 + 12^{-1} * 4 * 7.5^2 * 7.5^{-1})]^{-1} \sim 0$ . From Equation (1.5),  $d_f = 7$  km (e.g. Bray et al., 2004),  $h_f = 17$  km (e.g. Ambraseys et al., 2004) and  $k_c \sim 0$  it follows that a permanent horizontal displacement  $u_2 = 23$  cm on average and 90 cm on average plus one standard deviation and consequently the angle of the building permanent rotation =  $0.23 * 7.5^{-1} = 0.031$  radians on average and  $0.9 * 7.5^{-1} = 0.12$  radians on average plus one standard deviation i.e. 1.8° and 9° respectively. Temporal angles of building rotations may have been significantly greater than the calculated permanent value which may have been enough to cause a concentration of load and bearing capacity failure of soil under the foundations.

### 9.5.3 Gas Turbine Foundation Vibration in Gabon

It was required to check the vibration properties of the foundation under a gas turbine with accompanying compressors and driven packages in Gabon. The approximate centres of gravities of two compressors, two driven package lifts, and the gas turbine are shown in Fig. 9.11.

The reinforced concrete raft foundation width is 4.1 m, length 13.0 m and thickness 0.5 m. The foundation and machine mass is 101 t. The mass eccentricity (in Fig. 9.5) is  $e = 1.09$  m. Other input data are given in Table 9.2 for the shut down

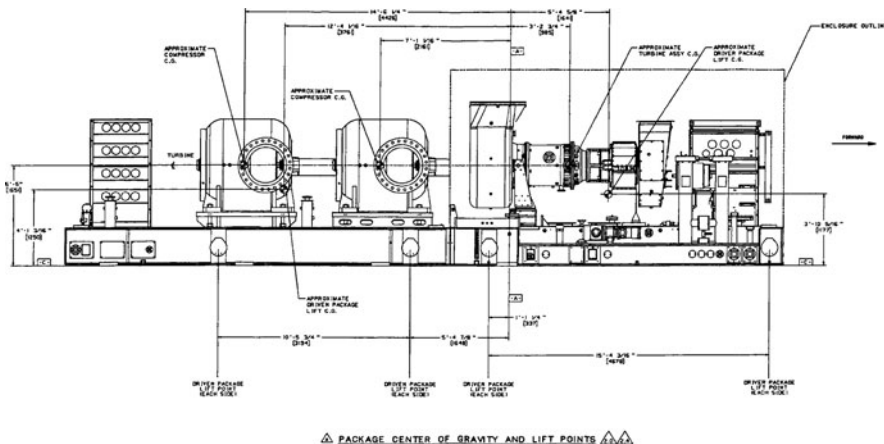


**Fig. 9.11** Side view of the locations of centres of gravities of two compressors, two driven package lifts and a gas turbine (the total length 12.0 m)

**Table 9.2** Dynamic loads and their frequencies in the case study in Section 9.5.3

Load No (direction:

h – horizontal, v – vertical)

Property	1(h)	2(h)	3(v)	4(h)	5(v)	6(h)	7(v)
Horizontal unbalanced force (N)	1148	3265	2980	5004	7073	5004	7073
Eccentricity (m) from the total mass centre of gravity	1.09	1.09	2*2.33/2	1.09	2*2.33/2	1.09	2*2.33/2
Rotational frequency (radians/s)	1571	1571	1571	1497	1497	1497	1497

case of the rotors. The horizontal and vertical load act simultaneously. The vertical loads on opposite sides of the machines are coupled so that when one acts upwards the other acts downwards and vice versa.

The machinery manufacturer requirements are:

- The componential velocity amplitude at the location of the machine bearing housing does not exceed 2 mm/s.
- The peak to peak amplitude of any part of the foundation is less than 0.05 mm.

The foundation is placed over in situ or compacted coarse granular laterite soil (weathered rock). The standard penetration test blow count varies in the range from 12 to over 30 at shallower depths under the foundation. The transversal wave velocity varies in the range from  $80 \times 12^{0.333} = 180$  m/s to over  $80 \times 30^{0.333} = 250$  m/s based in [Equation \(1.11\)](#).

$I = 101,000 * 12^{-1} * (0.5^2 + 4.1^2) = 143,588 \text{ kg m}^2$ ,  $\Delta M_\theta = 0$  for assumed Poisson's ratio of soil  $\nu = 0.3$ , assumed soil unit density  $\rho = 2000 \text{ kg/m}^3$ , the

second moment of area of the foundation  $J = 13*4.1^3*12^{-1} = 74.7 \text{ m}^4$ , the equivalent radius of foundation  $r = (4*74.7/\pi)^{1/4} = 3.1 \text{ m}$ , the foundation area  $A = 13*4.1 = 53.3 \text{ m}^2$ ,  $r_o = (53.3*\pi^{-1})^{1/2} = 4.1 \text{ m}$ , assumed transversal wave velocity  $v_t = 200 \text{ m/s}$ ,  $z_o = 4.1*\pi*8^{-1}*(2 - 0.3) = 2.7 \text{ m}$ ,  $K_o = 4.1*200^2*53.3/2.7 = 3,237,481 \text{ m}^4/\text{s}^2$ ,  $b_o = 1530*2.7*200^{-1} = 20.6 \text{ rad}$ ,  $\mu_o = 0$  for  $\nu < 1/3$ ,  $k_o = 1 - 0*\pi^{-1}*4.1*2.7^{-1}*20.6^2 = 1$ ,  $S_\omega = 3,237,481*(1 + i*20.6)$ ,  $v_l = 200*[(2 - 2*0.3)*(1 - 2*0.3)^{-1}]^{1/2} = 374 \text{ m/s}$ ,  $z = 9*3.1*\pi*32^{-1}*(1 - 0.3)*(374*200^{-1})^2 = 6.7 \text{ m}$ ,  $K_\theta = 3*2000*374^2*\pi*3.1^{4*4^{-1}}*6.7^{-1} = 9,085,656,402 \text{ kg m}^2/\text{s}^2$ ,  $\mu = 0$  for  $\nu < 1/3$ ,  $k_\theta = 1 - 4*0*3^{-1}*\pi^{-1}*3.1*6.7^{-1}*20.6^2 - 3^{-1}*20.6^{2*}(1 + 20.6^2)^{-1} = 0.98$ ,  $c_\theta = 3^{-1}*20.6^{2*}(1 + 20.6^2)^{-1} = 0.000075$ ,  $S_\theta = 9,085,656,402*(1 + i*0.00154)$ .

Equation (9.8) becomes:

$$\begin{aligned} & (-3.27 \cdot 10^{11} + 1.4 \cdot 10^7 \cdot i) \cdot \theta - (3528854 + 72694398 \cdot i) \cdot u \\ &= 55622 \cdot \sin(1530*t) \\ & -2.577 \cdot 10^{11} \cdot \theta + (-2.364 \cdot 10^{11} + 66692109 \cdot i) \cdot u \\ &= 14421 \cdot \sin(1530*t) \end{aligned} \quad (9.20)$$

The solutions are:

$$\begin{aligned} \theta &= \frac{\left( \begin{array}{l} 55622 \cdot \sin(1530*t) * (-2.364 \cdot 10^{11} + 66692109 \cdot i) \\ + 14421 \cdot \sin(1530*t) * (3528854 + 72694398 \cdot i) \end{array} \right)}{\left( \begin{array}{l} (-3.27 \cdot 10^{11} + 1.4 \cdot 10^7 \cdot i) * (-2.364 \cdot 10^{11} + 66692109 \cdot i) \\ - 2.577 \cdot 10^{11} * (3528854 + 72694398 \cdot i) \end{array} \right)} \\ u &= \frac{\left( \begin{array}{l} (-3.27 \cdot 10^{11} + 1.4 \cdot 10^7 \cdot i) * 14421 \cdot \sin(1530*t) \\ + 2.577 \cdot 10^{11} * 55622 \cdot \sin(1530*t) \end{array} \right)}{\left( \begin{array}{l} (-3.27 \cdot 10^{11} + 1.4 \cdot 10^7 \cdot i) * (-2.364 \cdot 10^{11} + 66692109 \cdot i) \\ - 2.577 \cdot 10^{11} * (3528854 + 72694398 \cdot i) \end{array} \right)} \end{aligned} \quad (9.21)$$

The denominator is  $3.27*2.364*10^{22} - 1.4*10^7*66,692,109 - (3.27*10^{11}*66,692,109 + 1.4*10^7*2.364*10^{11})*i - 2.577*10^{11}*3,528,854 - 2.577*10^{11}*72,694,398*i = 7.73*10^{22} + 6.41*10^{18}*i$ .

The nominator with  $\theta$  is  $\sin(1530*t) * \{55,622* - 2.364*10^{11} + 55,622*66,692,109*i + 14,421*3,528,854 + 14,421*72,694,398*i\} = \sin(1530*t) * (-1.31*10^{16} + 4.76*10^{12}*i)$ .

The real part of the ratio between the nominator and the denominator  $= (-1.31*10^{16}*7.73*10^{22} + 4.76*10^{12}*6.41*10^{18})*(7.73^2*10^{44} + 6.41^2*10^{36})^{-1} = \sin(1530*t)* - 1.7*10^{-7} \text{ rad}$ .

The imaginary part of the ratio between the nominator and the denominator  $= \sin(1530*t)*i*(1.31*10^{16}*6.41*10^{18} + 7.73*10^{22}*4.76*10^{12})*(7.73^2*10^{44} + 6.41^2*10^{36})^{-1} = \sin(1530*t)*7.5*10^{-11}*i$ .

The maximum absolute value of the real and imaginary part  $\theta = (1.7^2*10^{-14} + 7.5^2*10^{-22})^{1/2} = 1.7*10^{-7} \text{ rad}$ .

The nominator with  $u$  is  $\sin(1530*t)*(-3.27*10^{11}*14421 + 1.4*10^7*14,421*i + 2.577*10^{11}*55,622) = \sin(15,630*t)*(9.63*10^{15} + 2*10^{11}*i)$ .

The real part of the ratio between the nominator and the denominator =  $\sin(1530*t)*(9.63*10^{15}*7.73*10^{22} + 2*10^{11}*6.41*10^{18})*(7.73^{2*}10^{44} + 6.41^{2*}10^{36})^{-1} = \sin(1530*t)*1.2*10^{-7}$  m =  $\sin(1530*t)*1.2*10^{-4}$  mm.

The imaginary part of the ratio between the nominator and the denominator =  $\sin(1530*t)*i*(-9.63*10^{15}*6.41*10^{18} + 7.73*10^{22}*2*10^{11})*(7.73^{2*}10^{44} + 6.41^{2*}10^{36})^{-1} = \sin(1530*t)*i*7.7*10^{-12}$  m =  $\sin(1530*t)*i*7.7*10^{-9}$  mm.

The maximum absolute value of the real and imaginary part  $u$  =  $(1.2^{2*}10^{-8} + 7.7^{2*}10^{-18})^{1/2} = 1.2*10^{-4}$  mm.

The double value of the above amplitude is smaller than 0.05 mm specified by the manufacturer. The maximum horizontal velocity is  $1.2*10^{-4}*1530 = 0.18$  mm/s and the vertical velocity  $1.7*10^{-7}*0.5*4100*1530 = 0.53$  mm/s, which are both smaller than 2 mm/s specified by the manufacturer. The results should be checked by field measurements of actual values.

#### **9.5.4 Settlement of Foley Square Building Foundation Caused by Pile Driving at Manhattan in New York City – USA**

Lacy and Gould (1985) described several cases of the settlements of buildings on shallow and piled foundations, of ground surface and sewer pipes as a result of pile driving in narrowly graded, single sized clean sand with relative density less than about 50–55% even if the recorded peak particle velocities were much smaller than 50 mm/s, which is considered to be a safe limit for buildings. Lacy and Gould (1985) conclude that factors (the number, length and type of piles and driving resistance) that increase the total vibration energy input will increase settlements.

Foley Square building in Manhattan – New York City experienced settlement due to 14HP73 piles driving through 24 m of sand and silt. The building is 49.5 m long and of unspecified width. First, a 2.5 cm settlement of the building occurred as a result of the use of impact hammer with the input energy of 35.2 kJ per blow, with 22–40 blows per 0.305 m penetration causing the peak particle velocity of 4.8 mm/s at a distance of 6.1 m from the pile. Subsequently used ‘subsonic’ pile hammer with 29 blows per 0.305 m caused the peak particle velocity of 3.5 mm/s at a distance of 6.1 m from the pile and a ‘Bodine’-‘sonic’ pile hammer caused the same peak particle velocity at the same distance as the impact pile. Final measured settlements of the foundations reached 7.6 cm. Ground between the piles and the building settled 0.3 m. The bearing pressure under the 16 story building was quoted to be 480 kPa by Lacy and Gould (1985). However, it may be under individual footings as an expected overall pressure should be about  $16 \times 5 = 90$  kPa. The seismographs indicated a typical frequency of the glacial fine sand of 30 Hz. The recorded standard penetration blow count in sand and silt varied in the range from 22 to 50, with typical 29 blows under the building to a depth of 30.5 m. Lacy and Gould (1985) estimated initial relative density of sand and silt at the site of about 45%.

The graph shown in Fig. 9.6 is not available for this case. Based on data by Das (1985), it is assumed that for silty sand  $e_{\max} = 1$  ( $n_{\max} = 0.5$ ) and  $e_{\min} = 0.4$  ( $n_{\min} = 0.28$ ). For  $\Delta n_{\max}$  of  $0.5 - 0.28 = 0.22 = \varepsilon_{\max}$ , the soil compression over 1 m depth  $d$  is  $0.22$  m and the energy necessary to achieve such settlement over a unit area  $A$  of  $1 \text{ m}^2$  is  $\varepsilon_{\max}^* E'^* A^* \varepsilon^* d = 0.22 * 29^* 1 * 0.22 * 1 = 1.40 \text{ MJ}$ , where the soil modulus  $E' = N_{\text{SPT}}$  in MPa is assumed based on data by Stroud (1988), for example. For assumed a simple circular function with the horizontal tangent at the point ( $E = 1.40 \text{ MJ}$ ,  $n = 0.28$ ), it follows that

$$\begin{aligned} n &= 4454545.85 - \sqrt{4454545.565^2 - (E - 1400)^2} \\ E &= 1400 - \sqrt{4454545.565^2 - (n - 4454545.845)^2}, \end{aligned} \quad (9.22)$$

where energy  $E$  is in kJ. For estimated initial  $D_r = 0.45$ ,  $e = 0.73$ ,  $n_{\text{current}} = 0.42$ ,  $E_{\text{current}} = 283.2 \text{ kJ}$ . For assumed the building width close to the building length  $r_o = 27.9 \text{ m}$ . For  $N_{\text{SPT}} \sim 29$  and Equation (1.11),  $v_t = 246 \text{ m/s}$ . For assumed  $v = 0.3$  and Equation (1.12),  $v_l = 460 \text{ m/s}$ . From Equation (9.12),  $z_o = 53.6 \text{ m}$ . The recorded peak particle velocity of  $0.0048 \text{ m/s}$  at the ground surface at the frequency of  $30 \text{ Hz}$  corresponds to the amplitude of ground displacement of  $0.0048 (2\pi 30)^{-1} = 0.0000255 \text{ m}$ . The Rayleigh wave length was  $\lambda = 246 (2\pi 30)^{-1} = 1.3 \text{ m}$ . The number of cycles over  $24 \text{ m}$  depth was  $24^* (0.305)^{-1} * 30 \text{ blows/feet} = 2360 \text{ cycles}$  for an averaged recorded  $30 \text{ blow/feet}$  of the driving hammers. The results of the calculations of settlement without the soil-structure interaction effects considered are given in Table 9.3. The wave amplitudes along depths are obtained from Fig. 9.8.

The calculated settlement of  $0.19 \text{ m}$  is greater than the recorded settlement of the building of  $0.025 \text{ m}$  after driving of the first pile possibly due to the assumptions made in the calculation and/or the soil-structure interaction effect and/or considering the change of wave amplitudes with depth according to Fig. 9.8 which is applicable to the free field without structures. The effect of kinematic soil-structure interaction has not been considered in this case study because only amplitude and not time history of ground motion is available. If no stress from the building is considered (i.e.  $\Delta\sigma_v = 0$  in the free field), the calculated settlement is  $0.03 \text{ m}$  (Table 9.4), which is quite close to the recorded settlement of  $0.025 \text{ m}$  after driving of the first pile.

### 9.5.5 Settlement of a Quay Wall in Kobe Caused by the 1995 Hyogoken-Nanbu Earthquake in Japan

From Equation (9.14), the amplitude of vertical ground displacement =  $0.025 * 0.9 * 5.25 * 1.35 * 0.15 * 1 = 0.024 \text{ m} = \Delta w_z$ . From Equation (9.16), an average number of significant cycles  $N_{\text{cycles}} = 3 + 7/4^*(6.9 - 4) = 8$ . The graph in Fig. 9.6 is not available for this case. It is assumed that the same data apply as in Section 9.5.4. The calculation is given in Table 9.5. It is assumed that soil unit

**Table 9.3** Results of the calculation of the settlement under the building due to pile driving in the case study in Section 9.5.4

z (m)	r (m)	$r^2\pi (m^2)$	$\sigma_v$ (kPa)	$\Delta\sigma_v$ (kPa)	$\sigma_v + \Delta\sigma_v)^* r^2 \pi (kN)$	$V = (\sigma_v + \Delta\sigma_v)^* r^2 \pi (kN)$	$z/\lambda$	$\Delta_{w,z}$ (m)	$\Delta E = V^* \Delta_{w,z}^*$		$E_{current} + \Delta E (kJ)$	n	$\varepsilon = \Delta n$
									$\Delta E =$	$V^* \Delta_{w,z}^*$			
1	28.4	634	10	87	472	299,480	0.8	7.65E-06	5410	5690	0.28	0.13	
2	28.9	658	29	84	475	312,202	1.5	1.28E-06	939	1220	0.29	0.05	
3	29.5	682	48	81	478	325,835	2.3	2.55E-07	196	479	0.38	0.01	
4	30	706	67	78	482	340,404	3.1	1.28E-07	103	386	0.40	0.00	
5	30.5	731	86	75	487	355,932	3.8	2.60E-08	21.8	305	0.42	0.00	
6	31	756	105	73	493	372,445	4.6	1.30E-08	11.4	295	0.42	0.00	
7	31.5	781	124	70	499	389,966	5.4	—	—	—	—	—	Settlement (m) = 0.19

**Table 9.4** Results of the calculation of the settlement in the free field due to pile driving in the case study in Section 9.5.4

z (m)	r (m)	$r^2\pi (m^2)$	$\sigma_v$ (kPa)	$\Delta\sigma_v$ (kPa)	$\sigma_v + \frac{V = (\sigma_v + \Delta\sigma_v)^* r^2 \pi(kN)}{\Delta\sigma_v(kPa)}$	$z/\lambda$	$\Delta_{w,z}$ (m)	$\Delta E = \frac{V^* \Delta_{w,z}^*}{23,600 (kJ)}$			$n$	$\varepsilon = \Delta n$
								$V^* \Delta_{w,z}^*$	$E_{current} + \frac{\Delta E(kJ)}{\Delta E(kJ)}$	$n$		
1	28.4	634	10	0	10	6027	0.8	7.65E-06	109	392	0.40	0.02
2	28.9	658	29	0	29	18,748	1.5	1.28E-06	56	340	0.41	0.01
3	29.5	682	48	0	48	32,381	2.3	2.55E-07	19	303	0.42	0.00
4	30	706	67	0	67	46,950	3.1	1.28E-07	14	297	0.42	0.00
5	30.5	731	86	0	86	62,478	3.8	2.60E-08	4	287	0.42	0.00
6	31	756	105	0	105	78,991	4.6	1.30E-08	2	286	0.42	0.00
7	31.5	781	124	0	124	96,512	5.4	—	—	—	—	Settlement (m) = 0.03

weight in submerged condition is  $10 \text{ kN/m}^3$ . From Section 7.5.1.1 it follows that the contact pressure beneath the rock rubble is  $(2700 + 680) * 19^{-1} = 178 \text{ kPa}$ . Equation (9.11) is used for the calculation of  $\Delta\sigma$  with depth. The calculated settlement of 17 m thickness of sand fill is 2.2 m, which is equal to the observed settlement of about 2 m.

Ground settlement during earthquakes can be estimated from the formulas developed by Takada and Tanabe (1988) based on the regression analysis of 404 instances of ground settlement from five major Japanese earthquakes ( $7.4 \leq M_{JMA} \leq 7.9$ ). The expressions were derived specifically for the purpose of earthquake design of lifeline facilities, motivated by the high levels of settlement-induced pipeline damage observed in the earthquakes under investigation. Two expressions are given, the first for settlement of an embankment ( $\delta_1$ ) and the second for settlement of a plain (level) site ( $\delta_2$ ), when  $\delta_1$  and  $\delta_2$  are both measured in cm.

$$\delta_1 = \frac{C_1 \cdot B \cdot H_{\text{sand}} \cdot a_p}{N_{\text{SPT}}} + C_2, \quad (9.23)$$

$$\delta_2 = \frac{C_3 \cdot H_{\text{sand}} \cdot a_p}{N_{\text{SPT}}} + C_4$$

where  $B$  is the embankment height (m),  $H_{\text{sand}}$  is the thickness of the sandy layer (m),  $N_{\text{SPT}}$  is the Standard Penetration Test (SPT)  $N$ -value of the sandy layer,  $a_p$

**Table 9.5** Results of the calculation of the settlement beneath the caisson in Kobe port during the earthquake in the case study in Section 9.5.5

z (m)	$\sigma_v$ (kPa)	$\Delta\sigma_v$ (kPa)	$V = \sigma_v + \Delta\sigma_v$ (kN)	$\Delta w_z$ (m)	$\Delta E =$	$E_{current} + \Delta E$ (kJ)	n	$\varepsilon = \Delta n$
					$(V^* \Delta w_{w,z})^*$			
1	10	178	188	0.024	35.7	1435.7	0.29	0.13
2	20	44.5	64.5	0.024	12.2	1412.2	0.29	0.13
3	30	20	50	0.024	9.5	1409.5	0.29	0.13
4	40	11	51	0.024	9.7	1409.7	0.29	0.13
5	50	7	57	0.024	10.8	1410.8	0.29	0.13
6	60	5	65	0.024	12.4	1412.4	0.29	0.13
7	70	4	74	0.024	14	1414	0.29	0.13
8	80	3	83	0.024	15.8	1415.8	0.29	0.13
9	90	2	92	0.024	17.5	1417.5	0.29	0.13
10	100	2	102	0.024	19.4	1419.4	0.29	0.13
11	110	1.5	111.5	0.024	21.2	1421.2	0.29	0.13
12	120	1	121	0.024	23	1423	0.29	0.13
13	130	1	131	0.024	24.9	1424.9	0.29	0.13
14	140	1	141	0.024	26.8	1426.8	0.29	0.13
15	150	1	151	0.024	28.7	1428.7	0.29	0.13
16	160	0.5	160.5	0.024	30.5	1430.5	0.29	0.13
17	170	0.5	170.5	0.024	32.4	1432.4	0.29	0.13

**Table 9.6** Regression coefficients for calculation of  $\delta_1$  and  $\delta_2$  (Takada and Tanabe, 1988)

Settlement type	Site type	Cases considered	$C_1$	$C_2$	Correlation coefficient	No of sites
$\delta_1$	Embankment	Liquefied soil	0.123	19.3	0.88	35
$\delta_1$	Embankment	Liquefied and non-liquefied soil	0.118	19.9	0.88	42
Settlement type	Site type	Cases considered	$C_3$	$C_4$	Correlation coefficient	No of sites
$\delta_1$	Level ground	Liquefied soil	0.339	3.79	0.81	41
$\delta_2$	Level ground	Liquefied and non-liquefied soil	0.332	4.86	0.82	43

is the peak ground acceleration ( $\text{cm/s}^2$ ), and  $C_i$  are coefficients of regression.  $C_1$  has dimensions of  $\text{s}^2/\text{m}^2$ ;  $C_2$  and  $C_4$  have dimensions of  $\text{cm}$ ;  $C_3$  has dimensions of  $\text{s}^2/\text{m}$ . For both expressions, coefficients were derived for two different datasets: settlements in liquefied soil, and settlements in both liquefied and non-liquefied soil. The coefficients are summarised in Table 9.6.

Two sets of regressions were carried out using two different peak ground acceleration datasets (calculated using two different, unspecified attenuation relationships). The coefficients quoted in Table 9.6 are, in each case, the values associated with the peak ground acceleration dataset which gave the best correlation coefficient. Separate coefficients were presented for expressions which used the peak ground velocity and the peak ground displacement instead of the peak ground acceleration, although the investigators recommend the use of the peak ground acceleration expressions for predictive purposes. The calculated settlement for level ground in front of the quay wall is about 1.1 m for  $H_{\text{sand}} = 17.5$  m,  $a_p = 525 \text{ cm/s}^2$  and  $N_{\text{SPT}} = 29$ , without taking account of the weight of the wall and backfill behind it.

## 9.6 Discussion and Conclusion

Based on the results of considered case histories, it can be noted that:

- The bearing capacity of soil beneath shallow foundation can be calculated using a pseudo static method providing that the soil properties used correspond to the cyclic condition during an earthquake and the effect of inertia forces on soil is replaced by the effect of inclined ground surface or the inclination of foundation base.
- The simple model used for the analysis of building and foundation rotational motion during an earthquake provided a reasonable value of the rotational angle but could not account for accumulation of building inclination when soil yielding

occurred during an earthquake. Instead, the rotating block model can be used for an estimate or permanent rotation.

- The simple model used for consideration of coupled horizontal and rotational motion of the foundation of a gas turbine provided reasonable results.
- The simple model used for calculation of foundation settlement during an earthquake provided reasonable results. The model provided reasonable result for foundation settlement during a pile driving when free field condition was considered without structure.

In all cases, more case histories based on the simple models need to be analysed and reported in technical literature.

## References

- Ambraseys NN, Srbulov M (1995) Earthquake induced displacements of slopes. *Soil Dyn Earthquake Eng* 14:59–71
- Ambraseys NN, Douglas J, Sigbjornsson R, Berge-Thierry C, Suhadolc P, Costa G, Smit P (2004) European strong motion database – volume 2. The Engineering and Physical Science Research Council of the United Kingdom GR-52114-01
- ASTM D1556 – 00 Standard test method for density and unit weight of soil in place by sand-cone method. Annual Book of ASTM Standards 04.08, American Society for Testing and Materials
- ASTM D4253 – Standard test method for maximum index density and unit weight of soils using a vibratory table. Annual Book of ASTM Standards 04.08, American Society for Testing and Materials
- ASTM D4254 – Standard test method for minimum index density and unit weight of soils and calculation of relative density. Annual Book of ASTM Standards 04.08, American Society for Testing and Materials
- ASTM D4914 – Standard test methods for density of soil and rock in place by the sand replacement method in a trial pit. Annual Book of ASTM Standards 04.08, American Society for Testing and Materials
- Boussinesq J (1885) Application des potentiels à l'étude de l'équilibre et du mouvement des solides élastiques. Gauthier-Villard, Paris
- Bray JD, Rodolfo BS, Turan D, Akin O, Youd TL, Stewart JP, Seed RB, Cetin OK (2004) Subsurface characterization at ground failure sites in Adapazari, Turkey. *ASCE J Geotechn Geoenviron Eng* 130(7):673–685
- BS 1377-2 (1990) Soils for civil engineering purposes. Part 2: classification tests. British Standard Institution
- BS 1377-4 (1990) Soils for civil engineering purposes. Part 4: compaction related tests. British Standard Institution
- CP 2012-1 (1974) Code of practice for foundations for machinery – part 1: foundations for reciprocating machines. The British Standards Institution
- Das BM (1985) Advanced soil mechanics. McGraw-Hill, Singapore
- EN 1998-1 (2004) Eurocode 8 – design of structures for earthquake resistance, part 1: general rules, seismic actions and rules for buildings. European Committee for Standardization, Brussels
- EN 1998-5 (2004) Eurocode 8 – design of structures for earthquake resistance, part 5: foundations, retaining structures and geotechnical aspects. European Committee for Standardization, Brussels
- FEMA 356 (2000) Prestandard and commentary for the seismic rehabilitation of buildings. Building Seismic Safety Council, Washington, DC

- Gazetas G, Apostolou M, Anastasopoulos J (2004) Seismic bearing capacity failure and overturning of 'Terveler' building in Adapazari, 1999. In: Proceedings of the 5th international conference on case histories in geotechnical engineering, New York, NY. Paper No. SOAP.11, pp 1–5
- Gazetas G, Anastasopoulos I, Apostolou M (2007) Shallow and deep foundations under fault rupture or strong seismic shaking. In: Ptililakis KD (ed) Earthquake geotechnical engineering, 4th international conference on earthquake geotechnical engineering – invited lectures, Thessalonica, Greece. Springer, Berlin, Chapter 9, pp 185–215
- Giek K, Giek R (1997) Engineering formulas, 7th edn. McGraw-Hill, New York, NY
- Green RA, Terri GA (2005) Number of equivalent cycles concept for liquefaction evaluations – revisited. *J Geotechn Geoenviron Eng* 131:477–488
- Hancock J, Bommer JJ (2004) Predicting the number of cycles of ground motion. In: The 13th world conference on earthquake engineering, Vancouver, Canada 1989
- Hansen JB (1970) A revised and extended formula for bearing capacity. Bulletin No. 28, Geoteknisk Institut, Akademiet for dde Tekniske Videnskaber, Copenhagen, Denmark
- Idriss IM, Kausel E, Kennedy RP, Lysmer J, Agrawal PK, Seed HB, Hadjian AH, Whitman RV (1980) Analyses of soil-structure interaction effects for nuclear power plants. Report by Ad Hoc Group on Soil-Structure Interaction of the Committee on Nuclear Structures and Materials of the Structural Division of ASCE
- Ishihara K, Koga Y (1981) Case studies of liquefaction in the 1964 Niigata earthquake. *Soils Foundations* 21(3):35–52
- Ishihara K, Yoshimine M (1992) Evaluation of settlements in sand deposits following liquefaction during earthquakes. *Soils Foundations* 32:173–188
- Kishida H, Matsushita K, Sakamoto I (1969) Soil-structure interaction of the elevator tower and concrete footings. In: Proceedings of the 4th world conference on earthquake engineering, vol 3, Santiago de Chile, pp 101–115
- Lacy HS, Gould JP (1985) Settlement from pile driving in sands. In: Gazetas G, Selig ET (eds) Vibration problems in geotechnical engineering, Proceedings of ASCE convention, Detroit, MI, pp 152–173
- Lunne T, Robertson PK, Powell JJM (2001) Cone penetration testing in geotechnical practice. Spon Press, London
- Newmark NM (1965) Effect of earthquakes on dams and embankments. *Geotechnique* 15:139–160
- Novak M (1985) Experiments with shallow and deep foundations. In: Gazetas G, Selig ET (eds) Vibration problems in geotechnical engineering, ASCE convention, Detroit, MI, pp 1–26
- Sarma SK, Chen YC (1995) Seismic bearing capacity of shallow strip footings near sloping ground. In: Elnashai AS (ed) Proceedings of the 5th SECED conference on European seismic design practice. Balkema, Rotterdam, pp 505–512
- Sarma SK, Chen YC (1997) Seismic bearing capacity of rigid deep strip foundations. In: Special technical session on earthquake geotechnical engineering at the 14th international conference on soil mechanics and foundation engineering. Madrid, Spain, pp 287–295
- Sarma SK, Srbulov M (1998) A uniform estimation of some basic ground motion parameters. *J Earthquake Eng* 2:267–287
- Seed HB, Idriss IM, Makdisi F, Banerje N (1975) Representation of irregular stress time histories by equivalent uniform stress series in liquefaction analyses. Report EERC 75-29, Earthquake Engineering Research Center, University of California, Berkeley, CA
- Srbulov M (2008) Geotechnical earthquake engineering – simplified analyses with case studies and examples. Springer, New York, NY
- Srbulov M (2010) Ground vibration engineering – simplified analyses with case studies and examples. Springer, New York, NY
- Stroud MA (1988) The standard penetration test – its application and prediction. In: Proceedings of the geotechnology conference 'penetration testing in the UK' organized by the Institution of Civil Engineers, Birmingham

- Tajimi H (1984) Predicted and measured vibrational characteristics of a large-scale shaking table foundation. In: Proceedings of the 8th world conference on earthquake engineering, vol 3, San Francisco, CA, pp 873–880
- Takada S, Tanabe K (1988) Estimation of earthquake induced settlements for lifeline engineering. In: Proceedings of the 9th world conference on earthquake engineering, vol 7, Tokyo, Japan, pp 109–114
- Templeton JS III (2008) Time domain FR seismic analysis of mat-supported jackup structure on soft clay. Paper OTC 19645, Offshore Technology Conference, Houston, TX
- Terzaghi K, Peck RB (1948) Soil mechanics in engineering practice. Wiley, New York, NY
- Tokimatsu K, Seed HB (1987) Empirical correlation of soil liquefaction based on SPT N-value and fines content. *Soils Foundations* 23:56–74
- Verruijt A (1994) Soil dynamics. Delft University of Technology, Delft, The Netherlands
- Wolf JP (1994) Foundation vibration analysis using simple physical models. PTR Prentice Hall, Upper Saddle River, NJ
- Yamagami T, Hangai Y (1988) Response observation of a reinforced concrete tower. In: Proceedings of the 9th world conference on earthquake engineering, Tokyo, Japan, Paper 5-4-10, pp 715–720

# Chapter 10

## Piled Foundations

### 10.1 Introduction

EN 1998-5 (2004) specifies that the effects of dynamic soil-structure interaction shall be taken into account when P-δ effects are important (i.e. the bending moment caused by axial force times column deflexion), for structures with massive or deep-seated foundations, such as bridge piers, caissons and silos, for slender tall structures, such as towers and chimneys, and for structures supported on very soft soil, with average shear wave velocity less than 100 m/s. The code also states that piles and piers shall be designed to resist the following two types of action effects:

- (a) Inertia forces from the superstructure.
- (b) Kinematic forces arising from the deformation of the surrounding soil due to passage of seismic waves.

The code requires that analyses to determine the internal forces along a pile, as well as the deflection and rotation at the pile head, shall be based on discrete or continuum models that can realistically (even if approximately) reproduce:

- The flexural stiffness of the pile,
- The soil reaction along the pile, with due consideration to the effects of cyclic loading and the magnitude of strains in the soil,
- The pile to pile dynamic interaction effects (also called dynamic pile-group effects)
- The degree of freedom of the rotation at/of the pile cap, or of the connection between the pile and the structure.

Unfortunately, besides the requirements, the code does not provide a method for analyses of soil-pile interaction effects.

The aim of this chapter is to summarize briefly main mechanism and factors affecting behaviour of foundations in dynamic conditions, to mention available methods for analyses of soil-pile interaction, to describe simple considerations of the kinematic and inertial effects on piles during earthquakes and to apply these

simple considerations to back analyses of eleven case histories of piled foundations under seismic loading in order to assess the accuracy and applicability to everyday routine designs. The chapter is based on a paper by Srbulov (2010) with kind permission of Patron Editore. The emphasis is on the use of simple analyses for the case histories considered.

## 10.2 Mechanism and Factors

### 10.2.1 Kinematic Interaction

The phenomenon of kinematic interaction is the result of different stiffness of pile and surrounding ground. Stiffer pile tends to average ground motion and as a results experience additional stresses. The additional stresses can be significant in layered soil when softer layers tend to move more in relation to stiffer layers. An extreme case is when sand liquefies during earthquake. Many piles developed cracks or plastic hinges at the top and bottom of a liquefied layer (e.g. Hamada, 1992). A special case arises if soil liquefaction leads to flow type failure on sloping ground with ground displacements exceeding the displacement necessary to activate full passive resistance of top non-liquefied layer. Frequently, the top (part of) soil layer does not liquefy because it is above ground water level and because shear stress during earthquake is zero at the ground surface. Large movement of non-liquefied soil crust can exert lateral stresses on piles and pile caps equal to the passive pressure of soil (e.g. Berrill et al., 2001). Kinematic interaction effects depend on (e.g. Nikolaou et al., 2001):

- Pile length, diameter and inclination
- Pile and soil stiffness (Young's modulus)
- Free field acceleration at the soil surface
- Depth below ground level
- Shear wave velocities of soil layer at the interface

### 10.2.2 Inertial Interaction

So called inertial interaction is caused by the existence of structural and foundation mass. The structures above ground level are free to vibrate with different periods (frequency) of vibration than the supporting ground. If the vibration periods of structure, foundation and supporting ground coincide (i.e. they are in resonance) then superposition of amplitudes of incoming and outgoing waves can occur, which can cause failure of foundations and structures.

Inertial interaction effects depend on:

- Structural mass and acceleration
- Period of vibration of a structure and its foundation

- The flexural stiffness of the pile
- The soil reaction along the pile
- The pile to pile dynamic interaction
- The degree of freedom of the rotation at/of the pile cap

## 10.3 Existing Methods

Methods for analyses of soil-pile interaction are broadly classified as:

- Simplified methods based on equivalent soil springs,
- Rigorous numerical analyses (based on finite elements/differences, boundary/discrete elements), Publicly available computer programmes are listed for example on <http://www.ggsd.com/>,
- Small scale tests, such as centrifuge and shaking table,
- Full scale prototypes, e.g. ASTM D1143, D3966.

### 10.3.1 Simplified Analyses

In these methods, the horizontal movement of ground is calculated in time for the case of ground wave propagation in the vertical direction in the free field, without piles. The piles, which are connected to ground using non-linear p-y springs – Fig. 10.1, are then affected by such ground movement depending on their flexural stiffness. The p-y springs can be obtained from recommendations in codes and standards, e.g. API RP2A-WSD (2000), or from full scale testing, e.g. ASTM D3966.

Sometimes, it is assumed that the springs are with fixed ends, which is not realistic. Several iterations are required to calculate force  $p$  as  $y$  is the relative horizontal displacement between pile and adjacent ground ( $\Delta$  ground –  $\Delta$  pile) and not ground horizontal displacement in the free field.

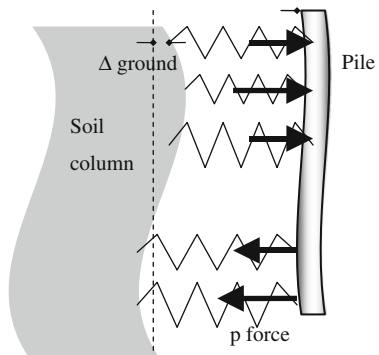


**Fig. 10.1** Schematic of simplified analyses based on p-y springs (plotted as zig-zag polygons)

### ***10.3.2 Rigorous Numerical Analyses***

Their development is connected with the advancements in speed and capacity of digital computers. In principle, numerical methods fulfil equilibrium conditions of stresses, constitutive relations between the stresses and corresponding strains, and compatibility conditions between strains and displacement gradients. However, there is considerable debate about the constitutive relationships between stresses and strains in soil and how to model them. Often simplified relationships like Mohr-Coulomb are used because of lack of data. Numerical methods are often complex in implementation and should not be used without validation of considered model.

### ***10.3.3 Small Scale Models***

Testing of large pile groups is very difficult if not impossible and therefore small scale models are tested instead. The use of such models is not without problems.

Shaking table scale models are conducted under Earth's gravity. The major disadvantage of these models is that actual stresses are not correctly reproduced in the scaled model because of their small size, which can lead to major differences between behaviour of the model and soil in the field as soil behaviour is stress dependent. These model tests have been demonstrated to be sensitive to container boundary effects, scale modelling techniques, and non-adherence to similitude laws (e.g. Meymand, 1998).

Centrifuge tests are performed on small scale models in laboratory using acceleration many times greater than the gravity acceleration. The enhanced acceleration produced by centrifuge force is such that stresses at homologous points in model and full scale prototype can be made identical. This ensures that soil in the model behaves in the same way as in the prototype. Wilson (1998), for example, mentions that difficulties or limitations with dynamic centrifuge testing can include: non-repeatability of test results, undesirable vertical motions, including rocking of soil, inability to produce input motions with the broad frequency content of real earthquake motion, and container effects.

### ***10.3.4 Full Scale Test Prototypes***

Testing of actual piles should be used when possible. However, only single or a small group of piles can be tested because of costs involved. Test results from a single pile in highly heterogeneous soil may not be representative. Also, test loads are applied at pile head, representing inertial effects. Even if ground motion is simulated by using blasting, the frequency content and amplitudes of ground displacements are likely to be different from those during earthquakes and some interpretation of the results obtained is still required.

## 10.4 Simple Model

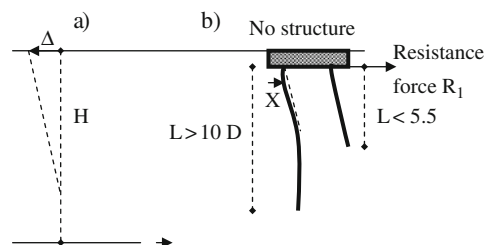
### 10.4.1 Kinematic Effects

The case of non-liquefied soil is considered here. A sketch of pile bending caused by ground movement is shown in Fig. 10.2. Fixed headed piles are likely to experience some lateral soil resistance (force  $X$  in Fig. 10.2b) because of different horizontal displacement exhibited by the piles and soil. However, the lateral soil resistances are small for small differential horizontal displacement between pile and soil and near ground surface, except in very stiff clay.

Averaged transversal wave velocity  $v_s$  is obtained from field tests or calculated as  $v_t = 4HT_h^1$ , where  $T_h$  is predominant period of horizontal ground vibration and  $H$  is layer thickness. The period  $T_h$  can be inferred from the peak of displacement response spectrum (e.g. EN 1998-1, 2004). An average equivalent ground shear modulus  $G$  is calculated as  $G = \rho v_s^2 c$ ,  $c = \text{maximum of } 1 - 0.222a_{\text{peak,surface}}$  and 0.35, where  $\rho$  is ground unit density,  $c$  is a correction coefficient based on EN 1998-5 (2004) table. The resultant horizontal acting force  $F_1$  over pile cap area  $A$  or twice the area of a single pile and pile depth  $L$  is calculated following the expression for shear stress at depth  $L$  (e.g. Seed and Idriss, 1971)  $F_1 = 0.65a_{\text{peak,surface}}A_{\text{pilecap}}\rho L r_d$ , where  $a_{\text{peak,surface}}$  is the peak horizontal ground acceleration at the ground surface in the free field,  $r_d$  is the reduction factor with depth of (e.g. Seed and Idriss, 1971, in EN 1998-5 (2004),  $r_d = 1$ ), area  $A_{\text{pilecap}}$  is taken approximately equal to the area of pile cap for a pile group or twice the cross section area of a single pile to represent a trapped soil mass in front of the pile,  $L$  is pile length. Averaged shear strain  $\gamma$  over pile length  $L$  is calculated as  $\gamma = F_1 * A_{\text{pilecap}}^{-1} * G^{-1}$ . An equivalent horizontal displacement  $\Delta$  at the ground surface is calculated as  $\Delta = \gamma L$ . For displacement  $\Delta$ , the resistance force  $R_1$  of a pile group with at least two piles in direction of  $\Delta$  is calculated as for beams with fixed end subjected to end displacement  $\Delta$  (e.g. Jenkins, 1989):

$$\begin{aligned} R_1 &= \frac{12 \cdot E \cdot J \cdot \Delta}{L^3} \cdot N_{\text{piles}}, \quad L \geq 10 \cdot D \\ R_1 &= \frac{3 \cdot E \cdot J \cdot \Delta}{L^3} \cdot N_{\text{piles}}, \quad L \leq 5.5 \cdot D \end{aligned}, \quad (10.1)$$

**Fig. 10.2** (a) Cross section through a soil layer with thickness  $H$  and horizontal displacement  $\Delta$  at the ground surface, (b) deflection of long ( $L \geq 10D$ ) and short ( $L \leq 5.5D$ ) vertical pile with length  $L$  and diameter  $D$



where  $EJ$  is pile flexural stiffness ( $E$  is Young's modulus,  $J$  is the second moment of cross sectional area). A linear interpolation is assumed for the multiplying coefficients between 12 and 3 for  $5.5D \leq L \leq 10D$ . The effect of resistance force  $R_1$  on the shear strain  $\gamma$  and displacement  $\Delta$  due to kinematic interaction is calculated as:

$$\gamma_{\text{new}} = \frac{(F_1 - R_1)/A_{\text{pilecap}}}{G}, \quad (10.2)$$

$$\Delta_{\text{new}} = \gamma_{\text{new}} \cdot L$$

The effect is usually small; otherwise an iterative loop using equations for  $R_1$  and  $\gamma_{\text{new}}$  can be applied until the difference between calculated and initial value is smaller than a target value. The transversal force at pile top  $T_1 = R_1 N_{\text{piles}}^{-1}$ . The bending moment  $M_1$  at pile top due to horizontal displacement  $\Delta$  (i.e.  $\Delta_{\text{new}}$ ) is calculated for a pile group with at least two piles in direction of  $\Delta$  as for beams with fixed ends subjected to displacement  $\Delta$  (e.g. Jenkins, 1989):

$$M_1 = \left( \frac{6 \cdot E \cdot J \cdot \Delta}{L^2} + P \cdot \Delta \right) \cdot N_{\text{piles}}, \quad L \geq 10 \cdot D, \quad (10.3)$$

$$M_1 = \left( \frac{3 \cdot E \cdot J \cdot \Delta}{L^2} + P \cdot \Delta \right) \cdot N_{\text{piles}}, \quad L \leq 5.5 \cdot D$$

where  $P$  is axial force in pile from the static and inertial load. For inclined (raking) piles, the additional axial force in the piles from kinematic interaction is  $\pm F_1 N_{\text{piles}}^{-1} \sin \psi^{-1}$ , where  $\psi > 0$  is the angle of pile inclination to the vertical. A linear interpolation is assumed for the multiplying coefficients between 6 and 3 for  $5.5D \leq L \leq 10D$ . For a single long pile ( $L \geq 10D$ ) or a single row of long piles bended in direction perpendicular to the row, the multiplying coefficient in equations for  $R_1$  and  $M_1$  is 3. For a single short pile ( $L \leq 5.5D$ ) or a single row of short piles bended in direction perpendicular to the row, the multiplying coefficient in equations for  $R_1$  and  $M_1$  is 0. A linear interpolation is assumed for the multiplying coefficients between 0 and 3 for  $5.5D \leq L \leq 10D$ .

#### 10.4.2 Inertial Effects

As foundations and structures are connected to ground, ground acceleration during earthquakes causes structural acceleration in the same direction but inertial force in opposite direction of the acceleration. The maximum value of inertial force equals to the product of structural mass  $m_s$  and structural acceleration  $a_{\text{structure}}$  at the centre of gravity of the mass  $m_s$ . Structural acceleration is usually obtained from acceleration response spectra or from measurements for existing structures exposed to earthquakes. Design spectrum is defined in EN 1998-1 (2004), for example.

Response spectra acceleration is dependent on fundamental period of structural vibration  $T_s$ , for structures on rigid bases such as rock. However, majority

of structures are founded on and in soil layers, which are flexible and exhibit their own motion. An equivalent period of structural vibration  $T_e$  can be calculated as (e.g. Wolf, 1994):

$$T_e = \sqrt{T_s^2 + T_h^2 + T_r^2}, \quad (10.4)$$

where  $T_s = 2\pi(m_s k_s)^{-1/2}$ ,  $k_s$  is structural stiffness in horizontal direction (= ratio between applied horizontal force and caused structural displacement),  $T_h$  is the fundamental period of horizontal vibration of ground layers  $= 4^*H^*v_t^{-1}$ ,  $T_r$  is the fundamental period of rocking of structure and its foundation (i.e. for an inverted pendulum)  $= 2\pi[I_\theta(k_\theta - m_s^*g^*B)^{-1}]^{1/2}$ ,  $I_\theta$  is mass moment of inertia of structure with respect to the top of foundation,  $k_\theta$  is foundation stiffness in rocking (= ratio between applied turning moment and foundation rotation in radians),  $g$  is the gravitational acceleration,  $B$  is structural height above its foundation. Clause 4.3.3.2.2 of EN 1998-1 (2004), states that for building with height of up to 40 m, an approximation of  $T_s = C_t^*B^{3/4}$ , where  $C_t$  is 0.085 for moment resistant space frames, 0.075 for moment resistant space concrete frames and for eccentrically braced steel frames and 0.050 for all other structures.

The inertial force in a structure acts in the same direction as the resistance force in Fig. 10.2b from kinematic interaction. Corrected peak ground surface acceleration  $a_{\text{new,peak,surface}}$ , to represent inertial interaction effects can be calculated from the following equation as:

$$a_{\text{new,peak,surface}} = \frac{F_1 - m_s \cdot a_{\text{structure}}}{0.65 \cdot \rho \cdot A_{\text{pilecap}} \cdot L \cdot r_d} \quad (10.5)$$

Change in  $a_{\text{peak,surface}}$  also affect change in  $\Delta$  and the kinematic effect.

Of particular interest is to calculate additional transversal force and bending moments at pile tops due to inertial effects. While the transversal forces due to inertial effects are in opposite direction to the transversal forces due to kinematic effects, the bending moments act in the same direction and therefore are additive. The transversal forces at pile tops due to inertial effects are calculated as:

$$T_2 = \frac{m_s \cdot a_{\text{structure}} - A_{\text{pilecap}} \cdot (a \cdot c_u \text{ or } \sigma_v' \cdot \tan \delta)}{N_{\text{piles}}}, \quad (10.6)$$

where  $A_{\text{pilecap}}$  is area of pile cap for a pile group or twice the cross section area of a single pile to represent a trapped soil mass in front of the pile,  $\alpha$  is soil cohesion mobilisation factor ( $\sim 0.5$ ),  $c_u$  is undrained shear strength of fine grained soil (clayey) including the rate effect,  $\sigma_v'$  is effective vertical stress at the underside of pile cap,  $\delta$  is friction angle between soil and pile cap in coarse grained soil (silt, sand, gravel). For cast in place foundation,  $\delta = \phi$ , where  $\phi$  is friction angle of coarse grained soil. Whole area of piled cap is considered because the part of area occupied by piles transfers the inertial force to piles and further into surrounding soil in lateral direction.

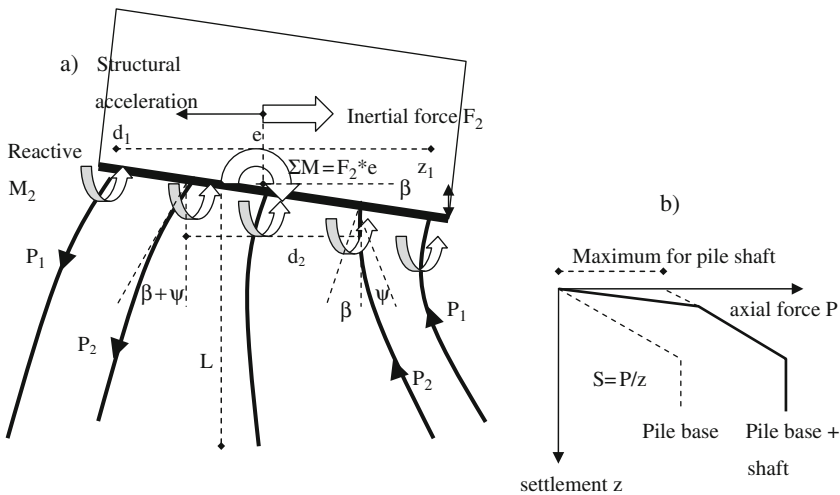


**Fig. 10.3** (a) Sketch of rotated pile cap with bending moments  $M$  and reactive forces  $P$ , (b) linearized axial pile force  $P$  – pile settlement  $z$  relationship

The bending moments  $M_2$  at pile tops due to inertial effects are calculated based on sketch in Fig. 10.3. The effect of inertial force on horizontal pile displacement and its bending is taken into account implicitly when using Equation (10.5).

In Fig. 10.3a,  $\Sigma M = m_s * a_{\text{structure}} * e$ , where  $e$  is eccentricity of the mass centre of gravity with respect to the pile cap underside level. For a linear relationship between reactions forces  $P_i$  and their distances from the centre of pile cap i.e. distances  $d_i$  between reaction forces in the case of a rigid pile cap, it follows:

$$\Sigma M = M_2 \cdot N_{\text{piles}} + \frac{P_1}{d_1} \cdot \sum d_i^2 \cdot (\cos \psi - \sin \psi), \quad (10.7)$$

when  $P_i = P_1 \cdot \frac{d_i}{d_1}$

where  $\psi$  is the angle of pile inclination to the vertical. The angle of rotation of pile cap  $\beta$  is calculated as:

$$\beta = 2 \cdot \frac{z_1}{d_1} = \frac{M_2 \cdot L}{3.5 \cdot EJ}, \quad (10.8)$$

where the coefficient 3.5 is taken as an average value between 3 and 4 for long and short piles i.e. beams with fixed or free rotating end that is rotated for an angle  $\beta$  (e.g. Jenkins, 1989). Pile settlement  $z_1 = P_1 * S^{-1} * \cos \psi$ , where axial pile stiffness  $S$  (= ratio between applied force and pile settlement) can be defined from pile tests results, which linearized form is sketched in Fig. 10.3b.

When  $z_1$  from above equation is placed into left hand side of equation for  $\beta$ , it follows that:

$$M_2 = \frac{7 \cdot P_1 \cdot E \cdot J \cdot \cos \psi}{S \cdot d_1 \cdot L}, \quad (10.9)$$

where  $P_1$  is the axial force in the most distant piles,  $EJ$  is pile flexural stiffness ( $E$  is Young's modulus,  $J$  is second moment of cross sectional area),  $S$  is axial pile stiffness,  $d_1$  is the horizontal distance between most distant piles in a group,  $L$  is pile length. When above equation is placed in equation for  $\Sigma M$  it follows:

$$P_1 = \frac{\Sigma M \cdot S \cdot d_1 \cdot L}{N_{piles} \cdot 7 \cdot E \cdot J \cdot \cos \psi + S \cdot L \cdot \sum d_i^2 \cdot (\cos \psi - \sin \psi)} \quad (10.10)$$

For a single pile or pile group bended in direction perpendicular to the group  $M_2 = \Sigma M^* N_{piles}^{-1}$  and  $P_1 = 0$ . For axial forces in pile equal to about a half of the ultimate pile capacity (factor of safety about 2), the external force is carried mostly by pile shaft friction, displacement  $z$  is only a few millimetres and can be estimated from laboratory shear tests between soil and the interface representing pile shaft. For larger axial force, an exponential increase in displacement  $z$  occurs and displacement  $z$  at ultimate pile capacity can be of the order of 10% $D$ , where  $D$  is pile diameter.

The simplified analysis does not consider the bending moments in piles at the interfaces of soil layers with different stiffness. The numerical analyses, field measurements and small-scale tests indicate that the bending moments in piles at the layer interfaces are of similar value as the bending moments at the pile tops (e.g. Finn and Fujita, 2002; Nikolaou et al., 2001; Gazetas and Mylonakis, 1998).

## 10.5 Case Histories

The simple analyses are used for eleven case histories of piled foundation subjected to earthquakes in order to assess the applicability and accuracy of the analyses.

### 10.5.1 Ten Storey Building in Mexico City

Mendoza and Romo (1989) described the failure of a ten storeys building supported on piles through soft soil (Fig. 10.4) during the 1985 Michoacan earthquake with magnitude  $M_s = 8.1$  at an epicentral distance of 350 km from Mexico City. The peak acceleration of the record obtained at Ciudad Universitaria was only 0.035g.

Mexico City is situated partly on soft lake deposits, which likely amplified bedrock motion. Transversal wave velocities through the lake deposits vary in the range from 30 m/s from 2.6 m below the ground surface to 75 m/s at 49 m depth, with exception of two stiffer layers at 28–29 m depth with transversal wave velocity of 150 m/s and 32–35 m depth with transversal wave velocity of 130 m/s according to Stephenson and Lomnitz (2005). They also indicated that the layer at 49–160 m depth has transversal wave velocity of 475 m/s. The top 2.6 m of soil above ground water level is hard crust with the transversal wave velocity likely comparable to the

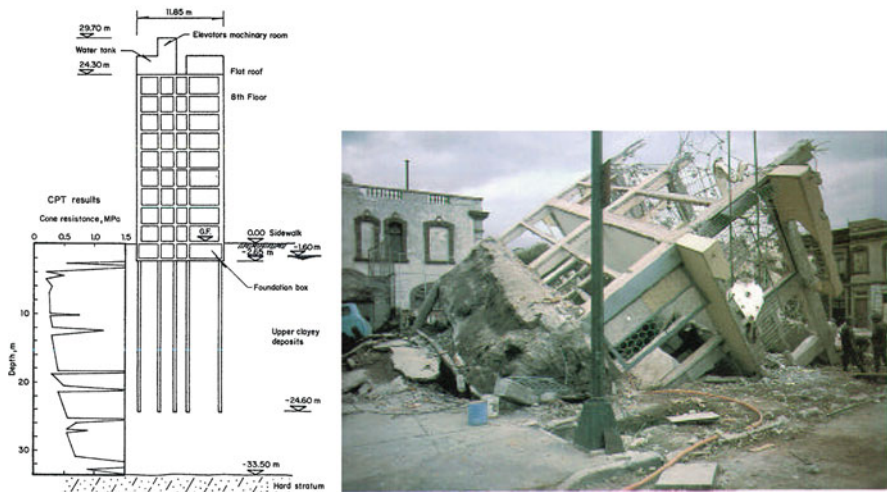


**Fig. 10.4** Elevation of the ten storeys building in Mexico City and after toppling (Meymand, 1998)

velocity of stiffer deep layers. The basement of the building was located at 2.6 m depth within top dry crust.

Several input data have been assumed:  $a_{\text{peak,surface}}$  of  $1.5 \text{ m/s}^2$  is adopted from Idriss (1990), the period of vibration  $T_e = 2.17 \text{ s}$  and  $a_{\text{structure}}$  of  $7.5 \text{ m/s}^2$  is adopted from Romo and Seed (1986),  $m_s$  of  $385,000 \text{ kg}$  is calculated from the floor area of  $70 \text{ m}^2$ , the number of storeys plus basement of 11 and assumed mass per storey of  $500 \text{ kg/m}^2$ , static  $P_o$  of  $2.5 \times 10^5 \text{ N} = 385,000 \times 9.81 / 15$  per pile out of 15 piles,  $r_d$  from Seed and Idriss (1971),  $S$  of  $1 \times 10^8 \text{ N/m}$  as  $2.5 \times 10^5 / 0.0025 \text{ m}$ , where  $0.0025 \text{ m}$  is assumed displacement necessary to activate shaft friction initially.

### 10.5.2 Twelve Storey Building in Yokohama – Japan

Nikolaou et al. (2001) critically reviewed some existing design methods for kinematic pile loading, developed new simple formula for piles in homogeneous and layered soil and presented a case study involving instrumented piled foundation of a twelve storey building in Yokohama – Japan. They showed that the magnitude of kinematic moments depends mainly on the stiffness contrast between soil layers, the pile-soil stiffness contrast, the excitation frequency, and the number of excitation cycles.

The building basement is supported by 20 reinforced concrete piles, 35 m long and 1.7 m in diameter. The soil profile consists of about 39 m of soft saturated highly plastic silty clay (plasticity index~50%) with measured shear wave velocity in the range from 135 to 240 m/s. Clay is underlain by stiff mudstone with shear wave velocity of approximately 480 m/s. The earthquake of 2 February 1992 had a magnitude of 5.9, focal depth of 93 km and epicentral distance from the site of

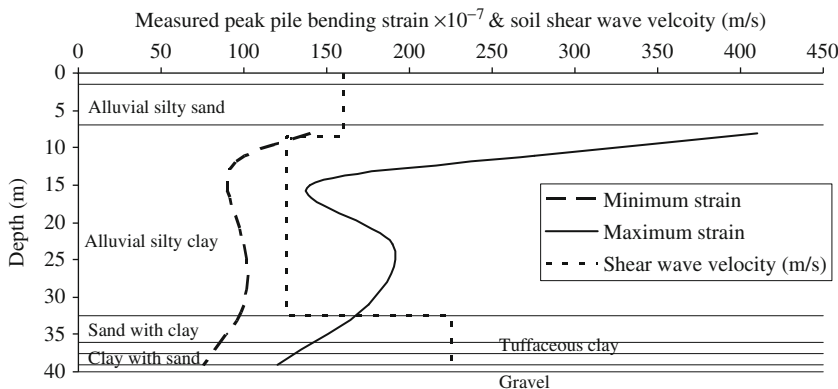


**Fig. 10.5** Peak pile bending strain and soil shear wave velocity profiles under the twelve storeys building in Yokohama – Japan (based on data from Nikolau et al., 2001)

32 km. The largest acceleration recorded on the ground surface was about  $0.05g$ . The fundamental period of vibration of the clay layer was approximately 1 s based on the peak of the response spectral acceleration.

Several input data have been assumed:  $m_s$  of 4,577,950 kg is calculated from the floor area of  $704.3 \text{ m}^2$ , the number of storeys plus basement of 13 and assumed mass per storey of  $500 \text{ kg/m}^2$ , static  $P_o$  of  $2.25 \times 10^6 \text{ N}$  =  $4,577,950 \times 9.81 \times 20^{-1}$  per pile out of 20 piles,  $r_d$  from Seed and Idriss (1971),  $S$  of  $2.5 \times 10^8 \text{ N/m}$  as  $2.25 \times 10^6 \times 0.009^{-1} \text{ m}$ , where 0.009 m is pile shortening plus assumed its toe settlement due to  $P_o$ , the structural period  $T_s = 0.05 \times 49.6^{3/4} = 0.93 \text{ s}$ ,  $E = 2 \times 10^7 \text{ kPa}$ ,  $J = 1.7^4 \times \pi \times 64^{-1} = 0.41 \text{ m}^4$ ,  $EJ = 8.2 \times 10^6 \text{ kN m}^2$ ,  $\beta = 2 \times 4,577,950 \times 9.81 \times 49.6^* 0.5 \times 35^* (20^* 7^* 8.2^* 10^6 + 2.5^* 10^8 \times 35^* 2870)^{-1} = 0.003 \text{ rad}$ ,  $k = 4,577,950 \times 9.81 \times 49.6^* 0.5 / 0.003 = 3.7 \times 10^{11} \text{ Nm/rad}$ , the rocking period  $T_r = 2\pi^* [4,577,950^* (49.6^* 0.5)^2 \times (3.7 \times 10^{11} - 4,577,950 \times 9.81 \times 49.6)^{-1}]^{1/2} = 0.55 \text{ s}$ , the equivalent period of vibration of the structure and soil  $T_e = (1^2 + 0.93^2 + 0.55^2)^{1/2} = 1.47 \text{ s}$ ,  $a_{\text{structure}}$  of  $0.04g$  from the acceleration spectrum of recorded near surface acceleration at period of 1.47s (Fig. 10.5).

### 10.5.3 Imperial Valley County Services Building in California

Hadjian et al. (1990) reported the case of the building severely damaged in the 1979 Imperial Valley earthquake with a local magnitude 6.6. Lee et al. (1982) reported the horizontal peak accelerations in the free field (104 m away from the building) as  $0.20g$  (N02E component) and  $0.22g$  (N92E component) and on the ground floor of  $0.29g$  (NS component) and  $0.34g$  (EW component). The recording instrument is located about 38 m from the centre of the building. Both torsion and/or soil-structure (near) resonance could have caused the increased peak accelerations.

The ground profile consists of layers of mixed clay, silt and sand. The 6 storey reinforced concrete building has an area of  $60 \times 124 \text{ m}$ . It is supported on 204

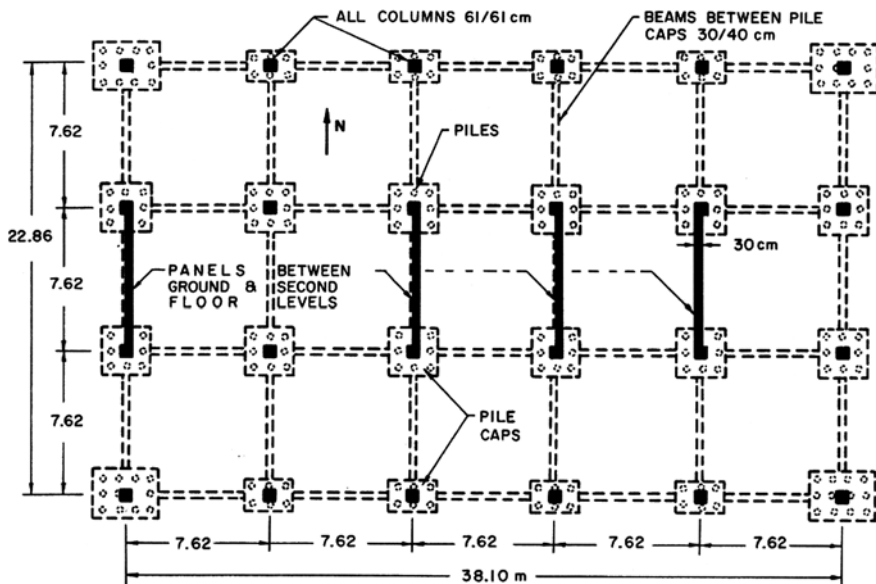


**Fig. 10.6** Foundation and ground level of Imperial County services building in El Centro – California (Kojic et al., 1984)

Raymond step-taper piles driven 14 m trough soft to stiff sandy clay. The predominant period of the structure is 0.61 and 1.75 s in NS and EW direction respectively according to Hadjian et al. (1990).

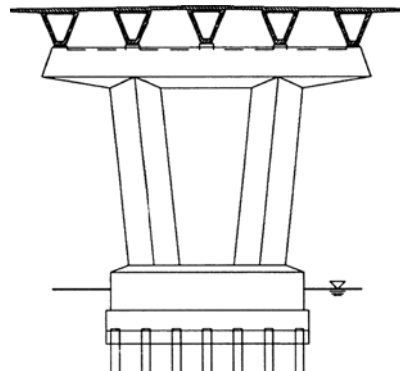
Several input data have been assumed:  $m_s$  of  $3.1 \times 10^7$  kg based on assumed 1.5MN design bearing capacity of Raymond piles, ground properties based on Porcella (1984) (Fig. 10.6).

#### 10.5.4 Dumbarton Bridge in California

Fenves et al. (1992) described and analyzed by finite elements the response of 2226 m long bridge with 43 spans affected by the 1989 Loma Prieta earthquake. The 1989 Loma Prieta earthquake had a magnitude  $M_L = 7.1$  and the epicentre at approximately 55 km from the bridge. The peak horizontal accelerations in two orthogonal directions were  $0.127g$  in the free field at a site approximately 1.2 km from the west approach to the bridge. The peak horizontal accelerations recorded at the bases of piers were from  $0.167g$  to  $0.266g$  in the longitudinal direction of the bridge and from  $0.077g$  to  $0.126g$  in the transversal direction. At the tops of the instrumented piers, the peak longitudinal acceleration varied between  $0.327g$  and  $0.442g$ , and the peak transversal acceleration was between  $0.097g$  and  $0.176g$ .

The approach structure piers are founded within 12 to 18 m and the main structure piers within 2 to 17 m thick soft clay. The soft clay layer is underlain by stiffer

**Fig. 10.7** Elevation of pier for approach structure of Dumbarton Bridge in California (adapted from Fenves et al., 1992)



silty clay, older bay clay, and the formation of very stiff clay. The depth of bedrock is believed to be at least 180 m. The piers of the approach structures have from 28 to 43 piles. These are either 0.5 m diameter pre-stressed concrete piles or 0.56 m diameter steel piles. The pile lengths are from 12 to 17 m. The pier foundations of the main structure have either 21–32 pre-stressed concrete piles with 1.37 m diameter, or 52 steel piles with 0.56 m diameter. The piles are embedded approximately 15 m through bay clay and silty clay. The bridge has a large number of vibration modes, many of which are spaced at periods greater than 0.5 s. The fundamental vibration period of the main structure is 1.9 s in the longitudinal direction and 1.6 s in the transversal direction. The west approach structure has the period of 1.6 s in the longitudinal direction and 2.2 s in the transversal direction.

Several input data have been assumed:  $H$  of 50 m based on  $T_h$  of 2 s from the peak in the Fourier response spectra and estimated  $v_s$  of 100 m/s,  $m_s$  of 550,000 kg is calculated from the geometry of the reinforced concrete pier and pre-stressed lightweight concrete girder of the approach structure, static  $P_o = 550,000 * 9.81 * 28^{-1} \sim 2 * 10^5$  N,  $S$  of  $3 * 10^8$  N/m is based on the ratio between the  $P_o$  and  $z$  of 0.00065 m, which is estimated from the pile shortening plus some settlement of its toe (Fig. 10.7).

### 10.5.5 Northwest Connector in California

Fenves and Desroches (1994) described and analyzed by finite elements the response of 775 m long and 16 spans connector to the 1992 Landers and Big Bear earthquakes. The Landers event, with a magnitude of  $M_s = 7.6$  and at an epicentral distance of 85 km, induced the free field peak horizontal ground acceleration of 0.09g. The same day Big Bear event, with a magnitude of  $M_s = 6.6$  and at an epicentral distance of 30 km, induced the free field peak horizontal ground acceleration of 0.11g. The recorded peak horizontal accelerations of the pile cap located about a quarter length of the connector were about 0.1g during the Landers and Big Bear earthquake. However, the recorded peak horizontal accelerations of the pile

cap located at the mid span of the connector were about  $0.17g$  in both horizontal directions during the Landers earthquake and  $0.25g$  (in the longitudinal direction) and  $0.15g$  (in the transversal direction) during the Big Bear earthquake.

The site consists of deep unconsolidated alluvial deposits about 300 m thick. The top soil layer generally involves medium to dense clean and silty sand with varying thickness from 6 to 18 m. The 28–48 pile groups contain 0.3 m square pre-cast pre-stressed piles. The pile lengths range from 6.3 m (at bent 5) to 15 m (at bent 8). Thirty additional steel pipe piles driven around the perimeter have 0.4 m diameter, 12.5 mm wall thickness and 18 to 25 m length. The fundamental vibration mode of the structure has a period of 1.51 s, the second mode 1.19 s, the third mode 1.02 s and 0.79, 0.65 and 0.55 s respectively at higher modes during the Landers earthquake. The fundamental vibration mode of the structure has a period of 1.78 s, the second mode 1.24 s, the third mode 1.14 s and the fourth mode 0.95 s during the Big Bear earthquake. According to the response spectra, the free field predominant period was 0.6 s with a secondary period at about 1.9 s during the Landers earthquake and about 0.6 s with secondary period at about 1.8 s during the Big Bear earthquake.

Several input data have been assumed:  $H$  of 50 m based on  $T_h$  of 0.6 s, the equivalent structure and soil period of vibration  $T_e$  of 0.55 s (6th mode) based on the  $a_{\text{structure}}$  and  $a_{\text{peak,surface}}$  ratio of 6.4,  $m_s$  of 280,000 kg based on the geometry of the reinforced concrete pier and box girder,  $S$  of  $2 \times 10^8$  N/m based on  $P_o$  of  $1 \times 10^6$  N (100 t) and assumed  $z_1$  of 5 mm (Fig. 10.8).

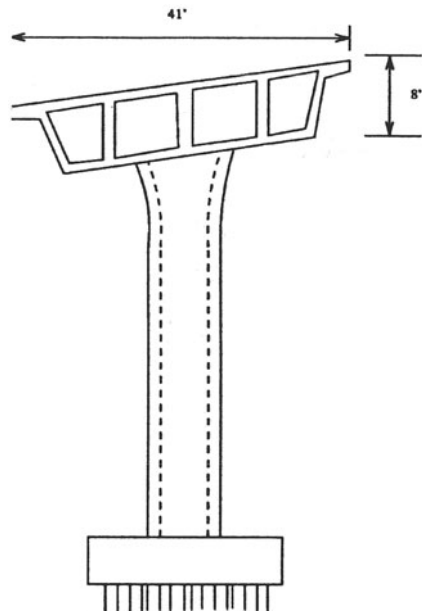


**Fig. 10.8** Original elevation of Northwest connector in California (adapted from Fenves and Desroches, 1994)

### 10.5.6 Painter Street Bridge in California

Makris et al. (1994) provided data on the response of a concrete bridge (Figs. 10.9 and 10.10) located near Rio Dell shaken by the Petrolia earthquake. The 1992 Petrolia earthquake had a local magnitude of 7.1. It occurred at a fault distance of 18 km. The earthquake induced the peak surface ground acceleration of  $0.55g$  in the transversal and  $0.39g$  in the longitudinal direction of the bridge in the nearby field some 20 m away. The recorded peak accelerations at the pile cap were  $0.48g$  in the transversal direction and  $0.34g$  in the longitudinal direction of the bridge.

Medium dense clayey to gravelly sand and sandy silt exists to a depth of 10 m below the ground surface. This layer is underlain by very dense gravelly and silty sand. The upper 10 m of soil has a shear wave velocity of 250 m/s and density  $1600 \text{ kg/m}^3$ . The shear wave velocity of 350 m/s and density of  $2200 \text{ kg/m}^3$  are assumed to 40 m depth. Two pile groups, each consisting of  $4 \times 5$  driven concrete piles of 0.36 m diameter and 7.62 m length, support the bridge. The pile cap dimensions are  $3.66 \times 4.57 \text{ m}$ . An estimated lumped mass is  $1.13 \times 10^6 \text{ kg}$  and the fundamental period of 0.3 s according to Makris et al. (1994).

Several input data have been assumed:  $T_h$  of 0.43 s based on the predominant frequency of the input motion obtained from the Fourier spectrum,  $H$  of 27 m based on  $T_h$  of 0.43 s and  $v_t$  of 250 m/s, static  $P_o$  of  $1.2 \times 10^5 \text{ N}$  based on  $m_s$  of 250,000 kg,  $S$  of  $1.2 \times 10^8 \text{ N/m}$  based on  $P_o$  and assumed  $z_1$  of 1 mm.

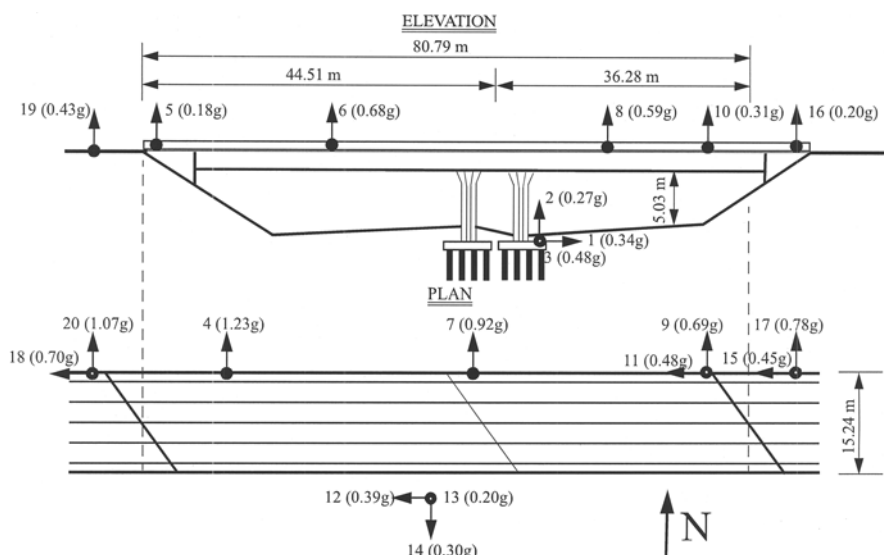
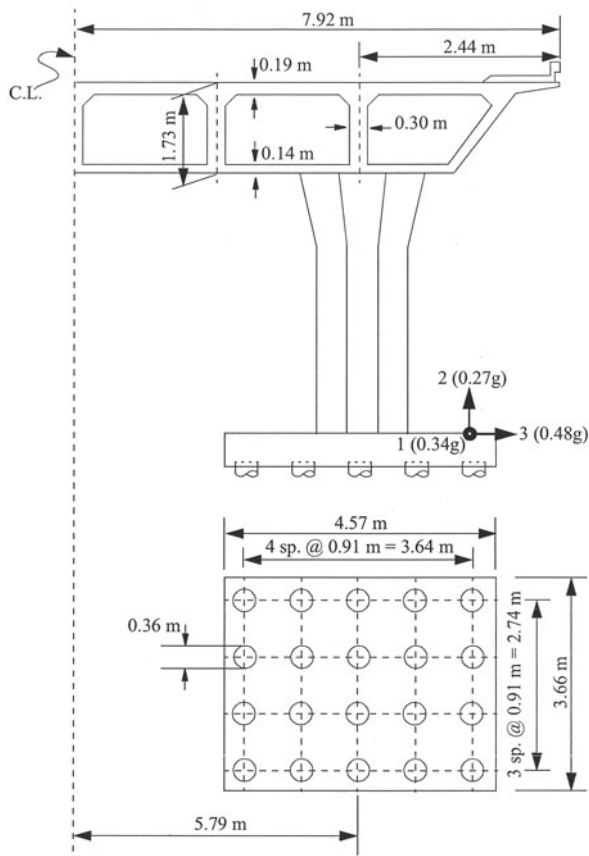


**Fig. 10.9** Elevation and plan view of Painter Street Bridge in California with recorded peak accelerations (Zhang and Makris, 2001)

**Fig. 10.10** Cross section of the bridge deck and pile layout of Painter Street Bridge in California with recorded peak accelerations (Zhang and Makris, 2001)



### 10.5.7 Meloland Road Overpass in California

Werner et al. (1987) applied a system identification methodology to the array of strong-motion recordings, in order to assess the seismic response characteristics of the bridge, which is located east of El Centro in California, shaken strongly by the 1979 Imperial Valley earthquake. A two-span reinforced concrete box girder structure (Figs. 10.11 and 10.12) is located only 0.5 km away from the causative fault for the earthquake, with a local magnitude 6.6. The horizontal peak accelerations in the free field were 0.315g (000 component) and 0.296g (270 component). The recorded peak accelerations of the pile cap were 0.28g (000 component) and 0.33g (270 component).

A single pier of the bridge is supported by 25 timber piles of 0.43 m diameter and 15.2 m length. The piles are driven into medium stiff sandy clay with an average SPT  $N$  value of 14 according to Meymand (1998). The transversal wave velocity of 240 m/s corresponds to the  $14 N_{SPT}$ , according to equation  $v_s = 100 * N_{SPT}^{1/3}$  (Japan

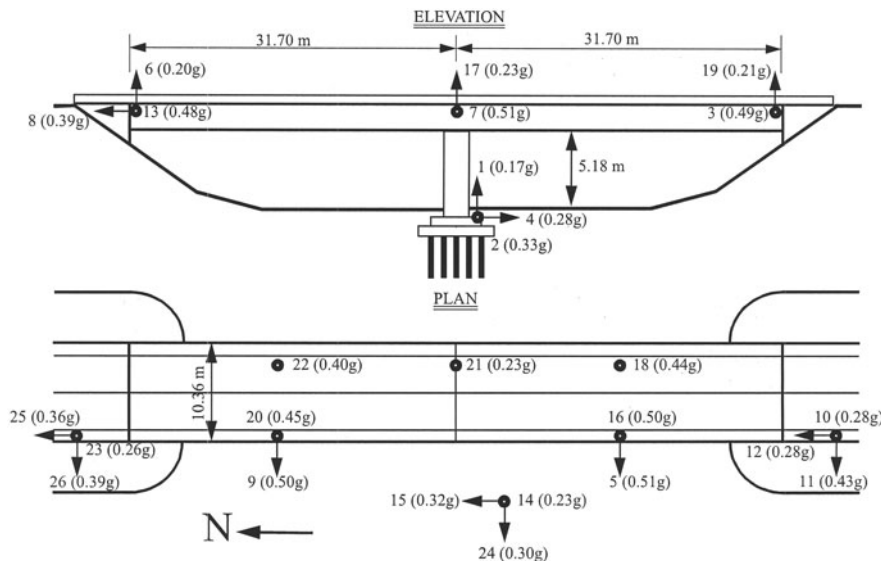


**Fig. 10.11** Elevation and plan view of Meloland Road Bridge in California with recorded peak accelerations (Zhang and Makris, 2001)

Road Association, 2002). The Fourier amplitude spectra (Werner et al. 1987) for the transverse (270 component) motion at the base of the pier indicate the predominant equivalent period of 2.66 s.

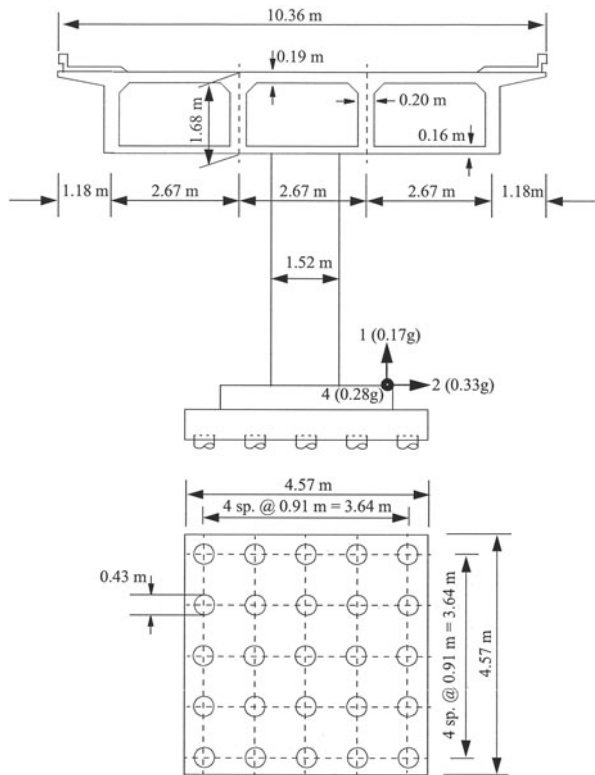
Several input data have been assumed:  $H$  of 160 m based on  $T_h$  of 2.66 s and  $v_s$  of 240 m/s,  $m_s$  of 364,000 kg based on the geometry of the bridge, static  $P_o$  of  $1.4 \times 10^5$  N based on  $m_s$  of 364,000 kg, the equivalent period of vibration of structure and soil  $T_e$  of 0.4 s based on Werner et al. (1987),  $S$  of  $1 \times 10^8$  N/m based on  $P_o$  of  $1.4 \times 10^5$  N and  $z_1$  of 1.4 mm.

### 10.5.8 Ohba-Ohashi Road Bridge in Japan

Ohira et al. (1984) presented the results of observations of the response of foundation piles of a road bridge in the city of Fujisawa in Kanagawa prefecture of Japan. The Kanagawa-ken Seibu earthquake had magnitude 6.0. The epicentral distance was 20 km and the hypocentral depth 42 km according to Ohira et al. (1984). The recorded peak horizontal acceleration of the foundation was  $36.7 \text{ cm/s}^2$  along the bridge axis and of the ground surface  $113.5 \text{ cm/s}^2$  at a distance of 70 m away from and parallel to the bridge axis.

The bridge spans a valley about 400 m wide at the location of the bridge crossing. The sediments in the valley involve diluvial deposits of cohesive soil and fine sand, with the shear wave velocity of 400 m/s, upon which extremely soft alluvial strata of humus and silt, with the shear wave velocity between 40 and 65 m/s, exist. The

**Fig. 10.12** Cross section of the bridge deck and pile layout of Meloland Road Bridge in California with recorded peak accelerations (Zhang and Makris, 2001)



depth of the top soil at the location of instrumented pier No. 6 is about 21 m. The instrumented pier No. 6 is supported by 64 steel pipe piles of diameter 600 mm and length 23 m; half are battered at 5 v:1 h. The pile cap size is 12 × 12 m, Fig. 10.13.

Several input data have been assumed:  $T_h$  of 0.83 s from the peak of power spectrum of the free field ground motion,  $r_d$  of 0.8 from Seed and Idriss (1971), static  $P_o$  of  $8.4 \times 10^4$  N from both the pile toe capacity and assumed  $m_s$  of 550,000 kg, the equivalent period of vibration of the structure and soil  $T_e$  of 1.3 s from the peak of power spectrum of the foundation motion,  $S$  of  $1.7 \times 10^7$  N/m from  $P_o$  of  $8.4 \times 10^4$  N and  $z_1$  of 5 mm.

### 10.5.9 Landing Road Bridge in New Zealand

Berrill et al. (2001) presented a case study of the effect of lateral spreading on the piled foundation of the Landing Road Bridge, Whakatane, New Zealand, during the 1987 Edge-cube earthquake with magnitude 6.3. The earthquake epicentre was 17 km and the closest point on the ground surface rupture by a tectonic fault was 8 km from the site. A peak acceleration of 0.33g was recorded at the base of a

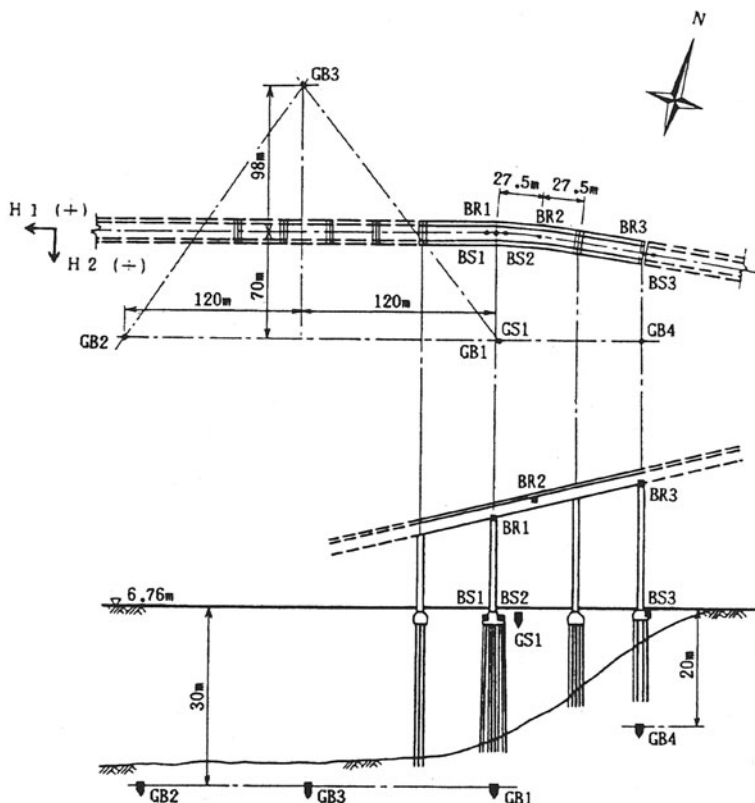


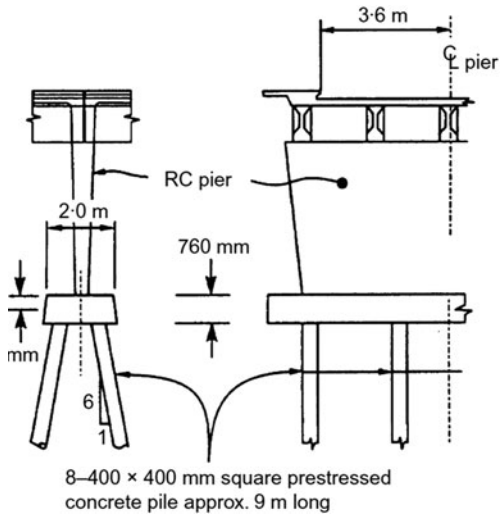
**Fig. 10.13** Layout and elevation of Ohba-Ohashi Road Bridge in Japan with the locations of instruments around the pier No. 6 (Ohira et al., 1984)

rock-fill dam that is also located about 8 km from the nearest ground surface brake by the fault. The ground shaking caused widespread liquefaction.

The bridge comprises 13 simply supported spans, which are bolted together and to the piers forming stiff moment resisting connections. The piers are supported by eight 406 mm square pre-stressed concrete piles raked at 1:6. Cracking of piles and piers occurred during the earthquake. Piers B and C leaned towards the river by about  $1^\circ$ , possible as a result of lateral force imposed by about 2 m thick non-liquefied crust movement, which is evident as mound of soil next to the pier C. Below the top crust, about 2 m thick soil layer liquefied based on the cone penetration test resistance of about 5 MPa and the standard penetration test blow count in the range from 5 to 10. The crust contains mainly silt with woodchips while the liquefied layer contains mainly loose silty sand and sand. The sand at greater depths is medium dense to dense.

Several input data have been assumed:  $v_s$  of 213 m/s based averaged cone penetration resistance of 10 MPa over 16 m depth, which corresponds to standard

**Fig. 10.14** Side and front elevations of typical pier of Landing Road Bridge in New Zealand (adapted from Berrill et al., 2001)



penetration test blow count of 20,  $m_s$  of 210,000 kg based on the geometry of the reinforced concrete pier and five precast post-tensioned concrete I beams and cast in place concrete deck (Fig. 10.14), static  $P_o$  of  $2.5 \times 10^5$  N based on  $m_s$  of 210,000 kg,  $S$  of  $2.5 \times 10^8$  N/m based on the  $P_o$  and  $z_1$  of 1 mm.

### 10.5.10 Yachiyo Bridge in Japan

Hamada (1992) described damage to the abutment and piers of Yachiyo bridge during the 1964 Niigata earthquake with magnitude 7.5. The earthquake caused extensive soil liquefaction in Niigata City and the surrounding areas and severe damage to many buildings, bridges, quay walls and lifeline systems. The epicentre was about 50 km from the city. The peak acceleration of 0.16g was measured in the basement and 0.18g on the roof of a building in the city. The predominant period was up to 0.8 s.

The bridge pier P2 was supported by 33 reinforced concrete piles with 0.3 m diameter and about 11 m long. The pier 2 was broken at the level of the ground surface due to permanent ground displacement of 1.1 m. The piles were severely destroyed at a depth of about 8 m from the top of the piles. Numerous horizontal cracks, which could have been caused by large bending, were found when the piles were extracted and examined after the earthquake (Fig. 10.15). Similar damage to the abutment and piers were observed on other river bank. The permanent ground displacements on both banks were from 4 to 6 m toward the river.

Several input data have been assumed:  $H$  of 35 m based on  $T_h$  of 0.8 s and  $v_s$  of 175 m/s ( $\sim 80 \times 10^{1/3}$ ), where 10 is an averaged blow count of the standard penetration test and the formula is from (Japan Road Association, 2002),  $m_s$  of 200,000 kg



**Fig. 10.15** Cracked pre-cast reinforced concrete piles from Yachiyo Bridge during the 1964 Niigata earthquake in Japan (Meymand, 1998)

based on the approach slab dimensions of  $0.5 \times 16 \times 10$  m, static  $P_o$  of  $6 \times 10^4$  N based on  $m_s$  of 200,000 kg,  $S$  of  $6 \times 10^7$  N/m based on the  $P_o$  and  $z_1$  of 1 mm.

### 10.5.11 Hanshin Expressway in Kobe – Japan

Gazetas and Mylonakis (1998), among others, analysed the toppling (Fig. 10.16) of 630 m of the Hanshin expressway in Higashi-nada during the 1995 Hyogoken-Nanbu (Kobe) earthquake with magnitude 7.2 and epicentral distance of about 20 km from Kobe. The accelerogram recorded on 10–15 m thick stiff soil had peak of  $0.83g$ , on softer and thicker deposit to about 70 m depth had peaks of  $0.85g$  and  $0.65g$ .

The 3.1 m diameter and 11 m high bridge piers were supported on 17 reinforced concrete piles of about 1 m diameter and 15 m length. Soil around the piles is medium dense to dense sand with the standard penetration test blow count in the



**Fig. 10.16** A part of collapsed section of Hanshin Expressway in Japan (adapted from [www.hp1039.jishin.go.jp/eqchreng/f7-15.htm](http://www.hp1039.jishin.go.jp/eqchreng/f7-15.htm))

range from 10 to over 50 down to a depth of 20 m. The shear wave velocity was found to be between 200 and 300 m/s down to 30 m depth. The acceleration response spectra from the three accelerograms indicate structural acceleration between 2.1 and  $2.7g$ .

Several input data have been assumed:  $T_h$  of 0.6 s based on  $H$  of 30 m and  $v_s$  of 200 m/s,  $m_s$  of 1,100,000 kg based on the geometry of 3.1 m diameter and 11 m high pier and ribbed deck slab, static  $P_o$  of  $1 \times 10^7$  N based on the geometry of piles and assumed concrete strength in compression,  $S$  of  $2 \times 10^9$  N/m based on the  $P_o$  and  $z_1$  of 5 mm.

## 10.6 Discussion and Conclusions

The input data and the results are shown in Tables 10.1 and 10.2. Homogeneous cross sections of piles without cracks and reinforcement have been considered for calculation of maximum shear force  $T_{\max}$  and bending moments  $M_{\max}$ . The sums of

**Table 10.1** Input data and results of consideration of kinematic effects

No	Structure	H (m)	$T_h$ (s)	$v_s$ (m/s)	$\rho$ ( $\text{kg}/\text{m}^3$ )	$a_{\text{peak,surface}}$ ( $\text{m}/\text{s}^2$ )	$L_{\text{pile}}$ (m)	$A_{\text{pilecap}}$ ( $\text{m}^2$ )	$r_{d,\max}$	G (Pa)	$F_{1-R_1}$ (N)	$\gamma$	$\Delta$ (m)
1	10 storey building in Mexico City	34	2.00	68	1400	1.5	22	70	0.8	6.47E+06	1.68E+06	0.004	0.082
2	12 storey building in Yokohama – Japan	39	1.00	156	1500	0.49	35	704.3	0.7	3.65E+07	8.24E+06	0.000	0.011
3	Imperial Valley County services building in California	55	1.10	200	1800	2.1	14	7440	1	7.20E+07	2.56E+08	0.000	0.007
4	Dumbarton bridge in California – pier 13	50	2.00	100	1400	1.25	13	108	1	1.40E+07	1.60E+06	0.001	0.014
5	Northwest connector in California – bent 8	50	0.60	333	1900	1.1	15	94.5	1	2.11E+08	1.93E+06	0.000	0.001
6	Painter street bridge in California	27	0.43	251	1600	5.5	7.62	16.7	1	1.01E+08	7.28E+05	0.000	0.003
7	Meloland road overpass in California	160	2.66	241	1800	3.1	15.2	20.9	1	1.04E+08	1.15E+06	0.001	0.008
8	Ohba-Ohashi road bridge in Japan – pier 6	21	0.83	101	1100	1.1	22	144	0.8	1.13E+07	1.27E+06	0.001	0.017
9	Landing road bridge in New Zealand – pier C	16	0.30	213	1800	3.2	9	16	1	8.19E+07	5.39E+05	0.000	0.004
10	Yachiyo bridge in Japan – pier P2	35	0.80	175	1800	1.6	11	33	1	5.51E+07	6.80E+05	0.000	0.004
11	Hanshin expressway in Higashi-nada – Japan	30	0.60	200	1900	8.3	15	108	1	7.60E+07	1.45E+07	0.002	0.026

ratios between calculated and maximum shear force  $T/T_{\max}$  and bending moments  $M/M_{\max}$  for kinematic and inertial interaction show that the simple considerations predict failures of the piles belonging to the 10 storeys building in Mexico City, Yachiyo bridge, Landing road bridge in New Zealand and Hanshin expressway in Japan. The simple considerations indicate that the piles of Landing road bridge in New Zealand have failed in bending and the piles at edges of the pile groups of Dumbarton and Painter Street Bridge may have been overstressed according to the simple considerations possibly because the results are based on a number of assumptions.

The simplified analysis of dynamic soil-pile interaction during earthquakes considers:

1. The flexural stiffness of piles using EJ
2. The soil reaction using axial pile stiffness S
3. Pile to pile dynamic (and static) interaction as  $P_i = P_1 d_i / d_1$
4. The degree of freedom of the rotation at/of the pile cap using the angle  $\beta$

$D_{\text{pile}}$ (m)	Pile type	R Coef.	EI (Nm <sup>2</sup> )	N <sub>piles</sub>	$R_1$ (N)	$R_1/F_1$ (%)	$T_1/T_{\max}$ (%)	M Coeff.	$P_0$ (N)	$M_1$ (Nm)	$M_1/M_{\max}$ (%)	Notes	
0.50	concrete	44	12	6.10E+06	15	8.42E+03	0.5	<b>3.4</b>	6	2.50E+05	9.78E+04	<b>626.2</b>	Building failed in toppling mode
1.70	concrete	20.59	12	8.20E+08	20	5.15E+04	0.6	<b>1.7</b>	6	2.25E+06	8.17E+04	<b>17.1</b>	
0.44	Raymond	31.82	12	3.70E+06	204	2.21E+04	0.0	<b>0.1</b>	6	1.50E+06	2.19E+04	<b>26.5</b>	
0.50	concrete	26	12	6.10E+06	28	1.28E+04	0.8	<b>3.4</b>	6	2.00E+05	1.35E+04	<b>107.6</b>	
0.34	0.3m×0.3m+ 16"dia. tubes 1/2" thick	44.12	12	1.40E+06	78	5.62E+02	0.0	<b>0.0</b>	6	1.00E+06	2.22E+03	<b>5.2</b>	After retrofitting
0.36	concrete	21.17	12	1.60E+06	20	2.86E+03	0.4	<b>1.8</b>	6	1.20E+05	6.55E+03	<b>121.4</b>	
0.43	timber	35.35	12	1.68E+07	25	1.15E+04	1.0	<b>0.2</b>	6	1.40E+05	2.03E+04	<b>51.9</b>	
0.60	0.6m dia. ~11 mm w.t.	36.67	12	1.77E+08	64	2.20E+05	17.3	<b>6.1</b>	6	8.40E+04	5.28E+04	<b>6.0</b>	
0.45	concrete square	20	12	4.27E+07	8	2.08E+04	3.9	<b>15.6</b>	6	2.50E+05	4.01E+04	<b>285.2</b>	
0.30	concrete	36.67	12	7.95E+06	33	9.72E+03	1.4	<b>7.4</b>	6	6.00E+04	3.52E+03	<b>156.6</b>	Bridge damaged due to formation of plastic hinges in the piles at the top and bottom of a loose sand layer
1.00	concrete	15	12	9.82E+08	17	1.57E+06	10.8	<b>13.8</b>	6	1.00E+07	3.09E+06	<b>247.0</b>	Expressway failed in toppling mode

**Table 10.2** Input data and results of consideration of inertial effects

No	Structure	$T_h$ (s)	$T_e$ (s)	$a_{peak,structure}$ ( $m/s^2$ )	$m_s$ (kg)	$e$ (m)	$\sum M$ (Nm)	S (N/m)	$d_1$ (m)	$\sum d_i^2 (m^2)$	$L_{pile}$ (m)
1	10 storey building in Mexico City	2.00	2.17	7.5	385,000	9.3	17,454,937.5	1.00E+08	11	405	22.0
2	12 storey building in Yokohama – Japan	1.00	1.47	0.4	4577950	23.3	27,733,221.1	2.50E+08	23.1	2870	35.0
3	Imperial Valley County services building in California	1.10	0.61	3.3	31,000,000	9	598,455,000	3.00E+08	123.5	561710	14.0
4	Dumbarton bridge in California – pier 13	2.00	1.60	3.2	550,000	10	11,440,000	3.00E+08	5	196	13.0
5	Northwest connector 0.60 in California – bent 8	0.60	0.55	7	280,000	13.5	17,199,000	2.00E+08	8.4	1209	15.0
6	Painter street bridge 0.43 in California	0.43	0.27	9.2	250,000	5	7,475,000	1.20E+08	3.65	66	7.6
7	Meloland road overpass in California	2.66	0.40	5	364,000	6	7,098,000	1.00E+08	3.64	82.5	15.2
8	Ohiba-Ohashi road bridge 0.83 in Japan – pier 6	0.83	1.30	0.55	550,000	10	1,966,250	1.70E+07	11.2	358.2	22.0
9	Landing road bridge 0.30 in New Zealand – pier C	0.30	0.40	4	210,000	4	2,184,000	2.50E+08	1.2	5.8	9.0
10	Yachiyo bridge in Japan – pier P2	0.80	1.10	1.8	200,000	9	2,106,000	6.00E+07	1.8	35.6	11.0
11	Hanshin expressway 0.60 in Higashi-nada – Japan	0.60	0.70	24	1,100,000	12	205,920,000	2.00E+09	9.5	410	15.0

Therefore, the simplified analysis satisfies formally the basic requirements of EN 1998-5 (2004) for dynamic soil-pile interaction consideration. The simple considerations can be used for indication of the need of using detail analyses and for rough check of the results of sophisticated analyses providing that the following data are known and considered:

- Fundamental period of horizontal motion of ground in the free
- Thickness of ground layers or shear wave velocity through ground
- Unit density of ground
- Peak horizontal ground surface acceleration
- Pile length
- Pile inclination
- Area of pile cap
- Pile diameter
- Pie flexural stiffness
- Axial and shear capacity of pile
- Number of piles in a group
- Axial force in pile in static condition
- Fundamental period of structural vibration
- Mass moment of inertia of structure with respect to the top of foundation
- Foundation stiffness in rocking (= ratio between applied turning moment and foundation rotation in rad)
- Structural height above its foundation
- Peak horizontal acceleration of a structure at the centre of gravity from acceleration response spectrum or recorded from past earthquakes

EI (Nm <sup>2</sup> )	N <sub>piles</sub>	P <sub>1</sub> (N)	M <sub>2</sub> (Nm)	M <sub>2</sub> /M <sub>max</sub> (%)	A <sub>pilecap</sub> (m <sup>2</sup> )	c <sub>0</sub> or σ <sub>v'</sub> tan φ (Pa)	R <sub>2</sub> (N)	R <sub>2</sub> /F <sub>1</sub> (%)	T <sub>2</sub> /T <sub>max</sub> (%)	Notes
6.10E+06	15	4.74E+05	8.36E+02	5.3	70	10,000	1,876,875	112	470.8	Building failed in toppling mode
8.20E+08	20	2.22E+05	6.31E+03	1.3	704	75	1,190,267	14	37.9	
3.70E+06	204	1.32E+05	6.57E+00	0.0	7440	8000	66,495,000	26	34.2	
6.10E+06	28	2.91E+05	6.38E+02	5.1	108	8000	1,144,000	72	75.0	
1.40E+06	78	1.19E+05	4.65E+01	0.1	95	20	1,274,000	66	24.5	After retrofitting
1.60E+06	20	4.12E+05	1.38E+03	25.6	17	85,000	1,495,000	205	47.2	
1.68E+07	25	3.06E+05	6.50E+03	16.6	21	40	1,183,000	103	24.4	
1.77E+08	64	3.87E+04	1.14E+04	1.3	144	10	196,625	15	5.4	
4.27E+07	8	4.50E+05	4.98E+04	354.3	16	30000	546,000	101	49.5	
7.95E+06	33	9.88E+04	4.63E+03	205.7	33	0	234,000	0	177.3	Bridge damaged due to formation of plastic hinges in the piles at the top and bottom of a loose sand layer
9.82E+08	17	4.73E+06	1.14E+05	9.1	108	75000	17,160,000	119	79.9	Expressway failed in toppling mode

- Mass of structure supported by a pile group
- Eccentricity of structural mass above pile cap
- Axial stiffness of a pile
- Largest horizontal distance between piles in a group
- Sum of squared horizontal distances between piles in a group
- Cohesion of fine soil or friction angle of coarse soil beneath pile cap

Possibility of the presentation of the structures considered in the case histories as single degree of freedom oscillators (SDOFO) enable the use of the amplification factor for harmonic motion of a SDOFO (e.g. Clough and Penzien, 1993) as:

$$\frac{a_o}{a_i} = \sqrt{\frac{1 + (2\beta_t\xi)^2}{(1 - \beta_t^2)^2 + (2\beta_t\xi)^2}}, \quad (10.11)$$

where  $\beta_t = T_e T_h^{-1}$  is the tuning ratio,  $T_h$  is the period of an input motion i.e. ground,  $T_e$  is the period of the output motion i.e. structure,  $\xi$  is the damping ratio,  $a_o$  is the amplitude of acceleration of SDOFO,  $a_i$  is the amplitude of acceleration of input motion (ground). Damping ratio is the ratio between actual and critical damping, which prevents ground vibration. The results for the case histories are shown in Fig. 10.17.

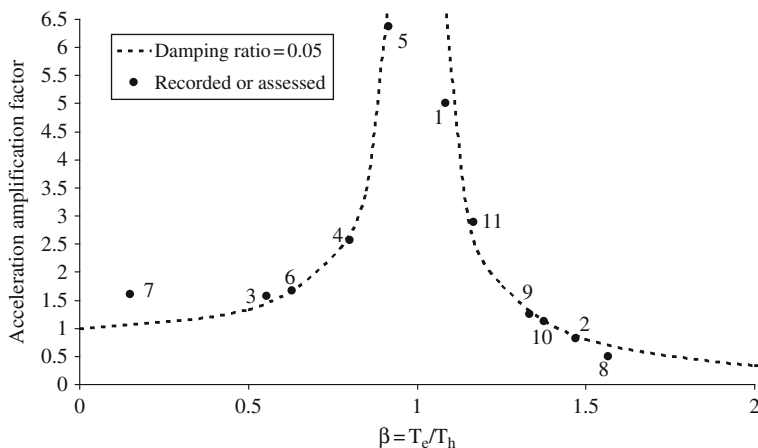


**Fig. 10.17** Acceleration amplification factor (ratio between structural and ground acceleration) for the case histories considered and SDOFO for 5% of the critical damping (The number by the points refer to the numbers in Tables 10.1 and 10.2)

## References

- API RP2A-WSD (2000) Recommended practice for planning, designing and constructing fixed offshore platforms – working stress design – 21st edn. American Petroleum Institute, Washington, DC
- ASTM D1143 Standard test method for piles under static axial compressive load. Annual Book of ASTM Standards. American National Standards Institute
- ASTM D3966 Standard test method for piles under lateral loads. Annual Book of ASTM Standards. American National Standards Institute
- Berrill JB, Christensen SA, Keenan RP, Okada W, Pettinga JR (2001) Case study of lateral spreading forces on a piled foundation. *Geotechnique* 51(6):501–517
- Clough RW, Penzien J (1993) Dynamics of structures, 2nd edn. McGraw Hill, New York, NY
- EN 1998-1 (2004) Eurocode 8 – design of structures for earthquake resistance, part 1: general rules, seismic actions and rules for buildings. European Committee for Standardization, Brussels
- EN 1998-5 (2004) Eurocode 8 – design of structures for earthquake resistance, part 5: foundations, retaining structures and geotechnical aspects. European Committee for Standardization, Brussels
- Fenves GL, Desroches R (1994) Response of the Northwest connector in the Landers and Big Bear earthquakes. Report UCB/EERC-94/12, Earthquake Engineering Research Centre, College of Engineering, University of California at Berkley, Berkeley, CA
- Fenves GL, Filippou FC, Sze DT (1992) Response of the Dumbarton bridge in the Loma Prieta earthquake. Report UCB/EERC-92/02, Earthquake Engineering Research Centre, College of Engineering, University of California at Berkley
- Finn WDL, Fujita N (2002) Piles in liquefiable soils: seismic analysis and design issues. *Soil Dyn Earthquake Eng* 22:731–742
- Gazetas G, Mylonakis G (1998) Seismic soil-structure interaction: new evidence and emerging issues. In: Geotechnical earthquake engineering and soil dynamics III – volume 2. Proceedings of a specialty conference, University of Washington. ASCE Geotechnical Special Publication 75

- Hadjian A, Fallgen R, Lau L (1990) Imperial County services building revisited: a re-evaluation with pile-soil-structure interaction. In: The 4th U.S. national conference on earthquake engineering, vol 3, Palm Springs, pp 835–844
- Hamada M (1992) Large ground deformations and their effects on lifelines: 1964 Niigata earthquake. In: Hamada M, O'Rourke T (eds) Case studies of liquefaction and lifeline performance during past earthquakes – volume 1: Japanese case studies. Technical report NCEER-92-0001, National Centre for Earthquake Engineering Research, State University of New York at Buffalo
- Idriss IM (1990) Response of soft soil sites during earthquakes. In: Duncan JM (ed) Proceedings of H. Bolton Seed memorial symposium, BiTech Publishers, Vancouver, British Columbia, vol 2, pp 273–289
- Japan Road Association (2002) Specifications for highway bridges, part V: seismic design. PWRI, Japan
- Jenkins WM (1989) Theory of structures, chapter 3. In: Blake LS (ed) Civil engineer's reference book – 4th edn. Butterworth, Oxford, UK, pp 3–16
- Kojic S, Trifunac MD, Anderson JC (1984) A post-earthquake response analysis of the Imperial County services building in El Centro. University of Southern California, Department of Civil Engineering, report No CE 84-02, Los Angeles, CA
- Lee VW, Trifunac MD, Feng CC (1982) Effects of foundation size on Fourier spectrum amplitudes of earthquake accelerations recorded in buildings. *Soil Dyn Earthquake Eng* 1(2):52–58
- Makris N, Badoni D, Delis E, Gazetas G (1994) Prediction of observed bridge response with soil-pile-structure interaction. *ASCE J Struct Eng* 120(10):2992–3011
- Mendoza M, Romo M (1989) Behaviour of building foundations in Mexico City during the 1985 earthquake: second stage. In: Bertero V (ed) Lessons learned from the Mexico earthquake. Publication 89-02. Earthquake Engineering Research Institute, pp 66–70
- Meymand PJ (1998) Shaking table scale model tests of nonlinear soil-pile-structure interaction in soft clay. PhD thesis, University of California, Berkeley, CA (<http://nisee.berkeley.edu/meymand/files/>)
- Nikolaou S, Mylonakis G, Gazetas G, Tazoh T (2001) Kinematic pile bending during earthquakes: analysis and field measurements. *Geotechnique* 51(5):425–440
- Ohira A, Tazoh T, Dewa K, Shimizu K, Shimada M (1984) Observations of earthquake response behaviours of foundation piles for road bridge. In: Proceedings of the 8th world conference on earthquake engineering, vol III, San Francisco, CA, pp 577–584
- Porcella RC (1984) Geotechnical investigations at strong motion stations in the Imperial Valley, California. Report USGS-OFR-84-562. US Geological Survey, Menlo Park, CA
- Romo MP, Seed HB (1986) Analytical modelling of dynamic soil response in the Mexico earthquake of September 19, 1985. In: Proceedings, ASCE international conference on the Mexico earthquakes – 1985, Mexico City, pp 148–162
- Seed HB, Idriss IM (1971) Simplified procedure for evaluating soil liquefaction potential. *ASCE J Soil Mech Foundation Div* 107:1249–1274
- Srbulov M (2010) Simple considerations of kinematic and inertial effects on piles during earthquakes. *Ingegneria Sismica XXVII*(2):7–19
- Stephenson WJ, Lomnitz C (2005) Shear wave velocity profile at the Texcoco strong motion array site, Valley of Mexico. *Geofisica Int* 44:3–10
- Werner SD, Beck JL, Levine MB (1987) Seismic response evaluation of Meloland road overpass using 1979 Imperial Valley earthquake records. *Earthquake Eng Struct Dyn* 15:249–274
- Wilson DW (1998) Soil-pile-structure interaction in liquefying sand and soft clay. PhD dissertation, Department of Civil & Environmental Engineering, College of Engineering, University of California at Davis (<http://www.cgm.ucdavis.edu/publications/ucdegm9804.pdf>)
- Wolf JP (1994) Foundation vibration analysis using simple physical models. PTR Prentice Hall, Upper Saddle River, NJ
- Zhang J, Makris N (2001) Seismic response analysis of highway overcrossings including soil-structure interaction. Pacific Earthquake Engineering Research Centre report 2001/02 ([http://peer.berkeley.edu/publications/peer\\_reports/reports\\_2001/reports\\_2001.html](http://peer.berkeley.edu/publications/peer_reports/reports_2001/reports_2001.html))

# Chapter 11

## Tunnels, Vertical Shafts and Pipelines

### 11.1 Introduction

Traditional belief is that tunnels are not affected much by earthquakes except if an active tectonic fault moves across a tunnel. Dowding and Rozen (1978) studied the response of 71 tunnels in rock to earthquake motions. The damage ranged from cracking to closure in total 42 cases. Sharma and Judd (1991) compiled a database on the response of 192 tunnels during 85 earthquakes throughout the world; 94 of the tunnels suffered from small to heavy damage. More than half the damage reported was caused by events that exceeded magnitude 7 of the Richter scale, and nearly 75% of the damage reported occurred within 50 km of the earthquake epicentre. There was no damage in tunnels where the horizontal peak ground acceleration was up to 0.2g. In most cases where damage was reported, the peak ground accelerations were larger than 0.4g. The data show that shallow tunnels are at greater risk during earthquakes than deeper tunnels; roughly 60% of the total cases had overburden depths less than 50 m and suffered some damage. Ground type is also important; 79% of the openings excavated in soil were reported to have suffered some damage. Dean et al. (2006) reviewed data of 1108 tunnels worldwide with diameters larger than 3 m, of which only twelve were subjected to earthquakes with magnitudes greater than 6 that caused the peak horizontal ground accelerations in excess of 0.16g since 1980. Only four tunnels were reported damaged none of which had precast concrete tunnel linings.

Earthquake can cause a number of different failure modes of pipelines. The principal failure modes for corrosion-free continuous pipelines (e.g. steel pipe with welded joints) are rupture due to axial tension, local buckling of the walls due to axial compression and flexural failure. For shallow burial depths, continuous pipelines in compression can also fail by general buckling of a pipeline. For corrosion-free segmented pipelines with bell and spigot type joints, the main failure modes are axial pull-out at the joints, crushing at the joints and round flexural cracks in pipe segments away from the joints. Failure criteria for each of these modes are given by O'Rourke and Liu (1999), Table 11.1.

The aim of this chapter is to describe basic mechanism and factors affecting tunnels, shafts and pipelines during earthquakes, to provide a brief review of existing

**Table 11.1** Typical yield stresses and strains for some pipe materials (O'Rourke and Liu, 1999)

Abbreviation	Type	Yield stress (MPa)	Yield strain
AC	Asbestos cement	—	—
C	Concrete	2–28	0.0001–0.0013
CI	Cast iron	97–290	0.001–0.003
DI	Ductile iron	290–360	0.0018–0.0022
PE	Polyethylene	15–17	0.022–0.025
PVC	Polyvinyl chloride	35–45	0.017–0.022
S	Steel	227–517	0.00134–0.00231
SG	Steel (threaded joints)	—	—

Note: AC does not have yield value due to its brittleness

methods for the analyses, to present some simple methods and their assumptions and to assess their accuracy and precision based on several case histories analysed. The emphasis is on the use of simple analyses for the case histories considered.

## 11.2 Mechanism and Factors

As strain (displacement over considered distance) is proportional to the ratio between peak particle velocity and ground wave velocity and stress (force per the area acted upon) is proportional to a product of unit density, peak particle velocity and ground wave velocity, as well as that buried structures must follow the movements of surrounding ground, it is evident that the main influential factors are:

- Peak ground velocity
- Peak ground displacement
- Ground wave velocity
- Tunnel/pipeline wall ductility (strain at failure)
- Tunnel/pipeline wall strength (stress at failure)

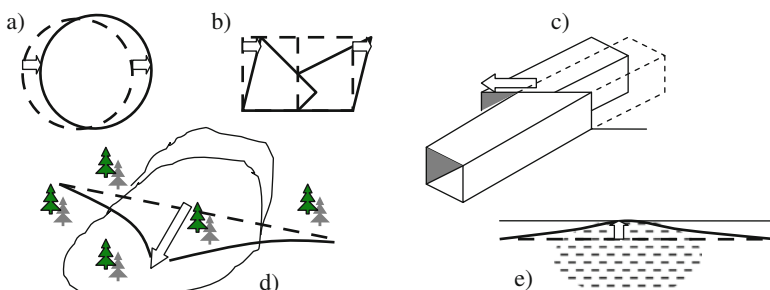


**Fig. 11.1** Sketches of some of deformation mechanisms of tunnels and pipelines (a) decrease in diameter and change of radius of curvature, (b) collapse of the central columns and top slab, (c) shear by tectonic fault movement, (d) break due to slope failure, (e) uplifting by buoyancy in liquefied soil

The main mechanism that affects damage of tunnels and pipelines during earthquakes is the movement of ground surrounding them, which may result in the change of their shape and the radius of curvature, breaking (in tension, compression or shear) of their walls or internal partitions if any, the change of their initial location due to movements of tectonic faults crossing them, because of failure of ground slope containing them or uplifting by buoyancy if ground liquefaction occurs, as sketched in Fig. 11.1.

## 11.3 Existing Methods

### 11.3.1 Empirical Based on Formulas and Graphs

#### 11.3.1.1 Tunnels

Penzien (2000) evaluated the racking deformation of rectangular and circular tunnel linings by soil structure interaction during earthquakes and provided formulae for calculation of sectional forces and bending moment in a **circular lining without slippage between soil and lining**:

$$\begin{aligned}
 P_\alpha &= \frac{-24 \cdot E \cdot J \cdot \Delta}{D^3 \cdot (1 - v^2)} \cdot \cos \left[ 2 \cdot \left( \alpha + \frac{\pi}{4} \right) \right] \\
 M_\alpha &= \frac{-6 \cdot E \cdot J \cdot \Delta}{D^2 \cdot (1 - v^2)} \cdot \cos \left[ 2 \cdot \left( \alpha + \frac{\pi}{4} \right) \right] \\
 T_\alpha &= \frac{-24 \cdot E \cdot J \cdot \Delta}{D^3 \cdot (1 - v^2)} \cdot \sin \left[ 2 \cdot \left( \alpha + \frac{\pi}{4} \right) \right], \\
 \Delta &= R \cdot \Delta_s \\
 R &= \pm \frac{4 \cdot (1 - v_s)}{(c + 1)} \\
 c &= \frac{24 \cdot (3 - 4 \cdot v_s) \cdot E \cdot J}{D^3 \cdot G_s \cdot (1 - v^2)}
 \end{aligned} \tag{11.1}$$

where the angle  $\alpha$  is measured in a cross section from the horizontal tunnel axis downwards,  $E$  is Young modulus of tunnel lining,  $J$  is the second moment of circumferential cross section area,  $D$  is the diameter of the middle of lining,  $v$  is Poisson's ratio, subscript  $s$  is for soil,  $G$  is soil shear modulus. Positive axial force  $P_\alpha$  is tensile, positive bending moment  $M_\alpha$  is stretching internal side and compressing external side of lining, positive shear force  $T_\alpha$  is oriented towards outside at the cross section inclined at an angle  $\alpha$  to the horizontal. The formula is applicable to a uniform strain field around a tunnel, negligible inertial interaction between a tunnel and surrounding soil and sufficiently deep tunnels so that the free surface boundary conditions has little effect on the racking soil structure interaction.

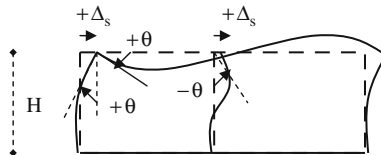


**Fig. 11.2** Positive signs of the top drift  $\Delta$  and rotation  $\theta$  in the cross section of a rectangular tunnel (displacements and rotations shown on an exaggerated scale)

Hashash et al. (2001) reviewed available methods for tunnel design and analyses. They stated that rectangular shaped tunnels can be analysed using a conventional frame analysis. Hashash et al. (2005) performed quasi static elastic finite element analyses to validate the extended Hoeg and Penzien methods for non-slip conditions, and concluded that Penzien method significantly underestimates the thrust in the tunnel lining.

For **rectangular tunnels** represented by a simple frame shown in Fig. 11.2, the transversal forces  $T$  and bending moments  $M$  at the top of tunnel wall/partition due to horizontal differential displacement  $\Delta$  and rotational angle  $\theta$  at the top can be calculated from the formulas for engineering beams, which bottom ends have prevented rotation (e.g. Jenkins, 1989):

$$\begin{aligned} T_\Delta &= \frac{12 \cdot E \cdot J \cdot \Delta_s}{H^3} \\ M_\Delta &= \frac{6 \cdot E \cdot J \cdot \Delta_s}{H^2} \\ T_\theta &= -\frac{6 \cdot E \cdot J \cdot \theta}{H^2}, \\ M_\theta &= -\frac{4 \cdot E \cdot J \cdot \theta}{H} \end{aligned} \quad (11.2)$$

where  $E$  is Young modulus of tunnel wall,  $J$  is the second moment of cross section of tunnel wall,  $H$  is tunnel wall height, the positive signs of the top drift  $\Delta$  and rotation  $\theta$  are shown in Fig. 11.2.

The **horizontal drift  $\Delta$  over a tunnel height  $H$**  can be determined from the difference of horizontal ground displacements  $d_g$  at the top and bottom of a tunnel. If a specific actual data or attenuation relationship for peak horizontal ground displacement, such as Equation (1.3) and Fig. 1.3, does not exist for a location then EN 1998-1 (2004) specifies that the design ground displacement  $d_g$ , corresponding to the design ground acceleration, may be estimated using the formula:

$$d_g = 0.025 \cdot a_g \cdot S \cdot T_C \cdot T_D, \quad (11.3)$$

where  $a_g$  is design ground acceleration on rock,  $S$  is soil factor ranging from 1 for rock to 1.4 for soil type E (alluvium with transversal wave velocity between 100 and 360 m/s and thickness varying between 5 and 20 m underlain by stiffer material

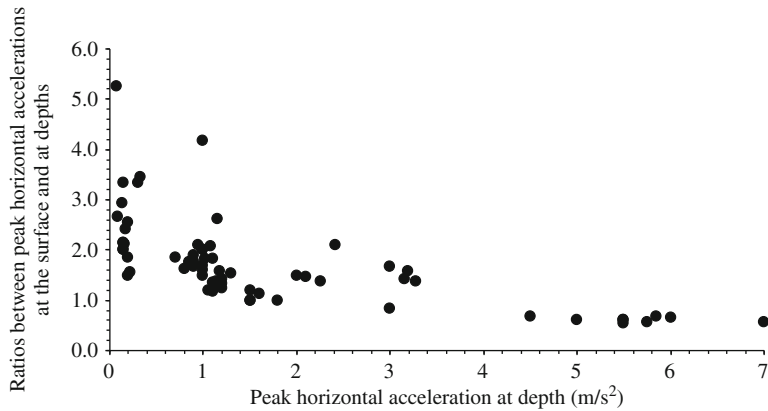


**Fig. 11.3** Ratios between reported in literature peak horizontal accelerations at the surface and at depths

with the transversal wave velocity  $>800$  m/s), period  $T_C$  varies in the range from 0.4 for rock to 0.8 for soil type D (loose to medium dense cohesionless soil or soft to firm cohesive soil with transversal wave velocity  $<180$  m/s),  $T_C = 0.5$  for type E soil, period  $T_D = 2$ .

Srbulov (2003), for example, plotted ratios between the peak horizontal ground acceleration at ground surface and at depths that are reported in literature, Fig. 11.3.

The range of depths considered varies from 6 to 150 m and of transversal wave velocities from 54 to 458 m/s. A correlation between the upper and lower bound acceleration ratios and depths and transversal wave velocities was not found. One possible reason for this maybe that the peak accelerations were not always connected with the fundamental vibration period of soil. Srbulov (2003) used Equation (1.17) to assess which vibration mode is most likely to cause the peak acceleration, Fig. 11.4. The acceleration ratio is less than one for peak

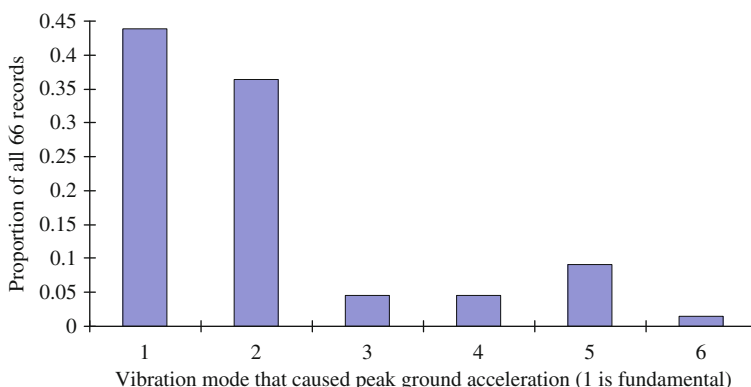


**Fig. 11.4** Proportion of vibration modes that likely caused peak horizontal ground acceleration

horizontal ground acceleration greater than 4 m/s<sup>2</sup> because of soil yield at larger accelerations.

The **rotational angle  $\theta$  at the top** can be estimated from the drift  $\Delta$  at the top using the formulas for deflection and rotation of the end of a cantilever beam uniformly loaded (e.g. Giek and Giek, 1997).

$$\theta = \arctan\left(\frac{4}{3} \cdot \frac{\Delta}{H}\right) \quad (11.4)$$

### 11.3.1.2 Vertical Shafts

Wong and Kaiser (1988) used the convergence – confinement method (usually applied to tunnels), which accounts for in situ stresses and ground properties, to define analytical predictive formulas for pressures  $\sigma_{v,r,t}$  (vertical, radial, tangential) and soil horizontal deformation  $u_i$  around vertical shafts.

$$\sigma_v = \gamma \cdot h = p_o$$

$$\sigma_r = p_i$$

$$\sigma_t = 2 \cdot K_o \cdot p_o - p_i$$

For  $\phi \neq 0$

$$K_o = (1 - \sin \phi) \cdot OCR^{\sin \phi}$$

$$K_p = \tan^2(45^\circ + \phi/2)$$

$$p_i = \frac{2 \cdot K_o \cdot p_o}{K_p + 1}, \quad K_o > K_{cr} \quad (11.5)$$

$$p_i = \frac{p_o}{K_p}, \quad K_o < K_{cr}$$

$$K_{cr} = \frac{K_p + 1}{2 \cdot K_p}$$

For  $c_u \neq 0$

$$p_i = K_o \cdot p_o - c_u, \quad 1 - c_u/p_o < K_o < c_u/p_o + 1$$

$$p_i = p_o - 2 \cdot c_u, \quad K_o < 1 - c_u/p_o$$

The radial horizontal displacement  $u_i$  before soil yield,

$$u_i = r \cdot \frac{(K_o \cdot p_o - p_i) \cdot (1 + \nu)}{E}, \quad (11.6)$$

where  $r$  is the shaft radius,  $E$  is Young modulus of soil,  $\nu$  is Poisson's ratio of soil. After soil yield, the value of displacement depends on the yield amount. Wong and Kaiser (1988) obtained a good agreement between the results obtained using Equations (11.5) and (11.6) and finite element analyses. They also concluded

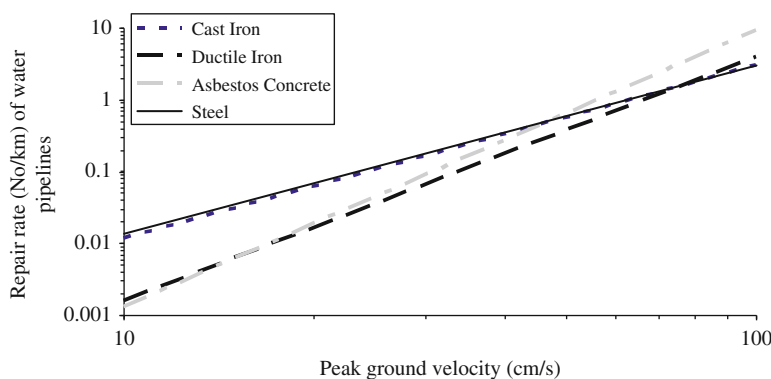
that the conventional design methods that provide the minimum support pressures required to maintain stability are not conservative. These pressures are generally less than those actually encountered if ground movements during construction are restricted with good ground control.

Wong and Kaiser (1988) considered only static condition. In seismic condition, the additional lateral earth pressure on vertical shafts can be estimated using Equation (7.12).

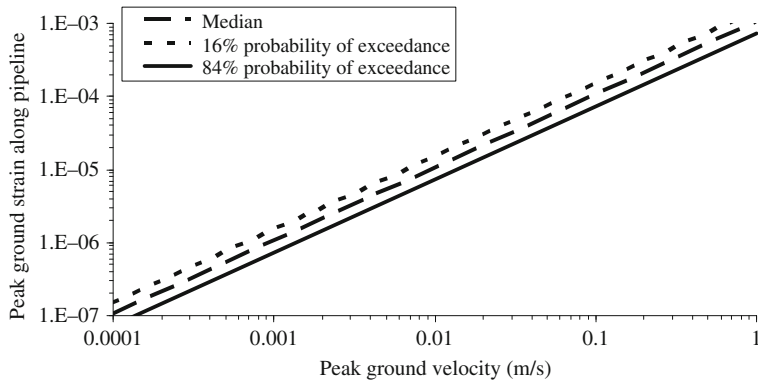
### 11.3.1.3 Pipelines

Figure 11.5 shows the linear regression that was developed between water supply cast iron (CI), steel, ductile iron (DI) and asbestos cement (AC) pipeline repair rates and peak ground velocity (PGV) based on data from the Northridge and other US earthquakes as reported by O'Rourke and Bonneau (2007). “The regressions indicate that the highest rate of damage for a given PGV was experienced by steel pipelines. Steel pipelines in Los Angeles are used to carry the highest water pressures and are subject to corrosion that has been shown to intensify their damage rates in previous earthquakes (Isenberg, 1979). The regressions were developed after the data were screened for lengths of pipelines that represent approximately 1.5 to 2.5% of the total length or population for each type of pipe affected by the earthquake (O'Rourke and Jeon, 1999). This procedure reduces the influence of local erratic effects that bias the data derived from small lengths of pipeline. The use of this filtering procedure leads to statistically significant trends and regressions that are applicable for  $\text{PGV} \leq 75 \text{ cm/s}$ . For the Northridge earthquake, zones with PGV exceeding 75 cm/s generally correspond to locations where PGD, from suites such as liquefaction and land sliding, was observed. Hence, this screening technique tends to remove damage associated with PGD, resulting in correlations relevant for TGD”; TGD is transient ground deformation.

Figure 11.6 shows the peak values of the largest principal ground strain (PGS) as a function of the largest absolute value of ground velocity (PGV) by Paolucci and



**Fig. 11.5** Repair rate of water pipelines (adapted from O'Rourke and Bonneau, 2007)



**Fig. 11.6** Peak ground strain along pipelines versus peak ground velocities (adapted from Paolucci and Pitilakis, 2007)

Pitilakis (2007) “*This selection of PGS and PGV has been chosen to make these parameters invariant with respect to the reference system, and, as a consequence, to the specific direction selected. The notable feature is that all data tend to be aligned, with a relatively small dispersion and irrespective of the earthquake magnitude, distance, site conditions or prevailing wave type, along a line with equation*

$$\log_{10} PGS = 0.955 \cdot \log_{10} PGV - 3.07, \quad (11.7)$$

where  $PGV$  is in m/s. If multiplier of  $\log_{10} PGV$  is forced to be unity, the best fit line turns to be  $PGS = PGV/\Psi$  where  $\Psi = 963$  m/s for the median value, 671 m/s and 1382 m/s correspond to the 16 and 84 percentile, respectively. A good agreement is found with the relationship proposed by Trifunac and Lee (1996), based on a large set of artificially generated synthetic time histories for different soil conditions, who also found a weak dependence of the PGS-PGV relationship on earthquake magnitude, epicentral distance and local site conditions.”

The interpretation of value  $\Psi$  as the propagation velocity of the prevailing wave velocity (either apparent velocity of body waves or phase velocity of surface waves) may be misleading. Abrahamson (2003) has recently proposed a model for transient ground strain evaluation, where the relative contribution of wave passage (WP), spatial incoherence (SI) and site effects (SE) are made explicit and summarised in an empirical relationship between PGS and peak ground displacement (PGD).

$$\begin{aligned} PGS/PGD &= WP + SI + SE \\ WP &= \frac{\exp(5.8 - 0.69 \cdot M)}{C}, \\ SI &= SE = 3 \cdot 10^{-5} \end{aligned} \quad (11.8)$$

where PGD is measured in cm,  $M$  is earthquake magnitude,  $C$  is a constant with dimension of distance over time. In Fig. 11.7, the PGS-PGD pairs are shown for the four data sets considered by Paolucci and Pitilakis (2007).

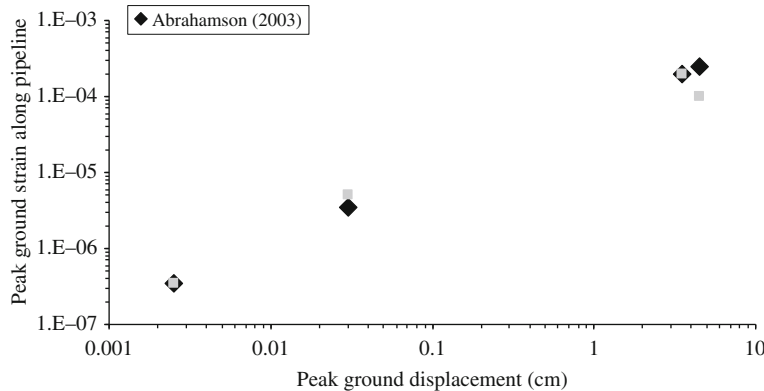


**Fig. 11.7** Peak ground strain along pipelines versus peak ground displacements (adapted from Paolucci and Pitilakis, 2007)

For both body and surface waves, for a fixed value of PGV, ground strain will generally be greater in soft soils (i.e. low velocity value) than stiffer soils. This has been confirmed by Nakajima et al. (2000) in a series of field measurements using strain gauges and accelerographs. As shown in Fig. 11.8, for the same value of PGV, maximum ground strain observed in soft ground (Shimonaga) is on average three to four times that observed in hard ground (Kansen). In this case, the predominant period of the soft ground was 1.3 s whilst the predominant period of the hard ground was around 0.4 s.

Pipe joints may dictate behaviour of a pipeline. A gas-welded joint renders a steel pipe as vulnerable to damage as a CI or AC pipe, even though the tensile strength of a steel barrel is much greater than that of CI or AC. For a specific joint type (bell & spigot/ rubber gasket/restrained/unrestrained) steel and ductile iron pipes are less vulnerable than more brittle pipe types (PVC, AC, CI). A summary of data collected by Shirozu et al. (1996) is shown in Fig. 11.9.

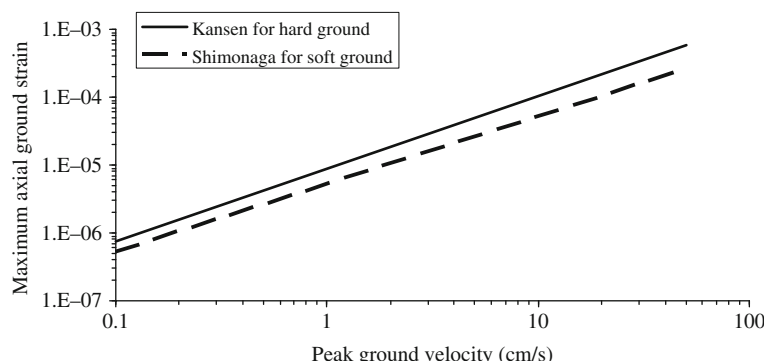


**Fig. 11.8** Dependence of maximum axial ground stain on peak ground velocity (adapted from Nakajima et al., 2000)

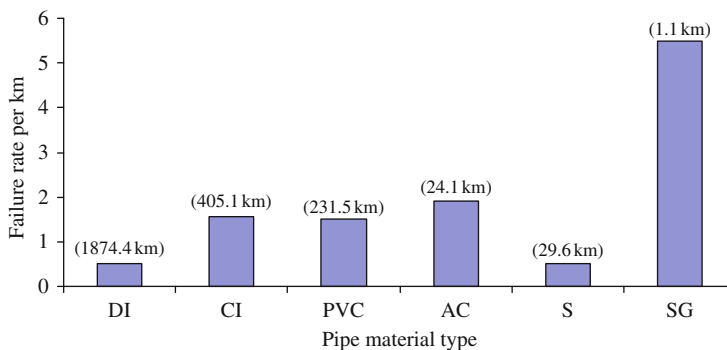


**Fig. 11.9** Failure rate per km dependence on pipe material type and their lengths in km (adapted from Shirozu et al., 1996)

### 11.3.2 Numerical Analyses Using Computer Programs

Numerical analyses are performed in design practice usually in two dimensions using commercial software. Non-linear and three dimensional studies in cyclic conditions are more demanding and are reserved for special cases, as indicated in the following examples.

Alheid (1994) reported on non-linear dynamic analyses by ANSALT of a deep underground drift in rock salt as a part of the safety analysis for a nuclear waste disposal. The results of the calculations were verified by in-situ measurements using detonations of chemical explosives to approximate high frequency sources. Alheid (1994) pointed out that a numerical algorithm can be verified initially, but applied geometrical discretization, time step, the boundary conditions etc. need to be appropriate for each implementation. The biggest problem is an appropriate numerical model of ground behaviour in cyclic conditions.

Kramer et al. (2007) reported a number of analyses performed to predict radial and circumferential joint behaviour of precast tunnel linings during seismic ovaling (racking) and wave propagation. Their analyses involved a complex, three dimensional finite element based ground-structure interaction model that incorporates inelastic constitutive soil behaviour, cracked concrete properties and no-tension, frictional segment joint surfaces in ADINA.

Kontoe et al. (2008) used static and dynamic plane strain finite element analyses of the response of Bolu highway twin bench pilot tunnels that were under construction when the 1999 Duzce earthquake in Turkey occurred, which caused extensive damage during the earthquake. The calculated maximum total hoop stress during the earthquake exceeds the compressive strength of 0.3 m thick shotcrete placed as an initial primary lining. The occurrence of lining failure and the predicted failure mechanism compare very favourably with field observations. However, the ground model used with seven input parameters is not appropriate for design practice as requires experience in numerical analyses and specialist knowledge of modelling of soil properties in cyclic condition, which are well beyond requirements present in

codes and standards. Kontoe et al. (2008) found that “*the Penzien solution for non-slip conditions should be avoided because it severely underestimates the seismically induced maximum thrust*”.

### 11.3.3 Experimental on Small Scale Models and Prototypes

Mostly centrifuge testing is used and the results reported in specialty conferences Centrifuge.

## 11.4 Simple Methods and Assumptions

It is frequently the case that nearly vertically propagating transversal seismic waves (Fig. 3.1a) cause greatest ground movements and effects on tunnels and pipelines. The ovaling (racking) effect on a circular cross section is sketched in Fig. 11.10.

Equations (11.1) can be used to calculate the additional sectional forces and bending moment in a circular cross section due to a differential ground displacement in the free field  $\Delta_s$  over tunnel diameter. Similarly, Fig. 11.2 and Equations (11.2) can be used for a rectangular cross section. The assumptions and limitations of Equations (11.1) and (11.2) are mentioned previously.

## 11.5 Case Histories

The simple analyses are used for the case histories of failures during earthquakes of a cut and cover and bored tunnel in order to assess the applicability and accuracy of the simple analyses.

### 11.5.1 Cut and Cover Daikai Station in Japan

The station was built between 1962 and 1964 by cut and cover method in Kobe city in Japan. The station is located about 15 km from the epicentre of the 1995

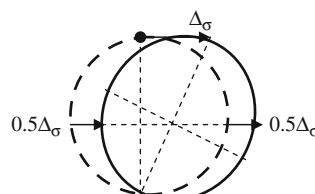


**Fig. 11.10** Sketch of ovaling (rocking) of a circular cross section due to differential horizontal ground displacement  $\Delta_s$  (displacements and rotations shown on an exaggerated scale)

Hyogoken-Nanbu earthquake with a moment magnitude of 6.9. According to the PEER database (Subsection 2.2.2.1), the two horizontal and vertical peak ground accelerations were  $2*0.61g$  and  $0.27g$  respectively at Takatori station, which is located about 13 km from the epicentre of the 1995 Hyogoken-Nanbu earthquake. The peak horizontal displacements were in the range from 33 to 36 cm in the horizontal directions at Takatori station, with the averaged ground transversal wave velocity  $<180$  m/s in the upper 30 m below the ground surface according to PEER data base. During the earthquake, more than 30 columns of the central section of the Daikai station completely collapsed over a total length of about 110 m, which caused the failure of the overlying concrete roof slab and resulted in a 2.5 m subsidence on the road above the subway according to Huo et al. (2005). Figure 11.11 shows a detail of the collapsed columns.

The Daikai station contains three main parts: the main section of the station, which collapsed, the subway tunnels section and the station access section with two underground levels where no severe damage occurred, Fig. 11.12.

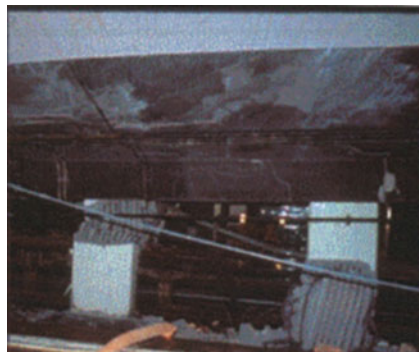


**Fig. 11.11** Detail of collapsed columns of Daikai station (adapted from [www.geerassociation.org/.../Kobe\\_1995/ch6-2.html](http://www.geerassociation.org/.../Kobe_1995/ch6-2.html))

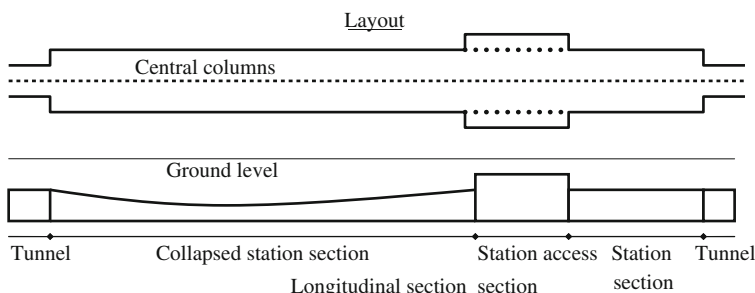


**Fig. 11.12** Sketch of the layout and longitudinal section of the Daikai Station

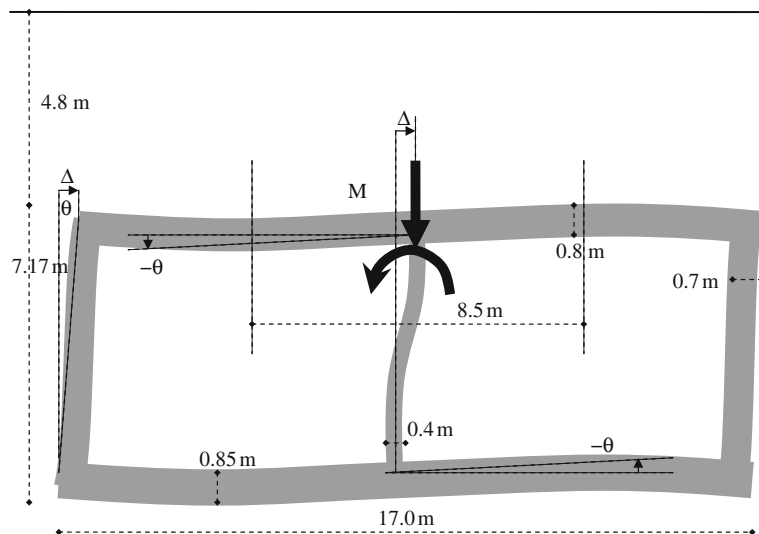


**Fig. 11.13** Sketch of the cross section of collapsed section of the Daikai Station

- **The collapsed section** consisted of a rectangular reinforced concrete box structure, which was 17 m wide and 7.17 m high, with central columns spaced at 3.5 m in the longitudinal direction. The columns were about 5.5 m high and had a rectangular reinforced concrete cross section of 0.4 m by 1.0 m. The columns in the failed section had 30 bars of 32 mm diameter in the axial direction and ties of 9 mm diameter spaced at 350 mm as transverse reinforcement. The compression tests on column's concrete specimen indicated compressive strength values of about 39.7 MPa. The yield stress of the reinforcing steel was 235.2 MPa. The top of the concrete roof in this section was located about 4.8 m below the ground surface. It is worth mentioning that the station section of the same cross section like the collapsed section but on the other side of the station access section did not collapse. The cross section of Daikai station which failed is shown in Fig. 11.13.
- **The tunnel section** consisted of a smaller rectangular reinforced concrete box structure 6.36 m high by 9.0 m wide, with a series of central columns with reinforced concrete cross section 0.4 m by 0.6 m spaced at 2.5 m. The top of the concrete roof in this section was located about 5.2 m below the ground surface.
- **The station access section** consisted of a reinforced concrete structure 10.12 m high and 26.0 m wide, with central columns identical to those in collapsed section. The top of the concrete roof in this section was located about 1.9 m below the ground surface according to Huo et al. (2005).

The site of the Daikai Station is composed of man made fill up to 2 m thick, soft Holocene alluvial deposits about 5–7 m thick and dense Pleistocene deposits down to the bedrock at several kilometers depth. The ground profile at the failed section was investigated by two boreholes. Transversal wave velocity profile is

**Table 11.2** Transversal wave velocity profile at Daikai station in Japan (based on Huo et al., 2005)

Depth to (m)	2	5	7	13	19	23	30
$v_t$ (m/s)	100	140	250	200	240	400	300
Average $v_t$ (m/s)	100	121	142	164	182	201	218

given in Table 11.2. The average transversal wave velocities are calculated from the formula:

$$v_{t,avr} = \frac{\sum d_i}{\sum \frac{d_i}{v_{t,i}}}, \quad (11.9)$$

$v_{t,i}$  is transversal wave velocity over sub-layer thickness  $d_i$ .

The station had a drainage system at the bottom slab. The ground water level was located at a depth of 6–8 m below the ground surface, which was 3–5 m lower than in 1959, prior to the construction of the station (e.g. Huo et al., 2005).

Based on Fig. 11.14 from PEER data base it follows that the fundamental period of ground vibration  $T$  could have been about 2 s.

From Equation (1.18) and for averaged transversal wave velocities from Table 11.2, it follows that a ground wave length that caused the peak horizontal ground surface displacement of up to 0.36 m could have been about  $4H = Tv_t = 2*200 = 400$  m in the fundamental mode and about  $2*2/3*400/4 = 133$  m in the second vibration mode, Fig. 1.14. The maximum differential horizontal displacement  $\Delta$  over the collapsed section height of 7.17 m could have been  $36*\sin(2\pi*400^{-1}*7.17) = 4.0$  cm in the fundamental mode or  $36*\sin(2\pi*133^{-1}*7.17) = 12.0$  cm in the second vibration mode. From Equation (11.4),  $\theta = \arctan(4*3^{-1}*12.0*717^{-1}) = 1.3^\circ = 0.022$  rad in the second vibration mode. For assumed  $E = 20$  GPa and for  $J = 1*0.4^3*12^{-1} = 0.00533$  m<sup>4</sup> of a homogeneous cross section, it follows for the central columns for which the effects of differential horizontal displacement  $\Delta$  of 12.0 cm and rotation  $\theta$  of 1.3° on the transversal force and bending moment at the top are additive instead of subtractive like for the walls because of the negative sign of  $\theta$ ,

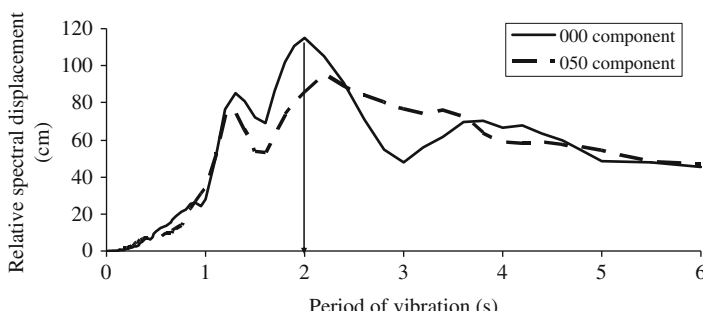


**Fig. 11.14** Relative spectral displacement at Takatori station during the 1995 Hyogoken-Nanbu earthquake (from PEER data base)

$$T_{\Delta-\theta} = 20 \cdot 10^6 \cdot 0.00533 \cdot \left( \frac{12 \cdot 0.12}{7.17^3} + \frac{6 \cdot 0.022}{7.17^2} \right) = 689 \text{kN} \quad (11.10)$$

$$M_{\Delta-\theta} = 20 \cdot 10^6 \cdot 0.00533 \cdot \left( \frac{6 \cdot 0.12}{7.17^2} + \frac{4 \cdot 0.022}{7.17} \right) = 2785 \text{kNm}$$

The vertical load per column in the collapsed section could have been  $8.5*3.5*(4.8*19 + 0.8*25) = 3308 \text{kN}$ . The additional bending moment due to  $P-\Delta$  effect could have been  $3308*0.12 = 397 \text{kNm}$ , so that the total moment = 3182 kNm. For a homogeneous cross section, the maximum axial stress could have been  $3308*(0.4*1)^{-1} + 3182*(1*0.4^2*6^{-1})^{-1} = 8270 + 119,325 = 127,595 \text{kPa}$ , which is about 3.2 times greater than the concrete compressive strength of 39,700 kPa. If only the fundamental mode of ground vibration is considered then for  $\Delta = 36*\sin(2\pi*400^{-1}*7.17) = 4.0 \text{m}$  and  $\theta = \arctan(4*3^{-1}*4*717^{-1}) = 0.43^\circ = 0.0074 \text{ rad}$ ,  $M = 20*10^6*0.00533*(6*0.04*7.17^{-2} + 4*0.0074*7.17^{-1}) = 938 \text{kNm}$  and the total moment  $3308*0.04 + 938 = 1070 \text{kNm}$ ; the maximum axial stress =  $8270 + 1070*(1*0.4^2*6^{-1})^{-1} = 48,395 \text{kPa}$ , which is about 1.2 times the concrete compressive strength of 39,700 kPa.

For the walls with  $\Delta = 0.12 \text{ m}$  and  $\theta = 0.022 \text{ rad}$  in the second mode of vibration and  $J = 1*0.7^3*12^{-1} = 0.0286 \text{ m}^4$ ,

$$T_{\Delta+\theta} = 20 \cdot 10^6 \cdot 0.0286 \cdot \left( \frac{12 \cdot 0.12}{7.17^3} - \frac{6 \cdot 0.022}{7.17^2} \right) = 801 \text{kN} \quad (11.11)$$

$$M_{\Delta+\theta} = 20 \cdot 10^6 \cdot 0.0286 \cdot \left( \frac{6 \cdot 0.12}{7.17^2} - \frac{4 \cdot 0.022}{7.17} \right) = 972 \text{kNm}$$

The vertical load per metre length of the wall in the collapsed section could have been  $4.25*1*(4.8*19 + 0.8*25) = 473 \text{kN}$ . The additional bending moment due to  $P-\Delta$  effect could have been  $473*0.12 = 57 \text{kNm}$ , so that the total moment = 1029 kNm. For a homogeneous cross section, the maximum axial stress could have been  $473*(0.7*1)^{-1} + 1029*(1*0.7^2*6^{-1})^{-1} = 676 + 12,600 = 13,276 \text{kPa}$ , which is about one third of the concrete compressive strength of 39,700 kPa even in the second mode of vibration.

The station access section has two storeys and three rows of columns so that simple analysis may not apply. For the tunnel section and its central columns, the simple analysis shows that  $\Delta = 36*\sin(2\pi*400^{-1}*6.36) = 3.6 \text{ cm}$  in the fundamental mode or  $36*\sin(2\pi*133^{-1}*6.36) = 10.6 \text{ cm}$  in the second vibration mode and  $\theta = \arctan(4*3^{-1}*3.6*636^{-1}) = 0.43^\circ = 0.0075 \text{ rad}$  i.e.  $\theta = \arctan(4*3^{-1}*10.6*636^{-1}) = 1.3^\circ = 0.022 \text{ rad}$  respectively. For  $J = 0.6*0.43*12^{-1} = 0.0032 \text{ m}^4$ ,  $M = 20*10^6*0.0032*(6*0.036*6.36^{-2} + 4*0.0075*6.36^{-1}) = 641 \text{kNm}$  in the fundamental mode and  $M = 20*10^6*0.0032*(6*0.106*6.36^{-2} + 4*0.022*6.36^{-1}) = 1890 \text{kNm}$  in the second mode of vibration. The vertical load per column in the collapsed section could have been  $4.5*2.5*(5.2*19 + 0.4*25) = 1224 \text{kN}$ . The additional bending moment

due to  $P\Delta$  effect could have been  $1224 \times 0.036 = 44$  kNm in the fundamental mode and  $1224 \times 0.106 = 130$  kNm in the second mode of vibration, so that the total moments could have been 685 kNm and 2020 kNm respectively. The maximum axial stress in a homogeneous section could have been  $1224 \times (0.4 \times 0.6)^{-1} + 685 \times (0.6 \times 0.4^2 \times 6^{-1})^{-1} = 5100 + 42,812 = 47,912$  kPa, which is about 1.2 times the concrete compressive strength of 39,700 kPa even in the fundamental mode of vibration, i.e. the same as in the collapsed section. The fact that the tunnel section did not fail indicates that assumed horizontal differential displacement and rotation for the simple analyses are exaggerated. Even if assumed values are reduced, the maximum axial stress in the central columns would remain greater than the concrete compressive strength when the second mode of vibration is considered instead of the fundamental mode. If the bottom slab of a rectangular tunnel exhibits deformation similar to its top slab (such as in Fig. 11.13) then the effect of the bottom slab synchronous deformation is to increase the bending moment in the central columns at its top 50% more (i.e. to  $-6EJ\theta H^{-1}$ ) and the transversal force to 100% more (i.e. to  $-12EJ\theta H^{-2}$ ) in comparison with the top bending moment and transversal force when the bottom end has no rotation. The effect of the bottom slab synchronous deformation on the walls is to eliminate the opposite effect of the rotation on the bending moment and transversal force so that the remaining effect of the horizontal displacement is not decreased, which means that the bending moment and transversal force are also increased as in the central column.

Huo et al. (2005) used a numerical model to explain the survival of the tunnel section by its higher stiffness in comparison with the collapsed section.

### **11.5.2 Bolu Highway Twin Shotcrete Supported Bench Pilot Tunnels in Turkey**

Kontoe et al. (2008) analysed the response of two shotcrete supported bench pilot tunnels that were severely damaged within a zone of fault gauge clay where the two tunnels overlapped during the 1999 Duzce earthquake. The earthquake moment magnitude was  $M_w = 7.2$ , the west portals of Bolu tunnels are located 3 km from the east tip of the Duzce rupture propagation in roughly east west direction and within 20 km from the earthquake epicentre. The closest to the tunnel Bolu seismic station at 18 km fault distance had recorded peak horizontal ground acceleration of  $7.88 \text{ m/s}^2$  ( $0.80g$ ) leading to the peak horizontal ground displacement of 12.0 cm. The predominant period of ground displacement is about 1 s (Fig. 11.15) in east-west direction at Bolu seismic station according to Ambraseys et al. (2004). East west direction is perpendicular to the north-south direction of the tunnel.

The external diameters of the tunnels are 5.0 m, the shotcrete thickness 0.3 m, the depth of the horizontal axes 162 m below the ground surface and the distance between the vertical tunnel axes is 19.0 m. The part of the left pilot tunnel that had advanced 15 m in fault gauge clay and 10 m in sandstone in front of the right part had experienced no severe damage unlike the overlapped part in fault gauge clay

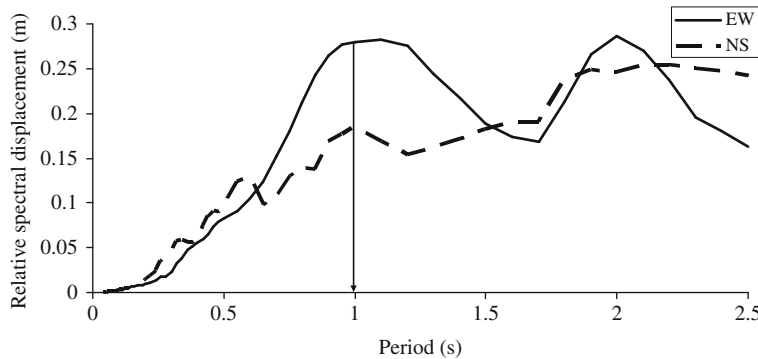


**Fig. 11.15** Relative spectral displacement at Bolu station during the 1999 Duzce earthquake (from Ambraseys et al., 2004)

alone that experienced crushing of the shotcrete primary lining near the crown and invert, buckling of the reinforcement and invert uplift up to 0.5–1 m.

The horizontal differential displacement  $\Delta_s$  at the tunnel axis during the earthquake is not known. From 12.0 cm ground surface displacement in east-west direction at Bolu seismic station, the maximum amplitude of at depth displacement in sandstone/marl and quartzite rock underlying the layer of fault gouge clay is assumed to be also 0.12 m. For maximum elastic shear modulus of the fault gauge clay  $G_{s,\max} = 850$  MPa according to Kontoe et al. (2008) and assumed unit density of 2000 kg/m<sup>3</sup> it follows that the maximum transversal wave velocity  $v_t = (850*10^6*2000^{-1})^{1/2} = 652$  m/s. Similarly, for underlying sandstone/marl formation and for  $G_{s,\max} = 2500$  MPa according to Kontoe et al. (2008) and assumed unit density of 2400 kg/m<sup>3</sup> it follows that the maximum transversal wave velocity  $v_t = (2500*10^6*2400^{-1})^{1/2} = 1020$  m/s.

Increase in the amplitudes of waves when they propagate into media of lower density  $\rho_1$  and wave propagation velocity  $v_1$  (usually towards surface) can be explained by considering the principle of conservation of energy and the energy-flux density per unit of time in the direction of wave propagation (upwards).

$$\frac{1}{2} \cdot v_1 \cdot \rho_1 \cdot \Delta_{w1}^2 \cdot \omega^2 \cdot dS = \frac{1}{2} \cdot v_2 \cdot \rho_2 \cdot \Delta_{w2}^2 \cdot \omega^2 \cdot dS \text{ from which} \\ \frac{\Delta_{w1}}{\Delta_{w2}} = \sqrt{\frac{\rho_2 \cdot v_2}{\rho_1 \cdot v_1}}, \quad (11.12)$$

where  $\omega$  is circular frequency, the product  $\rho v$  is called soil impedance  $(\rho_2 v_2)(\rho_1 v_1)^{-1}$  is called the impedance contrast between two adjacent layers. From Equation (11.22) it follows that at small strain  $\Delta_{w1} = 12*(2400*1020*2000^{-1}*652^{-1})^{1/2} = 16.4$  cm in fault gouge clay. Further steps of the iterations are given in Table 11.3.

The shotcrete modulus  $E = 28$  GPa, Poisson's ratio  $\nu = 0.2$ ,  $J = 1*0.3^{3*12^{-1}} = 0.00225$  m<sup>4</sup>, soil Poisson's ratio  $\nu_s = 0.3$  according to Kontoe et al. (2008).

**Table 11.3** Iterative determination of soil parameters in Section 11.5.2

Parameter	Initial small strain <10 <sup>-6</sup>	Strain = 0.0016	Strain = 0.003
Fault gouge clay modulus G <sub>s</sub> (MPa)	850	297.5 <sup>a</sup>	255 <sup>a</sup>
Fault gouge clay transversal wave velocity v <sub>t</sub> (m/s) = (G <sub>s</sub> *ρ <sup>-1</sup> ) <sup>1/2</sup>	652	385	357
Sandstone/marl shear modulus G (MPa)	2500	1000	750
Sandstone/marl transversal wave velocity, v <sub>t</sub> (m/s) = (G*ρ <sup>-1</sup> ) <sup>1/2</sup>	1020	645.5	559
Maximum amplitude of ground wave in fault gouge clay, Δ <sub>w1</sub> (m) based on Equation (11.22)	0.164	0.170	0.164
Wave length λ (m) in fault gouge clay = v <sub>t</sub> times period of 1 s <sup>b</sup>	652	385	357
Horizontal differential displacement Δ <sub>s</sub> over the tunnel height of 5 m is assumed to be = Δ <sub>w1</sub> * sin(2π*λ <sup>-1</sup> *5)	0.008	0.014	0.0145
Shear strain corresponding to Δ <sub>s</sub> over 5 m tunnel height is Δ <sub>s</sub> *5 <sup>-1</sup>	0.0016	0.003	0.0029–0.003

<sup>a</sup>The shear modulus reduction from Fig. A2 by Kontoe et al. (2008). The values correspond to PI~25% in Fig. 1.10

<sup>b</sup>The period of 1 s from Fig. 11.15

The results of calculations based on Equation (11.1) are shown in Fig. 11.16 for  $D = 5 - 0.3 = 4.7$  m and  $\Delta_s = 0.015$  m.

It is interesting to note that calculated maximum axial force  $P$  and bending moment  $M$  are located at about 45° and 225° around the tunnel circumference, which is in good agreement with the locations of observed maximum damage to the lining as shown in Fig. 11.17.

Damage to the tunnel lining occurred because the compressive strength of shotcrete was exceeded. The calculated stresses in the tunnel lining are shown in Fig. 11.18, where the area  $A = 1*0.3 = 0.3$  m<sup>2</sup>,  $W = J*(0.5*\text{thickness})^{-1} = 1*0.3^{2*6^{-1}} = 0.015$  m<sup>3</sup>, the multiplier 1.5 is for the maximum shear stress due to its parabolic distribution in the cross section.

While the calculated maximum average axial stress does not exceed 1.9 MPa in compression and tension and the maximum calculated shear stress does not exceed 2.9 MPa, the maximum calculated bending stress is 45 MPa. The calculated maximum axial stress due to the bending is greater than the estimated compressive strength of 30 MPa of 7 days old and 40 MPa of 14 days old shotcrete cubes according to Kontoe et al. (2008). Equation (11.1) is applicable to additional sectional forces and moment because for  $\Delta = 0$  the forces and moment become equal to zero, which is not the case in static condition. It is possible to calculate the **static stresses in the lining before the earthquake** using the formulas according to Hoeg (1968) for the case of no slippage and at the location of tunnel extrados.

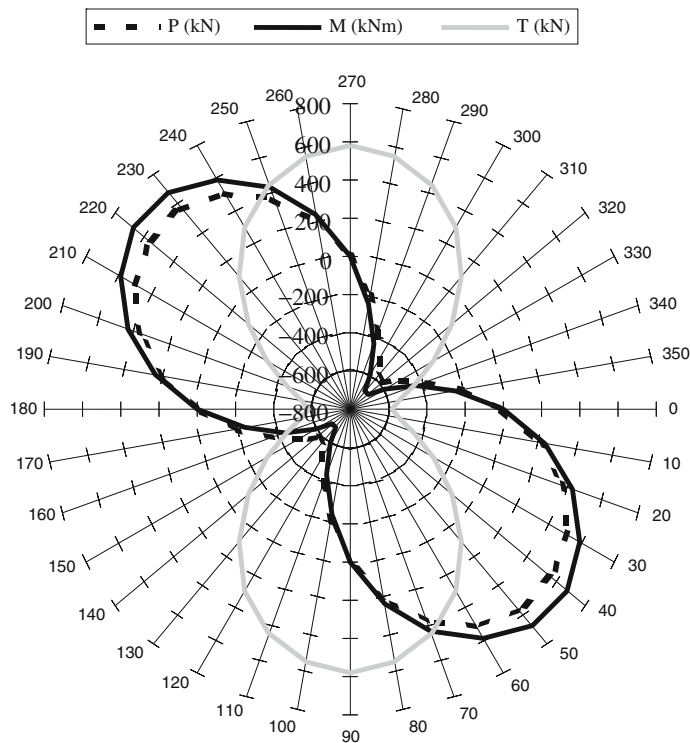


**Fig. 11.16** Axial (P) and transversal (T) force and bending moment (M) in the shotcrete lining of the bench pilot Bolu tunnel due to differential horizontal ground displacement  $\Delta_s$  of 0.015 m i.e.  $\Delta$  of 0.038 m over the tunnel diameter of 5 m

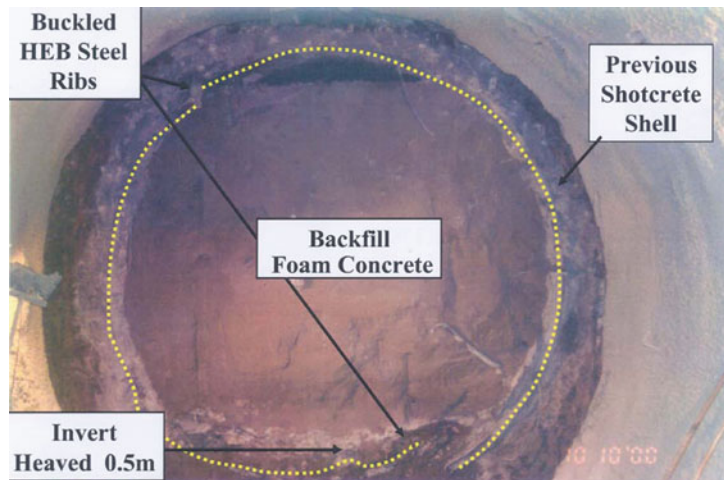


**Fig. 11.17** A cross section of the bench pilot Bolu tunnel with marked locations of the maximum damage to the shotcrete lining (Kontoe, 2009)

$$\begin{aligned}
\sigma_r &= \frac{\sigma_v}{2} \cdot [(1+k) \cdot (1-a_1) - (1-k) \cdot (1-3 \cdot a_2 - 4 \cdot a_3) \cdot \cos(2 \cdot \alpha)] \\
\sigma_\alpha &= \frac{\sigma_v}{2} \cdot [(1+k) \cdot (1+a_1) + (1-k) \cdot (1-3 \cdot a_2) \cdot \cos(2 \cdot \alpha)] \\
\tau_{r\alpha} &= \frac{\sigma_v}{2} \cdot (1-k) \cdot (1+3 \cdot a_2 + 2 \cdot a_3) \cdot \sin(2 \cdot \alpha) \\
s_r &= \frac{\sigma_v}{2} \cdot \frac{R}{M_s} \cdot \left[ (1+k) \cdot (1-v_s) \cdot \left( 1 + \frac{a_1}{1-2 \cdot v_s} \right) \right. \\
&\quad \left. - (1-k) \cdot \frac{1-v_s}{1-2 \cdot v_s} \cdot [(1+a_2 + 4 \cdot (1-v_s) \cdot a_3) \cdot \cos(2 \cdot \alpha)] \right] , \\
s_\alpha &= \frac{\sigma_v}{2} \cdot \frac{R}{M_s} \cdot \frac{1-v_s}{1-2 \cdot v_s} \cdot (1-k) \cdot [(1-a_2 + 2 \cdot (1-2 \cdot v_s) \cdot a_3) \cdot \sin(2 \cdot \alpha)] \\
a_1 &= \frac{(1-2 \cdot v_s) \cdot (C-1)}{(1-2 \cdot v_s) \cdot C + 1} \\
a_2 &= \frac{(1-2 \cdot v_s) \cdot (1-C) \cdot F - 0.5 \cdot (1-2v_s)^2 \cdot C + 2}{[(3-2 \cdot v_s) + (1-2 \cdot v_s) \cdot C] \cdot F + (2.5 - 8 \cdot v_s + 6 \cdot v_s^2) \cdot C + 6 - 8 \cdot v_s} \\
a_3 &= \frac{[1 + (1-2 \cdot v_s) \cdot C] \cdot F - 0.5 \cdot (1-2 \cdot v_s) \cdot C - 2}{[(3-2 \cdot v_s) + (1-2 \cdot v_s) \cdot C] \cdot F + (2.5 - 8 \cdot v_s + 6 \cdot v_s^2) \cdot C + 6 - 8 \cdot v_s} \\
C &= 0.5 \cdot \frac{1}{1-v_s} \cdot \frac{M_s}{E} \cdot \frac{D}{t} \\
F &= 0.25 \cdot \frac{1-2 \cdot v_s}{1-v_s} \cdot \frac{M_s}{E} \cdot \left( \frac{D}{t} \right)^3 \\
M_s &= \frac{E_s \cdot (1-v_s)}{(1+v_s) \cdot (1-2 \cdot v_s)} \\
E_s &= G_s \cdot 2 \cdot (1+v_s)
\end{aligned} \tag{11.13}$$

where  $\sigma_v$  is the vertical overburden stress,  $k$  is the ratio between horizontal and vertical overburden stress,  $R$  and  $D$  are the average radius and diameter of a cylinder,  $t$  is cylinder thickness,  $E$  is Young modulus,  $v$  is Poisson's ratio,  $s$  subscript is for soil, angle  $\alpha$  is measured from the horizontal cylinder axis upwards,  $s_r$  and  $s_\alpha$  are the tangential and radial displacements respectively. For  $\sigma_v = 83*23 + 83*21 + (5+14)*20 = 3500$  kPa and assumed  $k = 1$ , it follows from Equation (11.23) that the average axial stress in the lining in static condition is 2.7 MPa. The maximum axial stress during the earthquake is then  $45 + 1.9 + 2.7 = 49.6$  MPa, which is greater than the 14 days old shotcrete cube strength of 40 MPa. Moreover, one of the two tunnels was under construction when the earthquake occurred so that the shotcrete strength may not have been even 30 MPa. Collapse of one of the tunnels may have triggered the collapse of the adjacent tunnel. Also, compressive strength

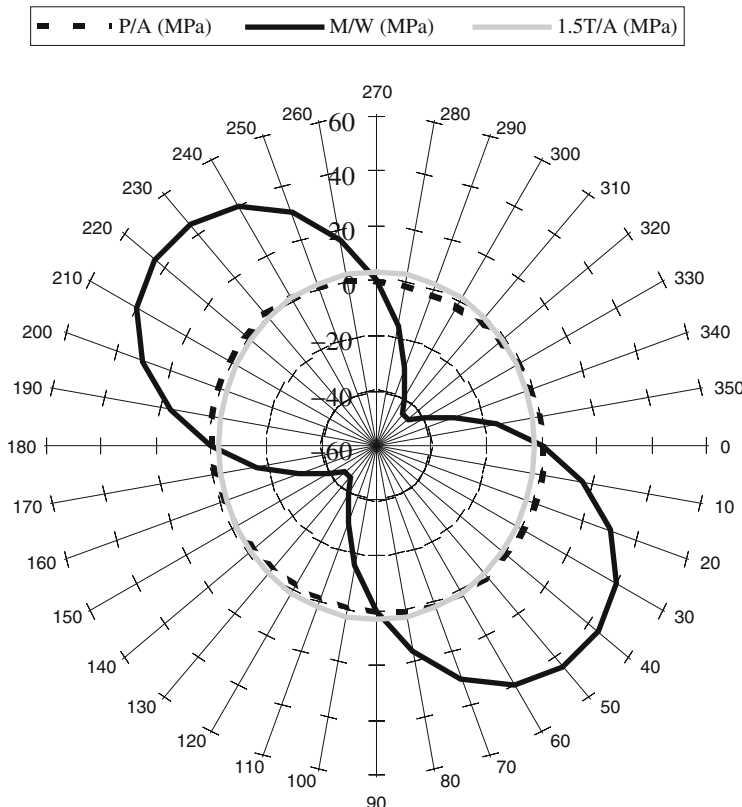


**Fig. 11.18** Axial (P/A), maximum shear (1.5 T/A) and bending stress (M/W) in the shotcrete lining of the bench pilot Bolu tunnel due to differential horizontal ground displacement  $\Delta_s$  of 0.015 m i.e.  $\Delta$  of 0.038 m over the tunnel diameter of 5 m

of a concrete cylinder is only about 80% of the strength of a cube because of the end constrains effects so even the 7 days old lining compressive strength could have been less than  $0.8 \times 30 = 24$  MPa. On the other hand, concrete strength increase because of the strain rate of  $0.003 \times (0.25 \times 1)^{-1} = 0.012$  per second could have been less than 1.4 times the static strength (e.g. Malvar and Crawford, 1998) i.e. less than  $1.4 \times 24 = 33.6$  MPa.

### 11.5.3 Duzce Pipelines in Turkey

Tromans (2004) analysed, using a geographical information system (GIS), water supply pipelines damage rate following the 1999 Kocaeli (with the moment magnitude  $M_w = 7.4$ ) and the 1999 Duzce earthquake with the moment magnitude

**Table 11.4** Peak ground motion parameters recorded at Duzce seismological station (Tromans, 2004)

Earthquake	Component	PGA (g)	PGV (cm/s)	PGD (cm)
Kocaeli	NS	0.31	41	15
	EW	0.36	54	15
Duzce	NS	0.38	37	16
	EW	0.51	84	47

$M_w = 7.1$  but at the epicentral distance of 9 km from the town seismological station unlike the 1999 Kocaeli earthquake with the epicentral distance of 101 km. The town seismological station recorded peak ground motions are given in Table 11.4.

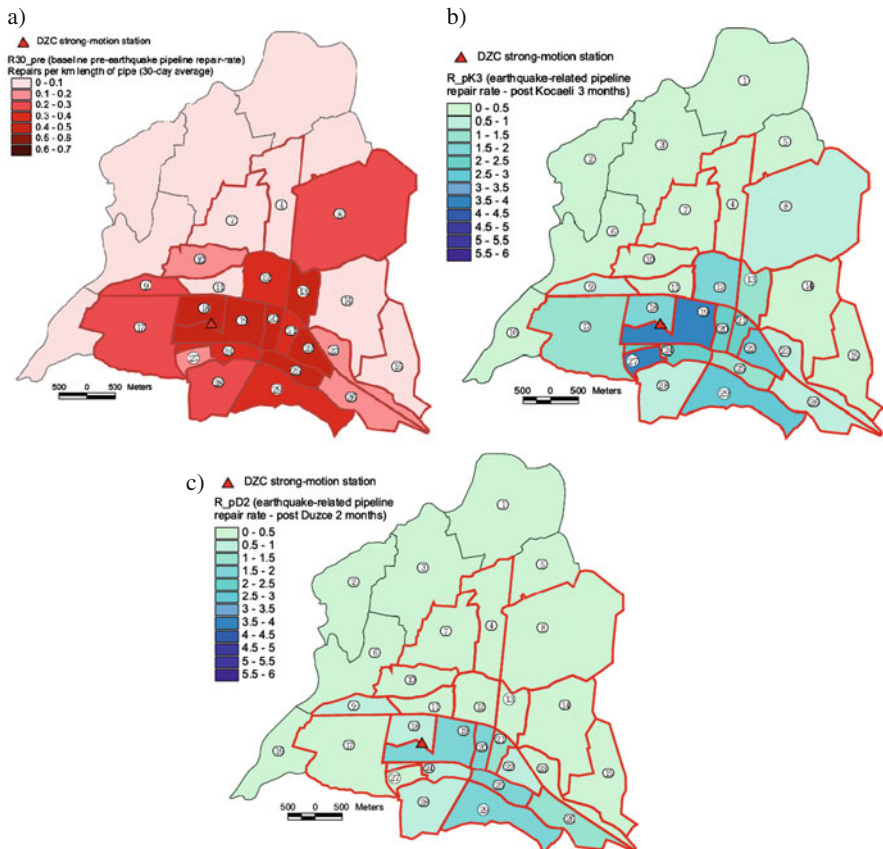


**Fig. 11.19** Different pipeline repair rates in the pre and post earthquake periods in Duzce (a) pre earthquakes averaged for 1 month period, (b) post Kocaeli earthquake for 3 months period, (c) post Duzce earthquake for 2 months period (Tromans, 2004)

The older about 500 km long pipelines are made mainly of cast iron (CI) with some asbestos cement (AC) while newer about 280 km long pipelines in September 2000 consist of PVC with diameter between 100 and 200 mm.

Simsek and Dalgic (1997) provided a geological section in NW-SE direction across the sediment basin under Duzce. The basin is about 18 km long and up to 250 m deep in the middle. Near the edges of the basin, the thickness of the sediment decreases to about 50 m. The sediments include river alluvium along the rivers forming the basin, lacustrine levels of clayey-silty sand and pebbles in the north, northeast and east and clay, silty clay and clayey silt levels dominated in the south west of Duzce.

The results are plotted in Fig. 11.19.

Repair rates were greater about twice from the Kocaeli than from the Duzce earthquake although the later event induced about double peak ground motion amplitudes in EW direction in comparison with the former event. Tromans (2004) observed a close correlation between the spatial distribution of pipeline damage and building damage although this may have been influenced by the impact of building collapse on buried pipelines. Tromans (2004) has not found significant correlation between the spatial distribution of pipeline damage and the predominant frequency of the ground vibration, lateral variations in ground conditions and horizontal to vertical spectral Fourier amplitude spectra ratios. The greatest damage has been concentrated in the central part where the greatest concentration of pipelines is possible.

## 11.6 Discussion and Conclusions

Simplified analyses can predict the response of tunnels, vertical shafts and pipelines in seismic conditions at least approximately. The greatest contributory factor to the response of underground structures is the displacement of adjacent ground, which properties are usually unknown or only partially defined.

## References

- Abrahamson N (2003) Model for strain from transient ground motion. In: Proceedings workshop on the effects of earthquake induced transient ground surface deformation on at-grade improvements. CUREE publication No. EDA-04, [curee.org/projects/EDA/docs/CUREE-EDA04.pdf](http://curee.org/projects/EDA/docs/CUREE-EDA04.pdf), Oakland, CA
- Alheid HJ (1994) Seismic response of deep underground openings, chapter 1. In: Bull JW (ed) Soil-structure interaction: numerical analyses and modelling. E&FN Spon. London, UK, pp 1–36
- Ambraseys NN, Douglas J, Sigbjornsson R, Berge-Thierry C, Suhadolc P, Costa G, Smit P (2004) European strong motion database – volume 2. The Engineering and Physical Science Research Council of the United Kingdom GR-52114-01
- Dean A, Young DJ, Kramer GJE (2006) The use and performance of precast tunnel linings in seismic areas. IAEG paper No 679, The Geological Society of London, UK
- Dowding CH, Rozen A (1978) Damage to rock tunnels from earthquake shaking. ASCE J Geotechn Eng Div 104:175–191

- EN 1998-1 (2004) Eurocode 8 – design of structures for earthquake resistance, part 1: general rules, seismic actions and rules for buildings. European Committee for Standardization, Brussels
- Giek K, Giek R (1997) Engineering formulas, 7th edn. McGraw-Hill, New York, NY
- Hashash YMA, Hook JJ, Schmidt B, Yao JIC (2001) Seismic design and analysis of underground structures. *Tunnel Underground Space Technol* 16:247–293
- Hashash YMA, Park D, Yao JIC (2005) Ovaling deformations of circular tunnels under seismic loading, an update on seismic design and analysis of underground structures. *Tunnel Underground Space Technol* 20(5):435–441
- Hoeg K (1968) Stresses against underground structural cylinders. *ASCE J Soil Mechanics Foundations Div* 94(SM4):833–858
- Huo H, Bobet A, Fernandez G, Ramirez J (2005) Load transfer mechanism between underground structure and surrounding ground: evaluation of the failure of the Daikai station. *ASCE J Geotechn Geoenviron Eng* 131:1522–1533
- Isenberg J (1979) Role of corrosion in water pipeline performance in three US earthquakes. In: Proceedings of the 2nd US national conference on earthquake engineering, Stanford, CA, pp 683–692
- Jenkins WM (1989) Theory of structures, chapter 3. In: Blake LS (ed) Civil engineer's reference book, 4th edn. Butterworth, Oxford, UK, pp 3–16
- Kontoe S (2009) Case study: geotechnical structures. *Soc Earthquake Civil Eng Dyn UK, Newslett* 21(3):12–14
- Kontoe S, Zdravkovic L, Potts DM, Menkiti CO (2008) Case study on seismic tunnel response. *Canad Geotechn J* 45:1743–1764
- Kramer GJE, Sedarat H, Kozak A, Liu A, Chai J (2007) Seismic response of precast tunnel linings. In: Proceedings of the conference rapid excavation and tunnelling, Toronto, pp 1225–1242
- Malvar LJ, Crawford JE (1998) Dynamic increase factors for concrete. In: 28th Department of Defence explosives safety board seminar, Orlando, FL, pp 1–17
- Nakajima Y, Abeki N, Watanabe D (2000) Study on the stability of H/V spectral ratio of micro tremor in short period range for the estimation of dynamic characteristics of surface geology. In: Proceedings of the 12th world conference on earthquake engineering, Auckland, New Zealand. CD-ROM, Paper No. 2904
- O'Rourke TD, Bonneau AL (2007) Lifeline performance under extreme loading during earthquakes. In: Pitilakis KD (ed) Proceedings of 4th international conference on earthquake geotechnical engineering, Thessalonica, Greece. Springer, New York, NY, pp 407–432
- O'Rourke TD, Jeon S-S (1999) Factors affecting the earthquake damage of water distribution systems. In: Proceedings of the 5th US conference on lifeline earthquake engineering, Seattle, WI, pp 379–388
- O'Rourke TD, Liu X (1999) Response of buried pipelines subjected to earthquake effects. Multidisciplinary Center for Earthquake Engineering Research monograph No. 3. University at Buffalo, New York, NY, USA
- Paolucci R, Pitilakis K (2007) Seismic risk assessment of underground structures under transient ground deformations. In: Pitilakis KD (ed) Proceedings of 4th international conference on earthquake geotechnical engineering, Thessalonica, Greece. Springer, New York, NY, pp 433–459
- Penzien J (2000) Seismically induced racking of tunnel linings. *Earthquake Eng Struct Dyn* 29:683–691
- Sharma S, Judd WR (1991) Underground opening damage from earthquakes. *Eng Geol (Amsterdam)* 30:263–276
- Shirozu T, Yune S, Isoyama R, Iwamoto T (1996) Report on damage to water distribution pipes caused by the 1995 Hyogoken-Nanbu (Kobe) earthquake. In: Hamada M, O'Rourke T (eds) Proceedings from the 6th Japan-US workshop on earthquake resistant design of lifeline facilities and countermeasures against soil liquefaction. Technical Report NCEER-96-0012, Waseda University, Tokyo, Japan, pp 93–110
- Simsek O, Dalgic S (1997) Consolidation properties of the clays at Duzce plain and their relationship with geological evolution. *Geol Bull Turkey* 40(2):29–38

- Srbulov M (2003) An estimation of the ratio between horizontal peak accelerations at the ground surface and at depth. *Eur Earthquake Eng* XVII(1):59–67
- Trifunac MD, Lee VW (1996) Peak surface strains during strong earthquake motion. *Soil Dyn Earthquake Eng* 15:311–319
- Tromans I (2004) Behaviour of buried water supply pipelines in earthquake zones. PhD thesis, Imperial College, University of London. <http://www3.imperial.ac.uk/geotechnics/publications/phdtheses>
- Wong RCK, Kaiser PK (1988) Design and performance evaluation of vertical shafts: rational shaft design method and verification of design. *Canad Geotechn J* 25:320–337

# Chapter 12

## Ground Vibration Caused by Industry

### 12.1 Introduction

Ground vibration caused by industry can result in cracking of structures, disruption of processes and annoyance to people. Vibration consideration involves its source, propagation path and its recipient. A starting point of vibration consideration should be definition of acceptable vibration effect on a recipient. For example, both ANSI S3.29 (1983) and BS 6472 (1992) recommend the same basic root mean square (r.m.s.) accelerations in the vertical direction for critical working areas such as hospital operating theatres and precision laboratories shown in Fig. 12.1. The r.m.s. acceleration is the square root of the average of sum of squares of componential accelerations. Both codes recommend the multiplication factor of 4 of the basic r.m.s. acceleration for offices, and 8 for workshops for continuous (and intermittent vibrations and repeated impulsive shock according to ANSI S3.29, 1983) and 128 for both offices and workshops for impulsive vibration excitation (with duration less than 2 s) with up to 3 occurrences a day. These two codes differ only concerning the multiplication factors of the basic r.m.s. accelerations for residential buildings as shown in Table 12.1. In addition, BS 6472 (1992) recommends the use of the same multiplication factors for the peak velocity.

Excessive vibration can cause malfunction and damage of sensitive equipment. Manufacturers of equipments specify tolerable levels of vibrations for their equipment. For example, Amick (1997) and BS 5228-2 (2009) provide the following limits:

- optical microscope with magnification 400 times, microbalances, optical balances, proximity and projection aligners etc.: 0.050 mm/s at 8+Hz
- optical microscope with magnification 1000 times, inspection and lithography equipment (including steppers) to 3  $\mu\text{m}$  line width: 0.025 mm/s at 8+Hz
- most lithography and inspection equipment (including electron microscopes) to 1  $\mu\text{m}$  detail size: 0.0125 mm/s at 8+Hz
- electron microscopes (TEM's and SEMs) and E-Beam systems: 0.006 mm/s at 8+Hz

- long path laser based small target systems 0.003 mm/s at 8+Hz. Dowding (2000) quotes the following limits: IBM 3380 hard disk drive: 18 mm/s between frequencies from 1 to 200 Hz (0.3g in the vertical direction, 0.1g for 5 Hz, 0.3g for 16 Hz, and 0.4g above 20 Hz in the horizontal direction),
- operating theatre (ISO): 0.13 mm/s between frequencies from 60 to 1000 Hz,
- analytical balance: 0.076 mm/s between frequencies from 45 to 1000 Hz,
- electronic microscope (Phillips): 0.025 mm/s between frequencies from 50 to 1000 Hz

It is worth mentioning that footfall induced floor vibration velocity is in the range from 1.1 to 3.8 mm/s between frequencies from 5 to 10 Hz according to Dowding (2000). New (1986), instead, reports peak particle velocities between 0.02 and 0.5 mm/s from footfalls, 0.15 to 3.0 mm/s from foot stamping, 3–17 mm/s from door slamming and 5–20 mm/s from percussive drilling in buildings. Not only precise equipment but also other industrial machine manufacturers specify tolerable levels of vibration.

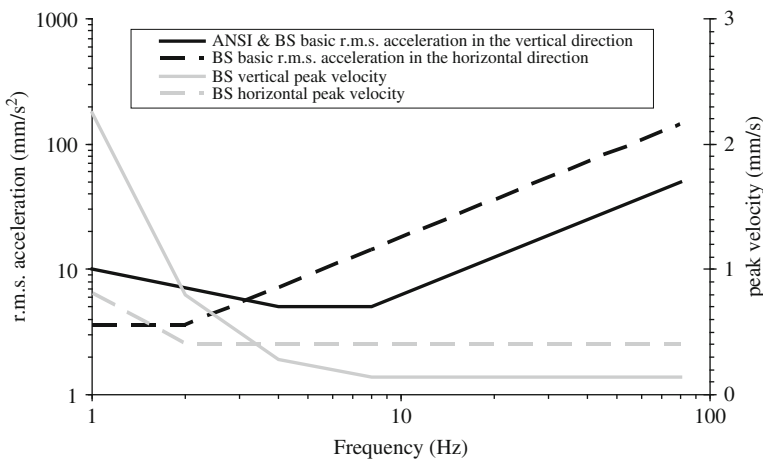


**Fig. 12.1** Limiting for humans basic root mean square accelerations and componential peak velocities for the vertical and horizontal directions versus frequency of vibration in buildings according to ANSI S3.29 (1983) and BS 6472 (1992)

**Table 12.1** Multiplication factors of the basic r.m.s. acceleration in residential buildings

Time	Continuous vibration		Impulsive vibration (duration <2 s) with up to three occurrences	
	ANSI S3.29 (1983)	BS 6472 (1992)	ANSI S3.29 (1983)	BS 6472 (1992)
Day (7 h to 22 h)	1.4–4	2–4	90	60–90
Night (22 h to 7 h)	1–1.4	1.4	1.4	20

Vibration can cause from cosmetic (superficial) damage of plaster on walls to serious structural damage. For example,

- German DIN 4150-3 (1999) specifies peak velocities of foundations by transient vibrations causing so called cosmetic damage (opening of cracks in plaster on walls, increase of existing cracks, and detachment of non-structural partitions from structural walls and columns) as shown in Fig. 12.2.
- British BS 7385-2 (1993) specifies peak velocities of building bases arising from transient vibrations causing cosmetic damage to buildings as shown in Fig. 12.2. For non-reinforced or light frames, at frequencies below 4 Hz, a maximum displacement of 0.6 mm (zero to peak) should not be exceeded.
- USBM (U.S. Bureau of Mines) RI 8507 (1980) specifies peak velocities causing visible damage to residential houses as a result of open mine blasting as shown in Fig. 12.2.

British standard BS 5228-2 (2009) recommends the threshold peak particle velocities for minor or cosmetic (i.e. non-structural) damage shown in Table 12.2.

The aim of this chapter is to describe basic mechanism and factors affecting ground vibration caused by transportation, shallow soil compaction, pile driving and blasting, several existing methods for analyses of such ground vibration, simple models and their assumptions used for prediction of such ground vibration and to demonstrate the model accuracy and precision based on several case histories. More detailed consideration of ground and foundation vibration is provided in specialist books, e.g. by Srbulov (2010). The emphasis is on the use simple formulas for

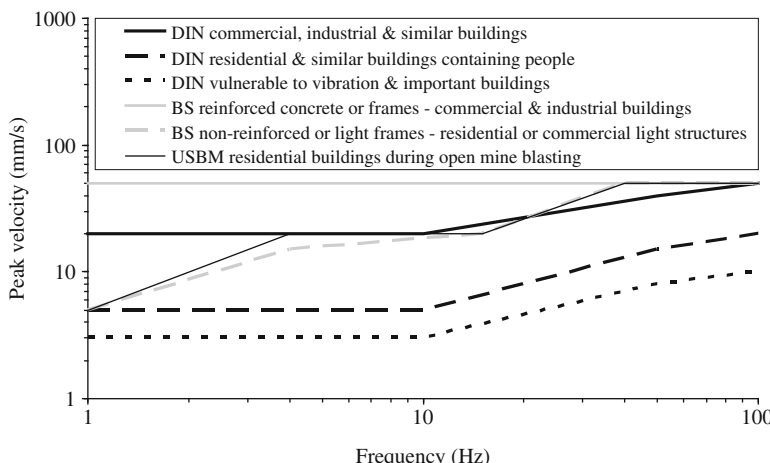


**Fig. 12.2** Peak velocity of foundations/basements for appearance of cosmetic cracking in buildings due to transient vibration based on DIN 4150-3 (1999), BS 7385-2 (1993) and USBM RI 8507 (1980)

**Table 12.2** Threshold peak particle velocities in mm/s for minor or cosmetic damage according to BS 5228-2 (2009)

Vibration type	Reinforced or framed structures. Industrial and heavy commercial buildings	Not reinforced or light framed structures. Residential or light commercial buildings	Slender and potentially sensitive masonry walls	Propped or tied walls or mass gravity walls	Underground services (for elderly and dilapidated brickwork sewers to use 20–50% reduction)
Intermittent vibration	50	15 @4 Hz 20@15 Hz, 50@40 Hz	10 @the toe 40 @the crest	50–100% greater than for slender and potentially sensitive masonry walls	30
Continuous vibration	50% lower than the intermittent vibration limits	reduced 1.5–2.5 the intermittent vibration limits	15		

comparisons of their results with the results of field measurements reported in the case histories considered.

## 12.2 Transportation and Ground Compaction

### 12.2.1 Introduction

Two types of traffic vibration sources are mainly considered:

- trains
- road vehicles

Other sources of vibrations such as landing planes, off-road vehicles, fluids flow in large pipelines, tunnel boring machines may also be considered. The following main types of soil compaction can cause significant ground vibrations:

- compaction of fill layers by vibrating rollers
- dropping of heavy weights (dynamic compaction)
- vibro float (pendulum like probe oscillation) and vibro rod
- compaction piles
- deep blasting

The use of compaction piles is equivalent to pile driving using impact hammers and the use of vibratory rod is equivalent to pile driving using vibrating hammers. Both compaction of fill layers by vibrating rollers and dynamic compaction by dropping heavy weight cause mainly near surface propagating ground waves shown in Fig. 3.1c. Vibratory floatation uses pendulum like probe to penetrate and compact soil in horizontal direction and therefore generates mainly horizontal axial and transversal waves. Deep blasting is subject of Section 12.4.

### 12.2.2 Mechanism and Factors

A vibrating source causes movements of soil particles in its vicinity, which in turn cause movement of particles further away so that a near ground surface wave is created. Particle velocity is different from velocity of wave propagation and even direction of particle movement can be different from direction of wave propagation. The energy (product of force and displacement) at the source is transmitted by waves further away in order that propagating medium – soil is able to achieve a state of minimum energy. The main factors affecting peak particle velocities are:

- Maximum amplitude of cyclic force at the source
- Frequency of vibration of the source

- Distance from the source
- Soil shear modulus and Poisson's ratio

### 12.2.3 Existing Methods

Empirical methods are based on attenuation relationships established using recorded values from past events. For example, U.S. Department of Transport (U.S. D.O.T., 1998) considers the effect of a large number of influential factors on the root mean square (r.m.s.) particle velocity. The effect of train speed on basic r.m.s. particle velocity is shown in Fig. 12.3 for the train speed range from 120 to 480 km/h.

Hiller and Crabb (2000) carried out linear regression analysis on data from different compaction passes of **vibratory rollers** from both the controlled trial and from construction sites and obtained the following expression for the resultant particle velocity (mm/s) that is obtained from the three componential velocities (also BS 5228-2, 2009)

$$v_{res} = k_s \cdot \sqrt{n_d} \cdot \left( \frac{A_r}{x_r + w_d} \right)^{1.5}, \quad (12.1)$$

where the coefficient  $k_s = 75$  for an average value i.e. a 50% probability of the vibration level being exceeded,  $= 143$  for a 33% probability of the vibration level being exceeded and  $= 276$  for a 5% probability of the vibration level being exceeded,  $n_d \leq 2$  is the number of vibration drums,  $A_r$  is the nominal amplitude of the vibrating roller (mm) in the range from 0.4 to 1.7 mm,  $x_r$  is the distance along the ground surface from the roller (m) in the range from 2 to 110 m,  $w_d$  is the width of the vibrating drum (m) in the range from 0.75 to 2.2 m. Equation (12.1) is applicable for a travel speed of approximately 2 km/h. For significantly different operating speeds of rollers,  $v_{res}$  in Equation (12.1) could be scaled by the ratio between  $2^{1/2}$  and (roller speed in km/h) $^{1/2}$  according to Hiller and Crabb (2000).

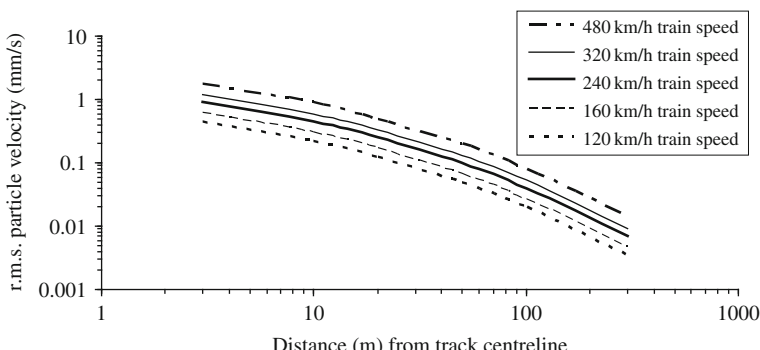


**Fig. 12.3** Basic root mean square (r.m.s.) particle velocities versus distance from high speed train tracks (based on U.S.-D.O.T., 1998)

For dynamic ground compaction by **dropping heavy weights**, Mayne (1985), for example, presented the following formula for the resultant particle velocity (mm/s):

$$v_{\text{res}} \leq 92 \cdot \left( \frac{\sqrt{M_d \cdot H_d}}{x_i} \right)^{1.7}, \quad (12.2)$$

where  $M_d$  is the tamper mass (tonnes),  $H_d$  is the drop height (m),  $x_i$  is the distance from impact (m). BS 5228-2 (2009) recommends to use 0.037 multiplying coefficient instead of 92 but for the product  $M_d H_d$  expressed in J instead of tm like Mayne (1985). Also BS 5228-2 (2009) limits the values of  $x_i$  in the range from 5 to 100 m.

For **vibrating stone columns**, BS 5228-2 (2009) provides the following formula for the resultant particle velocity:

$$v_{\text{res}} = \frac{k_c}{x^{1.4}}, \quad (12.3)$$

where  $k_c = 33$  (for 50% probability of exceedance), 44 (for 33.3% probability of exceedance), 95 (for 5% probability of exceedance),  $x$  is the horizontal distance range from 8 to 100 m.

BS 5228-2 (2009) provides the following equation for the resultant particle velocity due to **tunnelling**:

$$v_{\text{res}} \leq \frac{180}{r^{1.3}}, \quad (12.4)$$

where the slant distance  $r$  range is from 10 to 100 m.

Unterberger et al. (1997) used FLAC for prediction of surface vibrations caused by high-speed rail traffic in tunnels. Kaynia et al. (2000) developed numerical model, VibTrain, to simulate the track response to the passage of X-2000 trains at different speeds from 70 to 200 km/h and to estimate the effectiveness of strengthening the embankment for mitigating ground vibrations. Nabeshima et al. (2004) presented the results of measurements, numerical modelling and field tests performed to assess effectiveness of a precast concrete embedded wall barrier. Takemiya (2004) used two and three dimensional finite element computer program FLUSH and FLUSH/3DS to investigate the effectiveness of theoretically designed innovative countermeasure, called honeycomb wave impeding barrier, against vibrations induced by passage of high speed trains. Kogut et al. (2004) validated a numerical prediction model for train induced vibration by means of vibration measurements during the passage of an IC train and a Thalys HST at variable speed.

Field measurements are also conducted for known traffic and location condition. For example, summary of road traffic induced peak particle velocities at distances from 3 to 6 m from vehicles is shown in Fig. 12.4, based on data by Barneich (1985). The vibration frequency range was mainly from about 10 to 20 Hz (with extremes from 3 to 35 Hz).

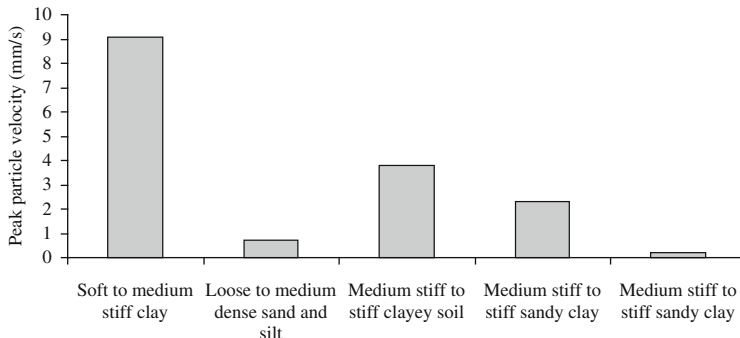


**Fig. 12.4** Peak particle velocities induced by road traffic at 3–6 m distances from vehicles (based on Barneich, 1985)

Watts (1987), for example, reported on vibration measurements at a number of houses from a sample of 1600 that were identified from an earlier survey of vibration nuisance at 50 residential sites. Heavy goods vehicles and buses produce most noticeable vibration. The vibration levels from such vehicles tend to increase with vehicle speed as well as with increase in maximum height or depth of the road surface irregularity, particularly within 5 m from buildings and the irregularity depth/height greater than approximately 20 mm. Watts (1987) also stated that “*At none of the measurement sites did passing heavy vehicle produce peak levels of vibration near the façade or on the ground floor which exceeded one of the lowest thresholds for minor damage that has been proposed for this type of building*”. However, for non-maintained roads with deep holes, significant vibrations may be generated by the impact of wheels of heavy vehicles.

#### 12.2.4 Simple Model and Assumptions

The maximum amplitude  $\Delta_w$  of ground displacement in the near field at a horizontal distance  $r < r_f$  (Equation 3.2) from a **point vibration source** with the maximum force amplitude  $P_f$  at the ground surface is defined by the following Green function (e.g. Wolf, 1994)

$$\Delta_w = \frac{1 - \nu}{2 \cdot \pi \cdot G \cdot r} \cdot P_f, \quad (12.5)$$

and in the far field at a distance  $r > r_f$

$$\Delta_w = \frac{1 - \nu}{2 \cdot \pi \cdot G \cdot \sqrt{r_f \cdot r}} \cdot P_f, \quad (12.6)$$

where  $\nu$  is Poisson’s ratio,  $G$  is ground shear modulus, which is dependent on the maximum shear modulus  $G_{max}$  (Section 4.2.1.3) and shear strain (Fig. 1.10) i.e. the

peak horizontal ground acceleration (Fig. 4.3) or the peak horizontal ground velocity when the peak horizontal ground acceleration is divided by  $2\pi f$ , where  $f$  is the (predominant) vibration frequency. The peak ground velocity  $\Delta_w \Delta_t^{-1} = \Delta_w 2\pi f$ , where  $f$  is the (predominant) vibration frequency.

For a **linear vibration source** (e.g. drum of a vibration roller, truck of a bulldozer) at/near the ground surface, which radiates energy uniformly at the ground surface, the maximum velocity  $\Delta_w \Delta_t^{-1}$  in the near field at a distance  $r \leq r_f$  from a vibration source with the maximum force amplitude  $P_f$  at/near the ground surface is using two Gauss integration points shown in Fig. 12.5a with  $0.5P_f$  each:

$$\frac{\Delta_w}{\Delta t} = \frac{f \cdot (1 - v)}{G} \cdot \frac{P_f}{2} \cdot \sum_{i=1}^2 \frac{1}{r_i}, \quad (12.7)$$

and in the far field at a distance  $r > r_f$

$$\frac{\Delta_w}{\Delta t} = \frac{f \cdot (1 - v)}{G} \cdot \frac{P_f}{2} \cdot \sum_{i=1}^2 \frac{1}{\sqrt{r_f \cdot r}} \quad (12.8)$$

For a planar vibration source (e.g. vibration plate) at/near the ground surface, which radiates energy uniformly at the ground surface, the maximum velocity

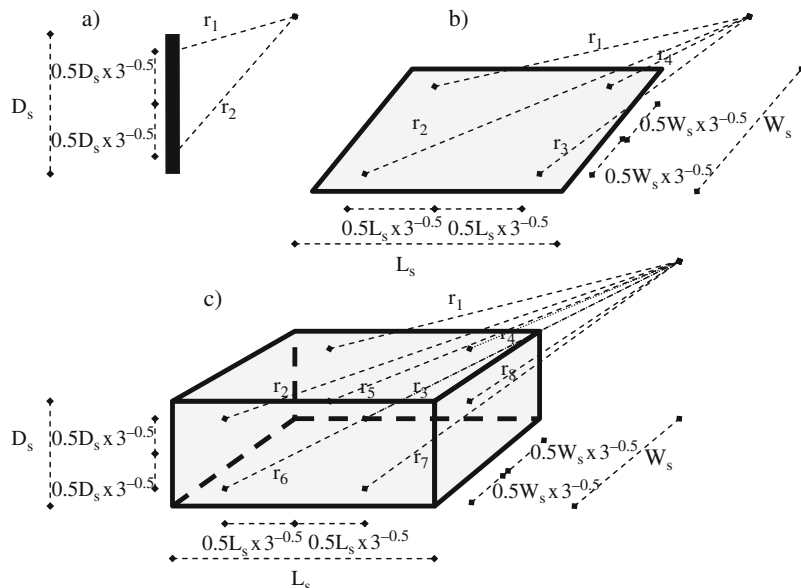


**Fig. 12.5** (a) linear, (b) planar, and (c) prismatic vibration sources with locations of Gauss integration points (e.g. Zienkiewich and Tabor, 1991)

$\Delta_w \Delta_t^{-1}$  in the near field at a distance  $r \leq r_f$  from a vibration source with the maximum force amplitude  $P_f$  at/near the ground surface is using four Gauss integration points shown in Fig. 12.5b with  $0.25P_f$  each:

$$\frac{\Delta_w}{\Delta t} = \frac{f \cdot (1 - \nu)}{G} \cdot \frac{P_f}{4} \cdot \sum_{i=1}^4 \frac{1}{r_i}, \quad (12.9)$$

and in the far field at a distance  $r > r_f$

$$\frac{\Delta_w}{\Delta t} = \frac{f \cdot (1 - \nu)}{G} \cdot \frac{P_f}{4} \cdot \sum_{i=1}^4 \frac{1}{\sqrt{r_f \cdot r}} \quad (12.10)$$

For a **prismatic vibration source** (e.g. set of vibration rods mounted on a common frame) near the ground surface, which radiates energy uniformly at the ground surface, the maximum velocity  $\Delta_w(\Delta t)^{-1}$  in the near field at a distance  $r \leq r_f$  from a vibration source with the maximum force amplitude  $P_f$  near the ground surface is using eight Gauss integration points shown in Fig. 12.5c with  $0.125P_f$  each:

$$\frac{\Delta_w}{\Delta t} = \frac{f \cdot (1 - \nu)}{G} \cdot \frac{P_f}{8} \cdot \sum_{i=1}^8 \frac{1}{r_i}, \quad (12.11)$$

and in the far field at a distance  $r > r_f$

$$\frac{\Delta_w}{\Delta t} = \frac{f \cdot (1 - \nu)}{G} \cdot \frac{P_f}{8} \cdot \sum_{i=1}^8 \frac{1}{\sqrt{r_f \cdot r}} \quad (12.12)$$

A vibration source is considered to be near the ground surface when it does not induce body waves, which propagate towards the ground surface.

### 12.2.5 Case History

Hiller and Crabb (2000) reported on the results of measurements of ground vibration caused by fill compaction using vibratory rollers during construction and from a test site. They also commented on a number of factors that affect ground vibration induced by vibratory rollers such as:

- **Centrifugal force and frequency.** Hiller and Crabb (2000) stated that “preliminary analysis had indicated that the centrifugal force is not an appropriate parameter for predicting vibration. Since rollers are designed to operate at frequencies above the resonance, the frequency per se appears to be unlikely to make a significant contribution to the resulting level of vibration. However, if the operating frequency were to coincide with the characteristic frequency of the

soil, then problems might be expected". The resonance can happen during start and stop of vibratory roller operation.

- **Static linear load.** A linear relation between the static linear load and the resultant peak particle velocity is suggested from an upper bound envelope to the data.
- **Nominal amplitude.** There was clearly an increase in the resultant peak particle velocity with increasing amplitude of vibration.
- **Travel speed.** From tests carried out using one vibratory roller over a range of speeds between zero and 6.7 km/h, it was found that the resultant peak particle velocity was approximately related to the inverse of the square root of the travel speed.
- **Number of drums.** The particle velocity arising from a double drum roller was approximately proportional to  $2^{1/2}$ .
- **Energy transmitted into the fill.** A linear regression analyses provided the following relationship for the resultant peak particle velocity

$$v_o = 2.07 \cdot \sqrt{A_r \cdot L_s \cdot w_d \cdot g} - 1.4, \quad (12.13)$$

where  $A_r$  is the nominal drum amplitude,  $L_s$  is the static linear load,  $w_d$  is the drum width,  $g$  is the gravitational acceleration, the square root expression is in J when  $A_r$ ,  $L_s$ ,  $w_d$ ,  $g$  are in SI units and  $v_o$  is in mm/s. [Equation \(7.16\)](#) does not account for the travel speed or the number of vibrating drums and is applicable at a distance of 2 m from a roller operating on clay.

- **Fill properties.** Hiller and Crabb ([2000](#)) stated that "The first pass of any item of plant always gave rise to lower levels of vibration than subsequent passes. Vibration from rollers operating on the clay was greater than when operating on the hogging in all cases except for the Bomag Variomatic". (Hogging is sandy gravel.) Also, larger vibration arising from plant operating on less stiff fill in majority of cases although contradictory evidence was observed. Hiller and Crabb ([2000](#)) stated that "Comparing the vibration levels with the stiffness for all materials showed no correlation between the stiffness and the peak particle velocity. For individual materials, however, there was some evidence that the particle velocity was higher when the stiffness was higher for a particular material".

The test fill was placed in a trench having fine sand at its bottom at a depth of 1.5 m. Well graded granular fill was used for the first three layers across the whole base of the excavation. First two layers of the fill were compacted using five passes of a smooth drum tandem roller because of the presence of loose sand underneath. The third final layer of the fill was compacted with two passes of a vibratory roller and two passes using the roller as a dead weight. Above the three initial layers, the further 13 test layers from excavated London Clay and sandy gravel were placed until the compacted fill level had reached original ground level. Vibration measurements were made for the final compaction pass of each test layer. Triaxial arrays of geophones were positioned at distances of 1, 4, 10, 40 and 100 m from the edge



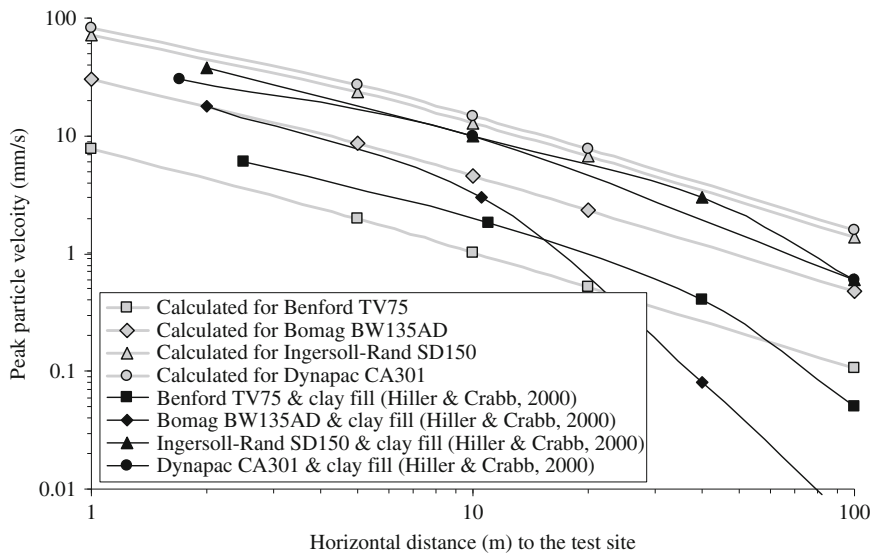


**Fig. 12.6** Peak particle velocities versus the horizontal distances based on the calculations and the recordings for a number of vibratory rollers

of the test fill. Details of four among other vibratory rollers used at the test and construction sites are given in Table 12.3 from Hiller and Crabb (2000).

The calculations are performed using Equation (12.7) for assumed Poisson's ratio  $\nu$  of 0.35 and transversal wave velocity of 130 m/s i.e. shear modulus  $G$  of 30 MPa while the results are shown in Fig. 12.6 together with the upper bounds of the recorded peak particle velocities from the controlled trials.

From Fig. 12.6, it is evident that the agreement between the calculated and recorded peak particle velocities is better at the source to site distances up to about 10 m, where it matters more because the velocities are larger. Differences between the calculated and recorded values for the source to site distances up to about 10 m are most likely caused by assumed soil properties (Poisson's ratio and shear modulus). Increased attenuation of peak ground velocities at the distances greater than about 10 m could be caused by the presence of soil with greater stiffness than the soil present at the test field as the amplitudes are inversely proportional to soil stiffness according to Equation (12.7).

## 12.2.6 Summary

Simple Equations (12.5) to (12.12) are capable of providing reasonable results for estimation of peak particle velocities of ground vibration caused by transportation and ground compaction.

## 12.3 Pile Driving

### 12.3.1 Introduction

Two main types of pile driving hammers are used: impact and vibration based. A large number of pile hammers exist and their rated properties are provided by their manufacturers.

### 12.3.2 Mechanism and Factors

The use of **impact hammers** causes emission of transient waves along pile shaft and from pile toe each time pile driving hammer hits the cushion on pile top. The pile driving energy transmitted from a pile shaft into surrounding ground as vertical transversal waves is proportional to the product of the shaft friction force and pile vertical displacement, which both vary along depth; the shaft friction force increases with depth and pile displacement decreasing with depth because of pile elastic shortening. The stress pulse that is generated by hammer impact at pile top propagates along a steel pile at about 5.1 km/s and along a concrete pile at about 2.9 km/s. For example, the stress pulse travels 0.004 s along 20 m long pile if it is made of steel and 0.007 s if the pile is made of concrete. As ground waves propagate at about one order of magnitude (ten times) slower than the speed of stress pulse along a pile, it will be assumed in a simplified approach that the driving energy is uniformly distributed along pile shaft. Jaksa et al. (2002), for example, measured acceleration time histories of ground vibration during installation of enlarged base driven cast in situ pile (Frankie type) and obtained the distribution of peak particle velocities along depth and around the pile similar to the distributions of wave fronts shown in Fig. 12.7.

Pile driving energy emitted from a pile toe is proportional to the product of force and displacement at pile toe. Both longitudinal and transversal ground waves are generated at pile toe because of the Poisson's effect in a continuum resulting in soil compression accompaniment by shearing. Attewell and Farmer (1973) observed that the pile driving involved generation of compression waves that propagate from the area of the pile toe and expand outwards over a spherical front. In a simplified approach, pile toe will be considered as a point source of energy emition into surrounding ground, as shown in Fig. 12.7a.

The use of **vibration hammers** causes continuous vibration of ground and emission of the vertical shear waves from the surface of sheet piles, Fig. 12.7b. One or more pairs of horizontally opposed contra-rotating eccentric weights are used by vibration hammers to cause ground vibration in order to reduce the friction between the pile and soil so that combined weight of the pile and hammer cause the pile to penetrate into ground. Operating frequencies of vibration hammers are between 25 and 50 Hz (e.g. Hiller and Crabb, 2000) i.e. between 0 and 1400 Hz (e.g. Dowding, 2000). The energy emitted from sheet pile surface is proportional to the product of the shaft friction force and pile vertical displacement, which both vary with depth.

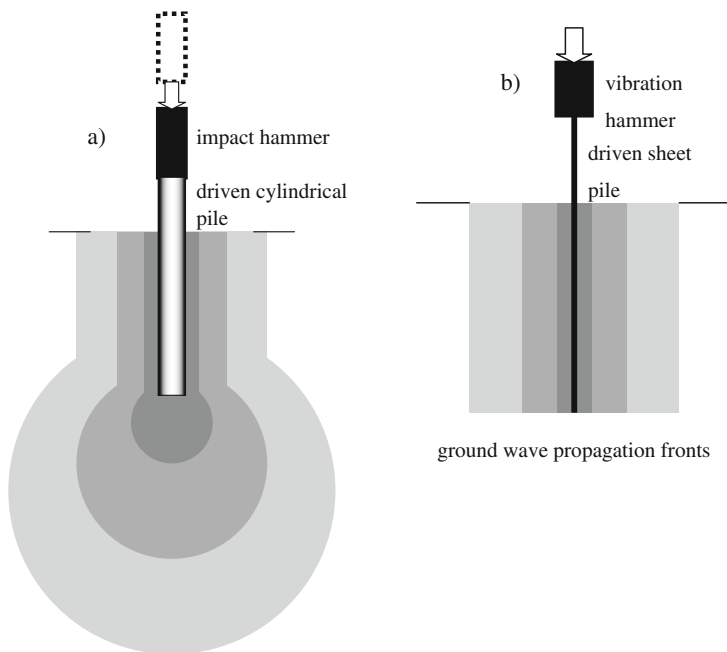


**Fig. 12.7** Schematic pile driving using impact (a) and vibration (b) based hammers with cross sections of fronts of propagating waves in homogeneous ground

The main factors affecting peak particle velocities arising from impact and vibratory hammers are:

- Energy released at the source
- Soil unit density
- Slant distance from the source
- Material damping

### 12.3.3 Existing Methods

Empirical methods are based on attenuation relationships established using recorded values from past events. For example, BS 5228-2 (2009) provides the following relationships for the resultant peak particle velocity (mm/s):

$$\text{For vibratory hammers } v_{\text{res}} = \frac{k_v}{x^{1.3}}, \quad (12.14)$$

where  $k_v = 60$  (for 50% probability of exceedance), 136 (for 33.3% probability of exceedance) and 266 (for 5% probability of exceedance);  $x$  is the horizontal distance along the ground surface in the range from 1 to 100 m.

$$\text{For impact hammers } v_{\text{res}} \leq k_p \frac{\sqrt{W}}{r_s^{1.3}}, \quad (12.15)$$

where  $W$  is the nominal energy (J) of an impact hammer in the range from 1.5 to 85 kJ,  $r_s$  is the radial (slant) distance (m) between source and receiver (for the pile depth range from 1 to 27 m and the horizontal distance along the ground surface range from 1 to 111 m);  $k_p = 5$  at pile refusal, otherwise in the range from 1 to 3 for loose to very stiff/dense soil.

Numerical analyses of the effect of pile driving on the ground motion are conducted. For example, Ramshaw et al. (1998) used finite element code ABAQUS to analyse the effects of dynamic testing of bored cast in situ piles by dropping 2.2 t hammer from 1.2 m height. Madheswaran et al. (2007) used a finite element code, PLAXIS, to study the ground vibration with and without concrete trenches during driving of steel casing with bottom shoe. Masoumi and Degrande (2008) considered a coupled finite element-boundary element method using a sub-domain formulation for the prediction of free field vibrations due to vibratory and impact pile driving.

A number of field measurements of peak particle velocities induced by pile driving are also performed. Examples of recorded values are shown in Fig. 12.8.

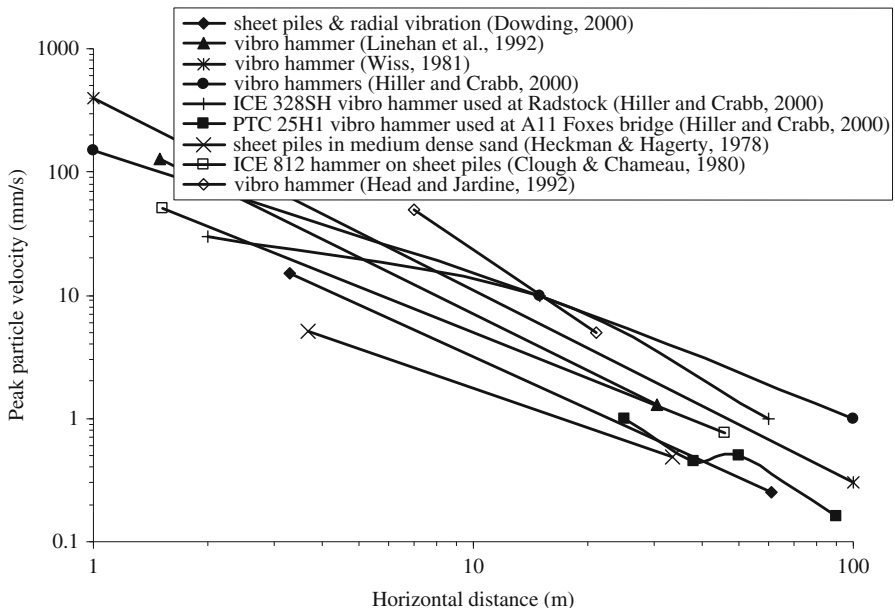


**Fig. 12.8** Examples of recorded peak particle velocity attenuations with distance from vibratory hammers

### 12.3.4 Simple Model and Assumptions

Ambraseys and Hendron (1968) considered the **vibration from blasting** using the Buckingham  $\pi$  theorem of dimensionless analysis (e.g. Langhaar, 1951) and found that the peak particle velocity  $\partial \Delta_{wr}(\partial t)^{-1}$  is inversely proportional to the site to source slant distance  $r_s$  on cube power. Hence,

$$\frac{\partial \Delta_{wr}}{\partial t} \approx \sqrt{\frac{2}{\rho} \cdot \frac{E_o}{4/3 \cdot r_s^3 \cdot \pi \cdot e^{k \cdot r_s}}}, \quad (12.16)$$

where  $E_o$  is energy released at a point source i.e. pile tip,  $\rho$  is ground unit density and  $4/3r_s^3\pi$  is the volume of ground between the source and the site,  $k$  is material damping ratio (i.e. ratio between actual damping and the critical damping that prevents vibration). For **linear vibration sources**, the ground amplitudes ratio can be calculated using simple Gauss integration scheme (e.g. Zienkiewich and Taylor, 1991; Potts and Zdravkovic, 1999) for the characteristic points, which locations are shown in Fig. 12.5, instead of analytical or numerical integration over the source extent. From Equation (12.16) and Fig. 12.5a with  $0.5E_o$  at each point:

$$\frac{\Delta_{wr}}{\Delta t} = \sqrt{\frac{3 \cdot E_o}{4 \cdot \rho \cdot \pi} \cdot \sum_{i=1}^2 \frac{1}{r_i^3 \cdot e^{k \cdot r_i}}} \quad (12.17)$$

Calculation of the source energy  $E_o$  in Equations (12.16) and (12.17) should be straight forward providing that the basic properties of impact hammer used and of the adjacent ground are known. The source energy  $E_o$  is product of resultant force acting along pile shaft and at pile toe and the ground displacements along pile shaft and at pile toe respectively that caused by such forces. Calculated energy  $E_o$  cannot exceed the rated energy of pile hammer multiplied by the hammer efficiency factor. For tubular unplugged piles, the internal shaft friction causes the vibration of the internal soil column within the pile and not of soil surrounding the pile.

**In coarse grained soil without cohesion** (i.e. with zero shear strength at zero effective stress):

- The force along pile shaft is commonly calculated as:

$$\sigma'_{v,avr} \cdot K_s \cdot \tan \delta_\phi \cdot D_p \cdot \pi \cdot L_p, \quad (12.18)$$

where  $\sigma'_{v,avr}$  is an average effective overburden pressure along pile shaft length  $L_p$  in ground,  $K_s$  is the coefficient of lateral effective stress acting on pile shaft,  $\delta_\phi$  is friction angle between ground and pile shaft (usually assumed equal to about 2/3 of the ground friction angle for pre-cast driven piles and equal to  $\phi$  for cast in place piles using compaction of concrete by a weight drop inside the retrieving steel tube of Franki type piles), and  $D_p$  is pile diameter. For sheet pile walls,

$D_p 2 L_p$  is used instead of  $D_p \pi L_p$  in Equation (12.18), where  $D_p$  is the width of the wall member being driven by a hammer.

- The force at the toe of a plugged pile is commonly calculated in non-cohesive ground as:

$$\sigma'_v \cdot N_q \cdot \frac{D_p^2 \cdot \pi}{4}, \quad (12.19)$$

and of an unplugged pile as:

$$\sigma'_v \cdot N_q \cdot (D_p - d_p) \cdot \pi \cdot d_p, \quad (12.20)$$

in which case the internal shaft friction will be taken into account, where  $\sigma'_v$  is effective overburden pressure at the level of pile toe,  $N_q$  is ground bearing capacity factor,  $D_p$  is external pile diameter,  $d_p$  is pile wall thickness for hollow piles. For sheet pile walls, the toe force is much smaller in comparison with the side force and can be ignored.

**In fine grained soil with cohesion** in fully saturated and undrained condition (i.e. when there is no time for soil consolidation to take place under applied load):

- The force along pile shaft is commonly calculated as:

$$\alpha_p \cdot c_{u,avr} \cdot D_p \cdot \pi \cdot L_p, \quad (12.21)$$

where  $\alpha_p$  is ground cohesion mobilization factor along pile shaft,  $c_{u,avr}$  is an average ground cohesion in undrained condition along pile shaft length  $L_p$  in ground, and  $D_p$  is pile diameter. For sheet pile walls,  $D_p 2 L_p$  is used instead of  $D_p \pi L_p$  in Equation (12.21), where  $D_p$  is the width of the wall member being driven by a hammer.

- The force at the toe of a plugged pile is commonly calculated in cohesive ground as:

$$9 \cdot c_u \cdot \frac{D_p^2 \cdot \pi}{4}, \quad (12.22)$$

and of an unplugged pile as:

$$9 \cdot c_u \cdot (D_p - d_p) \cdot \pi \cdot d_p, \quad (12.23)$$

in which case the internal shaft friction will be taken into account, where  $c_u$  is cohesion of ground under/around pile tip. For sheet pile walls, the toe force is much smaller in comparison with the side force and will be ignored.

**In layered ground** containing layers of cohesive and non-cohesive, Equation (12.18) is applied along non-cohesive and Equation (12.21) along cohesive layers.

Cone penetrometer ([Section 3.5.2.3](#)) is a scaled model of a pile. Forces acting along a pile shaft and at the pile toe can be calculated by applying the scaling factor of  $D/3.57$  to the force acting along the shaft of cone penetrometer and  $0.25*\pi D^2(10)^{-1}$  to the force acting at cone penetrometer tip, where the pile diameter  $D$  is in cm and pile squared diameter  $D^2$  is in  $\text{cm}^2$ , the cone diameter is 3.57 cm and the cone cross sectional area is 10  $\text{cm}^2$ .

### 12.3.5 Case History

Hiller and Crab ([2000](#)) provided results of recorded ground peak particle velocities caused by vibratory hammers and detailed data for two locations. The 900 mm diameter and 14 m long casing at A11 Foxes Bridge was driven by a vibratory hammer type PTC 25H1 (with energy per cycle of 4.97 kJ and frequency of 29 Hz) through 3 m of very dense sand overlying chalk of variable grade. The 5 m long steel sheet L40 was driven by a vibratory hammer type ICE 328SH (with energy per cycle of 0.99–1.17 kJ and frequency of 46.7 Hz) through colliery waste. Dividing the peak horizontal ground acceleration in [Fig. 4.3](#) by  $2\pi f$ , where  $f$  is the hammer vibration frequency, dependence of an averaged material damping ratio on the peak particle velocity is shown in [Fig. 12.9](#).

The results of the calculations together with the recorded peak particle velocities are shown in [Fig. 12.10](#). The calculated peak particle velocities over predicted the maximum recorded values possibly because of the use of an averaged material damping ratio. Also, it has not been possible to calculate the peak particle velocities at smaller distances because [Fig. 12.9](#) is for a limited range of peak particle velocities. It is better to use the results of tests performed on soil at the site under consideration instead of averaged values.

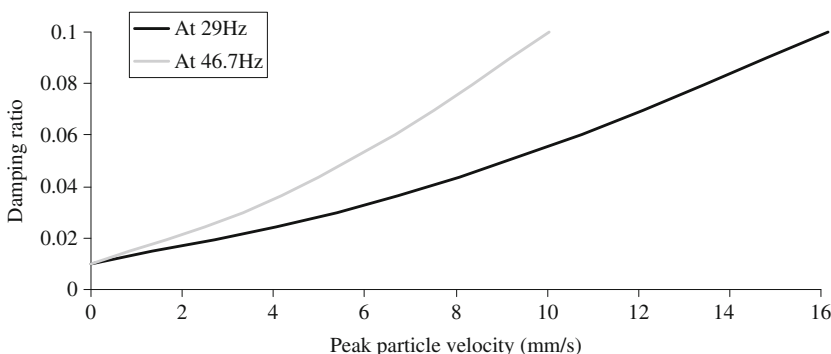


**Fig. 12.9** Dependence of an average material damping ratio on peak particle velocity at different vibration frequencies

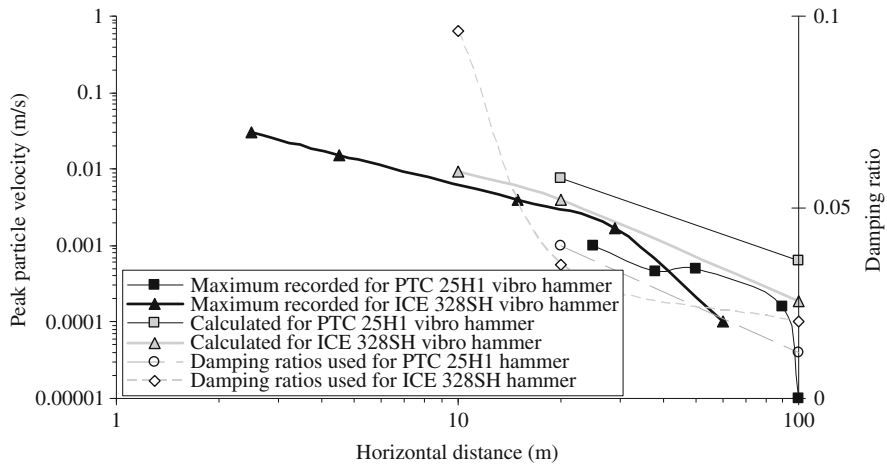


**Fig. 12.10** Recorded and calculated peak particle velocities and material damping coefficients used in Section 12.3.5

### 12.3.6 Summary

The Equations (12.16) and (12.17) can predict peak particle velocities caused by pile driving rather well providing that the values of material damping ratios are defined based on testing of actual soil present at the site under consideration. The results obtained using an averaged material damping ratio are likely to over predict the actual peak particle velocities because of built in conservatism in the values of the average material coefficient. Figure 1.10 shows possible range of material damping ratio for a range of shear strain  $\gamma$ , which is the ratio between the horizontal peak particle velocity (PPV) and transversal wave velocity ( $v_t$ ) so the  $PPV = \gamma^* v_t$ .

## 12.4 Blasting

### 12.4.1 Introduction

Explosives are used in both construction and mining industry for digging tunnels in rock (e.g. Hoek and Brown, 1980; Gregory, 1984) and for cutting slopes of trenches in rock (e.g. Hoek and Bray, 1981; Gregory, 1984). The transient ground waves caused by the use of explosives are dependent on the energy of explosions of individual charges, which is specified by the manufacturers of explosives. In simplified approach, the explosion at the face of a tunnel can be considered coming from a point source. The explosions used to cut rock slopes are considered in the simplified approach as a planar energy source. Soil deep compaction by explosive is not frequently used technique but is very cost effective when applicable. Gohl et al. (2000)

and Towhata (2007) provide more information on this technique, which causes transient ground vibrations. In the simplified analyses, prismatic volume of compacted soil is considered as a source.

### **12.4.2 Mechanism and Factors**

The energy released at a source is transported by ground waves away. Radiation damping that occurs as a result of wave spread affects wave amplitudes and to a lesser amount the frequency. Material damping also decreases energy of propagating waves with distance. Material damping results from heat generated by particle friction caused by their motion with wave passage. The effect of material damping is much smaller than the effect of radiation damping except near the blasting location where cracks and plasticization occurs.

The main factors affecting peak particle velocities arising from blasting are:

- Energy released at the source
- Ground unit density
- Slant distance from the source
- Material damping

### **12.4.3 Existing Methods**

Different peak particle velocity attenuation relationships exist in literature. For example, U.S. Bureau of Mines (1971) established an upper limit of ground vibrations caused by blasting as:

$$PPV = 714 \cdot \left( \frac{\sqrt{W_e}}{D_b} \right)^{1.6}, \quad (12.24)$$

where PPV is peak particle velocity (mm/s),  $D_b$  is distance (m) to blast location,  $W_e$  mass (kg) of explosive used. Peak particle velocities predicted by Equation (12.24) are situated roughly in the middle between the upper and lower bound limits by Caltrans (2001), Fig. 12.11. Kahriman (2004) found that the upper limit by Caltrans (2001) was exceeded in the case of ground vibration produced from bench blasting at a limestone quarry.

Numerical analyses are used as well. For example, Hao et al. (2002) used the concept of anisotropic damage mechanics to analyze dynamic responses of a granite site under blasting loads. Wang and Lu (2003) formulated a new three-phase soil model for shock loading and employed it to facilitate a full simulation of explosion and the subsequent stress wave propagation in soil. Torano et al. (2006) used a finite element model to predict ground vibration due to blasting with consideration of adjustment factors: for local ground behaviour, explosive charge in each borehole, explosive confinement within rock mass and fringing sequence. Saiang

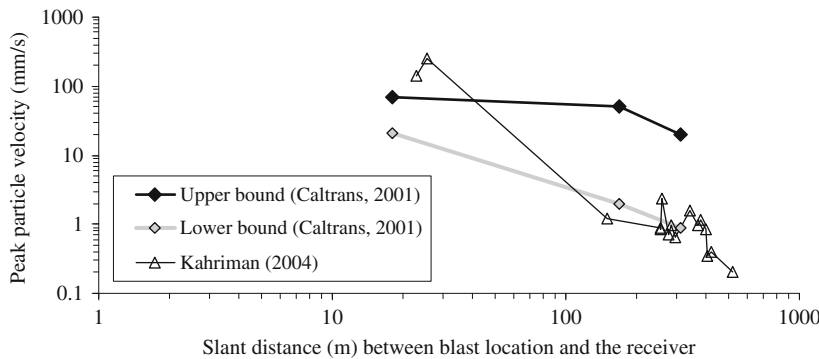


**Fig. 12.11** Peak particle velocities versus slant distances

and Nordlund (2009) used numerical analyses for near-field rock mass response evaluation of the influence of blast-induced damaged rock around shallow tunnels in brittle rock.

Field measurements of peak particle velocities caused by blasting are also performed. An example of the attenuation relationships of the peak particle velocity against scaled distance is shown in Fig. 12.12.

#### 12.4.4 Simple Model and Assumptions

For prediction of peak particle velocity from a point vibration source (single charge), Equation (12.16) is applicable. For prediction of peak particle velocity from a linear

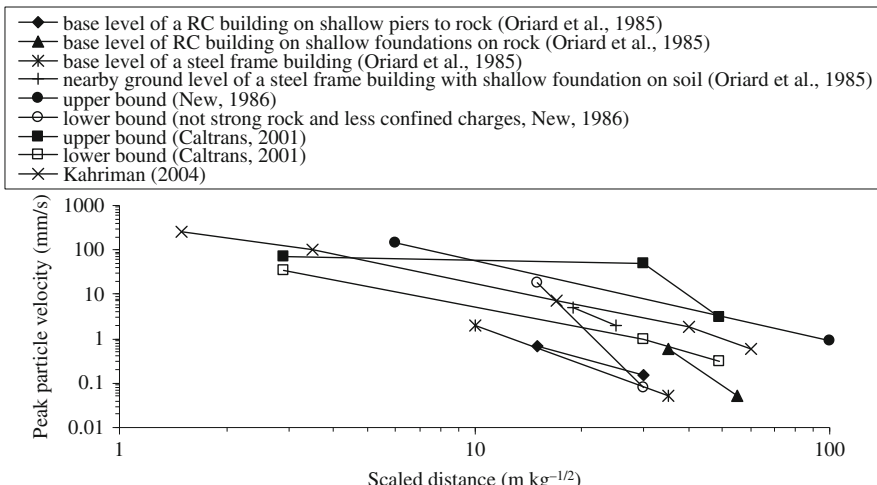


**Fig. 12.12** Peak particle velocities versus scaled distances  $\text{m}^* \text{kg}^{-1/2}$

vibration source (charge in a boreholes fired instantaneously), Equation (12.17) is applicable. For prediction of peak particle velocity from a **prismatic vibration source** (soil compaction), the following equation is applicable based on Equation (12.16) and Fig. 12.5c with  $0.125E_o$  at each point:

$$\frac{\Delta_{wr}}{\Delta t} = \sqrt{\frac{3 \cdot E_o}{16 \cdot \rho \cdot \pi} \cdot \sum_{i=1}^8 \frac{1}{r_i^3 \cdot e^{k \cdot r_i}}}, \quad (12.25)$$

where  $E_o$  is energy released at a point source i.e. pile tip,  $\rho$  is ground unit density and  $4/3r_s^3\pi$  is the volume of ground between the source and the site,  $k$  is material damping ratio (i.e. ratio between actual damping and the critical damping that prevents vibration).

#### 12.4.5 Case History from a Limestone Quarry in Istanbul

Kahriman (2004) provided results of measurements of peak particle velocities from 73 blast events during the bench blast optimization studies in a limestone quarry near Istanbul in Turkey. The heights of the 1st and 3rd benches were 20 m and of the 2nd and 4th benches 30 m. The holes for explosive charges were vertical and 105 mm in diameter. Three rows of holes for explosive charges per bench were used. The row spacing was 2 m for the 1st and 3rd bench and 2.5 m for the 2nd and 4th bench. The spacing of the holes per row was 2.5 m for the 1st and 3rd bench and 3 m for the 2nd and 4th bench. The first row of the holes was placed 3.5 m (burden thickness) from the slope for the 1st and 3rd bench and 4 m for the 2nd and 4th bench. Explosive length within the holes was 15 m of which 1 m was located below the bench level (sub drilling) with a plug (stemming) of 6 m for the 1st and 3rd bench and 24 m of which 2 m was located below the bench level (sub drilling) with a plug (stemming) of 8 m for the 2nd and 4th bench. The blasting operation used 42 ms delay between rows and a 17 ms delay between holes within a row with 25 ms interval used for inner borehole detonation. The explosive used was ANFO + 5% A1 (blasting agent), Rovex 650 and gelatine dynamite (priming). ANFO's detonation velocity is about 4200 m/s according to various sources. The energy released was proportional to the product of a half of the mass of explosive and the detonation velocity squared. A sketch of the benches with holes for explosive charges is shown in Fig. 12.13 while the test data are given in Table 12.4.

Energy of vibration source is product of a half of explosive mass per delay and its detonation velocity squared. The material damping ratio has been determined based on the reported frequency of vibration of ground and average material damping from Fig. 4.3 as shown in Fig. 12.14. The results of use of Equation (12.16) for calculation of PPV (with assumed  $\rho$  of  $2500 \text{ kg/m}^3$  and material damping according to Fig. 12.4) are shown in Fig. 12.15.

The calculated peak particle velocities over predicted the maximum recorded values possibly because of the use of an averaged material damping ratio. Also, it

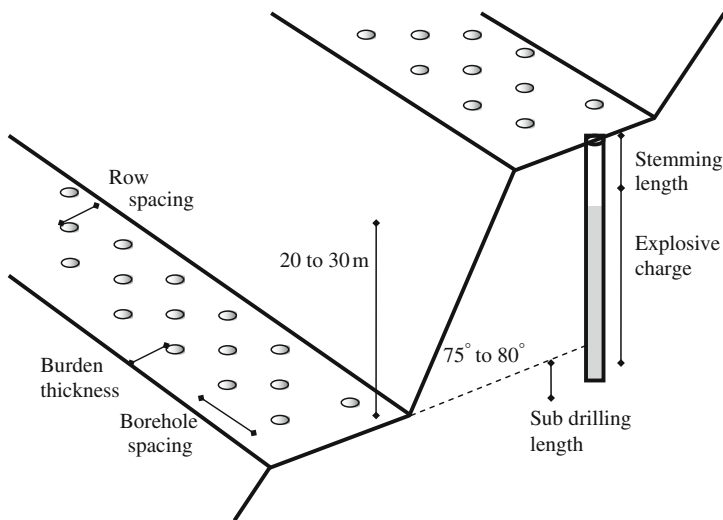


**Fig. 12.13** Sketch of cross section through benches in a rock slope with the holes for explosive charges in the case study in Section 12.4.5

**Table 12.4** Test data in the case study in Section 12.4.5

No	Charge per delay (kg)	Frequency (Hz)	Distance (m)	Peak particle velocity (mm/s)
1	180	20	23	144
2	242	45	25.6	250
3	69	10	150	1.2
4	175	9.4	254	0.9
5	81	11	255	0.85
6	538	10	257	2.35
7	97	91	275	0.7
8	206	5.6	283	0.95
9	93	67	295	0.65
10	165	17	340	1.55
11	83	16	368	0.95
12	242	9.1	376	1.15
13	354	9.6	400	0.85
14	180	41	403	0.35
15	180	20	418	0.4
16	170	9	520	0.2

has not been possible to calculate the peak particle velocities at smaller distances because Fig. 12.14 is for a limited range of peak particle velocities. It is better to use the results of tests performed on ground at the site under consideration instead of the average values.

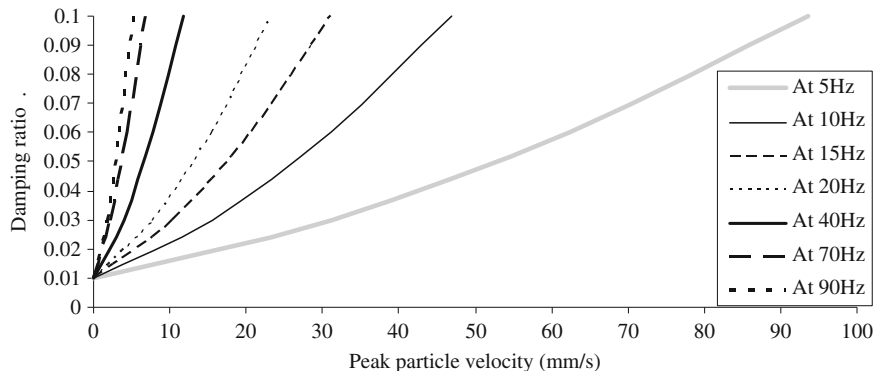


**Fig. 12.14** Dependence of an average material damping ratio on peak particle velocity at different vibration frequencies

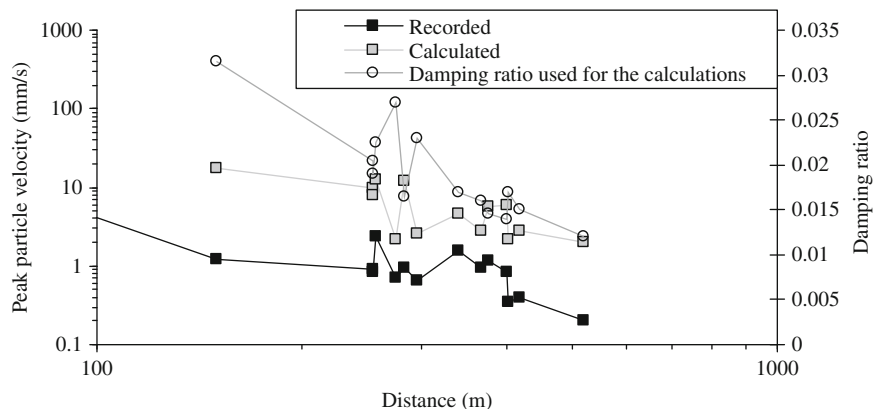


**Fig. 12.15** Peak particle velocities versus distances in the case study in Section 12.4.5

## 12.4.6 Summary

The Equations (12.16), (12.17) and (12.25) can predict peak particle velocities caused by blasting rather well providing that the values of material damping ratios are defined based on testing of actual ground present at the site under consideration. The results obtained using an averaged material damping ratio are likely to over predict the actual peak particle velocities because of built in conservatism in the values of the average material damping ratio. Figure 1.10 shows possible range of material damping ratio for a range of shear strain  $\gamma$ , which is the ratio between the horizontal peak particle velocity (PPV) and transversal wave velocity ( $v_t$ ) so the PPV =  $\gamma^* v_t$ .

## 12.5 Discussion and Conclusions

Prediction of peak particle velocity of ground vibration is based on simple formulas of attenuation of source energy by radiation and material damping. The accuracy of predictions can be improved if actual material damping ratio is determined by tests and used instead of an average value from EN 1998-5 (2004).

## References

- Ambraseys NN, Hendron AJ (1968) Dynamic behaviour of rock masses. In: Stagg KG, Zienkiewicz OC (eds) Rock mechanics in engineering practice. Wiley, London, pp 203–227
- Amick H (1997) On generic vibration criteria for advanced technology facilities: with a tutorial on vibration data representation. *J Inst Environ Sci* XL(5):35–44
- ANSI S3.29 (1983) Guide to the evaluation of human exposure to vibration in buildings. American National Standards Institute, Acoustical Society of America, New York, NY, Secretariat for Committees 51, 52 and 53
- Attewell PB, Farmer IW (1973) Attenuation of ground vibrations from pile driving. *Ground Eng* 6(4):26–29
- Barneich JA (1985) Vehicle induced ground motion. In: Gazetas G, Selig ET (eds) Vibration problems in geotechnical engineering. Proceedings of ASCE Convention, Detroit, MI, pp 187–202
- BS 5228-2 (2009) Code of practice for noise and vibration control on construction and open sites – part 2: vibration. British Standards Institution
- BS 6472 (1992) Guide to evaluation of human exposure to vibration in buildings (1 Hz to 80 Hz). British Standards Institution
- BS 7385-2 (1993) Evaluation and measurement for vibration in buildings, part 2: guide to damage levels from ground borne vibration. British Standard Institution
- Caltrans (2001) Ground vibration monitoring for construction blasting in urban areas. Report F-00-OR-10. State of California Department of Transportation
- Clough GW, Chameau JL (1980) Measured effects of vibratory sheep pile driving. *ASCE J Geotechn Eng* 104(GT10):1081–1099
- DIN 4150-3 (1999) Erschütterungen im Bauwesen – Teil 3: Einwirkungen auf bauliche Anlage Norm Ausgabe, Deutsch, Deutsche Industries Norm
- Dowding CH (2000) Construction vibration. Reprinted 1996 version. Prentice Hall, Upper Saddle River, NJ
- EN 1998-5 (2004) Eurocode 8 – design of structures for earthquake resistance, part 5: foundations, retaining structures and geotechnical aspects. European Committee for Standardization, Brussels
- Gohl WB, Jefferies MG, Howie JA (2000) Explosive compaction: design, implementation and effectiveness. *Geotechnique* 50:6576–665
- Gregory CE (1984) Explosives for North American engineers, 3rd edn. Trans Tech Publications, Enfield, USA
- Hao H, Wu C, Zhou Y (2002) Numerical analysis of blast-Induced stress waves in a rock mass with anisotropic continuum damage models part 1: equivalent material property approach. *Rock Mech Rock Eng* 35(2):79–94
- Head JM, Jardine FM (1992) Ground-borne vibrations arising from piling. Construction Industry Research and Information Association, London, U.K., Technical Note 142
- Heckman WS, Hagerty DJ (1978) Vibrations associated with pile driving. *ASCE J Construct Div* 104(CO4):14205
- Hiller DM, Crabb GI (2000) Ground borne vibration caused by mechanised construction works. Transport Research Laboratory report 429, United Kingdom

- Hoek E, Bray JW (1981) Rock slope engineering, revised 3rd edn. The Institution of Mining and Metallurgy, London
- Hoek E, Brown ET (1980) Underground excavations in rock. The Institution of Mining and Metallurgy, London, UK
- Jaksa MB, Griffith MC, Grounds RW (2002) Ground vibrations associated with installing enlarged-base driven cast-in-situ piles. *Aust Geomech* 37:67–73
- Kahriman A (2004) Analysis of parameters of ground vibration produced from bench blasting at a limestone quarry. *Soil Dyn Earthquake Eng* 24:887–892
- Kaynia AM, Madshus C, Zackrisson P (2000) Ground vibration from high speed trains: prediction and countermeasure. *ASCE J Geotechn Geoenviron Eng* 126(6):531–537
- Kogut J, Degrande G, Lombaert G, Pyl L (2004) Measurements and numerical prediction of high speed train vibrations. In: Proceedings of the 4th international conference on case histories in geotechnical engineering, New York, NY, paper No. 4.02
- Langhaar HL (1951) Dimensionless analysis and theory of models. Wiley, New York, NY
- Linehan PW, Longinow A, Dowding CH (1992) Pipeline response to pile driving and adjacent excavation. *ASCE J Geotechn Div* 118(2):300–316
- Madheswaran CK, Natarajan K, Sundaravadivelu R, Boomianathan A (2007) Effect of trenches on attenuation of ground vibration during pile driving. In: Esin İnan, Dipak Sengupta, Muralimohan Banerjee, Basudeb Mukhopadhyay, Hilmi Demiray (eds) Vibration problems ICOVP 2007. Proceedings in Physics, vol 126. Springer, Berlin, pp 231–238
- Masoumi HR, Degrande G (2008) Numerical modelling of free field vibrations due to pile driving using a dynamic soil-structure interaction formulation. *J Comput Appl Math* 215(2): 503–511
- Mayne PW (1985) Ground vibrations during dynamic compaction. In: Gazetas G, Selig ET (eds) Vibrations problems in geotechnical engineering. Proceedings of ASCE convention, Detroit, MI, pp 247–265
- Nabeshima Y, Hayakawa K, Kani Y (2004) Experimental and numerical studies on ground vibration isolation by PC wall-pile barrier. In: Proceedings of the 5th international conference on case histories in geotechnical engineering, New York, NY, paper No. 4.06
- New BM (1986) Ground vibration caused by civil engineering works. U.K. Transport and Road Research Laboratory research report 53
- Oriard LL, Richardson TL, Akins KP (1985) Observed high rise building response to construction blast vibration. In: Gazetas G, Selig ET (eds) Vibration problems in geotechnical engineering. Proceedings of a symposium of geotechnical engineering division of ASCE, Detroit, MI, pp 203–228
- Potts DM, Zdravkovic L (1999) Finite element analysis in geotechnical engineering – theory. Thomas Telford, London, UK
- Ramshaw CL, Selby AR, Bettess P (1998) Computation of the transmission of waves from pile driving. In: Skip BO (ed) Ground dynamics and man-made processes. Thomas Telford, London, UK, pp 115–128
- Saiang D, Nordlund E (2009) Numerical analyses of the influence of blast-induced damaged rock around shallow tunnels in brittle rock. *Rock Mech Rock Eng* 42(3):421–448
- Srbulov M (2010) Ground vibration engineering – simplified analyses with case studies and examples. Springer, New York, NY
- Takemiya H (2004) Field vibration mitigation by honeycomb WIB for pile foundations of a high-speed train viaduct. *Soil Dyn Earthquake Eng* 24(1):69–87
- Torano J, Rodriguez R, Diego I, Rivas JM, Casal MD (2006) FEM models including randomness and its application to the blasting vibrations prediction. *Comput Geotech* 33:15–28
- Towhata I (2007) Developments of soil improvement technologies for mitigation of liquefaction risk. In: Pitilakis KD (ed) Earthquake geotechnical engineering. Springer, New York, NY, pp 355–383
- Unterberger W, Poisel R, Honeger C (1997) Numerical prediction of surface vibrations caused by high speed rail traffic in tunnels. In: Golser, Hinkel, Schubert (eds) Tunnels for people. Balkema, Rotterdam, pp 417–422

- U.S. Bureau of Mines (1971) Blasting vibrations and their effects on structures. Bulletin 656, by Nicholiss HR, Johnson CF, Duvall WI
- USBM RI 8507 (1980) by Siskind DE, Stagg MS, Kopp JW, Dowding CH. Structure response and damage produced by ground vibrations from surface blasting. U.S. Bureau of Mines, Washington, DC
- US DOT-293630-1 (1998) High-speed ground transportation noise and vibration impact assessment. U.S. Department of Transportation, Office of Railroad Development, Washington, DC
- Wang Z, Lu Y (2003) Numerical analysis on dynamic deformation mechanism of soils under blast loading. *Soil Dyn Earthquake Eng* 23(8):705–714
- Watts GR (1987) Traffic-induced ground-borne vibrations in dwellings. Transport and Road Research Laboratory Report 102, United Kingdom
- Wiss JF (1981) Construction vibrations: state of the art. *ASCE J Geotechn Div* 94(9):167–181
- Wolf JP (1994) Foundation vibration analysis using simple physical models. PTR Prentice Hall, Upper Saddle River, NJ
- Zienkiewich OC, Taylor RL (1991) The finite element method, vol 2, 4th edn. McGraw Hill, London

# Index

## A

- Accelerometers range, 44–46, 64
- Active faults, 33
- Aliasing, 42, 44, 48, 64
- Allowable permanent wall displacements, 121, 133
- Analogue type filters, 49
- Angles of inclination to the horizontal of a critical slip surface behind a wall, 119, 121
- Annual rate of exceedance, 2, 8–9
- Average soil damping ratios, 69–70
- Average transversal wave velocities, 220
- Axial vertical stress at a depth, 161

## B

- Background noise, 48, 56
- Base line error, 50
- Bearing capacity, 112–116, 126, 130–132, 140–141, 152–153, 167, 175, 190, 250
- Bench blasting, 36, 253
- Bernoulli's equation, 89–90
- Big Bear earthquake, 191–192
- Bishop method, 117
- Body waves, 29, 39–41, 82, 158, 162, 214, 242
- Boundaries between liquefiable and non-liquefiable (silty) sand, 10
- Boussinesq formula, 161
- Buckling, 139, 207, 223

## C

- Central Chile earthquake, 94, 96
- Centrifuge tests, 121–122, 134, 182, 217
- Chaotic behaviour in non-linear dynamics, 18
- Chilean earthquake, 29
- Co-seismic permanent displacements, 5, 83
- Co-seismic sliding, 73, 83, 124, 127, 129
- Cosmetic damage of walls, 235–236
- Cyclic stress ratio, 2, 10–11, 14, 60, 86, 89, 105, 153

Cyclic stress ratio for slopes, 86, 89, 153

Cyclic triaxial, 61, 63, 125

## D

- Damage in tunnels, 207
- Damping ratio, 2, 11–12, 14, 16, 57, 60–62, 69–71, 153, 203–204, 249, 251–252, 255, 257–258
- Decoupling, 42, 44, 64
- Demolition of structures, 36
- Discrete element model, 155, 159
- Dropping heavy weights, 237, 239
- Duration of flow, 91
- Duration of sliding, 78, 80, 83
- Duzce earthquake, 216, 222–223, 227–229
- Dynamic earth pressure increment, 122, 134

## E

- Earthquake intensity, 30–31
- Earthquake magnitude scales, 28
- Edge-cube earthquake, 196
- Environmental sensitivity, 42
- Equivalent frictional angle of a sliding block, 88
- Equivalent number of significant stress cycles, 59, 163
- Equivalent period of structural vibration, 185
- Equivalent sliding block, 87–88
- Equivalent two sliding blocks, 124
- Euler equation, 139
- European Earthquake Data Base, 30
- European-Mediterranean seismic hazard map, 30
- Explosives, 216, 252

## F

- Failure modes of pipelines, 207
- Fast Fourier transform, 49

- Fault rupture area, 28  
Final factor of safety on sliding, 79–83, 127  
Fixation of transducers, 43, 64  
Fling step, 3–5, 27  
Footfall induced floor vibration, 234  
Fourier amplitude spectrum, 8, 49, 154, 195, 229  
Free vibration of an infinite soil layer, 16  
Frequency range, 35, 42, 45, 64, 158–159
- G**  
Gauss integration points, 241–242  
Geophysical cone, 57–58, 64, 69  
Geophysical cross hole method, 56–57  
Geophysical reflection, 54–55  
Geophysical surveying, 51  
Geotechnical centrifuge, 19–20  
Global seismic hazard map, 30  
Grand Banks earthquake, 106  
Green function, 240  
Gross lateral forces moment equilibrium, 140
- H**  
High speed trains, 35, 238–239  
High-strain dynamic (STATNAMIC), 19  
Horizontal drift over a tunnel height, 210  
Horizontal ground displacement, 5, 162, 210, 217, 222, 225, 227  
Hyogoken-Nanbu earthquake, 121, 125, 159, 171–175, 218, 220
- I**  
Impact hammers, 35, 170, 237, 246–249  
Imperial Valley earthquake, 189, 194  
Inertial interaction, 154, 158, 180, 185, 201, 209  
Initial factor of safety before sliding, 76–77, 79–80, 83, 127  
Inverted pendulum, 158, 166, 185  
Iran, 9  
Izmit (Kocaeli) earthquake, 165
- K**  
Kanagawa-ken Seibu earthquake, 195  
Kinematic interaction, 154, 158, 180, 184–185  
Kinematic soil pile interaction, 17  
Kishiro-Oki earthquake, 97  
Kocaeli earthquake, 228  
Kyoshin Network K-NET, 30
- L**  
Landers earthquake, 192  
Landslides occurrence, 32  
Lateral soil force acting on a retaining wall in seismic condition, 118–119  
Lateral soil forces on a retaining wall in static condition, 119  
Linear vibration source, 241, 249  
Local soil layers effect, 28  
Loma Prieta earthquake, 190  
Longitudinal wave velocity, 15, 41, 62–63, 71  
Love waves, 41  
Low-pass (anti-aliasing) filter, 48–49
- M**  
Magnitude scaling factors, 10  
Maximum amplitude of ground displacement, 27, 224  
Maximum fault surface displacement, 28, 34, 220, 223  
Maximum shear modulus, 15, 69, 240  
Maximum slip, 78  
Maximum velocity and acceleration of sliding, 78–83, 127  
Michoacan earthquake, 187  
Moho surface, 3–5, 28  
Moment magnitude, 2–4, 29, 32, 163, 218, 222, 227  
Mononobe-Okabe method, 118, 127, 131, 144
- N**  
 $(N_1)_{60}$ , 28  
The National Geophysical Data Center - NGDC, 30  
Net lateral force moment equilibrium, 140  
Newmark sliding block method, 74, 83, 121, 124, 134, 157  
Nihonkai-Chubu earthquake, 101, 147  
Niigata earthquake, 198–199  
Non-basic errors, 47  
Normal faults, 33–34  
Number of effective acceleration cycles, 163  
Numerical filter, 49  
Nyquist frequency, 48, 50
- P**  
The Pacific Earthquake Engineering Research Center - PEER, 30  
Parnitha earthquake, 145–146  
Particle velocity caused by trains, 35  
Particle velocity due to tunnelling, 239  
Passive lateral soil force in front of a retaining wall in seismic condition, 119

- Peak horizontal ground acceleration, 2, 6, 10, 30, 36, 69–71, 83, 86, 88, 124, 147, 155–156, 163, 183, 191, 207, 211, 222, 241, 251  
Peak horizontal ground displacement, 5, 210, 222  
Peak horizontal ground velocity, 3, 241  
Peloponnesus earthquake, 128, 159  
Petrolia earthquake, 193  
Phase shift, 42, 158  
Pile driving, 21, 35, 42, 58, 64, 170–173, 176, 235, 237, 246–252  
Pile shaft force, 187  
Pile toe force, 246, 249  
Pipeline repair rates, 213, 228  
Planar vibration source, 241  
Point vibration source, 240, 254  
Post-seismic sliding, 83, 124, 127, 129  
Potential of liquefaction of sandy soil, 10  
Predominant period of ground acceleration, 30  
Principal ground strain, 213  
Prismatic vibration source, 241–242, 255  
Punch through type failure, 115  
P-y springs, 181
- R**  
Ratios between the peak horizontal ground acceleration at ground surface and at depths, 211  
Ratio between velocities of the longitudinal and transversal waves, 39  
Rayleigh waves, 9, 29, 40–41, 162, 171  
Residual shear strength, 70  
Resolution, 42, 47–48, 54–55  
Resonance, 36, 60, 166–167, 180, 189, 242–243  
Resonance column, 36, 60, 166–167, 180, 189, 242  
Response spectra, 2, 6–9, 144–147, 156, 163, 184, 189, 191–192, 200  
Return period of earthquakes, 9  
Reverse (thrust) faults, 3–4, 34  
Richter magnitude, 29  
R.m.s. acceleration, 233–234  
Road traffic, 35, 239–240  
Road traffic induced peak particle velocities, 239  
Rotating block model, 157, 176  
Rupture directivity, 3–5, 27, 163
- S**  
Sampling and testing of ground, 51  
San Fernando earthquake, 91  
San Francisco earthquake, 99  
Sectional forces and bending moment in a circular tunnel lining, 209, 217  
Sedimentation time, 91  
Sediment basin edge and depth effects, 3–5, 27  
Seismic gaps, 28  
Seismic moment, 29  
Sensitive equipment, 233  
Sensitivity, 42, 87  
Shaking table, 18–20, 121–122, 154, 181–182  
Shear modulus ratio, 15  
Shear modulus reduction factors, 224  
Shear strength of fine grained soil (fine silt and clay) in cyclic condition, 70  
Shear strength of fine grained soil (fine silt and clay) in static condition, 70  
Simple bearing capacity analogy, 141  
Simple shear test, 13–14, 59–60, 71  
Single degree of freedom oscillator, 7, 12, 203  
Slope failures, 30–33, 70, 72  
Soil dry density, 160  
Soil friction angle, 67, 69, 87–88, 95, 113–114, 116–118, 123, 125, 141  
Soil friction angle in cyclic condition, 69, 87, 123  
Soil liquefaction in static conditions, 86  
Soil permeability of water, 63  
Soil porosity, 63, 68, 160–161  
Soil relative density, 15, 67  
Soil shear modulus, 11, 15–16, 18, 155, 209, 238  
Soil stiffness decrease, 69  
Soil void ratio, 67–68, 160  
Source energy, 44, 249, 258  
Source to site distance, 27, 74, 83, 124, 127, 131, 133  
Specific gravity of soil solids, 160  
Standard penetration test, 10, 15, 57, 67, 69, 71, 86–87, 125, 129, 132, 160, 164, 168, 174, 197–199  
Static stiffness coefficients, 17  
Static stresses in tunnel lining, 224  
Stokes law, 91  
Strains, 41, 51, 58, 179, 182, 208, 227  
Stresses, 39, 41, 51, 59, 63, 65, 68, 86, 113–117, 141–142, 146–147, 163, 180, 182, 208, 212, 224  
Strike-slip faults, 3–4, 34  
Surface rupture length, 28  
Surface waves, 40, 107, 158, 214–215

**T**

- Transient ground strain, 214  
Transversal forces and bending moments in rectangular tunnels, 210  
Transversal wave velocity, 3–5, 15–16, 18, 41, 60, 71, 86, 144, 146, 154–155, 159, 162, 169, 183, 187, 194, 210–211, 218–220, 223–224, 245, 252, 257  
Truncated cone, 161  
Tsunamis, 29, 33, 35  
Turbidity current, 107  
Turbidity flow, 105  
Two-block sliding method, 74, 76, 134

**U**

- Ultimate bearing stress in undrained conditions, 115

The United States Geological Survey – USGS, 30

**V**

- Velocity transducer, 43  
Vertical shafts, 207–229  
Vibrating stone columns, 239  
Vibration from blasting, 249  
Vibration hammers, 246  
Vibration mode, 17, 191–192, 211, 220–221  
Vibrations from blasting, 235  
Vibratory hammers, 247–248, 251  
Vibratory rollers, 36, 238, 242, 245  
Viscous damping coefficients, 17–18  
Void ratio, 15, 67–68, 160

**Y**

- Yong modulus, 69